COMBINED EXPERIMENTAL-NUMERICAL INVESTIGATION OF MICROSTRUCTURE AND THERMAL CONDUCTION IN SQUEEZED THERMAL INTERFACE MATERIALS

by

Rajath Kantharaj

A Dissertation

Submitted to the Faculty of Purdue University

In Partial Fulfillment of the Requirements for the degree of

Doctor of Philosophy

School of Mechanical Engineering

West Lafayette, Indiana

December 2021

THE PURDUE UNIVERSITY GRADUATE SCHOOL
STATEMENT OF COMMITTEE APPROVAL

Dr. Amy M. Marconnet, Chair
School of Mechanical Engineering

Dr. Carl Wassgren
School of Mechanical Engineering

Dr. Aaron Morris
School of Mechanical Engineering

Dr. Edwin Garcia
School of Materials Engineering

Approved by:
Dr. Nicole L. Key

ACKNOWLEDGMENTS

I would like to thank my advisor Prof. Amy Marconnet for her relentless support throughout my PhD journey. It was an honor working with her and I will never forget her hands-on mentorship and guidance. In addition, I would like to thank my committee members Prof. Carl Wassgren and Prof. Aaron Morris who advised and provided feedback throughout the duration of this project. I have thoroughly enjoyed working with these professors and have immensely learned during my time as a graduate student. I am also grateful to Prof. Timothy Fisher for his support during my time as a visiting undergraduate research scholar during Spring 2016, and his guidance and mentorship during the initial stages of my PhD studies.

I would like to thank the Cooling Technologies Research Center (CTRC) for funding this project. I enjoyed speaking with the CTRC industry members about my project and greatly appreciate their feedback. I would also like to thank Prof. Justin Weibel, director of CTRC, who actively participated in the monthly teleconferences with the industry members. I am thankful to Dr. Dhanajay Pai for training me on the X-ray micro computed tomography machine, Zhengpu Chen for training me on the Instron mechanical tester, and Yumeng Zhao for training me on the particle size analyzer. I am also thankful to Dr. Clairmont Clementson for quickly addressing any laboratory equipment issues. I sincerely appreciate the technical support and guidance from my MTEC colleagues and friends – Dr. Collier Miers, Dr. Aaditya Candadai, Aalok Gaitonde, Rishav Roy, Dr. Saaketh Desai, Dr. Prabhu Kumar. It is impossible to say how much I have learnt by working with Dr. Miers and Aalok – these two are incredible at experimental research. I thank Harris Tariq Fathe and Grant Gauthier for designing and machining the squeeze rig. They accomplished it smoothly during the COVID-19 pandemic. I also thank my childhood friends Sanjay and Sujan for their support and friendship and the Manipal memories we share. I hope our 20+ years of friendship will continue forever.

Finally, I thank my parents and brother, best friend and confidant Dr. Bharath Kantharaj for their constant support spanning all dimensions. I would also like to thank my uncle Swaroop, aunt Lalitha, and their son Bhargava for their constant support and for being there whenever I needed them.

TABLE OF CONTENTS

LIST OF TABLES 7
LIST OF FIGURES 8
ABSTRACT 19
1. INTRODUCTION 22
1.1 Motivation and Background 22
1.2 Objectives and Major Contributions 24
1.3 Outline of the Document 26
2. LITERATURE REVIEW 28
2.1 Microstructure and Thermal Transport in TIMs 28
2.1.1 Heat Conduction in TIMs 28
2.1.2 Microstructure of Particulate Media 30
2.2 Particle Redistribution in TIMs 35
2.3 Thermal Conduction Modeling in TIMs 38
2.3.1 Network Thermal Model 40
2.3.2 Finite Element (FE) Thermal Model 45
2.4 3D X-ray Micro Computed Tomography (XRCT) Imaging 46
2.5 Discrete Element Method (DEM) Simulation 49
2.5.1 Contact Force Models 51
3. 3D X-RAY MICRO COMPUTED TOMOGRAPHY ANALYSIS OF DISPENSED AND SQUEEZED TIM MICROSTRUCTURES 54
3.1 Introduction 54
3.2 TIM Preparation and Constituent Materials 54
3.3 Manual Procedure for Application of the TIM 56
3.4 Automated Procedure for Application of the TIM 58
3.4.1 Automated Dispensing 58
3.4.2 Constant Velocity Squeezing 61
3.5 3D XRCT Scan Set-up, Reconstruction, and Image Processing 69
3.5.1 Experimental Set-up for 3D XRCT Scan 69
3.5.2 3D XRCT Reconstruction 71

3.5.3 3D Image Processing Workflow 74
3.6 Squeeze Process-induced Variation 89
3.7 TIM Microstructure Analysis 96
3.7.1 Bulk Particle Volume Fraction and Coordination Number 96
3.7.2 Radial Distribution Function 102
3.7.3 Local Particle Volume Fraction 106
3.8 Discussion on the Péclet Number 111
3.9 Concluding Remarks 113
4. PREDICTIVE MICROSTRUCTURE MODELING OF TIMs 116
4.1 Introduction 116
4.2 Simulation Workflow in MFIX 116
4.3 Constant Velocity Squeeze Model 119
4.3.1 Simulation Set-up in MFIX 119
4.3.2 Top Wall Dynamics and Fluid-Particle Coupling 122
4.3.3 Verification of the Squeeze Model 129
4.4 Squeezed TIM Microstructural Features 131
4.4.1 Predicted BLT, Bulk Particle Volume Fraction and Coordination Number 132
4.4.2 Radial Distribution Function (RDF) and Local Particle Volume Fraction 135
4.5 Comparison with Experimental Data 138
4.6 Concluding Remarks 140
5. THERMAL CONDUCTION MODELING IN TIMs 142
5.1 Introduction 142
5.2 Network Thermal Model 142
5.3 Particle Geometry-based Finite Element Thermal Model 145
5.4 Model Construction and Analysis 148
5.5 Concluding Remarks 153
6. CONCLUSIONS AND FUTURE WORK 155
6.1 Summary 155
6.2 Future Research Directions 157
APPENDIX A. 3D XRCT IMAGE ANALYSIS 160
APPENDIX B. REDUCED ORDER THERMAL MODEL 162

REFERENCES 164

LIST OF TABLES

Table 3.1. Materials used in this study and their properties 55

Table 3.2 Volume distribution based D-sizes of the spherical copper particles based on measurements from Malvern Mastersizer 3000. 57

Table 3.3 Volume distribution based D-sizes of the spherical copper particles for automated tests based on measurements from Malvern Morphologi G3-ID 68

Table 3.4. 3D XRCT scan settings for TIM samples produced manually and via automated procedures 71

Table 3.5. Software packages used for processing 3D XRCT image cross-section reconstruction, viewing and analysis 72

Table 3.6 Comparison of the volume distribution-based D-sizes of the equivalent sphere diameter between laser-diffraction measured and XRCT-detected particle sizes. The TIMs were manually dispensed and squeezed, and the particles (dry state) were measured using Malvern Mastersizer 3000 80

Table 3.7 Comparison of the volume distribution-based D-sizes of the equivalent sphere diameter between high resolution optical image-based measurements and XRCT-detected particle sizes of dispensed TIM samples produced via automated procedures. 82

Table 3.8 Comparison of the volume distribution-based D-sizes of the equivalent sphere diameter between high resolution optical image-based measurements and XRCT-detected particle sizes of squeezed TIM samples from *Set 1* produced via automated procedures. Note C refers to the Central and CE to the Center-Edge samples 85

Table 3.9 Comparison of the volume distribution-based D-sizes of the equivalent sphere diameter between high resolution optical image-based measurements and XRCT-detected particle sizes of squeezed TIM samples from *Set 2* produced via automated procedures. Note C refers to the Central and CE to the Center-Edge samples 88

Table 3.10 Comparison of the basic microstructural features, ϕp and CN, of the three dispensed TIM samples. 98

Table 3.11 Statistical variation in bulk microstructural properties, ϕp and CN, of the two Center-Edge squeezed TIM calibration samples. These samples were produced at $VS = 10$ mm s $- 1$ and $FS = 100$ N. <> denotes mean of the bulk property values of the two samples. 99

Table 3.12 Comparison of bulk microstructural properties, ϕp and CN, of the whole microstructures and rectangular subdomains used in the RDF computation and local particle volume fraction analysis. Center-Edge and Central squeezed TIM samples from *Set 1* and *Set 2* are denoted by CE and C, respectively. 105

Table 4.1 DEM squeeze simulation parameters 121

Table 6.1 Directions for future work 157

LIST OF FIGURES

Figure 1.1. Schematic showing dry contact area at a solid-solid interface. Surface roughness causes limited contact points and a high thermal resistance air gap between the solid surfaces. 23

Figure 2.1. (a) TIM applied at the interface between two materials and an accompanying temperature versus distance plot showing bulk and interface thermal resistance as temperature jumps. The bulk TIM thermal resistance is the temperature jump within the bulk of the material that depends on the characteristic length (known as BLT) across which heat is conducted and the material conductivity. In addition, there will be interface or contact thermal resistance between the TIM-material interfaces. (b) Schematic showing contact thermal resistance between the TIM and material due to imperfect wetting of the materials by the TIM. Note that even if the TIM perfectly wets the material, there will still be an interface thermal resistance due to the differences in chemical make-up and structure of the materials [48]. The overall TIM resistance is the sum of its bulk resistance and the interface resistance. Republished with permission of (a) Prasher [14] and (b) from Smoyer and Norris [4]; permission conveyed through Copyright Clearance Center, Inc. 29

Figure 2.2. Illustration of distribution of the local coordination number in a simulated bed of packed spheres. (a) DEM-generated packing of spherical particles with color coding based on coordination number and (b) histogram of the local coordination number. In this example the mean coordination number is 5.6. Reproduced from Roozbahani *et al*. [84]. 31

Figure 2.3. Fundamentals of radial distribution function. In a plot of RDF, the horizontal axis is generally distance normalized by diameter of atoms, molecules, or particles, and the vertical axis indicates number of nearest particles at that distances: **(a)** RDF for solid (solid curve) and liquid Argon (dashed line with fitted points plotted as circles) – liquid molecules have higher kinetic energy than their solid counterparts, therefore, possess more randomness and fewer peaks (adapted from Franchetti [88]), **(b)** Experimental (curves A, C) and theoretical (curves B, B') RDF profiles for liquid Argon at 90 K (reproduced from Kirkwood and Boggs [86]), **(c)** RDF of packed monodisperse acrylic beads ($58.6 - 64\%$ packing fraction) imaged using 3D XRCT technique; the first major peak indicates contacting neighbors and, with greater distances, there are a few neighbors and that indicates some ordering in the packing (reproduced from Aste *et al*. [87]) and **(d)** Experimentally determined RDF of self-assembled spherical particles under gravity and in the presence of vibration. Looking at the three plots top to bottom, we see more peaks in the RDF as the structure becomes more ordered (reproduced from Becerril-Gonzalez *et al*. [90]). Republication permission conveyed through Copyright Clearance Center, Inc. 32

Figure 2.4. Schematics of (**a**) random and (**b**) aligned microstructures of a TIM consisting of spherical particles. Higher bulk thermal conductivity is expected along the direction of alignment. 33

Figure 2.5. **(a)** Schematic of two contacting particles (A and B) showing the branch vector and contact normal vector. The branch vector connects the centroids of the two particles and the contact normal vector is a vector normal to the contact plane of the particles, pointing from A to B (reprinted from Stershic *et al*. [94] with permission from Elsevier). **(b)** Schematic of a particle with three neighboring contacts. To calculate the fabric tensor, first, the dyadic product of the vectors

$n1, n2,$ and $n3$ are calculated with themselves. Then, that quantity is averaged over all contacts in the microstructure (republished with permission of Olsen and Kamrin [95]; permission conveyed through Copyright Clearance Center, Inc.) 34

Figure 2.6. Two-dimensional schematic of the network thermal model. (**a**) Particle networks with imposed Dirichlet boundary conditions, TH (hot) and TC (cold), on either ends and adiabatic boundaries (top and bottom). (**b**) Network of equivalent electrical resistors through which heat conduction is modeled. 39

Figure 2.7. Schematics of heat flow paths considered in the network model: **(a)** between two intersecting particles, **(b)** between geometrically non-contacting particles that are close enough for the thermal resistance through the matrix to be relatively small, and **(c)** from a boundary to surface particles. Note that overlapping particle case (a) is strictly non-physical, but provides a treatment for DEM-simulated microstructures where slight overlap is used to compute contact conditions or for artifacts induced via XRCT image processing (*e.g.*¸ slightly non-spherical particles that are now modeled as spherical). The gray cylinders are the cylindrical zones across which heat is conducted. The radius of the regions with conduction ($Rij, rc,$ and Ri, BND) depends on the particle radii (Ri and Rj) for pairs (cases a and b) and on the single particle radius (Ri) for particles in close proximity to a boundary (case c). The effective conductance for the cylindrical zone is calculated and a global conductance matrix is constructed to solve for steady-state particle temperatures. 41

Figure 2.8. Schematics of XRCT working principle. A typical polychromatic source emits a conical beam of X-rays. As the object rotates through either $180°$ or $360°$, several intensity projections are collected by the detector, and these are collectively reconstructed using sophisticated algorithms to generate cross-sectional slices – stacking these up gives a full 3D representation of the object. Reprinted from Wildenschild and Sheppard [159] with permission from Elsevier. 47

Figure 2.9. 3D XRCT scan of particle-polymer composite material used in this work. **(a)** Intensity projection or raw image at one object orientation, **(b)** a cross-sectional slice from the 3D reconstruction, and **(c)** 3D reconstruction of the composite material. The TIM was prepared in-house by hand mixing a target of 30 vol% of $90 - 125$ μm copper particles with a UV-curable polymer (details are deferred to chapter 3). 48

Figure 2.10. Schematic of particles i and j interacting with each other at a time instant. They are approaching each other with velocities vi and vj, respectively. The normal nij points from particle i to j. The tangential direction points along tij. The magnitude of normal and tangential overlaps are δn and δt, respectively. 52

Figure 3.1 Manually (**a**) dispensed line pattern and (**b**) squeezed TIM on a glass slide covered with a copper foil. Dispensing is performed using a syringe fitted with a straight metallic needle, with an opening diameter of 838 μm (18 gauge). Squeezing is manually performed using a bare glass slide on the top. The white lines in (a) and the white rectangle in (b) denote the samples used for XRCT imaging. 56

Figure 3.2 Volume distribution, $q3$ ($\mu m - 1$), of the particle equivalent sphere volume diameter, Dp. The particles were initially sieved to a size range of $90 - 125$ μm. The measurement is performed using Malvern Mastersizer 3000. 57

Figure 3.3 Schematic of the experimental rig for controlled dispensing the TIM. The backbone frame structure is made out of aluminum. The syringe is mounted on the Z stage. The glass substrate (not shown) is on the X stage, which moves out of the page as the plunger pushes the TIM out of the syringe nozzle to deposit a line pattern. The rig was previously designed and developed in-house by former colleagues Sally Jia and Dr. Collier Miers. 58

Figure 3.4 (**a**-**b**) Schematic of the bottom glass slide showing three rectangular strips of double-sided tape used to affix the copper foil. (**c**) Two isolated line patterns of the TIM dispensed at the rate of ≈ 1.2 ml min $-$ 1 on a glass slide covered with copper foil. Note that gravity is into the plane of the page. (**d**) Sample cut out (length ≈ 5 x 10 $-$ 3 m or 0.2 inch) from near the center after a 2 hour UV cure, showing uncured TIM near the contact region with the copper foil (gray polygonal outline). The gray rectangle represents the sample region for analysis. The samples are flipped in the bottom image and enlarged (inset) to show uncured portions (gray outline). (**e**) Line pattern dispensed TIM on a bare glass slide. The gray rectangles approximately show the sample regions cut out with length ≈ 5 x 10 $-$ 3 m (0.2 inch). 60

Figure 3.5 Automated constant velocity squeezing using Instron mechanical tester: (**a**) Schematic of the off-axis squeezing process where two line dispense TIM patterns (deposited on the bottom glass substrate) are squeezed at constant velocity and then UV-cured while holding the load constant. (**b**) Model of the squeeze rig adapter designed and manufactured in-house to assist this process. (**c**) Bottom side of the squeeze rig adapter showing two rectangular strips of double-sided tape, on which the top glass substrate is attached. Then, 3M Scotch packaging tape is affixed on this to enable easy removal of samples after squeezing and curing. 62

Figure 3.6 (**a**) Load vs displacement during squeezing for squeeze rate of $VS = 1$ µm s $-$ 1 at two different ultimate squeeze forces $FS = 50$ N and 100 N. (**b, c**) Load vs displacement for the load-holding phase for the two cases, exhibiting variation around the set force over time. These variations are averaged to calculate applied pressure exerted on the TIM during squeezing..... 63

Figure 3.7 Constant velocity squeeze set-up using Instron machine and in-house designed squeeze rig using a (**a**) rigid and (**b**) flexible UV lamp fixture. The advantage with the flexible fixtures in (b) is the significantly shorter light source-to-sample distance. Optical images of the sample after (**c**) squeezing and 1 hour of UV curing, and (**d**) the squeeze rig is removed and the samples are ready to be retrieved from the bottom glass slide. 64

Figure 3.8 Schematic of samples cut out from the squeezed TIMs. (**a**) The ideal sample spans the width of the TIM in the X direction (*i.e.*, primary direction of particle redistribution). The reduced sample, obtained by cutting the ideal sample at its centerline, is used for XRCT imaging due to limited FOV and resolution implications. (**b**) Center-Edge and Central samples are manually cut out from two distinct TIMs produced in the squeeze tests. Samples are consistently prepared: Center-Edge samples are obtained from the left (L) TIM and Central samples from the right (R) TIM. In this work, w is dictated by the sample dimensions, and $d \approx d' \approx w' \approx 0.2$ inch $\approx$ 5.08 mm ≈ 47 median particle diameters Dm, ce. 65

Figure 3.9 Optical images of the squeezed and cured TIMs with different curing conditions. TIM cured using the rigid lamp fixture for (**a**) 45 minutes and (**b**) 1 hour. (**c**) Images of the TIM samples in (b) after removal from the squeeze rig. (**d**) TIM cured using the flexible lamp fixture for 1 hour. Gray polygonal regions outline the regions from where the TIM is removed and encompass the

slightly uncured portions. In panels (a), (b) and (d), the light yellow rectangles indicate regions that are illumiated by UV light. 67

Figure 3.10 Volume distribution, $q3\ \mu m - 1$, of the (**a**) circle equivalent particle diameter, Dce, and (**b**) circularity, Cp, analyzed from high resolution optical imaging of $\approx 11{,}400$ copper particles (dry state). The measurement is performed using the Malvern Morphologi G3-ID instrument for particles initially sieved to a size range of $90 - 106\ \mu m$. 68

Figure 3.11 XRCT imaging set-up: (**a**) Top view of a squeezed TIM sample placed on Styrofoam and photographed prior to scanning, (**b**) Cartoon of TIM samples assembled on a small piece of wooden block to enable parallelized, high resolution 3D XRCT imaging. Each TIM sample is doubly wrapped with Parafilm to affix it to the wooden block, which itself is tightly bound to the metal rod using a wider piece of Parafilm (wrapped horizontally). This minimizes relative motion between the sample, block and the rod to obtain a noise-free image reconstruction..... 70

Figure 3.12 3D XRCT reconstruction of the manually **(a, b)** dispensed and **(c, d)** squeezed TIMs performed using CTVox. The voxel resolution is 1.9 μm3. Samples for imaging are prepared by dispensing a line pattern of the TIM on a glass microscope slide (covered with copper foil) and then, squeezing it manually using another glass slide on top. The two samples are separately cured and small portions were cut out for XRCT imaging (see section 3.3). The median particle diameter is $114\ \mu m$. The squeezed TIM is approximately ~ 2.6 particles thick with a BLT of $\approx 297\ \mu m$. 73

Figure 3.13 **(a)** Front, (**b**) side, and (**c**) top views of the 3D XRCT reconstructed image of a TIM dispensed on bare glass slide using automated procedure. The voxel resolution is $3.5\ \mu m3$. 74

Figure 3.14 **(a)** Front, (**b**) side, and (**c**) top views of the 3D XRCT reconstructed image of the TIM dispensed on a glass slide covered with copper foil using automated procedure. The voxel resolution is $3.5\ \mu m3$. 74

Figure 3.15 **(a)** Front, (**b**) side, and (**c**) top views of the 3D XRCT reconstructed image of the TIM dispensed on a glass slide covered with copper foil and squeezed at $VS = 1\ \mu m\ s - 1$ and $FS = 50$ N using automated procedures. The voxel resolution is $3.5\ \mu m3$. 75

Figure 3.16 Flowchart of the 3D image processing using FIJI toolkit to extract particle locations and sizes. The algorithm involves noise filtering, thresholding, artifact removal (*i.e.*, a fill hole operation), watershed segmentation, and analysis of individual particles. Noise filters such as median, adaptive, non-local means, and minimum + median are available. The watershed segmentation involves a user-controlled "dynamic" parameter that balances over- and under-segmentation. 76

Figure 3.17 3D image processing flowchart showing the effect of various image operations such as filtering, thresholding, filling of holes, and watershed segmentation on a manually squeezed TIM sample. In this figure, a 3D median filter is used on the raw image dataset. As noted in the text, the NLM filter is used for all samples from the automated tests. The image size is approximately 1.88 mm x 2.03 mm. 76

Figure 3.18 Detected particle locations and sizes (*i.e.*, equivalent sphere diameter Dp) plotted using the open-source visualization software ParaView. Front and top views of the manually (**a, b**) dispensed and (**c, d**) squeezed TIM samples. 79

Figure 3.19 Particle size distribution (PSD) comparison between the XRCT-detected particle sizes of squeezed and dispensed TIMs, and that of laser diffraction measurement using Malvern Mastersizer 3000. 80

Figure 3.20 Visualization of line pattern dispensed TIM microstructure of the (**a-c**) center (*Sample 1*) and (**d-f**) off-center (*Sample 2*) samples. In both cases, the heap shape of the dispense pattern is distinctly visible (**a, d**). These TIMs are dispensed on bare glass microscope slide using automated procedures. 81

Figure 3.21 Visualization of line pattern dispensed TIM microstructure of a central sample (*Sample 3*). (**a**) Front, (**b**) top and (**c**) side views. This TIM is dispensed on glass microscope slide covered with copper foil using the automated procedures. 81

Figure 3.22 Volume distribution of particle size, $q3$, analyzed from the processed 3D images of dispensed TIM samples. There is a good agreement between measured size distribution from Malvern Morphologi G3-ID instrument and from the 3D XRCT image analysis. The XRCT scans are obtained at a voxel resolution of $3.5\ \mu m3$. The plot also suggests that the particle sizes do not significantly vary between the different samples. Note that area under each curve is ≈ 1. 82

Figure 3.23 Detected particle locations and sizes (*i.e.*, equivalent sphere diameter Dp) plotted using ParaView. Top view of the *Set 1* Center-Edge samples produced via the automated dispense and squeeze procedures. The centerline of the line dispense pattern is denoted by the black dashed line. 83

Figure 3.24 Detected particle locations and sizes (*i.e.*, equivalent sphere diameter Dp) plotted using ParaView. Top view of the *Set 1* Central samples produced via the automated dispense and squeeze procedures. The centerline of the line dispense pattern is denoted by the black dashed line. 83

Figure 3.25 Volume distribution of particle size, $q3$, analyzed from the processed 3D images of the two types of squeezed TIM samples from *Set 1* test: (a) Central and (b) Center-Edge samples. There is an acceptable level of agreement between the size distributions measured using the Malvern Morphologi G3-ID instrument and detected by processing the 3D XRCT images. The XRCT scans are obtained at a voxel resolution of $3.5\ \mu m3$. Note that area under each is ≈ 1.. 84

Figure 3.26 Measured (a) BLT and (b) squeeze pressure, PS, for the TIM samples from Set 1 test. FS is the set force and VS the squeeze rate. To compute pressure, the average force during the load-holding phase is estimated. Fast = $10\ \text{mm s} - 1$ and Slow = $10 - 3\ \text{mm s} - 1$ 85

Figure 3.27 Detected particle locations and sizes (*i.e.*, equivalent sphere diameter Dp) plotted using ParaView. Top view of the *Set 2* Center-Edge samples produced via the automated dispensing and squeezing procedures. 86

Figure 3.28 Detected particle locations and sizes (*i.e.*, equivalent sphere diameter Dp) plotted using ParaView. Top view of the *Set 2* Central samples produced via the automated dispensing and squeezing procedures. 87

Figure 3.29 Volume distribution of particle size, $q3$, analyzed from processing 3D images of the two types of squeezed TIM samples from *Set 2* test: (**a**) Central and (**b**) Center-Edge samples. There is an acceptable level of agreement between the size distributions measured using the

Malvern Morphologi G3-ID instrument and detected by processing the 3D XRCT images. The XRCT scans are obtained at a voxel resolution of 3.5 μm3. Note that area under each is ≈ 1... 87

Figure 3.30 Measured (**a**) BLT and (**b**) squeeze pressure, PS, for the TIM samples from *Set 2* tests. FS is the set force and VS the squeeze rate. To compute pressure, the average force during the load-holding phase is estimated. Fast = 10 mm s − 1 and Slow = 10 − 3 mm s − 1..... 88

Figure 3.31 Measured (**a**) BLT and (**b**) squeeze pressure as a function of squeeze rate VS for a fixed load of 100 N. The error bars are one standard deviation based on measurement of two TIM samples per test. The BLT values are almost constant in the range of $VS = 10 - 3 - 10$ mm s − 1. 89

Figure 3.32 Detected particle locations and sizes (*i.e.*, equivalent sphere diameter Dp) plotted using ParaView. These samples are produced by repeating two tests (parameters noted in the figure) based on results from *Set 1*. Top view of the (**a**) Center-Edge and (**b**) Central samples produced via the automated dispense and squeeze procedures. The axis of the line dispense pattern is denoted by the black dashed line. 90

Figure 3.33 Volume distribution of particle size, $q3$, analyzed from processing 3D images of the two types of squeezed TIM samples – (**a**) Central and (**b**) Center-Edge. These samples are produced from repeat tests at two different test conditions based on results from *Set 1*. The XRCT scans are obtained at a voxel resolution of 3.5 μm3. Note that area under each curve is ≈ 1..... 91

Figure 3.34 Measured TIM bond line thickness, BLT (μm), for samples produced from four tests, labeled "1" through "4", at the same squeeze condition of $VS = 10$ mm s − 1 and $FS = 100$ N. The red horizontal line (236.5 μm ≈ 2.2 $Dm,\ ce$) is the average from all measurements. The error bars are one standard deviation based on three measurements per sample. Left and Right TIMs denote the two samples produced in a single test. 92

Figure 3.35 Optical images of the (**a**) right and (**b**) left TIM samples from three tests under the same squeezing conditions. Lower particle concentration regions are observed near the edges for some cases. Its occurrence is not uniform, despite test conditions being held constant. 92

Figure 3.36 Comparison of TIM area, $ATIM$ measured in pixel units, for the samples from the last three tests. 93

Figure 3.37 (**a**) Gray-scale image of a TIM sample showing three horizontal lines along which the image intensity is compared for samples from the three tests. Line intensity profile at three locations near the (**b**) top, (**c**) center and (**d**) bottom. 93

Figure 3.38 Isolated line patterns of TIM dispensed on bare glass microscope slide for investigating the squeeze process induced variation under fixed test conditions. In (**b**), the teardrop shape at the edges of the dispensed TIM is highlighted by yellow ovals. The spreading area of the TIM is lower there..... 94

Figure 3.39 Optical images of the TIM squeezed on bare glass slide substrate (**a**) *Test 1* and (**b**) *Test 2*. In (b), the teardrop shape in the dispensed TIM has reduced the width near the edges.... 95

Figure 3.40 (**a**) Gray-scale image of a TIM sample showing three horizontal lines along which the image intensity is compared. (**b**) Intensity profile of the squeezed TIM at the edges and near the center, from the samples shown in Figure 3.39. 95

Figure 3.41 Examples of convex hull constructed over the representative microstructures of (**a**) dispensed and (**b**) squeezed TIM. This is the bounding box for computing the bulk particle volume fraction. Particles are colored based on size, but the color bar is omitted in this figure. 97

Figure 3.42 (**a**) Bulk volume fraction, ϕp, and (**b**) coordination number, CN, for *Set 1* squeezed TIM samples compared with the average properties of dispensed TIM based on *Sample 1* and *Sample 2* (see Table 3.10). Squeezing lowers ϕp and slightly increases CN. Center-Edge and Central samples are denoted by CE and C, respectively. Fast = 10 mm s $-$ 1 and Slow = $10 -$ 3 mm s $-$ 1. 99

Figure 3.43 Sample-to-sample variation in (**a**) bulk volume fraction, ϕp, and (**b**) coordination number, CN, for repeat tests of a subset of *Set 1* squeezed TIM samples. The numbers 1 (original test) and 2 (repeat test) on top of the bars denote the test type. Center-Edge and Central samples are denoted by CE and C, respectively. Fast = 10 mm s $-$ 1 and Slow = $10 -$ 3 mm s $-$ 1.... 100

Figure 3.44 (**a**) Bulk volume fraction, ϕp, and (**b**) coordination number, CN, for *Set 2* squeezed TIM samples compared with the average properties of dispensed TIM based on *Sample 1* and *Sample 2* (see Table 3.10). Squeezing lowers ϕp and slightly increases CN. Center-Edge and Central samples are denoted by CE and C, respectively. Fast = 10 mm s $-$ 1 and Slow = $10 -$ 3 mm s $-$ 1. 101

Figure 3.45 Front and top views of three different rectangular subdomain selections from the dispensed TIM microstructure. (**a**) "Tall" box, (**b**) "Normal" box, and (**c**) "Wide" box. These are named according to their appearance and aspect ratio. The number of particles in these regions are, respectively, $2656, 3572,$ and 4021. 102

Figure 3.46 (**a**) RDF of dispensed TIM Sample 1 for three different rectangular subdomains, namely, "Normal", "Tall" and "Wide", selected manually from the whole microstructure. The agreement is great, suggesting that the computation is region-independent. The number of particles in these regions are, respectively, 3572, 2656 and 4021. (**b**) Dispensed TIM RDFs for the three samples described earlier (see Table 3.10). The RDFs agree well with each other, suggesting a statistically similar microstructure. The rectangular subdomains analyzed here consist of 3572, 2628 and 4714 number of particles. 103

Figure 3.47 Top view of a large rectangular subdomain selected for RDF computation from a squeezed TIM Center-Edge microstructure. 104

Figure 3.48 RDF, $g(r)$, of *Set 1* (**a, b**) and *Set 2* (**c, d**) squeezed TIM samples compared with the dispensed TIM *Sample 1*. The radial distance is denoted by r. Fast = 10 mm s $-$ 1 and Slow = $10 -$ 3 mm s $-$ 1. 106

Figure 3.49 Top and side views of the rectangular boxes of size ≈ 5 x 5 particle diameters used in the computation of local volume fraction. This microstructure corresponds to a TIM produced at $VS = 10$ mm s $-$ 1 and $FS = 50$ N. As seen in the side views, the box thickness varies to ensure a tight fitting. An average box thickness is used in the local volume fraction computation. 107

Figure 3.50 Top view of the local volume fraction map for *Set 1* squeezed TIM samples. The computation is performed on a large rectangular subdomain whose bulk properties are approximately equal to that of the whole microstructure. The center to edge direction denotes the primary direction along which particles rearrange after squeezing. In the panels, the Center-Edge

and Central samples are arranged left and right figures, respectively. Black dashed line represents centerline of the dispense pattern. Fast = 10 mm s $-$ 1 and Slow = $10 - 3$ mm s $-$ 1. 108

Figure 3.51 Local volume fraction histogram for *Set 1* squeezed TIM samples. The vertical magenta, dash-dot line is the bulk particle volume fraction computed using the convex hull method for the subdomain microstructure. 109

Figure 3.52 Top view of the local volume fraction map for *Set 2* squeeze TIM samples. The computation is performed on a large rectangular subdomain whose bulk properties are approximately equal to that of the whole microstructure. The center to edge direction denotes the primary direction along which particles rearrange after squeezing. In the panels, the Center-Edge and Central samples are arranged left and right figures, respectively. Black dashed line represents centerline of the dispense pattern. Fast = 10 mm s $-$ 1 and Slow = $10 - 3$ mm s $-$ 1. 109

Figure 3.53 Local volume fraction histogram for *Set 2* squeezed TIM samples. The vertical magenta, dash-dot line is the bulk particle volume fraction computed using the convex hull method for the subdomain microstructure. 110

Figure 3.54 Local volume fraction plot along center-to-edge direction for (**a**) *Set 1* and (**b**) *Set 2* squeezed TIM samples. This is obtained by averaging the local volume fraction along Y, and then plotting along X, with reference to Figure 3.52 and Figure 3.54. Open circles are for Central samples and star markers are for Center-Edge samples. Fast = 10 mm s $-$ 1 and Slow = $10 -$ 3 mm s $-$ 1. 111

Figure 3.55 Péclet number, Pe, as a function of squeeze rate, VS, for the mock TIMs investigated in this work. 113

Figure 4.1. DEM squeeze simulation work flow in MFIX showing the use of two user-defined functions (*usr0_des* and *usr1_des*). These two functions are used to read initial particle configuration, and compute particle-top wall interactions and assist in drag force calculations, respectively. 118

Figure 4.2. Initial configuration for DEM simulation obtained from 3D XRCT image analysis of a line pattern dispensed TIM. (**a**) Dispensed TIM central sample (*Sample 1*) used for 3D XRCT imaging, (**b**) 3D reconstructed image dataset for that sample, (**c, d**) particle sizes and locations of the sample from (b) plotted using ParaView. The horizontal black dashed lines represent a section of the dispensed TIM ≈ 5 median particle diameters in length used in the squeeze simulation.119

Figure 4.3. Initial configuration (**a**) front and (**b**) top views, consisting of 966 particles, showing the gray simulation domain box. The initial location of the polymer matrix is highlighted by the light red region around the particles. Squeezing occurs along the $-Y$ direction and particles spread along the X direction, whereas the Z direction (along the axis of dispensing) is periodic. Although the domain height along the Y direction is large and there is a significant amount of empty space above the particle bed, the top wall is placed right above the topmost particle along Y. The length scale is different in (b) to clearly show the edge region where particles intersect the walls. 120

Figure 4.4. Ideal polymer matrix initial location outlined in red. This is an approximate polygonal representation of the heap shape. 121

Figure 4.5. Analytically derived 2D Newtonian fluid squeeze velocity profile based on [57]. The flow is creeping and time independent with pressure variation is only along X. (**a**) Domain set-up with a string of fluid of width α squeezed at a constant velocity, VS, between the plates separated by a distance b; (**b**) 2D velocity profile, as described by Eqns. 4.2 and 4.3, and (**c**) Evolution of the fluid front with time for a constant velocity squeezing simulation, highlighting the increasing width of the fluid string, $\alpha(t)$. Exploiting symmetry in (a), only the evolution of one half (the right-side) of the fluid front is shown with a half-width, $\alpha/2$. 123

Figure 4.6. Ding and Gidaspow drag force normalized by the Stokes drag force, $FDGFS$, plotted as a function of the local particle volume fraction, $\phi p, local$, for various Reynolds number Re. 126

Figure 4.7. Schematic of the simulation domain at an arbitrary time step showing the particles and the computational cells. Some of the cells are far away from the top wall, whereas some are intersected by it. Any partial or whole cell that lies above the top wall does not participate in the squeeze simulation. For cells intersected by the top wall, the local particle volume fraction is corrected by accounting for the actual cell volume. 127

Figure 4.8. Initial particle configuration plotted with rectangular computational cells. MFIX subdivides the simulation domain into these cells based on the domain length and maximum number of cells in $X, Y,$ and Z. 128

Figure 4.9. Evolution of the fluid width α during a squeeze simulation. The position of the fluid front is shown by the black curves visible in (b, c), whereas in (a) it coincides with the yellow vertical edges of the box. Effective area for squeeze pressure is calculated as $Ac = \alpha\ zo$, where zo is width into the plane of the page. The images are taken at x arbitrary time stamps during the squeezing process..... 129

Figure 4.10. Evolution of the maximum overlap-to-particle radius ratio for squeezing at $VS = 15$ mm s $- 1$. The overlap increases first and then drops. Then, it levels out until the end of simulations, where some variations are observed. Throughout the simulations, $\delta max \ll 0.2$.. 130

Figure 4.11. Evolution of the (**a**) fluid front profile and (**b**) farthest particle X positions during a squeeze simulation. The filled circles are the positions of the reference particle. Circles are colored the same as that of the fluid front profiles. The plot shows that the particles are always bound by the fluid, as they should be physically. For illustration, only five time stamps are shown in (a). 131

Figure 4.12. Front view of the squeezed state predicted from DEM simulations at three different velocities: (**a**) $VS = 1$ mm s $- 1$, (**b**) $VS = 10$ mm s $- 1$, and (**c**) $VS = 15$ mm s $- 1$. The dispensed TIM configuration obtained from dispensed *Sample 1* is used to simulate squeezing. 132

Figure 4.14. Predicted (**a**) bulk particle volume fraction, ϕp, and (**b**) coordination number, CN, across a range of squeeze rates, VS, for squeezing of *Sample 1* and *Sample 2* dispensed TIMs. ϕp is computed via the convex hull method described in Chapter 3.7.1. 133

Figure 4.13. Predicted BLT vs squeeze rate, VS for squeezing of *Sample 1* and *Sample 2* dispensed TIMs across a range of squeeze rates, VS. BLT increases monotonically with squeeze rate in this modeling framework. 133

Figure 4.15. Predicted (**a**) bulk particle volume fraction, ϕp, and (**b**) coordination number, CN, across a range of squeeze rates, VS, for squeezing of the dispensed TIM *Sample 1*. 134

Figure 4.16. Whole TIM predicted microstructure (center image) with (**a**) Central and (**b**) Center-Edge subdomains. The Central region is a section of length 10 particle diameters, whereas the Center-Edge region is the right-half subdomain. 135

Figure 4.17. Variation of the predicted (**a**) bulk particle volume fraction, ϕp, and (**b**) coordination number, CN, analyzed for the Central (C) and Center-Edge (CE) subdomain microstructures. 136

Figure 4.18. RDF, $g(r)$, of the predicted squeezed TIM subdomain microstructures: (**a**) Central (C) and (**b**) Center-Edge (CE), at a few different squeeze rates $VS = 1, 5, 10, 15$ mm s $-$ 1 compared with the dispensed TIM initial configuration. 136

Figure 4.19. Rectangular box constructed around the (**a**) Central and (**b**) Center-Edge subdomain microstructures from a simulation with $VS = 15$ mm s $-$ 1. This box is used in the RDF computation. 137

Figure 4.20. Comparison of measured and predicted BLT of the squeezed TIM for a range of squeeze rates. In experiments, the maximum force is set to $FS = 100$ N. The top wall pressure in the predicted squeezed state corresponds to the experimental pressure. 138

Figure 4.21. Comparison of ϕp and CN for the experimental and simulated squeezed TIM, computed for the Central (C) and Center-Edge (CE) microstructures. In experiments, the maximum force is set to $FS = 100$ N. Simulations are carried out up to a critical squeeze pressure that corresponds to the pressure in experiments. 138

Figure 4.22. Comparison of the RDF ($g(r)$) for (a) the Central (C) and (b) the Center-Edge (CE) subdomain microstructures of the predicted squeezed state for simulations at squeeze rate $VS =$ 10 mm s $-$ 1. 139

Figure 4.23. Normalized drag force, $FDGFS$, versus local particle volume fraction, $\phi p, local$, for three different models at various Reynolds numbers: (**a**) $Re = 10 - 6$, (**b**) $Re = 0.1$ and (**b**) $Re =$ 1. 140

Figure 5.1. Simple cubic packing of spherical particles of diameter $Dp = 100$ μm. The packing fraction is $\phi p \approx 52.4\%$. Here, the XY plane consists of a 15 x 15 grid of spheres. 143

Figure 5.2. Variation of bulk thermal conductivity, $kTIM$, of simple cubic packing with NS, the number of spheres along one side of the XY plane. The thickness of the packing is three particle diameters. The predicted conductivity is an order of magnitude higher than matrix conductivity. 144

Figure 5.3. Predicted in-plane temperature profile for a squeezed TIM sample using the network thermal model. 145

Figure 5.4. (**a**) Curved geometry of the squeezed TIM resulting from sample preparation. (**b**) Flattened TIM sample. Particles in (a) are displaced downward to flatten the microstructure. This is a Central sample produced at $VS = 10$ mm s $-$ 1 and $FS = 100$ N. 145

Figure 5.5. Schematics of the TIM particles showing regions where meshing can potentially become a heavy computational expense. (**a**) Intersecting neighboring particles, (**b**) multiple particles in close proximity and (**c**) edge particle surface near the bounding box. 147

Figure 5.6. 2D schematic of the particle size reduction method showing the TIM with (**a**) true and (**b**) reduced particle diameters. $L1$ and $L2$ are the bounding box side lengths that are fixed based on the true particle locations and size. 147

Figure 5.7. TIM microstructure constructed in COMSOL. 148

Figure 5.8. (**a, b**) Steady-state temperature profile in the TIM. (**b**) Side view shows nearly parallel isotherms, suggesting an approximately 1D conduction in the Z direction. 149

Figure 5.9. Cross-section averaged temperature, T, versus distance along the Z direction for various values of χ. 150

Figure 5.10. (**a**) Two-term exponential fit for a Central TIM sample produced at $VS = 10$ mm s $-$ 1 and $FS = 50$ N described by $kbulk \approx 0.23\, e - 4.39x + 0.12\, e0.11x$ and (**b**) error in the predicted bulk conductivity using the fit relative to the testing dataset. The pentagram marker and filled circles in (a) are, respectively, the extrapolated true bulk TIM thermal conductivity for this sample and the validation data points. 150

Figure 5.11. Predicted bulk TIM thermal conductivity for (**a**) *Set 1* and (**b**) *Set 2* squeezed TIM microstructures of Central (C) and Center-Edge (CE) samples. These values are obtained by extrapolating the two-term exponential fit to $\chi = 0$. Fast = 10 mm s $-$ 1 and Slow = 10 $-$ 3 mm s $-$ 1. 151

Figure 5.12. Predicted TIM bulk thermal conductivity, $kTIM$, for the simulated squeezed TIM microstructures at different squeeze rates, VS. 152

ABSTRACT

Thermal management of electronics is one of the biggest engineering challenges of this decade, as billions of transistors are put in each microprocessor and the increasing density leads to increased temperatures. Advances in transistor technology enable fabrication of transistors with dimensions on the order of $1\ \mathrm{nm}$. Due to the enormous number of transistors, a higher frequency of operations is achieved. This directly translates to more Joule heating and microprocessor chip power density exceeding $100\ \mathrm{W\ cm^{-2}}$. In addition, hotspots with heat fluxes in excess of $1\ \mathrm{kW\ cm^{-2}}$ locally increase the temperature leading to non-uniform chip temperatures. If the heat is not dissipated efficiently, the internal temperature of the chip rises, thereby reducing the efficiency and decreasing the lifetime. At the package level, various cooling technologies have been developed — air and liquid cooling, heat pipes, and vapor chambers — to effectively dissipate the heat. But interfaces between the different components of an electronics packaging arise during its assembly due to surface imperfections. These interfaces impede heat conduction from the chip to the heat sink leading to high temperatures. To overcome this issue, thermal interface materials (TIMs) have been developed.

The main goal of a TIM is to provide high effective thermal conductivity and minimize contact thermal resistance at a minimal thickness of the material after application. TIMs generally consist of high thermal conductivity filler particles (*e.g.*, ceramic, metallic, or carbon-based) in a polymer matrix that provides the mechanical conformability in a packaged electronic device. They are generally applied inside the package at the microprocessor chip-metallic lid (or integrated heat spreader) interface or outside the package at the metallic lid-heat sink interface. On an industrial assembly line, the TIM is generally dispensed over the substrate at a controlled flow rate and/or quantity and then squeezed to a final pressure to form the desired bond line thickness. The effective conductivity of the TIM itself depends on the filler particle size, morphology, and particle organization *i.e.*, when the particles form chains or networks of high conductivity pathways across the polymer matrix, the TIM can efficiently conduct heat in the "percolation" regime. There are only a handful of published works that discuss the TIM assembly process-induced modifications of the particle networks within the material and there is a lack of quantitative understanding of

particle rearrangements in the TIM induced by its assembly process, and the effect on its thermal performance during operation.

The objective of this thesis is to fundamentally understand the impact of the particle redistribution within the TIM during squeezing and its impact on the thermal conductivity using combined experimental and computational approaches. Automated procedures for dispensing and constant velocity squeezing are developed in this work to investigate constant velocity squeezing of isolated line dispense patterns of TIMs consisting of large spherical filler particles. In both the dispensed and squeezed/cured states, three-dimensional (3D) X-ray micro computed tomography (XRCT) identifies individual particle diameters and locations and quantifies metrics of the TIM microstructure such as the bulk and local particle volume fraction, coordination number, and radial distribution function (RDF). Squeeze tests are performed at different squeeze rates and loads and the TIM bond line thickness (BLT) is between $200 - 260$ μm ($2 - 2.4$ median particle diameters). The BLT is largely independent of the load at fast squeeze rate, and it decreases with increasing load at slow squeeze rate. The dispensed TIM microstructure is found to be statistically similar along the axis of the line pattern based on the bulk particle volume fraction and coordination number. Squeezing reduces the bulk particle volume fraction likely due to the formation of voids or air bubbles that can cause a volume expansion. Overall, the RDFs for all samples resembled that of disordered microstructures. Trends in the local volume fraction and coordination number did not match between the different tests, likely due to varying substrate surface characteristics resulting from the manual application of copper foil and packaging tape, as well as differing curing time scales. Squeezing the TIM on smooth substrates showed a uniform particle spatial distribution based on optical image analysis, whereas the TIM spreading characteristics appeared to be different on substrates covered with copper foil and packaging tape.

New user-defined functions are integrated into the open-source software Multiphase Flow with Interphase eXchanges (MFIX), authored by the National Energy Technology Laboratory (NETL), to enable discrete element methods (DEM) simulations of TIM squeezing. The experimentally measured dispensed TIM microstructure (particle diameters and locations) is fed as input for the squeezing simulations. The polymer matrix velocity profile is analytically-calculated assuming Newtonian behavior. A drag force couples the particles and fluid one-way and depends on the

relative velocity and the local particle volume fraction. At a fixed pressure, the predicted BLT increases monotonically with squeeze rate owing to the rapid increase of fluid pressure with squeeze rate under the Newtonian assumption. The predicted bulk particle volume fraction and coordination number also increase with squeeze rate. This is a direct consequence of greater spreading of particles at lower squeeze rates. The model predictions do not compare well with experimental data due to the Newtonian assumption on the fluid velocity profile, one-way coupling between the particle and fluids, and due to variations in the experiments introduced by the copper foil and plastic tape used to coat the surfaces. A finite element (FE) thermal conduction modeling framework is developed based on a particle size reduction method, proposed in published literature, to circumvent meshing issues caused by narrow interstitial regions and interparticle intersections. For the experimental data sets, the predicted conductivity is in the range of $0.23 - 0.35\ \mathrm{W\,m^{-1}\,K^{-1}}$, and trends with squeeze rate and load differ between tests. For the simulated microstructures, the predicted conductivity of the simulated microstructures decreased from $0.3\ \mathrm{W\,m^{-1}K^{-1}}$ by $\approx 16.7\%$ as the squeeze rate increased from $1\ \mathrm{mm\ s^{-1}}$ to $10\ \mathrm{mm\ s^{-1}}$.

1. INTRODUCTION

1.1 Motivation and Background

The desire for higher computational power has led to technological advances in transistor technology, but these advances, in turn, increase the heat generation in the microprocessor. The generated heat must be efficiently conducted away from the processor chip to the surroundings to regulate its temperature, ensure proper functionality of the chip, and extend its lifetime [1]. Modern microprocessors have more than 10 billion transistors [2] that are packed in a small footprint or die area. The characteristic transistor size is 7 nm [3] (published in 2019). As of 2015, the heat flux dissipated in a commercial processor was over $100\ \mathrm{W\,cm^{-2}}$ [4] and hot spots can cause localized and concentrated heat fluxes greater than $1\ \mathrm{kW\,cm^{-2}}$ [5]. In essence, the heat generation in the transistors is caused by Joule heating, and the net heat generated from all the transistors must ultimately be efficiently dissipated to the surroundings. For more details on heat generation in electronic devices, the reader is referred to Smoyer and Norris [4]. Thermal issues can be tackled at different length scales, for example, at the individual microprocessor chip-level or the whole electronics package-level. Various active cooling technologies (such as those based on forced air convection [6], liquid cooling technology [7–9]) and passive cooling technology (such as heat pipes and vapor chambers [10–13]) have been developed at the package level. Often a finned heat sink is attached to the metallic lid covering the microprocessor chip with either forced air or natural convection cooling.

Without any binder material, the interfaces between (a) the chip and the lid of the device package and (b) the lid and the heat sink tend to have poor thermal transport because surface roughness limits contact between surfaces. Specifically, these air gaps limit heat flow between the materials due to discrete contact points between the two solid surfaces (*i.e.*, processor chip (hot object) and heat sink (cold object)). In fact, the typical contact area for such dry mating surfaces is on the order of $1-2$ % of the nominal or apparent cross-sectional area of the solid mating objects [14]. A schematic representing the dry contact area at solid-solid interface is shown in Figure 1.1. This, in turn, leads to a high interface thermal resistance and a large temperature drop across the path of heat flow. This raises the device temperature and, eventually, deteriorates its computational

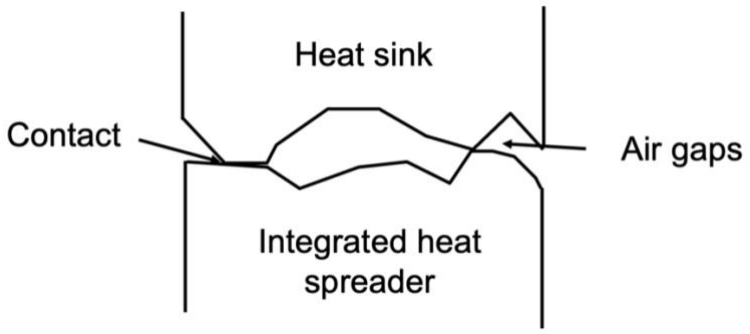

Figure 1.1. Schematic showing dry contact area at a solid-solid interface. Surface roughness causes limited contact points and a high thermal resistance air gap between the solid surfaces.

performance. The heat flow path from the microprocessor chip to the outer environment or surroundings is typically referred to with the terms “junction-to-ambient” or “overall”. An overall or junction-ambient thermal resistance, based on the temperature drop from the heat source (*i.e.*, the transistors) to the environment (*i.e.,* ambient) and the cooling power, is a key metric for understanding performance of an electronic package [1,6]. The heat transfer direction will be referred to as the through-thickness direction.

To aid in efficient heat conduction across the material interfaces, thermal interface materials (TIMs) have been developed. Different types of TIMs such as metal foils, phase change materials, carbon-based thermal gap pads, gels, and particulate composites including thermal greases and adhesives (*i.e.*, a cured and solidified material) exist and are used in different situations [15]. Thermal greases and adhesives are composite materials consisting of a high conductivity filler material in a polymeric matrix [1,14,16,17]. Thermal greases, as the name suggests, possess flowability, but can pose reliability issues such as dry out and pump out [18,19]. Thermal adhesives (also simply referred to as TIMs), on the other hand, are applied and then cured (often thermally [20]) to solidify and eliminate the major reliability issues of thermal greases. Both grease- and adhesive-based TIMs generally include high thermal conductivity ceramic particles, metal particles (*e.g.*, silver flakes), and/or carbon-based particles (like graphite flakes, graphene nanoplatelets, multilayer graphene [21–29] and carbon nanotubes [14,30]). A significant amount of research over the past two decades investigated unique combinations of filler particles (*i.e.*, its chemistry, size distribution and morphology) [31,32] and the material synthesis process [23]. While those works provided fruitful insights into the effects of particle morphology and the microstructure induced

by a synthesis process on the composite material bulk thermal properties [33,34], they generally ignore that the process of applying the material on a substrate can modify the microstructure.

A TIM is applied onto a substrate in two steps: (1) dispensing (in various patterns like dot, line, star, spiral, serpentine, and "X") and (2) squeezing. After dispensing the TIM on the substrate, pressure is applied to spread it over the substrate surface and connect to the mating surface with the goal of having the TIM occupy the entire surface area uniformly. Squeezing is either performed at a constant velocity [35] or a constant force [36]. On a manufacturing assembly line, constant velocity squeeze is more generally employed, and the squeezing process is terminated when the pressure reaches a desired value. Finally, for adhesive-type TIMs, the material is cured to form a solid rigid bond.

During squeezing, filler particles and the polymer matrix flow relative to each other, and this can modify the TIM microstructure – that is, the final microstructure or distribution of particles within the TIM might not be uniform. Only a handful of prior works experimentally investigated this phenomenon and its impact on the TIM bond line and effective thermal conductivity [35,36]. A few works optimized TIM performance by minimizing the bond line thickness using hierarchical nested channels that provided a flow path for the TIM, thus preventing local particle stacking [37–41]. However, follow-up work is lacking potentially because this approach could not easily be implemented on an assembly line. There is still a lack of research along the direction of practical optimization of TIM microstructure considering application parameters. Specifically, there is a need for a comprehensive understanding of the effect of TIM formulation (*e.g.*, particle shape and size distribution) and squeezing parameters (*e.g.*, squeeze velocity, pressure, dispensing pattern) on TIM microstructure and thermal performance. Therefore, in this thesis, a combined experimental and computational modeling approach is taken to investigate the impact of dispense and squeeze procedures on the TIM microstructure and bulk thermal conductivity, with the ultimate goal of developing validated models that are useful to optimize processing parameters.

1.2 Objectives and Major Contributions

This thesis primarily aims to investigate and understand the TIM application process-induced filler particle rearrangement or redistribution, and the impact of this particle redistribution on the

macroscopic thermal performance of the TIM. To reiterate, the focus of this work is on composites consisting of polymers with particulate filler materials. Various patterns for dispensing the TIM on the substrate and numerous combinations of particles (*i.e.*, material, shape, size, and size distribution) and polymers are viable options, but this investigation will focus on (a) TIMs consisting of relatively large spherical particles in a polymer that is representative of those in commercial TIMs and (b) a line dispense pattern. This thesis does not focus on optimizing particle morphology, polymer chemistry, or the material fabrication process to prepare the best performing TIM. Instead, this work focuses on the evolution of the material microstructure during its application and the resulting thermal performance.

A major objective of this study is to develop validated models for predicting microstructure of squeezed TIMs consisting of spherical particles and its effective thermal conductivity. Once validated, models will be used to optimize the TIM squeezing process for higher thermal conductivity, lower bulk thermal resistance during operation, and improved uniformity of the properties for a given particle size distribution. The investigation is two-fold, combining both experimental and modeling research with the ultimate goal of validating the TIM structure-property model. Specifically, a discrete element method (DEM) simulation framework is developed to simulate the constant velocity squeezing of the particle-laden TIMs and to predict the spatial distribution of particles. These results are compared with the microstructural features revealed by 3D X-ray micro computed tomography (XRCT) before and after squeezing. A finite element thermal conduction model is developed to predict the TIM bulk thermal conductivity.

The unique contributions of this thesis include: (a) development of combined experimental and modeling investigation framework for predicting and understanding process-induced variations in TIM performance and (b) the first, to the author's best knowledge, experimental study of the 3D microstructure of TIMs, and (c) the first effort towards simulating squeezing of TIMs using experimentally measured initial particle configuration. This work is a starting point towards developing validated models for realistic TIMs consisting of non-spherical filler particles. Such models will help minimize the experimental work that is typically employed to investigate the material characteristics and performance.

To accomplish the thesis objective, this work involved several components briefly described here:

1. Reviewed literature on particle redistribution in TIMs induced by the dispense and squeeze processes, thermal conduction modeling, and squeeze process protocols
2. Developed automated procedures for dispensing a line pattern of TIM and its constant velocity squeezing with *in situ* UV light cure.
3. Conducted 3D XRCT imaging of the dispensed and squeezed in-house prepared samples of mock TIM at a fixed particle loading of ~ 30 vol%, and developed an image processing algorithm to extract particle locations and sizes.
4. Analyzed basic microstructural features of the squeezed TIMs as a function of squeeze rate and load. In addition, the dispensed TIM microstructure is an input to the squeeze simulation.
5. Developed DEM simulations of constant velocity squeezing of TIMs to predict the BLT and other relevant microstructural characteristics. The model was developed with one-way coupling between particles and the polymer fluid through a drag force, with a pre-defined fluid flow distribution. This is accomplished by building user-defined functions into the open-source DEM software used in this thesis. The uniqueness of this model is that it simulates squeezing with experimental data as input.
6. Developed FE thermal conduction model using COMSOL Multiphysics to predict bulk TIM thermal conductivity. This model is compatible with both measured and simulated microstructures.

1.3 Outline of the Document

This thesis is divided into six chapters. Chapter 1 is focused on the motivation for this research and objectives, uniqueness, and major contributions. Chapter 2 reviews existing literature on heat conduction in TIMs and the microstructure of particulate media, particle redistribution in TIMs, and, finally, experimental and modeling techniques exploited in this investigation. Chapter 3 focuses on 3D XRCT imaging experimental set-up, image processing workflow and microstructure analysis of dispensed and squeezed TIMs. Chapter 4 is devoted to discussing the DEM simulations framework, protocols for squeezing simulations, and squeezed TIM microstructure predictions. In addition, the microstructure predictions are compared with experimental data from Chapter 3. Chapter 5 is focused on bulk thermal conductivity prediction

from the XRCT-measured and DEM-predicted microstructures. Finally, Chapter 6 summarizes and concludes this thesis, and provides recommendations for future work.

2. LITERATURE REVIEW

This chapter reviews literature pertinent to the fundamentals of thermal conduction in TIMs, the physics of particle redistribution in TIMs during application, and some previous work on optimization. In addition, fundamentals of the techniques used in this thesis such as 3D X-ray micro computed tomography (XRCT), the discrete element method (DEM), and steady-state thermal characterization are discussed. Section 2.1 is devoted to the fundamentals of thermal conduction in TIMs and granular media microstructural features. Section 2.2 is focused on particle redistribution in TIMs during application. An effort is made to refer the reader to prior, relevant research works. Sections 2.3 – 2.5 discuss principles of the experimental and modeling techniques exploited in this thesis for microstructure and thermal conduction, 3D microstructure characterization, and simulations to understand particle redistribution in TIMs.

2.1 Microstructure and Thermal Transport in TIMs

2.1.1 Heat Conduction in TIMs

TIMs aid in efficient conduction of heat generated from the microprocessor chip to the heat spreader and heat sink for dissipation to the surrounding environment. Thermal evaluation metrics of importance are the effective thermal conductivity (k_{eff}), bulk thermal resistance (R_{TIM}), and the total or overall resistance (R) [14,39,42]. The bond line thickness (BLT) is the effective TIM thickness across which heat is conducted (see Figure 2.1(a)), or in other words, it is defined as the effective thickness of the gap between the mating substrates that is occupied by the TIM. This parameter and k_{TIM} are used to calculate $R_{TIM} = \frac{BLT}{k_{TIM}}$ [43]. In addition to the bulk thermal resistance, contact resistances between the TIM and the mating substrates are critical (see Figure 2.1(b)) in determining the total or overall resistance: $R = R_{TIM} + R_{C,1} + R_{C,2}$, where $R_{C,1}$ and $R_{C,2}$ are the contact resistance at the top and bottom interfaces. Contact resistance arises from imperfect wetting (see Figure 2.1 (b)) of the material surfaces by the TIM or, even if there is perfect contact between smooth surfaces, there can still be a non-zero contact resistance due to differences in the properties of the contacting materials [4]. During squeezing of TIMs, the BLT and particle network within the material evolve and the final BLT is a function of the squeeze/assembly pressure used

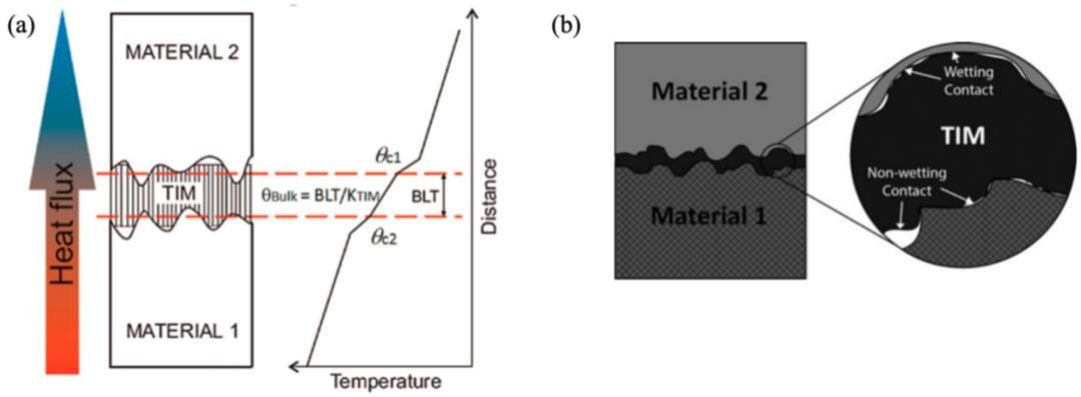

Figure 2.1. (a) TIM applied at the interface between two materials and an accompanying temperature versus distance plot showing bulk and interface thermal resistance as temperature jumps. The bulk TIM thermal resistance is the temperature jump within the bulk of the material that depends on the characteristic length (known as BLT) across which heat is conducted and the material conductivity. In addition, there will be interface or contact thermal resistance between the TIM-material interfaces. (b) Schematic showing contact thermal resistance between the TIM and material due to imperfect wetting of the materials by the TIM. Note that even if the TIM perfectly wets the material, there will still be an interface thermal resistance due to the differences in chemical make-up and structure of the materials [48]. The overall TIM resistance is the sum of its bulk resistance and the interface resistance. Republished with permission of (a) Prasher [14] and (b) from Smoyer and Norris [4]; permission conveyed through Copyright Clearance Center, Inc.

and the particle loading within the TIM [16,44–46]. Together, this can affect the TIM thermal resistance, R_{TIM}, as well as the contact resistances [47].

Effective properties of granular or particulate media are a function of their microstructure [49–55] [56]. In TIMs, large quantities (up to 50 vol%) of high conductivity filler particles are mixed with a polymer matrix to efficiently conduct heat through the material. Intuitively, higher particle loading should lead to increased effective thermal conductivity. However, higher particle loadings often increase the BLT as demonstrated in past works [46,47,57]. Ideally, the thermal conductivity will be high along the primary direction of heat transfer (see Figure 2.1(a)). Therefore, when applied, the filler particles in the TIM must be preferentially aligned in that direction to achieve high thermal conductivity. Continuous chains of high thermal conductivity particles between the hot and cold surfaces would be ideal for enhanced thermal conductivity. The existence of a continuous pathway that causes a sharp change in an effective property like thermal conductivity within the heterogeneous medium is a phenomenon known as percolation [58,59]. The

microstructure is imparted to the material during its manufacturing process and, specifically with respect to TIMs, the microstructure can evolve during application of the material on a substrate, as discussed in section 2.2.

Generally, the thermal conductivity of the polymer matrix is ~ 0.1 W m K^{-1} and the filler particle conductivity is several orders of magnitude higher. However, the effective conductivity of commercial TIM is typically on the order of $2 - 5$ W m K^{-1} [38]. The particle morphology, shape, size, and the contact topology of interparticle contacts govern the TIM effective conductivity. Several modeling techniques have been developed to estimate the thermal conductivity of composites such as the effective medium approach (analytical) [60–63], low fidelity numerical models (*e.g.*, network thermal model) [64–70], full-field thermal simulations (*e.g.*, finite element methods) [71,72], and other meshless methods (*i.e.*, higher fidelity numerical modeling) [73]. The TIM microstructure can be characterized using several statistical quantities [74,75] that characterize either the particle networks or the pore space (*i.e.*, part of the microstructure not occupied by the particles). Lower fidelity models incorporate statistics of the microstructure starting with volume fraction at the most basic (see section 2.1.2 for more details on microstructure), while higher fidelity models incorporate actual particle location, size, and contact information.

2.1.2 Microstructure of Particulate Media

The lowest order or simplest descriptor of particulate or granular media microstructure is the phase volume fraction (*i.e.*, the fraction of total material volume occupied by that material) [75]. TIMs generally consist of two material phases, namely the particle (or solid) phase and matrix (or polymer) phase. After it has been applied onto the substrates, air bubbles may form [35,76,77], thus possibly introducing a third phase. In this thesis, all analysis treats the TIM as a two-phase medium. Particle volume fraction alone does not govern the effective thermal conductivity of TIMs, because this simple microstructural descriptor is incapable of elucidating the spatial distribution of particles, information regarding number of nearest particle neighbors, and whether particles exhibit a tendency to align along a specific direction. Local particle volume fraction is a useful microstructural metric that can help in understanding the impact of squeeze rate and load on the spreading of particles. Coordination number is the average number of particles in contact

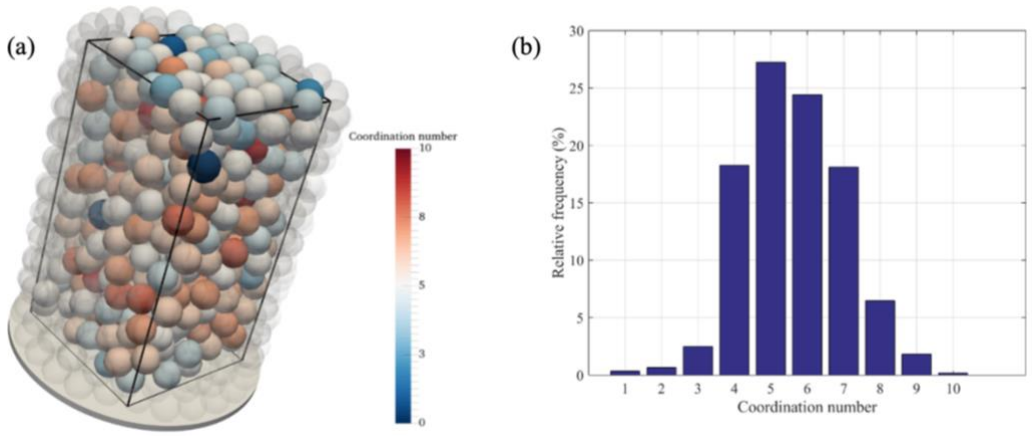

Figure 2.2. Illustration of distribution of the local coordination number in a simulated bed of packed spheres. (a) DEM-generated packing of spherical particles with color coding based on coordination number and (b) histogram of the local coordination number. In this example the mean coordination number is 5.6. Reproduced from Roozbahani *et al.* [84].

with a reference particle [78–82]. Generally, higher loading of particles leads to a higher coordination number [83]. Depending on the spatial distribution of particles, a variation in local coordination number is expected in a granular microstructure (see Figure 2.2) and, in experiments, a wider distribution may be observed due to wall effects [82,84]. Several other correlation functions are available to characterize the microstructure, but only those that are expected to be important for thermal conduction and meaningful for comparison with microstructure models are reviewed here. In the following paragraphs, the following statistics are reviewed: radial distribution function (RDF) and fabric tensor.

Radial distribution function

The radial distribution function (RDF), or pair correlation function, represented as $g(r)$, describes structural ordering in the system. It quantifies the number of particles at a distance, r, from a reference particle [85,86] (see Figure 2.3 (a)). This correlation reveals information about ordering in particulate systems [87] and the reader is referred to Kirkwood and Boggs [86], Franchetti [88], Yoon *et al.* [89] and Aste *et al.* [87] for more mathematical details. To understand this metric more intuitively, let us consider solids, liquids, and gases. In a liquid, one expects molecules to be relatively closer to each other than for a gas. Therefore, in a liquid, there is a higher likelihood of finding particles at further distances away from the reference particle. So, the RDF for a liquid will

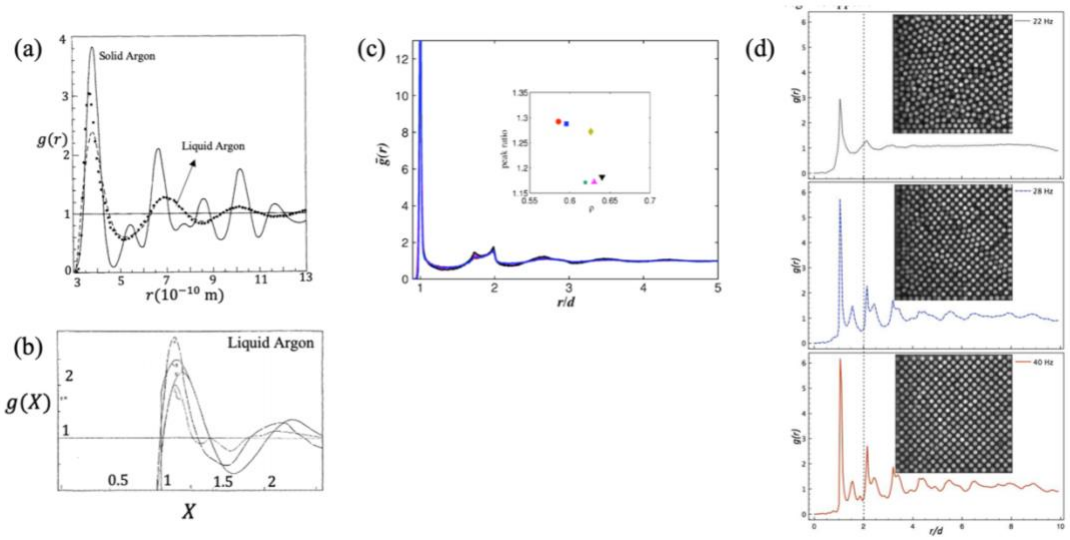

Figure 2.3. Fundamentals of radial distribution function. In a plot of RDF, the horizontal axis is generally distance normalized by diameter of atoms, molecules, or particles, and the vertical axis indicates number of nearest particles at that distances: **(a)** RDF for solid (solid curve) and liquid Argon (dashed line with fitted points plotted as circles) – liquid molecules have higher kinetic energy than their solid counterparts, therefore, possess more randomness and fewer peaks (adapted from Franchetti [88]), **(b)** Experimental (curves A, C) and theoretical (curves B, B') RDF profiles for liquid Argon at 90 K (reproduced from Kirkwood and Boggs [86]), **(c)** RDF of packed monodisperse acrylic beads ($58.6 - 64\%$ packing fraction) imaged using 3D XRCT technique; the first major peak indicates contacting neighbors and, with greater distances, there are a few neighbors and that indicates some ordering in the packing (reproduced from Aste *et al*. [87]) and **(d)** Experimentally determined RDF of self-assembled spherical particles under gravity and in the presence of vibration. Looking at the three plots top to bottom, we see more peaks in the RDF as the structure becomes more ordered (reproduced from Becerril-Gonzalez *et al*. [90]). Republication permission conveyed through Copyright Clearance Center, Inc.

exhibit more peaks than that of a gaseous material. In solids, the molecules are significantly closer to one another compared to liquid or gas. Therefore, the RDF will exhibit more peaks. In Figure 2.3 (b-e), several plots of RDF of various systems such as solid/liquid Argon [86,88] (Figure 2.3 (b, c)), packing of acrylic beads analyzed with the aid of XRCT imaging [87] (Figure 2.3 (d)), and self-assembly of spherical particles [90] (Figure 2.3 (e)) are discussed for an intuitive understanding. This distribution function will be useful in determining differences between different TIM microstructures.

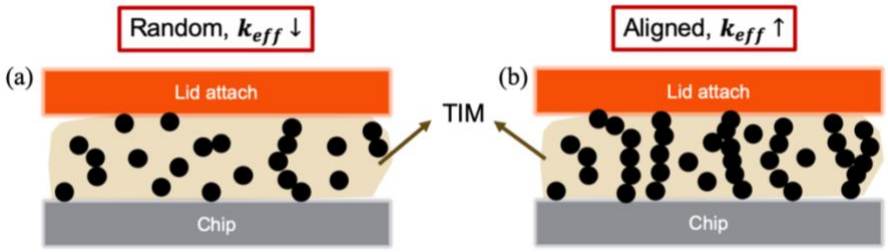

Figure 2.4. Schematics of (**a**) random and (**b**) aligned microstructures of a TIM consisting of spherical particles. Higher bulk thermal conductivity is expected along the direction of alignment.

Fabric tensor

More than three decades ago, an interest in characterizing and correlating microstructural anisotropy with macroscopic property emerged in the investigation of stress distribution in soils [91] and in medical sciences, particularly concerned with trabecular bone structures [92]. The fabric tensor is a second rank, symmetric tensor [92,93] used to characterize microstructural alignment in granular media, while the prior microstructural descriptors discussed in this thesis are scalar and agnostic to orientation. The fabric tensor has since been applied to a plethora of heterogeneous media microstructures—both simulated and measured—to investigate their structure-property correlations [51,94–100]. Microstructural anisotropy in the TIM is attributed to preferential alignment of particles along any of the principal directions and can likely be induced during its assembly process. Figure 2.4 illustrates several granular microstructures (simulated and real) that show signs of alignment. Effective thermal conductivity is expected to be higher along the preferred direction of particle alignment (see Figure 2.4(e)) as it is related to the number of percolating network of particles. To maximize TIM thermal conductivity along this direction, a higher number of such particle networks must form in that direction. Therefore, after dispensing and squeezing of TIMs on the microprocessor chip or the heat sink surfaces, it is hoped that a large number of particle networks preferentially form along the primary heat conduction direction (*i.e.*, from the chip to the heat sink or the through thickness direction).

Various directional measures of the fabric exist, such as those based on the mean intercept lengths [101,102], the Minkowski tensor [103], branch vector [94,95], contact normal vector [51], and star length/volume distributions [104–106]. In the field of granular mechanics, investigation of stress

distribution/transmission and force chains has been correlated with the fabric tensor – microstructural anisotropy will lead to mechanical stress anisotropy [107] as the mathematical formulation points out a direction relationship between the stress tensor and branch vector [108]. In this thesis, the contact vector fabric tensor will be employed to compute microstructural anisotropy – fortunately, since the focus is on spherical particles, the branch vector and contact normal vectors coincide and computational complexity is minimal. Branch vector is a vector connecting the centroids of two particles in contact and the contact normal vector is a vector normal to the contact plane between two particles, pointing from one particle to the other. These vectors are depicted in Figure 2.5 and the fabric tensor formulation, based on Olsen and Kamrin [95], is given by:

$$\mathbf{F}_l = \sum_i n_i \otimes n_i, \tag{2.1}$$

$$\mathbf{F} = \frac{1}{N_C} \sum_{l=1}^{N_C} \mathbf{F}_l, \text{ and} \tag{2.2}$$

$$\rho_{fabric} = \frac{e_{\mathbf{F},max}}{e_{\mathbf{F},min}}, \tag{2.3}$$

where $\mathbf{F}$ is the fabric tensor, ρ_{fabric} is the microstructural anisotropy, $\mathbf{F}_l$ is the local fabric tensor for a particle l, $e_{\mathbf{F}}$ are the eigenvalues of the fabric tensor $\mathbf{F}$, i is the set of contacting neighbors of particle l, n_i is the branch vector between contacting particle pairs and N_C is the number of interparticle contacts.

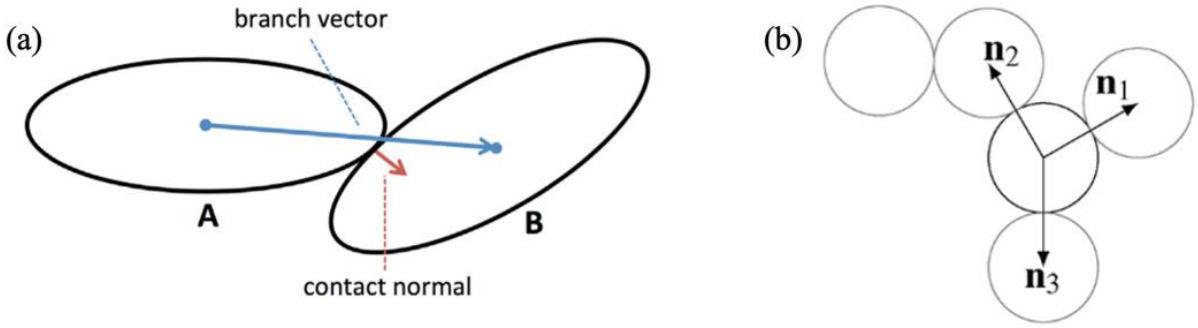

Figure 2.5. **(a)** Schematic of two contacting particles (A and B) showing the branch vector and contact normal vector. The branch vector connects the centroids of the two particles and the contact normal vector is a vector normal to the contact plane of the particles, pointing from A to B (reprinted from Stershic *et al.* [94] with permission from Elsevier). **(b)** Schematic of a particle with three neighboring contacts. To calculate the fabric tensor, first, the dyadic product of the vectors $n_1, n_2,$ and n_3 are calculated with themselves. Then, that quantity is averaged over all contacts in the microstructure (republished with permission of Olsen and Kamrin [95]; permission conveyed through Copyright Clearance Center, Inc.)

First, the dyadic products of all local contact vectors for a particle is summed up to obtain $\mathbf{F}_l$, which is then averaged over all contacts to obtain the fabric tensor **F**. The ratio of the maximum and minimum eigenvalues, $\rho_{\mathbf{F}}$, of this tensor is a metric that will be used to quantify microstructural anisotropy and the eigenvector associated with the maximum eigenvalue will represent the primary direction of alignment.

2.2 Particle Redistribution in TIMs

During application, the TIM is dispensed (in various patterns) and squeezed, by applying pressure, to spread on the substrate [38]. A typical squeeze pressure is ~ 200 kPa [15]. However, depending on the squeeze rate (*i.e.*, velocity or force), particles in the TIM redistribute during its squeezing [35,36] and this is also affected by the dispense pattern. Squeeze flow of fluid is a historically well-researched field – Josef Stefan first explored squeezing flow of a Newtonian fluid in 1874, as cited in Gibson *et al*. [109], to investigate the variation of gap thickness as a function of squeezing force of a fluid between two parallel plates. A few decades later, as succinctly summarized in McIntyre [110], squeeze flow theory and applications were extended to non-Newtonian fluids. In rheometry, squeeze flow is an important and advantageous characterization technique [109,111] and its physics gained importance due to numerous applications [112]. Prior works have reported on approximate solutions to the fluid velocity profile and pressure distribution [113,114], squeezing characteristics (such as plate separation, strain/strain-rate profiles, pressure field and viscosity) of non-Newtonian fluid (without particles) [111,115], and squeeze flow of suspensions, including studies that specifically focused on TIMs [44–46,116–118]. These rheological investigations of TIMs focused on prediction of BLT by understating their stress-strain rate relationships using either Bingham [20] or Herschel-Bulkley [117] models. However, that still assumes a macrohomogenized medium and, therefore, lacks understanding at the particle scale.

Local concentration of particles or matrix filtration during squeeze flow of particle-polymer composites is the separation of liquid and solid phases of the heterogeneous material, leading to local concentrations of the particle phase [116]. It can be physically thought of as a tendency of the particles to move to minimize frictional or viscous dissipation [119], and more rigorous mathematical treatment can be found in Poitou and Racineux [119]. This can be attributed to change in the overall behaviour of the material as a whole versus there being a relative motion

between the particles and the fluid. The phenomenon of liquid phase migration in particulate suspensions (or pastes or granular suspensions) has been previously investigated [117,119–124] and is observed in, for instance, petrochemical applications [125] and rheology of sewage [126]. Localized particle concentration was observed at lower squeeze velocity in these works. Particles may aggregate or stack up locally due to migration or separation of the polymer matrix and resist the squeeze force, thus resulting in a higher bond line thickness and large normal forces [116,127]. This effect is primarily governed by the particle volume fraction, squeeze rate and fluid viscosity. The critical squeeze velocity below which filtration occurs is a function of the particle size (D_p), particle volume fraction (ϕ_s), consistency parameter (K), and the flow index (n) [119,125,128]. Assuming power law fluid behavior, order of magnitude formulations for the critical squeeze velocity were presented in [116,119]. This may not be valid at higher particle volume fractions, since a finite yield stress is then expected, whereas the power law fluid flow does not account for that.

An early experimental work on squeeze flow characteristics pertaining to gel-type TIMs consisting of spherical alumina particles (45 vol% loading) by Davidson *et al.* [20] showed that thin bond lines of the TIM are mechanically weaker than thick bond lines, although thermal resistance was lower for the thin bond lines. The Bingham fluid model was used to predict the BLT with a reasonable accuracy. However, particle network characteristics in the cured TIM and its impact on measured thermal properties were not investigated. In another work [57], the TIM was homogenized and modeled as a Herschel-Bulkley fluid and the plate separation and viscosity were analyzed by solving the momentum conservation equations for a string of the material undergoing squeeze, and this approach will be used in this thesis to analytically calculate the polymer matrix velocity profile. In their work, the flow behavior remained Newtonian for particle volume fractions less than 30% and it was shown that, under assembly conditions, surface tension effects can be neglected.

To reiterate, depending on the dispense pattern and squeeze velocity (or squeeze force), particle redistribution within the TIM can be severe leaving large void or pore spaces that impede heat conduction through the material. In essence, the final thermal performance of the TIM (*i.e.*, during operation) is governed by its application process; therefore, understanding the squeeze flow

behavior of TIMs and its effects on the rearrangement or redistribution of the particle network is critical to optimizing the dispense and squeeze processes. In the past nearly two decades, only a few works [35,36] have recognized this intimate relationship between the nature of squeeze flow, evolution of TIM microstructure during squeezing, and its bulk thermal conductivity. Of these, only Rae *et al.* [35] made an effort to visualize the TIM particle networks after squeezing. In their work, a commercial TIM was squeezed at different constant velocities, ranging from $0.1 - 10\ \mu m\ s^{-1}$, to an ultimate squeeze force of $300\ N$. It was shown that relatively low squeeze velocity leads to severe separation of particles and the polymer matrix – this leads to a heterogeneous microstructure. This impacts the minimum achievable BLT as well as the bulk thermal resistance. In their work, the TIM was cured in two different ways after squeezing – with and without the critical squeeze force held on the material. It was found that fast squeezing and curing with the squeeze force held on the TIM led to a more homogeneous distribution of particles within the TIM and lowered the BLT and thermal resistance. The bulk thermal resistance was approximately half order of magnitude smaller when compared with slow squeezing followed by curing without the compressive force. Slow squeeze led to a locally concentrated region of particles caused by matrix filtration or separation of the liquid phase from the particles. This was confirmed by Shirazy *et al.* [36] that investigated two different TIMs with "extremely high" and "high" particle volume fractions. In their work, constant squeeze force rate was employed (as opposed to the constant squeeze velocity) to study particle distribution homogeneity. The BLT can be minimized by holding the squeeze force constant at the end of a high velocity squeezing. Now it can be established with reasonable confidence that the same TIM composition can possess higher or lower overall thermal resistance, depending on its application conditions. In the thesis of Rae [129], the effect of assembly conditions on the star-shaped dispense pattern as well as twenty one parallel line patterns was investigated at two different squeeze loads of $50\ N$ and $330\ N$. In both cases, fast squeeze rates resulted in lower thermal resistance. Substrate roughness led to an increased bond line thickness, particle spatial distribution heterogeneity and potentially increases the overall thermal resistance. Elevated temperature can reduce the polymer viscosity, which then reduces Pe. This, in turn, increases the critical squeeze rate for the onset of heterogeneity.

Although dramatic particle redistributions in the squeezed TIM were found by Rae *et al.* [35], quantitative characterization of the microstructural features was not completed. Their analysis of

particle redistribution was not only qualitative, but also the visualization was just 2D. Further, the BLT was inferred from the imaging technique and the effective thermal resistance was measured. Note that effective thermal resistance measurements in Rae *et al.* [35] indirectly hinted at potential variations in TIM microstructure, subject to different squeezing conditions such as fast or slow squeeze velocity. Further analysis, such as a more accurate characterization of TIM microstructure in both the dispensed and squeezed states requires the use of a 3D imaging technique like the XRCT. Such a technique will provide more accurate information regarding particle locations and sizes and will also enable analysis of a larger sample size that is likely more representative of the bulk material. Quantifying the TIM microstructure helps in identifying, for instance, high thermal conductivity chains of particles from the hot to cold surfaces. This serves two purposes – (a) direct comparison with and validation of TIM microstructure modeling and (b) input for effective thermal conductivity model. Predictive thermal modeling [130] will aid in the analysis of bulk TIM thermal conductivity – this will ultimately help in assessing different squeezing scenarios for optimizing the TIM dispense and squeeze procedure. In the subsequent sub-sections, thermal transport modeling and characterization techniques, principles of the 3D XRCT imaging technique, and the TIM squeezing modeling framework used in this thesis are discussed.

2.3 Thermal Conduction Modeling in TIMs

In this section, two common heat conduction modeling techniques are reviewed and discussed: network thermal models and Finite Element (FE) thermal models. Note that effective medium approaches (EMAs) [131] cannot fully consider the effect of particle size distribution, particle shape, interparticle contact topology that governs thermal contact resistance between two particles, and the global particle network. Traditional effective medium models that provide analytical expressions for the effective conductivity of a composite material fail to account for particle chains that form in the microstructure (reported in Table 1 in Kim *et al.* [61]). Note that in commercial TIMs, as mentioned in an earlier section, particle loading is generally greater than 50% [14], and the particles percolate at such high loadings. This will lead to sever underestimation of the conductivity. The prediction error increases at higher particle concentrations *i.e.*, conductivity is underpredicted, or when conductivity ratio between the particle and matrix phases is higher. Therefore, a higher fidelity numerical modeling is needed for a more accurate prediction of TIM effective conductivity that considers particle level thermal conduction. Kim *et al.* [61] formulated

the effective conductivity as a function of particle volume fraction, particle-matrix conductivities, particle shape aspect ratio and, finally, a term accounting for particle interactions. This formulation predicts the conductivity with an error of 30% for composites with up to a moderate particle volume loading of $\leq 40\%$. In their work the particle aggregate aspect ratio was correlated with the particle-matrix conductivity ratio and the particle volume fraction to calculate an aspect ratio used in their formulation. This does not physically make sense because the aspect ratio is a geometrical quantity that cannot be a function of the particle-matrix conductivity ratio or the particle volume fraction.

Network thermal model, which can consider these combined microstructural effects if the particle positions, sizes, and particle and polymer conductivities are known, are briefly introduced here. Good agreement was proven between network model and full field thermal simulation results by Kanuparthi *et al.* [65] for a filler loading of 58 vol%. A modified version of their model is evaluated in this thesis for the mock TIMs with lower filler loading. Then, a finite element heat conduction model recently developed for granular media is reviewed.

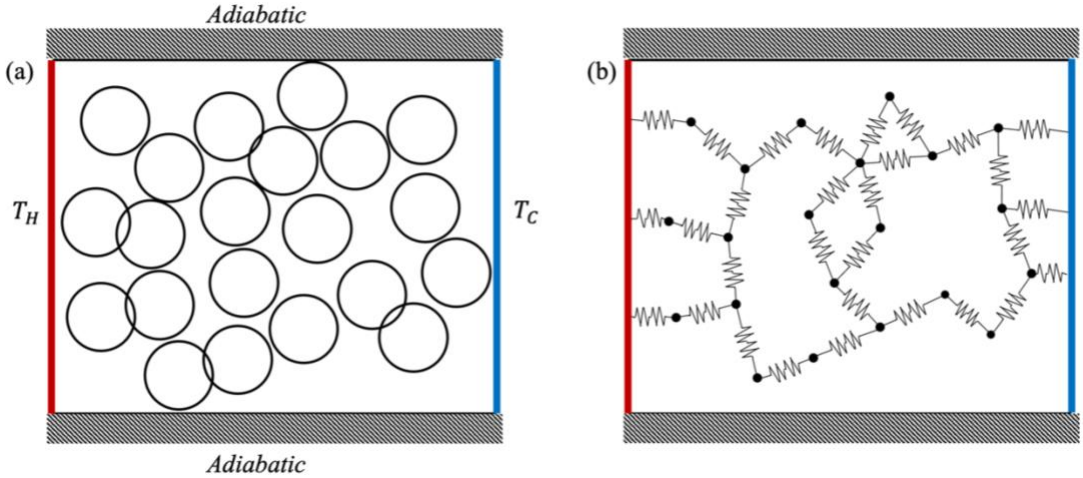

Figure 2.6. Two-dimensional schematic of the network thermal model. (**a**) Particle networks with imposed Dirichlet boundary conditions, T_H (hot) and T_C (cold), on either ends and adiabatic boundaries (top and bottom). (**b**) Network of equivalent electrical resistors through which heat conduction is modeled.

2.3.1 Network Thermal Model

Network thermal model uses the analogy between heat conduction and electrical conduction to predict thermal conductivity using a network of equivalent electrical resistors that represent the system based on particle locations, size, and the thermal conductivity of the particles and matrix (see Figure 2.6). Note each particle is approximated as isothermal with all the temperature drops occurring between particles. The network thermal model used in this thesis is based on that of Kanuparthi *et al*. [65]. Numerous prior works [64,98,132–135] have explored network thermal models. Most of these derive (or directly use) conductance formulations from Batchelor and O'Brien [136] in order to predict performance. In this steady-state modeling framework, a temperature gradient is imposed across the material domain via Dirichlet temperature boundary conditions, and all other boundary surfaces are assumed to be insulated. The net heat flow is zero at steady state for particles within the composite (internal nodes). Thus, by treating each particle as a node and applying Kirchoff's law (*i.e.*, an energy balance) for the net heat flow, a matrix of balance equations is generated based on:

$$q_{nodal} = K_g\, T, \tag{2.4}$$

where K_g is the global conductance matrix, T is the vector of nodal temperatures, q_{nodal} vector of net nodal heat flow rate. The solution to the set of equations (based on Eqn. 2.4) yields the nodal or particle temperatures. The effective conductivity can then be computed by using Fourier's law for heat conduction as given by:

$$q" = k_{TIM}\, \Delta T / L_{eff}, \tag{2.5}$$

where $q" = \frac{q_{in}}{A_{eff}}$ is the steady-state heat flux through the system, q_{in} is the heat flow in to the system, A_{eff} is the effective cross section area of the system, k_{eff} is the effective thermal conductivity of the particulate composite, ΔT is the imposed temperature difference, L_{eff} is the effective domain length across which heat flows. The geometrical parameters A_{eff} and L_{eff} are obtained by constructing a bounding box around the TIM microstructure. Note that Eqn. 2.5 can be used to compute thermal conductivity along the three principal directions by imposing the boundary condition on the appropriate faces.

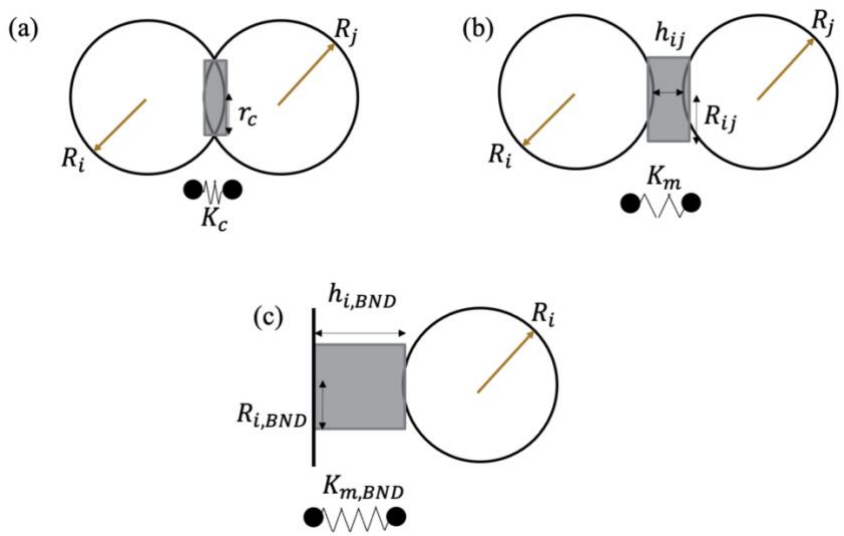

Figure 2.7. Schematics of heat flow paths considered in the network model: **(a)** between two intersecting particles, **(b)** between geometrically non-contacting particles that are close enough for the thermal resistance through the matrix to be relatively small, and **(c)** from a boundary to surface particles. Note that overlapping particle case (a) is strictly non-physical, but provides a treatment for DEM-simulated microstructures where slight overlap is used to compute contact conditions or for artifacts induced via XRCT image processing (*e.g.*¸ slightly non-spherical particles that are now modeled as spherical). The gray cylinders are the cylindrical zones across which heat is conducted. The radius of the regions with conduction (R_{ij}, r_c, and $R_{i,BND}$) depends on the particle radii (R_i and R_j) for pairs (cases a and b) and on the single particle radius (R_i) for particles in close proximity to a boundary (case c). The effective conductance for the cylindrical zone is calculated and a global conductance matrix is constructed to solve for steady-state particle temperatures.

The main challenge lies in the formulation of the global conductance matrix, specifically computing the conductance between neighboring particles (see Figure 2.7). Heat conduction between neighboring particles is often approximated as a conduction through a cylindrical zone of the matrix material that connects the two particles, as shown in Figure 2.7(b) building off the work of Kanuparthi *et al.* [65]. Particles near the boundaries need to be considered separately, as do particles that overlap due to non-physical reasons. Thus, every conductance considered falls into one of three cases (as shown in Figure 2.7), namely: (a) intersecting pairs; (b) geometrically non-contacting, but "thermally active" particle pairs; and (c) boundary particles. Note, the intersecting or overlapping particles, case (a), is strictly non-physical, but is a treatment of potential cases from DEM simulations (where soft particles overlap to interact) or from 3D XRCT analysis where particles are idealized as spheres based on a volume-averaged diameter that can lead to overlapping particles as an artifact. In reality, this case implies that the particle surfaces are likely in contact

and the zone of contact is approximated with a radius, r_c. For separated particles, case (b), the thermal network consists of the particle-matrix-particle pathway and there is a maximum allowable interparticle separation distance beyond which thermal conduction can be neglected.

The objective is to compute effective conductance between thermally active particle pairs to form the global conductance matrix (K_g). For the purpose, the cylinder length, radius (R_{ij}), particle (k_p) and matrix thermal conductivities (k_m) are required. The cylinder length is the overlap distance for overlapping particles (case a), the surface separation distance between the participating particles (case (b)), and the surface-to-wall distance for boundary particles (case (c)). For overlapping particles (case a), the cylinder radius $R_{ij} = r_c$. For neighboring but not intersecting particles (case b), the cylinder radius was calculated from the mean radius of curvature (a_{ij}) of the participating particles as given by [65]:

$$R_{ij} = \alpha_T \underbrace{\left(\frac{2R_iR_j}{R_i + R_j}\right)}_{a_{ij}} \tag{2.6}$$

where R_{ij} is the cylinder radius, R_i and R_j are the radii of thermally interacting particles, a_{ij} is the mean radius of curvature, and α_T is the radius tolerance parameter. A value of 0.5 for α_T was estimated by fitting the network model predictions to full-field thermal simulations in Kanuparthi *et al.* [65]. The maximum interparticle surface separation distance h_{ij} to account for thermal conduction between the participating particles for case (b) was formulated in their work as:

$$h_{ij} < \varepsilon_T \, a_{ij}, \tag{2.7}$$

where ε_T is the distance tolerance parameter estimated to be 0.5 based on matrix exclusion probability. This is the largest spherical matrix region of diameter $\varepsilon_T \, D_p$ that can be obtained in the microstructure with $\geq 10\%$ probability (Kanuparthi *et al*. [65]). For two neighboring particles, the effective interparticle conductance is calculated by:

$$K_{eff,ij}^{-1} = K_i^{-1} + K_{inter}^{-1} + K_j^{-1}, \tag{2.8}$$

where $K_{eff,ij}$ is the effective conductance between particles i and j, K_i is the conductance of cylindrical zone in particle$i$, and K_{inter} is the conductance of interstitial zone (*i.e.*, either the

interparticle contact region (Figure 2.7 (a)) or the matrix region (Figure 2.7 (b))). Note that interface resistance is neglected in this model. It is important to note that the heat flow through the parts of matrix far away from the interparticle contact region is not modeled. Therefore, the network thermal model predictions are expected to underpredict the bulk conductivity.

Since the particles are assumed to be isothermal, $K_i \to \infty$ and Eqn. 2.8 reduces to $K_{eff,ij} = K_{inter}$. Therefore, resistance to conduction is governed by the resistance in the interparticle contact zone for touching particles. The three conductance components are contributions from heat conduction across (a) the contact circle formed by touching particles (K_c), (b) the matrix layer (surrounding the particle surfaces just beyond the contact circle) (ΔK_g), and (c) the contact point of two touching particles (ln (α_{pm}^2) where $\alpha_{pm} = \frac{k_p}{k_m}$ is the ratio of particle to matrix conductivities). Thus, the interparticle contact conductance is given by [64]:

$$K_{inter} = K_{contact} = \pi k_m a_{ij}\left[K_c + \Delta K_g + \ln\left(\alpha_{pm}^2\right)\right]. \quad 2.9$$

The component conductances from Eqn. 2.9 depend on particle overlap parameter scaled by the ratio of particle to matrix conductivities: $\beta_{ij} = \alpha_{pm}\frac{r_c}{a_{ij}}$. For the limit of $\beta_{ij} \to \infty$, the conductance across the contact circle, K_c, and the conductance across the matrix layer in proximity to the particle surface, ΔK_g, are given by:

$$K_c = \frac{2\beta_{ij}}{\pi} \text{ and} \quad 2.10$$

$$\Delta K_g = -2 \ln(\beta_{ij}), \quad 2.11$$

and for the limit of $\beta_{ij} \ll 1$, K_c and ΔK_g, are given by:

$$K_c = \frac{0.22\,\beta_{ij}^2}{\pi} \text{ and} \quad 2.12$$

$$\Delta K_g = -0.05 \ln(\beta_{ij}). \quad 2.13$$

For a detailed derivation, the reader is referred to Batchelor and O'Brien [136]. Note that the interparticle contact conductance expressions taken from Yun and Evans [64] were originally derived in Batchelor and O'Brien [136]. This approach is used by many researchers including Lee *et al*. [68] and Khoubani *et al*. [137].

When neighboring particles are non-touching, the resistance to conduction is dominated by conduction through the interstitial zone, as given by:

$$K_{inter} = K_m = \pi k_m a_{ij} \log\left(1 + \frac{R_{ij}^2}{a_{ij} h_{ij}}\right) \quad 2.14$$

where h_{ij} is the interparticle surface separation distance. For a boundary particle (Figure 2.7 (c)), the effective conductance is just an extension of Eqn. 2.14 [65,136], where $a_{ij} = R_i$ and $h_{ij} = h_{i,BND}$.

A few works [98,132,133,138] have used Hertzian theory to compute interparticle contact radius and the contact conductance was formulated as shown in Eqn. 2.15.

$$K_{contact} \propto k_p r_c \quad 2.15$$

where k_p is the particle thermal conductivity and r_c is the contact radius determined by Hertzian theory. This theory is useful in instances where Hertzian force modeling is employed in the particle packing simulations. In this thesis, the interparticle intersections mainly arise from image processing artifacts related to geometrical approximations of experimental microstructures. In the simulations, a linear spring dashpot model is employed (see section 2.5.1). Therefore, it is not meaningful to use this theory to calculate a contact radius. Rather, it is computed purely from geometry.

After identifying all of the interacting particle pairs and boundary particles, the global conductance matrix is constructed. Note, particles close to the boundary are assigned the imposed boundary temperature to impose the temperature difference across the sample. The set of boundary particles is found by examining a histogram of particle positions. That is, lower and upper percentiles of particle positions, for example, 3% and 97%, are prescribed and particles whose centers lie below the lower and above the upper percentiles, respectively, are labelled as boundary particles. Then, the system of linear equations representing energy balances is solved. Finally, the conductivity is predicted by first computing the steady-state heat flow entering or leaving the system. This involves first determining the set of particles in contact with the boundary particles and computing

the net heat flow. The heat flow entering the system is computed with the temperature difference between these and the boundary particles:

$$q_{in} = \sum_{j} \sum_{i} \left(K_{eff,j,\mathbb{B}} \, (T_{hot} - T_i) \right) \qquad 2.16$$

where q_{in} is the heat flow entering the system, $K_{eff,j,\mathbb{B}}$ is the set $\mathbb{B}$ of particles in contact with boundary particle j, and T_i is the temperature of particle i in contact with the hot-side boundary particle.

2.3.2 Finite Element (FE) Thermal Model

Finite element thermal modeling framework has been used in prior works to predict bulk thermal conductivity of TIMs. For instance, the work of Dan *et al.* [139] used an FE approach to predict the bulk thermal conductivity of TIMs with various particle volume fractions and particle size polydispersity (with a fixed lognormal distribution). They found that, for a given particle volume fraction, an optimal value of the polydispersity parameter exists for maximum thermal conductivity. A relatively fine meshing is needed when (a) two particles are in close proximity, (b) the interparticle overlap magnitude is significantly smaller than either particle radii, or (c) a particle is in close proximity with a surface of the microstructural bounding box. This leads to a significant increase in the number of mesh elements, which then increases the computational expense. In some narrow regions, it is difficult to generate the mesh. A recent work by Lee *et al.* [140] discussed a particle size reduction method to overcome meshing complexity in FE thermal conduction modeling of particulate media with spherical particles. They conducted thermal conduction simulations by parametrically reducing the particle diameter then extrapolating back to full size particles. To account for interparticle thermal conduction, they introduced a "contact clearance" parameter. Particles with centers separated by a distance smaller than this parameter participate in heat conduction. Their model predictions were validated with bulk thermal conductivity measurements of saturated and saturated-frozen specimens of glass bead packing (porosities ranging between $0.3 - 0.4$) with an error of $< 5\%$. Then, it was applied to Jumunjin standard sand in the saturated and saturated-frozen states (porosities ranging between $0.4 - 0.45$) with a prediction error of $< 3\%$ based on measurements. Based on the work of Lee *et al.* [140], a finite element heat conduction modeling framework is developed in this thesis to predict the bulk

TIM thermal conductivity. The contact clearance parameter is not used in this thesis, but several particle size reduction factors are investigated. More details are provided in chapter 5.3.

2.4 3D X-ray Micro Computed Tomography (XRCT) Imaging

X-ray computed tomography (XRCT) is a non-destructive imaging technique that enables high resolution 3D representation of the object of interest [141]. Stock [141] refers to X-ray micro computed tomography as a technique that is capable of at least $50 - 100$ μm spatial resolution. Today, there exists X-ray nano-computed tomography [142] with a high resolution that is finer than 100 nm [143]. This technique is useful in a wide array of investigations ranging from engineering to biomedical sciences *e.g.*, heterogeneous material microstructure in battery electrodes [144–146] crack growth studies [147], energy research [148], food science [149], pharmaceutical studies [150,151], and investigations of trabecular bone structure [152,153]. Application of this imaging technique to porous media has contributed to better understanding of material microstructure and has helped correlate material microstructure with or directly measure its effective properties [154–157]. The basic principle of this technique involves bombarding the object of interest with X-rays to collect a set of 2D projections (or raw images) as the object rotates. A detector analyzes the intensity distribution of X-rays within the object based on transmitted radiation (see Figure 2.8) – from the set of projections, object cross-section can be reconstructed [158].

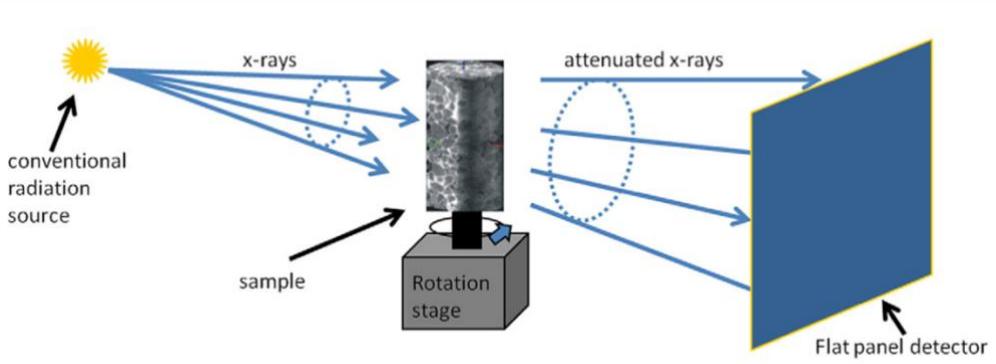

Figure 2.8. Schematics of XRCT working principle. A typical polychromatic source emits a conical beam of X-rays. As the object rotates through either 180° or 360°, several intensity projections are collected by the detector, and these are collectively reconstructed using sophisticated algorithms to generate cross-sectional slices – stacking these up gives a full 3D representation of the object. Reprinted from Wildenschild and Sheppard [159] with permission from Elsevier.

The 2D projections are a measure of the X-ray absorption of the object. The X-ray intensity drops exponentially (Eqn. 2.17), following Beer-Lambert law, as it passes through the object [159]:

$$\frac{I}{I_o} = \exp(-\mu x), \qquad 2.17$$

where I_o is the intensity of incoming X-rays, I is the X-ray intensity at distance x through the object, and μ is the attenuation coefficient (dependent on object density). Note that this mathematical description is strictly valid only for a homogeneous medium and monochromatic X-rays [158].

The exponential decay is governed by a physical quantity known as the attenuation coefficient, that depends on the overall material density as well as its electron density [159]. Moreover, the attenuation coefficient is a function of X-ray energy and, therefore, for a polychromatic X-ray source the intensity does not strictly exponential decay as in a homogeneous medium. The transmitted intensity, I, collected by the detector is the raw image or projection. The quantity $\frac{I}{I_o}$ is measured for different X-ray directions and different object positions (for a given X-ray direction). Then, by employing Fourier transforms on the series of projections, a map of the attenuation coefficient can be generated. This is then converted to a sequence of cross-sectional images or slices with associated computed tomography (CT) numbers for each voxel [160] by comparing

with a standard such as air or water. To convert to images, each CT number is mapped on to a $0-255$ greyscale intensity. The reader is directed to Stock [141] and Feldkamp *et al.* [161] for a detailed description of the reconstruction algorithms for a cone-beam XRCT instrument. During imaging, there should be minimal movement of the object during its rotation, to minimize sample disturbance or movement-based artifacts in the computed tomography. Other types of artifacts [162]—ring artifacts, beam hardening and streak artifacts—are discussed below. X-ray CT scan parameters must be optimized to obtain high resolution scans: (a) object rotation step must be low, (b) exposure time must be high and (c) several frames per object orientation must be averaged.

Figure 2.9 shows a raw projection, a reconstructed cross-sectional slice and the 3D reconstructed image of a squeezed TIM analyzed in this thesis. Beam hardening, ring artifacts [150,158], and other artifacts are briefly discussed here and the reader is referred to Ketcham and Carlson [162] for more details. Beam hardening is a common issue encountered in this technique that is nowadays correctable by using filters in the XRCT equipment during imaging, and during reconstruction [158,160]. This artifact is a result of the polychromatic nature of X-rays used during imaging. The higher energy X-rays are not attenuated as much as the lower energy radiation, which is more

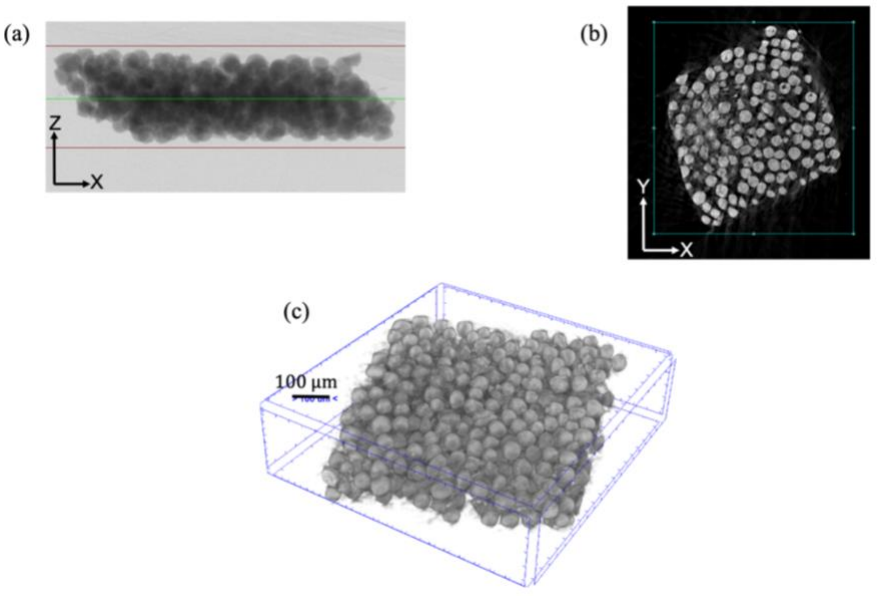

Figure 2.9. 3D XRCT scan of particle-polymer composite material used in this work. **(a)** Intensity projection or raw image at one object orientation, **(b)** a cross-sectional slice from the 3D reconstruction, and **(c)** 3D reconstruction of the composite material. The TIM was prepared in-house by hand mixing a target of 30 vol% of $90-125$ µm copper particles with a UV-curable polymer (details are deferred to chapter 3).

readily absorbed – the attenuation coefficient of a material decreases with increasing X-ray energy [159]. As a result, the object interior appears darker and the edges appear brighter [163]. Filtering the X-rays helps in narrowing down the wavelength range of the radiation at the source level and, thus, minimizes beam hardening by discarding the lower energy radiation [163]. Ring artifacts, as the name suggests, produce rings in the projections that contaminates reconstruction of the object cross-sections. This can be caused by a fault in the detector as well as due to the sensitivity of the detector to beam hardening. Software correction can usually be employed to eliminate this artifact. Streak artifact is an appearance of darker line between two high density objects [164], for instance, in metal particle-polymer composites imaging, dark streaks can be expected in a polymer region between the dense particles. These are a result of differing hardening of the X-rays that is caused as the radiation bombards the object at various orientations; additional causes are sample motion and under-sampling of data (such as coarser rotation step) and others, as detailed in Hsieh [165].

In this work, 3D XRCT imaging technique is used to quantify the TIM microstructural characteristics, provide input to squeeze simulations, and compare with predicted microstructures. The equipment used in this thesis is Bruker SKYSCAN 1272 with a pixel resolution of up to $0.35\ \mu m$ and is capable of imaging an object with a maximum diameter of $75\ mm$. XRCT images are further processed to perform numerous analyses, for example, for particulate media, quantities of interest are porosity, particle size, shape and location, and statistics of the microstructural arrangement of particle and void phases. A crucial requirement for distinguishing the different phases in the XRCT image of a heterogeneous medium is large differences in material density [151]. The particle and the polymer matrix have drastically different densities ($\approx 8x$) and, therefore, it is easier to distinguish the two phases from the 3D reconstruction. The difference in density leads to different absorption coefficients and, ultimately, to different grey values of the XRCT image voxels and a better contrast or phase segmentation is achievable during image processing. This helps in accurate analysis of particle locations and sizes.

2.5 Discrete Element Method (DEM) Simulation

In this section, a brief overview of the discrete element method (DEM) simulation technique is provided. Numerous prior works have reviewed the mathematical foundations in greater detail [166–168]. DEM modeling technique was first reported by Cundall and Strack [169]. It has been

used to investigate granular material flow features [170,171] and study particle packing or compaction characteristics [170–172]. In DEM, particle positions and velocities are tracked and interactions between particles are computed to advance its position and velocity in time. Particulate (both spherical and non-spherical or faceted) systems have been investigated by employing this technique – for instance, in the pharmaceutical industry [173], study of concrete, soils and rocks [100,169], characteristics of packed particle systems [174–178], rechargeable lithium-ion battery electrode microstructure characteristics and fracture [94], additive manufacturing [179–182], environmental science [183] and granular flow through hoppers [184–186]. Numerical algorithms employed to perform these simulations formulate interparticle contact forces (such as repulsive or attractive forces) and torques. Then, using Newton's laws of motion (Eqn. 2.18) the particle system dynamics are solved [169]:

$$\Sigma F_{p,net} = m_p \ddot{x}_p, \qquad 2.18$$

where $\Sigma F_{p,net}$ is the net force on particle p, m_p is the mass of particle p, and $\ddot{x}_p$ is the acceleration of particle p.

In these models, the particles are treated as "soft", that is, interparticle forces are caused by overlaps between particles and this drives the system dynamics. This overlap between particles, although strictly unphysical, is representative of deformation and allows for calculation of an interaction force. The overlaps are generally small compared to the particle size [169]. Moreover, multiple particles can be in contact at any given instant of time, and this simulation technique is capable of resolving such situations. Net force acting on a particle in contact with several particles at a given instant of time is the sum of interaction forces between each pair of particles. The total force acting on a particle is the sum of contact forces, gravitational force, and any applied external force:

$$m_p \ddot{x}_p = \Sigma F_{p,net} = \sum_{i \in C} F_{p,i} + F_{gravity} + F_{drag} + F_{external} \qquad 2.19$$

where $\Sigma F_{p,net}$ is the net force on particle p, $\sum_{i \in C} F_{p,i}$ is the net contact force on particle p, $F_{gravity}$ is the gravitational force on the particle, F_{drag} is the drag force on particles due to a fluid medium , $F_{external}$ is the any other external force on the particle , m_p is the mass of particle p, and $\ddot{x}_p$ is the

acceleration of particle p. Various relationships such as the linear spring dashpot and Hertzian models [187] exist between the interparticle overlap and magnitude of contact force. The simplest contact force law is the spring-dashpot model [166]. Similarly, the net torque acting on the particle determines its angular velocity [166]:

$$I_p \dot{\omega}_p = \Sigma T_{p,net} \qquad 2.20$$

where $\Sigma T_{p,net}$ is the net torque on particle p , $\dot{\omega}_p$ is the angular acceleration and I_p is the moment of inertia of particle p. In this thesis, an open-source software Multiphase Flow with Interphase Exchanges (MFIX) is used for simulating squeezing of TIMs and more details about this software, its capabilities and discussion of additional force models for simulating TIM squeeze are referred to chapter 4.

2.5.1 Contact Force Models

As particles interact in the DEM simulation, contact forces act along the normal and tangential directions defined in local coordinates. The normal direction is along the line joining the center of particles (for spheres). Due to the overlap between the particles (see Figure 2.10), a force is generated that provides new trajectories to the interacting particles. In addition, there might be frictional forces [188,189] and cohesive or attractive forces [190,191]. The contact force used in this thesis is the linear spring dashpot model and the reader is referred to Ref. [166] for an in-depth discussion.

These forces are formulated in Eqns. 2.21 and 2.22 for a pair of interacting particles i and j. The normal damping coefficient (ν_n) is correlated with the coefficient of restitution [192] and the tangential damping coefficient (ν_t) is usually set to half of the normal damping. Therefore, the specification of the coefficient of restitution is sufficient to calculate the normal and tangential damping coefficients. Similarly, the normal spring constant (k_n) is user-controlled and, in MFIX, the tangential spring constant is set as $k_t = \frac{2}{5} k_n$ [193]. At any instant, the total contact force on a particle is calculated by summing up the normal and tangential contact forces (Eqn. 2.21 and 2.22).

$$\boldsymbol{F_N} = -k_n \, \delta_n \, \hat{\boldsymbol{n}}_{\boldsymbol{ij}} - \nu_n \, \mathbf{v}_{\mathbf{n,ij}} \qquad 2.21$$

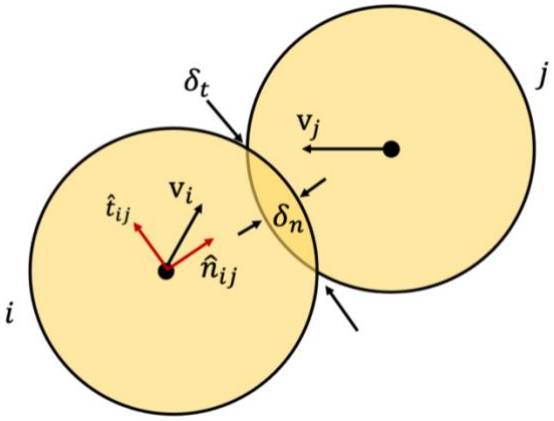

Figure 2.10. Schematic of particles i and j interacting with each other at a time instant. They are approaching each other with velocities v_i and v_j, respectively. The normal $\hat{n}_{ij}$ points from particle i to j. The tangential direction points along $\hat{t}_{ij}$. The magnitude of normal and tangential overlaps are δ_n and δ_t, respectively.

$$\boldsymbol{F_T} = -k_t\, \delta_t\, \hat{\boldsymbol{t}}_{\boldsymbol{ij}} - \nu_t\, \mathbf{v_{t,ij}} \qquad 2.22$$

where $\boldsymbol{F_N}$ is the normal contact force using the linear spring dashpot model, $\boldsymbol{F_T}$ is the tangential contact force using the linear spring dashpot model, k_n and k_t is the normal and tangential spring constants, δ_n and δ_t is the normal and tangential interparticle overlaps, $\hat{\boldsymbol{n}}_{\boldsymbol{ij}}$ and $\hat{\boldsymbol{t}}_{\boldsymbol{ij}}$ is the normal and tangential unit vectors, ν_n and ν_t is the normal and tangential damping coefficients, $\mathbf{v_{n,ij}}$ and $\mathbf{v_{t,ij}}$ is the normal and tangential relative velocity components. If the magnitude of tangential contact force, $\boldsymbol{F_T}$ is greater than the product of friction coefficient and the normal force, $\boldsymbol{F_N}$, then $\boldsymbol{F_T}$ is given by:

$$\boldsymbol{F_T} = -\mu_C |\boldsymbol{F_N}| \hat{\boldsymbol{t}}_{\boldsymbol{ij}} \quad \text{for } |\boldsymbol{F_T}| > \mu_C |\boldsymbol{F_N}| \qquad 2.23$$

where μ_C is the Coulomb friction coefficient between particles. Note that the total force acting on a particle is the sum of the (a) contact forces, (b) gravitational force, and (c) any external force. Time integration of the equations of motion yields future particle positions and velocities. Therefore, time stepping is crucial and a key to finely resolving system dynamics in DEM. In MFIX, the time step for integration, Δt, is set so that it is sufficiently smaller than the time of collision, $t_{collision}$, [193]:

$$\Delta t = \frac{1}{50} t_{collision}, \tag{2.24}$$

where the time of collision is given by:

$$t_{collision} = \pi \left(\frac{k_n}{m_{eff}} - \frac{v_n^2}{4\, m_{eff}^2} \right)^{-\frac{1}{2}} \tag{2.25}$$

and the effective mass of interacting particles with individual masses m_i and m_j is given by:

$$m_{eff} = \frac{m_i\, m_j}{m_i + m_j}. \tag{2.26}$$

Chapter 4 will discuss the modifications to the DEM simulation framework for the squeezing simulation to incorporate one-way particle-fluid interaction coupling via drag force. Briefly, the polymer fluid flow velocity profile is analytically solved assuming Newtonian behavior. A suitable drag law is then used to compute drag forces on the particles as a function of the relative particle fluid velocity, local particle volume fraction, particle diameter and fluid viscosity. This is a step towards better representing the complex particle fluid interactions in the real world.

3. 3D X-RAY MICRO COMPUTED TOMOGRAPHY ANALYSIS OF DISPENSED AND SQUEEZED TIM MICROSTRUCTURES

3.1 Introduction

This chapter discusses experimental investigation of the TIM microstructure and particle redistribution in the material after squeezing using 3D X-ray micro-computed tomography (XRCT) imaging. Section 3.2 discusses the in-house preparation of the TIM and constituent material characteristics. Sections 3.3 and 3.4 describe manual and automated procedures for the application of the TIM. In the early stages of this research work, the dispensing and squeezing procedures were manual because the focus was then on establishing an image processing workflow. In section 0, the XRCT experimental set-up and fundamentals of the image processing and the analysis procedure are described. Section 3.6 discusses the squeeze process-induced variation. Section 0 analyzes the microstructure of the dispensed and squeezed TIMs produced via automated procedures and section 3.8 discusses a Péclet number framework for predicting heterogeneity in the particle spatial distribution. Finally, section 3.9 summarizes the findings and provides guidance on next steps.

3.2 TIM Preparation and Constituent Materials

Spherical copper particles from US Research Nanomaterials, Inc. (Cu powder 150um spherical, Stock # US5002) (median diameter ≈ 110 μm) are manually mixed with a UV-curable epoxy (UV Cure 60-7158, purchased from Epoxies, Etc.) using a plastic spatula to prepare the mock TIM (see Table 3.1) at a target of 30 vol% particles. The target filler volume fraction is estimated based on weight and density of the constituents. The mixing is performed gently and slow enough such that there were no visible air bubbles present. Note that this mock TIM varies from commercial TIMs (larger particle sizes, UV-curable matrix, and a lower volume fraction of particles), but provides a starting point for developing experimental capabilities and validating models. Although commercial TIMs consist of a significantly higher loading of particles by volume, this poses image processing issues (*i.e.*, a high density of particles can block the X-rays completely). Moreover, higher filler loading renders the UV curing process more difficult, and solidification of the TIM will likely be incomplete. Therefore, 30 vol% filler loading is used in this work, and the focus is

Table 3.1. Materials used in this study and their properties

Constituent	Material	Density ($kg\ m^{-3}$)	Viscosity ($Pa\ s$)	Manufacturer
Particles	Copper	≈ 9000	---	US Research Nanomaterials, Inc., stock # US5002 (https://www.us-nano.com/inc/sdetail/29741)
Polymer	Polyurethane based	1100	20	*UV Cure 60-7158* (https://www.epoxies.com/products/uv-curable-illumabond/)[1]

on analyzing squeezing of individual line dispense pattern for TIMs consisting of large, spherical particles. Commercial TIMs often include variety of particles with sizes ranging from submicron to ~ 50 μm and can include both spherical and faceted shapes. The spherical shape of the particles makes validation of simulated microstructures with experimental data relatively easy when compared with arbitrary shaped particles and the larger particle size facilitates high resolution XRCT imaging. Initially, a mock TIM was prepared with 10 μm spherical copper particles, but the XRCT imaging was unable to resolve individual particles. Thus, larger particles were selected for this work.

Metal particles are used in this investigation for two reasons: (a) they have relatively high thermal conductivity and therefore are similar to the vast majority of the commercial TIMs which commonly consist of ceramic, metal, or carbon-based particles [194] and (b) using metal particle in a polymer matrix provides a significant density difference, ~8x higher for particles compared to the matrix, for a high contrast XRCT imaging. Spherical copper particles were found to be ideal for this research as they are affordable and have appropriate size. The particles are first sieved to a desired size range – for manual application tests, the sieved size range is $90 - 125$ μm and for the automated application, it is $90 - 106$ μm. The respective particle size distributions (PSDs) are discussed in the subsequent sections on manual and automated procedures for dispensing and squeezing TIMs.

[1] *The link contains information on cure times for the pure polymer based on different types of UV light intensity and set-up.*

3.3 Manual Procedure for Application of the TIM

Although the application for the TIM is generally automated on an industrial assembly line, the samples in this manuscript are initially prepared by manually dispensing and squeezing the TIM in order to help establish the experimental workflow such as the parameters of 3D XRCT image acquisition and image processing required to quantify the microstructural characteristics. An isolated line of TIM is dispensed through a syringe with a straight metallic needle opening diameter of 838 µm (or $\approx 7.4D_p$, 18 gauge) on a substrate (see Figure 3.1 (a)), which consists of a glass microscope slide covered with copper foil ($\approx 60\ \mu m$ thick). The isolated line pattern provides insights into the fundamentals of the squeezing process and is a starting point to understanding more complicated dispensed shapes. The copper foil mimics the metallic heat spreader surface found in electronics packaging and allows the TIM to be easily removed for analysis. Subsequently, another bare glass microscope slide is pressed on to the dispensed TIM to manually squeeze it. The samples are then cured for ~7.5 minutes using a UV flood light system. In this work, UV Cure Zone 2 (UV Process Supply, Inc.) with a 400 W metal halide lamp cures the dispensed TIM samples. Per the original system specifications, it illuminates an area of 8 x 8 sq. inches at an irradiance of– note that this system is relatively old and its effective irradiance may have dropped below the manufacturer's specifications. Manually squeezed TIMs were also cured in this system, whereas TIMs squeezed in the Instron machine were cured using UV lamps. This lamp illuminates an area of 0.2 x 0.2 m^2 (8 x 8 sq. inches) at an irradiance of 800 Wm^{-2} (80 mW cm^{-2}). Figure 3.1 shows the UV-cured dispensed and squeezed TIM materials and regions from near the center of the material for analysis.

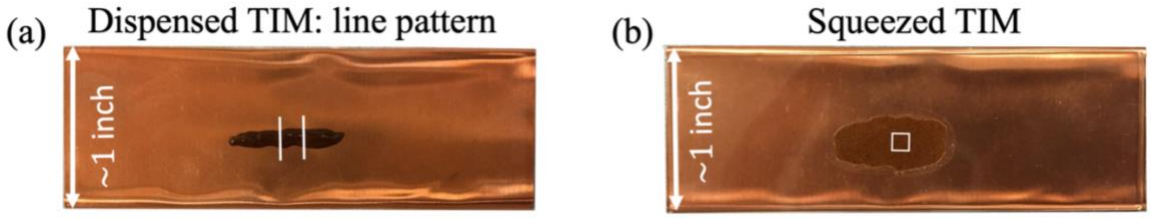

Figure 3.1 Manually (**a**) dispensed line pattern and (**b**) squeezed TIM on a glass slide covered with a copper foil. Dispensing is performed using a syringe fitted with a straight metallic needle, with an opening diameter of 838 µm (18 gauge). Squeezing is manually performed using a bare glass slide on the top. The white lines in (a) and the white rectangle in (b) denote the samples used for XRCT imaging.

TIM Preparation for Manual Tests

The mock TIM for these tests is prepared using particles sieved to a size range of $90 - 125$ μm to provide a narrow size distribution with relatively large particle size (≈ 100 μm). The particle size distribution (PSD) is measured using the Malvern Mastersizer 3000 laser diffraction particle size analyzer. The volume distribution of PSD is shown in Figure 3.2 and the median particle equivalent sphere volume diameter is $D_{m,s} = \mathrm{D50} = 114$ μm. Table 3.2 lists the D10, D50 and D90 sizes. Although the particle sizes should be in the range $90 - 125$ μm because of the sieving process, particle sizes outside this range are observed in the measured PSD. This is clearly observed in the D10 and D90 values. This could have occurred due to defects in the sieve, thus allowing larger particles to pass through the 125 μm sieve. Smaller particles likely agglomerated and did not pass through the 90 μm sieve.

Table 3.2 Volume distribution based D-sizes of the spherical copper particles based on measurements from Malvern Mastersizer 3000.

D-size	Value (μm)
D10	91.8
D50	114
D90	140

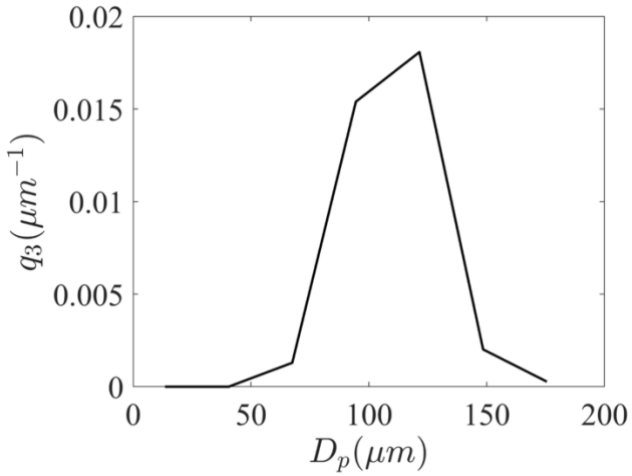

Figure 3.2 Volume distribution, q_3 (μm^{-1}), of the particle equivalent sphere volume diameter, D_p. The particles were initially sieved to a size range of $90 - 125$ μm. The measurement is performed using Malvern Mastersizer 3000.

3.4 Automated Procedure for Application of the TIM

3.4.1 Automated Dispensing

To improve repeatability in dispensing, isolated line patterns of the TIM are dispensed on a glass slide (covered with copper foil) using a dispense rig (see Figure 3.3). A 5 ml syringe fit with a 16 gauge tapered plastic needle (opening diameter 1.19 mm $\approx$ 11.2 $D_{m,ce}$) is mounted on the vertical axis of the dispense rig $\sim$2.4 mm away from the substrate on which the TIM is deposited. The idea here is to mount the syringe such that the needle is as close as possible to the substrate. The tapered geometry of the needle eliminates the issue of TIM agglomeration (or lump formation) at the end of dispensing, which is observed with straight metallic needles of varying diameters.

Note that the 18 gauge metallic straight needle used in manual dispensing (section 3.3) could not be used here as the motor torque is insufficient to exert sufficient force on the syringe to allow flow of TIM through the nozzle opening. The 16 gauge needle gauge diameter was selected after experimenting with a few different gauge diameters and based on qualitative observations of the dispense patterns (such as thickness and appearance). Dispensing with the needle very close to the substrate results in a flatter dispense pattern and the TIM flows to the sides; if the needle is far

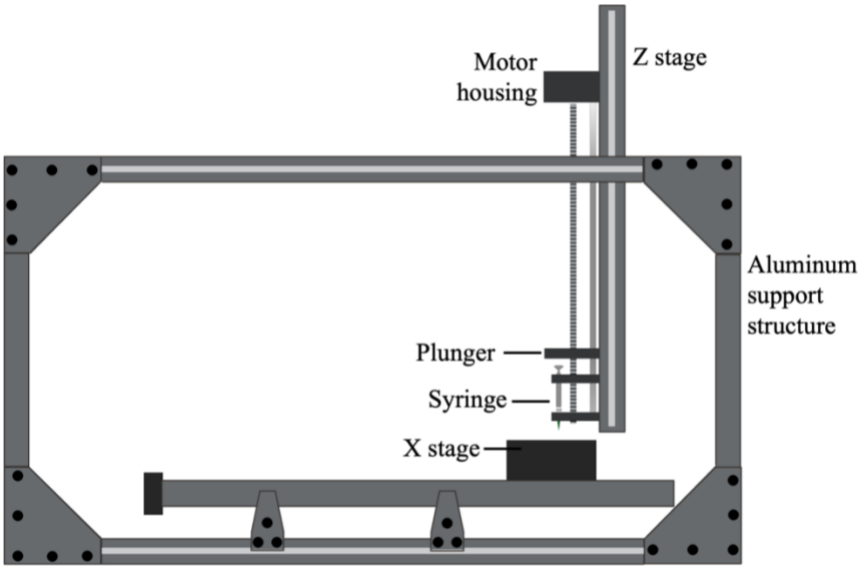

Figure 3.3 Schematic of the experimental rig for controlled dispensing the TIM. The backbone frame structure is made out of aluminum. The syringe is mounted on the Z stage. The glass substrate (not shown) is on the X stage, which moves out of the page as the plunger pushes the TIM out of the syringe nozzle to deposit a line pattern. The rig was previously designed and developed in-house by former colleagues Sally Jia and Dr. Collier Miers.

away from the substrate, it is difficult to obtain a line pattern. All three axes of the rig are controlled using RepRap DUET microcontrollers that read G-codes communicated via the Arduino integrated development environment.

The substrate for TIM deposition is a glass microscope slide – either bare or covered with copper foil ($\approx 60\ \mu m$ thick). The foil is affixed with the aid of three rectangular strips of double-sided tape (see Figure 3.4(a-b)). The metal foil serves two purposes: (a) it mimics the surface characteristics of the integrated heat spreader found in a commercial microprocessor, and (b) it enables easy sample retrieval after squeezing and curing. Two line patterns are dispensed on either ends of the glass slide (≈ 0.5 inch away from either ends). Hence, they are isolated, and intermixing of the particles from these two line patterns during squeeze does not occur (see Figure 3.4(c)). In contrast to the manual dispense/squeeze tests, two lines are dispensed because that aids in system symmetry during the squeeze process (see section 3.4.2). The volumetric dispense rate is $\sim$1.2 ml $(\text{min})^{-1} \approx 2\text{x}10^{-8}\ \text{m}^3\text{s}^{-1}$ as measured by volume of TIM deposited over time. To account for edge effects, the dispensing process begins a few millimeters away from the glass slide and ends a few millimeters beyond the slide. The dispensed TIM is UV-cured for 2 hours in the same 400 W metal halide UV flood lamp.

For 3D XRCT imaging, a TIM sample with length $\approx 0.15 - 0.2$ inch is cut out from near the center of the cured line dispense pattern. Note that curing the TIM deposited on the copper foil-covered slide was incomplete (Figure 3.4(d)), with the bottom portion remaining uncured. However, the TIM deposited on bare glass slide is completely solidified as it was flipped half-way through so that UV light could reach the bottom portion of the dispensed TIM (Figure 3.4(e)). The only disadvantage is that the TIM bonds to the glass slide and it is impractical to separate the two during sample preparation. Samples are cut out from both these cases from near the center of the line pattern (gray rectangle in Figure 3.4(d, e)). Attempts to cut out sample with the copper foil still intact beneath it failed as the uncured TIM near the bottom slips on the smooth surface of the foil and some of the particles are left behind sticking to the foil. Uncertainty in particle distribution is expected near the bottom portion of the TIM in this case. In Figure 3.4(e), center and off-center samples are analyzed – variation of microstructural features along the axis of the line pattern can be assessed by analyzing these sample regions.

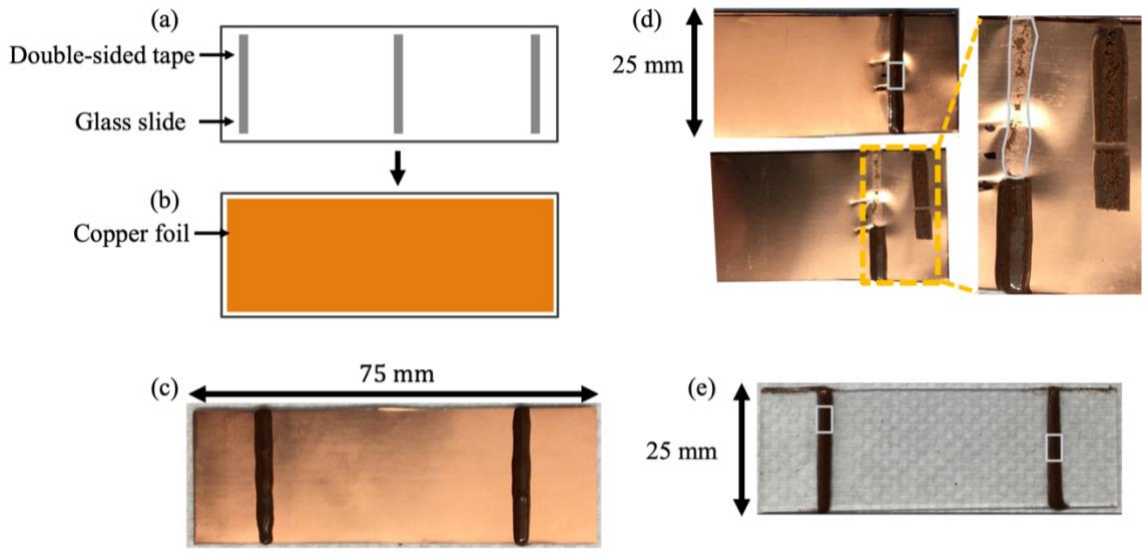

Figure 3.4 (**a-b**) Schematic of the bottom glass slide showing three rectangular strips of double-sided tape used to affix the copper foil. (**c**) Two isolated line patterns of the TIM dispensed at the rate of ≈ 1.2 ml $(\text{min})^{-1}$ on a glass slide covered with copper foil. Note that gravity is into the plane of the page. (**d**) Sample cut out (length $\approx 5 \times 10^{-3}$ m or 0.2 inch) from near the center after a 2 hour UV cure, showing uncured TIM near the contact region with the copper foil (gray polygonal outline). The gray rectangle represents the sample region for analysis. The samples are flipped in the bottom image and enlarged (inset) to show uncured portions (gray outline). (**e**) Line pattern dispensed TIM on a bare glass slide. The gray rectangles approximately show the sample regions cut out with length $\approx 5 \times 10^{-3}$ m (0.2 inch).

UV Curing for Dispense Tests

To be able to experimentally measure the microstructure of the TIM, its state right after dispensing and squeezing must be investigated. Therefore, the TIM must be cured immediately after dispensing and squeezing. Conventional thermal curing generally more than an hour [20,195,196] and is not be used in this study as the particles may settle during that time and any examination of the microstructure will not be representative of the dispensed or squeezed states. UV curing takes a few seconds to minutes (depending on the source power and intensity) to solidify polymeric materials was initially thought to be a viable alternative to thermal curing. Addition of particles increases the cure time depending on particle concentration and thickness of sample. The cure times are different for samples prepared manually and using automated procedures. The same 400 W metal halide UV flood lamp station is used to cure all dispensed TIM samples. Experimentally, it is found that a cure time of ≈ 7.5 minutes was sufficient to cure these manually prepared samples. However, after several tests, it is found that a cure time of 2 hours is necessary to completely solidify the as dispensed TIM prepared using automated procedure. The primary

reason for the long cure time is its thickness (≈ 1.1 mm) compared with that of manually dispensed TIM (≈ 0.67 mm). To achieve complete solidification, the glass substrate is flipped half-way through to expose the back side of the TIM to UV light.

Sample Preparation for the Dispensed TIM

As seen in Figure 3.4(e), the left sample region is cut out from an off-center region of the line dispense pattern. As noted in the previous section, comparing microstructural characteristics for the center and off-center samples provides information regarding variation of property along the axis of the dispensed TIM.

3.4.2 Constant Velocity Squeezing

Constant velocity squeezing is automated using an E-1000 series Instron mechanical tester. The TIM is squeezed in between two glass microscope slides as shown in the schematic in Figure 3.5 (a)). The two isolated line patterns that are dispensed on either ends of the bottom glass slide using the automated process in section 3.4.1 enable off-axis squeeze with the assistance of a squeeze rig (see Figure 3.5 (b)). The squeeze rig adapter is designed in-house[2] and machined out of aluminum to provide a rigid backbone to the glass slides during squeezing and, thereby, eliminate bending of the slide near its center, especially at high loads. The adapter also helps ensure that the plane of the glass slides are parallel during squeeze. In addition, there are two slots on the adapter that allow UV light to pass through to cure the TIM *in situ* after squeezing. The top glass slide (see Figure 3.5 (c)) is attached to the metallic squeeze rig adapter using double-sided tape (3M Scotch packaging tape). The tape is applied on the bottom surface of this glass slide to aid in easy removal of the squeezed and cured TIM. The bottom glass slide is covered with copper foil (see Figure 3.4 (a-b)). In this work, the TIMs are squeezed at constant velocity $V_S = 1\ \mu\text{m s}^{-1}$ or $10\ \text{mm s}^{-1}$ up to a force of $F_S = 50$ N or 100 N. The Reynolds number $Re = \frac{\rho_f V_S D_{m,ce}}{\mu_f} \ll 1$ for both cases.

[2] With the assistance of undergraduate students Harris Tariq Fathe and Grant Gauthier

This process is programmed and controlled by the Instron machine software. The load is held constant after the critical squeeze force is reached and curing is performed for 1 hour. Holding the load constant during cure is critical because, without it, the TIM will exhibit an elastic response and spring-back. This forms finger-like structures that are not representative of the desired squeezed state.

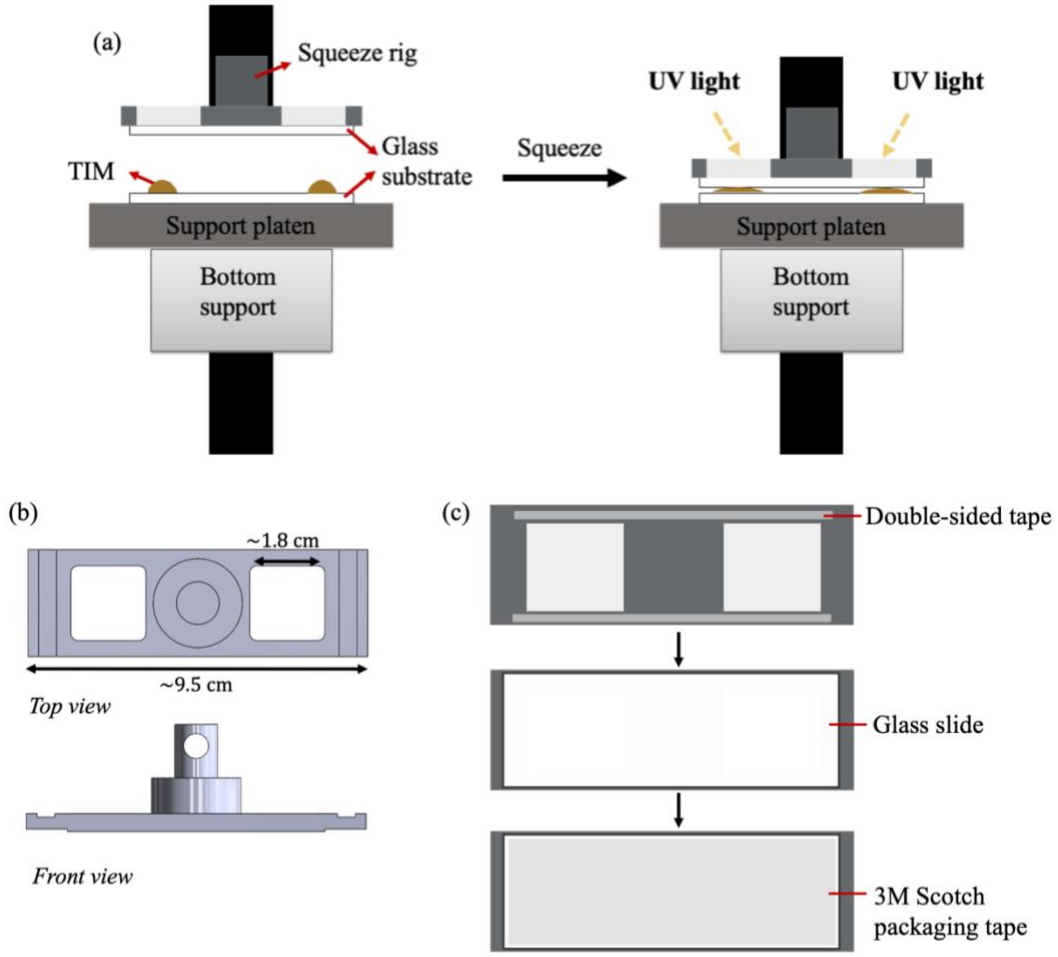

Figure 3.5 Automated constant velocity squeezing using Instron mechanical tester: (**a**) Schematic of the off-axis squeezing process where two line dispense TIM patterns (deposited on the bottom glass substrate) are squeezed at constant velocity and then UV-cured while holding the load constant. (**b**) Model of the squeeze rig adapter designed and manufactured in-house to assist this process. (**c**) Bottom side of the squeeze rig adapter showing two rectangular strips of double-sided tape, on which the top glass substrate is attached. Then, 3M Scotch packaging tape is affixed on this to enable easy removal of samples after squeezing and curing.

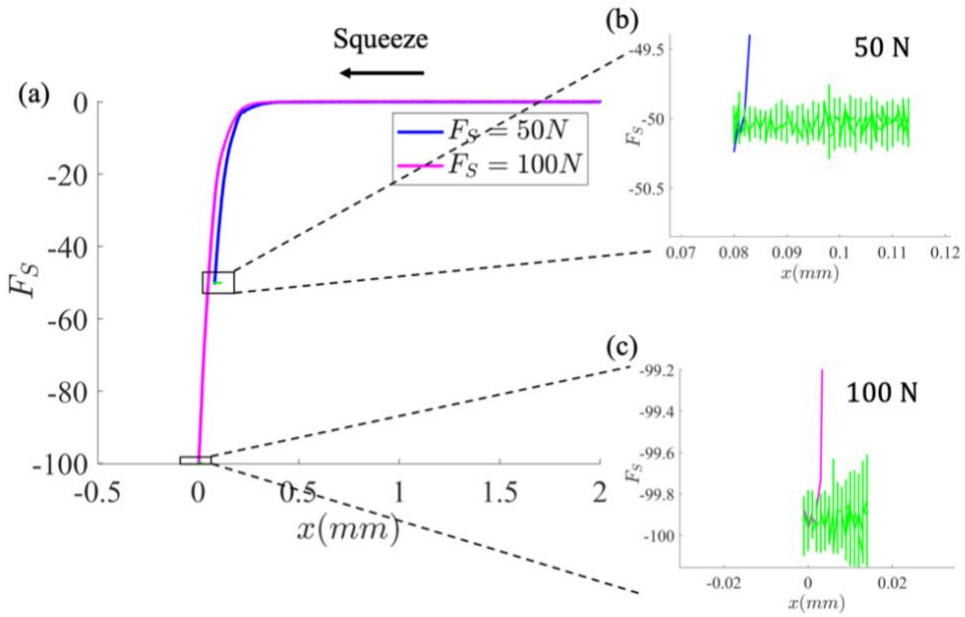

Figure 3.6 (**a**) Load vs displacement during squeezing for squeeze rate of $V_S = 1$ μm s^{-1} at two different ultimate squeeze forces $F_S = 50$ N and 100 N. (**b, c**) Load vs displacement for the load-holding phase for the two cases, exhibiting variation around the set force over time. These variations are averaged to calculate applied pressure exerted on the TIM during squeezing.

The load and displacement are recorded by the Instron at user-specified intervals. Figure 3.6 (a) shows the evolution of load vs displacement for squeezing at $V_S = 1$ μm s^{-1} for two different ultimate squeeze forces, $F_S = 50$ N and 100 N. Data acquisition in the load-holding phase is limited by monitoring displacement and load variations. Otherwise, continuous data acquisition leads to large file size and loss of data from earlier stages of the squeeze process. In the control program, the duration of the load-holding phase is ≈ 3 hours. Although cure duration is 1 hour, the extra time in this phase acts as buffer. After curing, the user can end the process on the Instron software. The squeeze pressure is calculated based on the average force (see Figure 3.6 (b, c)) and area of the squeezed TIM is computed by constructing a polygonal region of interest around the TIM based on optical image.

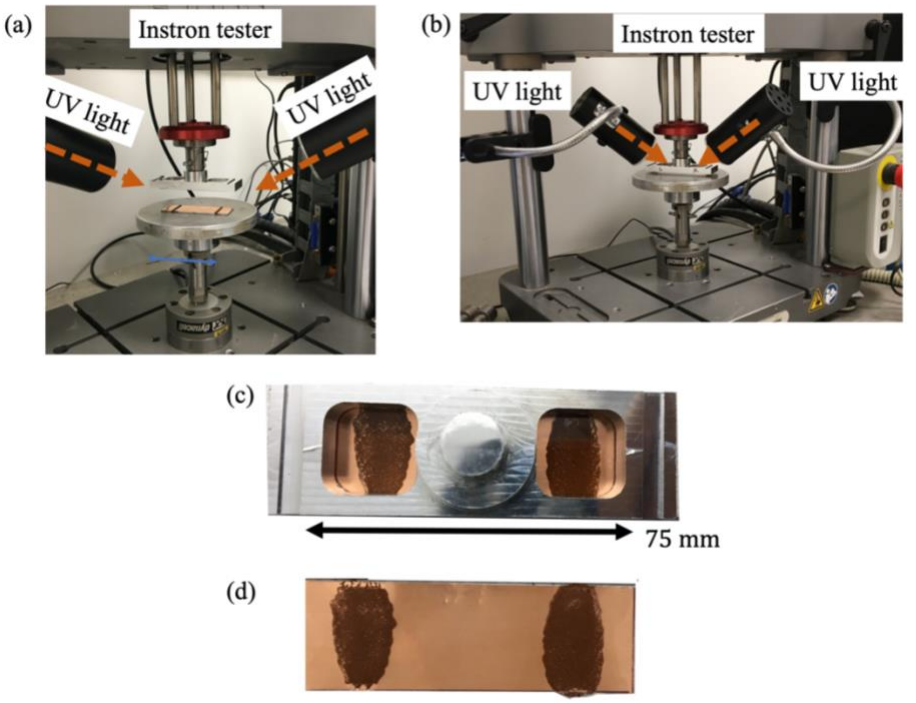

Figure 3.7 Constant velocity squeeze set-up using Instron machine and in-house designed squeeze rig using a (**a**) rigid and (**b**) flexible UV lamp fixture. The advantage with the flexible fixtures in (b) is the significantly shorter light source-to-sample distance. Optical images of the sample after (**c**) squeezing and 1 hour of UV curing, and (**d**) the squeeze rig is removed and the samples are ready to be retrieved from the bottom glass slide.

Two squeeze and curing set-ups are shown in Figure 3.7 using different lamp fixtures. Data from these tests, respectively labeled as *Set 1* and *Set 2*, are analyzed. In both cases, the bottom glass slide with dispensed TIM is placed on a circular plate whose area is significantly larger than that of the slide. This allows full support over the entire footprint of the slide during squeezing. Portable UV lamps[3], rated at 75 W, are attached to the support structures of the Instron tester. The UV bulbs are housed in a parabolic reflector, thus rendering the light rays approximately parallel as they are transmitted from the source. According to manufacturer's specifications, these lamps produce 97% UV-A light and 3% UV-B light. Heat generated during the cure process should further assist in solidifying the TIM, according to the epoxy technical datasheet. Initially rigid lamp fixtures were used (see Figure 3.7 (a)), but the curing process was improved by using flexible lamp holders allowing closer positioning of the lights.

[3] https://www.amazon.com/OMAYKEY-Reptile-Fixture-Holder-Clamp/dp/B07R33GTBN?ref_=ast_sto_dp

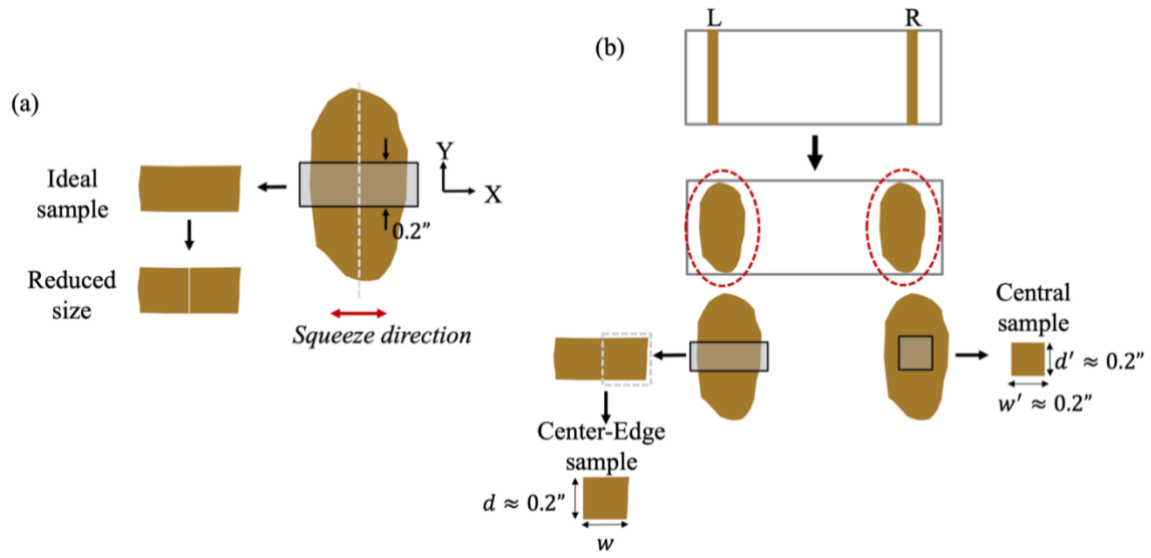

Figure 3.8 Schematic of samples cut out from the squeezed TIMs. (**a**) The ideal sample spans the width of the TIM in the X direction (*i.e.*, primary direction of particle redistribution). The reduced sample, obtained by cutting the ideal sample at its centerline, is used for XRCT imaging due to limited FOV and resolution implications. (**b**) Center-Edge and Central samples are manually cut out from two distinct TIMs produced in the squeeze tests. Samples are consistently prepared: Center-Edge samples are obtained from the left (L) TIM and Central samples from the right (R) TIM. In this work, w is dictated by the sample dimensions, and $d \approx d' \approx w' \approx 0.2$ inch ≈ 5.08 mm ≈ 47 median particle diameters $D_{m,ce}$.

Sample Preparation

One of the main objectives of microstructure analysis via 3D XRCT imaging is the quantification of local particle volume fraction along the direction where particles primarily redistribute during squeeze process (*i.e.*, along X direction in Figure 3.8 (a)). That helps delineate the effect of different processing conditions on the particle distribution uniformity and, ultimately, the bulk thermal conductivity. To investigate particle redistribution, the ideal sample (see Figure 3.8 (a)) must be sufficiently large to examine the spatial variation from the central region to outer edges. Such a sample is shaded by the grey rectangular region. However, high resolution imaging was found to not be feasible for this sample size due to field of view (FOV) limitations, and individual particle size and locations cannot be accurately resolved at lower voxel resolutions of $\geq (5\ \mu\text{m})^3$. Therefore, the sample is cut at its centerline to image one-half of the ideal sample. This sample is named "Center-Edge" (see Figure 3.8 (a)). One side length for this sample is chosen to be ≈ 0.2 inch, and the other dimension is governed by the sample geometry, while the BLT is

determined by the squeeze conditions. For comparative analysis, the local particle concentration near the centerline of the dispensed TIM is examined by imaging a central region (≈ 0.2 inch x 0.2 inch) from the second TIM produced in the same squeeze test (see Figure 3.8 (b)). This is named the "Central" sample. To be consistent, all Center-Edge samples are cut out from the left (L) TIM and Central samples are cut out from the right (R) TIM produced in the automated squeeze tests. The experimental imaging set-up is described in 3.5.1.

Note that quick scan tests were conducted for whole TIM specimen, and rectangular strip-type samples and one half of TIM specimen. In all these cases, resolution was not sufficient to identify individual particles. However, on a macroscopic scale, scanning large samples will reveal the presence of void regions within the TIM. This information is vita in understanding the influence of squeeze rate and force on the TIM thermal performance.

UV Curing for Squeeze Tests

The UV cure duration of 1 hour was experimentally optimized for the TIM at 30 vol% particle loading. Initial tests of cure duration for 15 and 30 minutes showed that significant portions of the squeezed TIM was not solidified. Then, it was increased to 45 minutes and subsequently to 1 hour. Qualitatively, the curing improves with the additional 15 minutes of UV exposure (Figure 3.9 (b)). UV cure duration is a function of the light source intensity, distance of the light source from the TIM (≈ 0.1 m or 4 inches) and light transmission losses through the two materials – glass and 3M tape in series. Using flexible lamp fixtures, the UV light source-to-TIM distance can be reduced to ≈ 0.025 m (1 inch). For the same cure duration of 1 hour, the solidification is nearly complete, except where the squeeze rig adapter physically blocks the light (see Figure 3.9 (c)). The gray polygonal regions shown in Figure 3.9 outline the TIM and emphasize an important observation that even at moderate filler loading of 30 vol%, the backside is not completely cured. This region felt greasy to touch and the uncured epoxy was visually confirmed to be present. Higher power UV lamp and a directed beam of light can help eliminate this phenomenon and thus completely solidify the TIM.

The lamps in Figure 3.7 (a) are ≈ 0.1 m (4 inches) away from the TIM. Flexible UV lamp fixtures are shown in Figure 3.7 (b). This arrangement enables better TIM solidification for the same cure

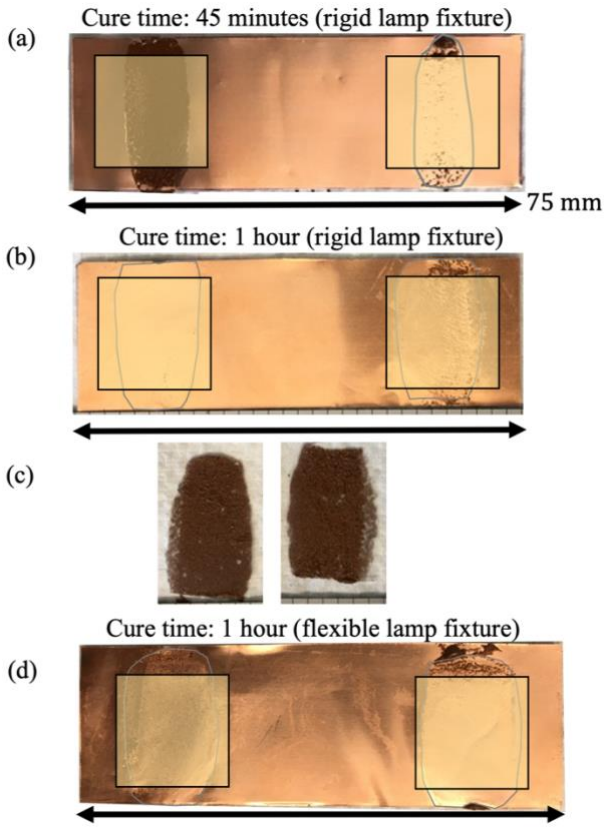

Figure 3.9 Optical images of the squeezed and cured TIMs with different curing conditions. TIM cured using the rigid lamp fixture for (**a**) 45 minutes and (**b**) 1 hour. (**c**) Images of the TIM samples in (b) after removal from the squeeze rig. (**d**) TIM cured using the flexible lamp fixture for 1 hour. Gray polygonal regions outline the regions from where the TIM is removed and encompass the slightly uncured portions. In panels (a), (b) and (d), the light yellow rectangles indicate regions that are illumiated by UV light.

duration of 1 hour as the sample to light source distance is just ≈ 1 inch. Figure 3.9 compares the squeezed and cured TIM samples with different curing processes.

TIM Preparation for Automated Tests

For automated squeezing, a fresh batch of TIM was prepared with a sieved particle size range of $90 - 106$ μm. The median circle-equivalent diameter of $D_{m,ce} = \mathrm{D50}$ is 107.7 μm (based on volume distribution) as measured by the Malvern Morphologi G3-ID instrument based on a sample size of $\approx 11{,}400$ particles (dry state). In this instrument, the particles are first dispersed on a circular area and then scanned linearly by a high resolution microscope. Circle equivalent diameter is measured by this technique by processing the particle images. The particle size distribution is

narrow, with a spread of 27.5 μm between the D10 and D90 sizes (see Table 3.3 and Figure 3.10 (a)). Approximately 75% of copper particles by volume used in this work are mostly circular ($C_p > 0.8$), with ≈ 5% (by volume) bearing poor circularity ($C_p \leq 0.5$) as seen in Figure 3.10 (b). Therefore, we can expect the 3D particle shape to be close to spherical.

Particle settling

The characteristic settling time, τ_{settle}, as calculated from Eqn. 3.1 [116] over a distance of a single particle diameter, $D_{m,ce}$, accounting for particle loading, is ≈ 7.4 minutes, which is significantly shorter than the experimental cure duration.

$$\tau_{settle} = \frac{18\mu_f}{\Delta\rho g D_{m,ce}} * \left(1 - \phi_p\right)^{-6.55} \qquad 3.1$$

Table 3.3 Volume distribution based D-sizes of the spherical copper particles for automated tests based on measurements from Malvern Morphologi G3-ID

D-size	**Value (μm)**
D10	97.1
D50	107.7
D90	124.6

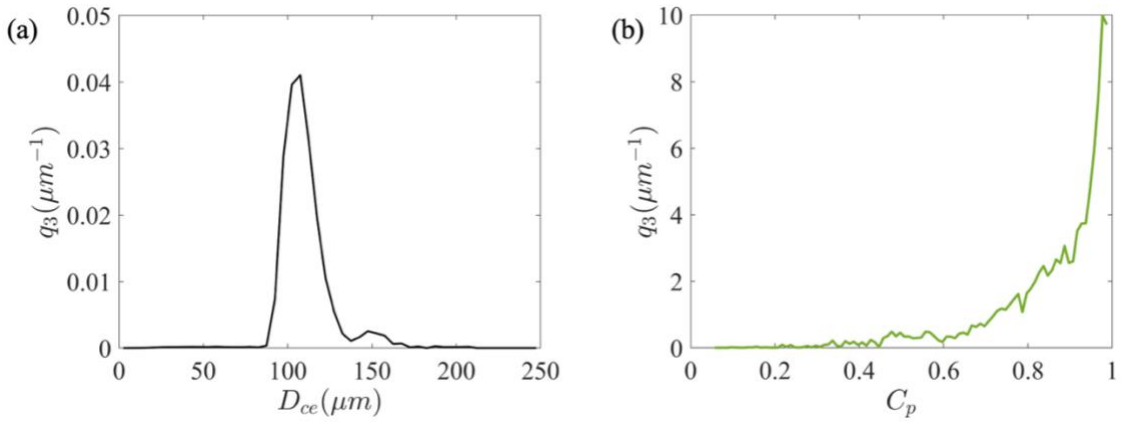

Figure 3.10 Volume distribution, q_3 (μm^{-1}), of the (**a**) circle equivalent particle diameter, D_{ce}, and (**b**) circularity, C_p, analyzed from high resolution optical imaging of ≈ 11,400 copper particles (dry state). The measurement is performed using the Malvern Morphologi G3-ID instrument for particles initially sieved to a size range of 90 − 106 μm.

where τ_{settle} is the particle settling time over a distance of one diameter $D_{m,ce}$, μ_f is the matrix viscosity, $\Delta\rho = \rho_p - \rho_f$ is density difference between particles (ρ_p) and matrix (ρ_f), g is acceleration due to gravity, $D_{m,ce}$ is D50 particle size, and ϕ_p is the target particle volume fraction in the TIM. In 2 hours, a particle within the TIM will traverse a distance of $\approx 16D_{m,ce}$. However, during curing, the viscosity of the matrix continuously increases as stronger chemical bonds are formed leading to TIM solidification. Experimentally, such a drastic particle settling is not observed. If it did, then the heap shape of the line dispense pattern presented in the next section would likely not have been observed. Note that there is $\approx 7 - 10$ minutes of time delay after dispensing and before beginning UV cure. So, settling is possible during this period.

3.5 3D XRCT Scan Set-up, Reconstruction, and Image Processing

3.5.1 Experimental Set-up for 3D XRCT Scan

In this work, the Bruker SKYSCAN 1272 is used for 3D XRCT imaging. This machine is capable of spatial resolution up to $0.35\ \mu m$. Samples are generally placed on relatively low-density materials such as Styrofoam or wooden blocks. In the manual TIM application case, the cut-out samples are assembled on top of Styrofoam that is mounted onto a metal rod and then this assembly is screwed in place inside the XRCT machine (see Figure 3.11 (a)). This is a rudimentary set-up and the main purpose was to establish an image processing workflow to extract particle locations and size.

The XRCT imaging set-up of the Center-Edge and Central samples produced from automated test procedures (see Figure 3.8) is shown in Figure 3.11 (b). Two samples are scanned simultaneously for time efficiency. Numerous imaging trials using Styrofoam as the sample housing showed that the samples curved or bent as a result of the assembly and this affected microstructure analysis. Moreover, separate imaging tests are performed where the samples are set-up on a piece of cardboard and Teflon. A combination of double-side tape and Parafilm to secure the sample also resulted in significant movement during the scan and a noisy dataset. Finally, a small wooden block is mounted on a metal rod to support the sample. A small piece of Parafilm is wrapped around the metal rod before inserting it into the wooden block. Then a larger piece of Parafilm is wrapped around the wooden block to tightly secure it to the metal rod. In all the tests, the Center-

Edge sample was placed on the block first and then the Central sample on top of it. After placing each sample, two thin strips of Parafilm are wrapped tightly around the sample in perpendicular orientation. Then, another strip of the film is wrapped sideways to secure the samples to the block. This minimizes relative movement during scan and thereby reduces noise in the image dataset.

The X-ray source is set to 100 kV at a power of 10 W and a 0.11 mm thick copper filter is used in all scans. This filter minimizes beam hardening effects. For denser objects, the X-ray energy can be tuned using the metallic filters available in the equipment which automatically set the source voltage and current. Prior to scanning, transmitted X-ray intensity is calibrated in the absence of the object in a process known as flat-field correction. Exposure time is adjusted for the desired resolution and filter to obtain an optimal intensity of 88% $\pm$ 1% during this correction. Then, the object rotation step, number of frames for averaging the intensity per rotation step and total scan angle are appropriately chosen. Recommended rotation step and number of averaging frames are available in the operation manual for various pixel resolution ranges. Four binning options are available: 1K, 1.5K, 2K, and 4K. In this work, 2K binning was used. Samples are scanned through 180° at a rotation step of 0.15° for samples produced from manual application and 0.1° for samples produced from automated procedures. At each sample orientation, a few frames are

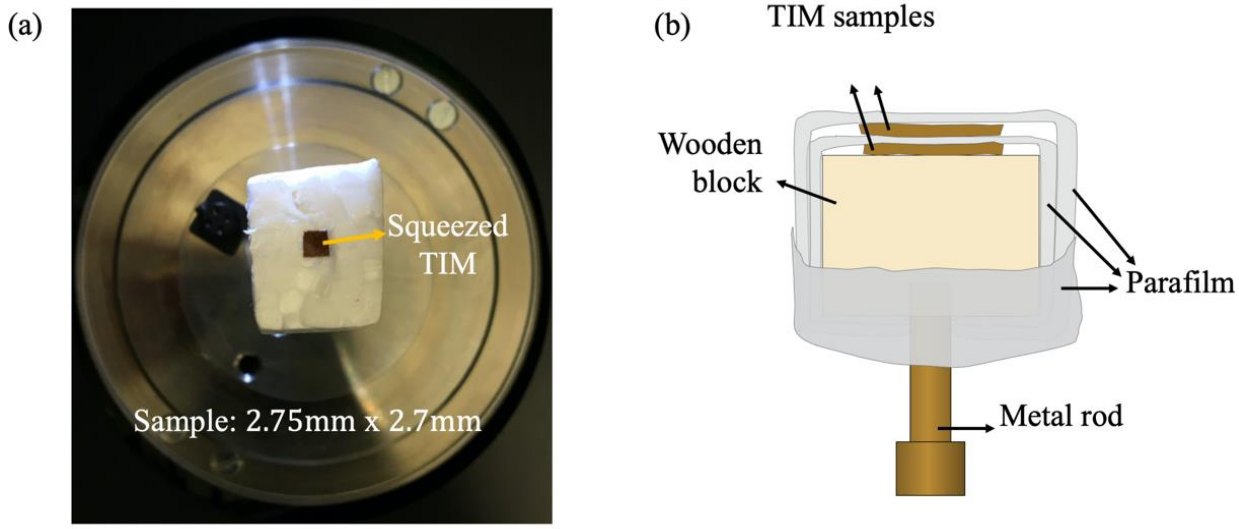

Figure 3.11 XRCT imaging set-up: (**a**) Top view of a squeezed TIM sample placed on Styrofoam and photographed prior to scanning, (**b**) Cartoon of TIM samples assembled on a small piece of wooden block to enable parallelized, high resolution 3D XRCT imaging. Each TIM sample is doubly wrapped with Parafilm to affix it to the wooden block, which itself is tightly bound to the metal rod using a wider piece of Parafilm (wrapped horizontally). This minimizes relative motion between the sample, block and the rod to obtain a noise-free image reconstruction

Table 3.4. 3D XRCT scan settings for TIM samples produced manually and via automated procedures

TIM Sample	Voxel Resolution (μm^3)	Rotation Step (°)	Number of Averaging Frames	Random Pixel Movement Parameter	Total Scan Time
Manual procedure					
Dispensed TIM	1.9	0.15	8	---	~19 hr
Squeezed TIM					~18 hr, 15 min
Automated procedure					
Dispensed TIM	3.5	0.1	4	20	~12 hr
Squeezed TIM					

captured and averaged (see Table 3.4). Random pixel movement parameter of 20 was used for the samples produced from automated procedures. This parameter minimizes ring artifacts in the reconstructed cross-sections. The X-ray spot size in this machine is < 5 μm. The total scan time for the TIM samples (of just a few millimeters in lateral dimension and a half millimeter in thickness) varied approximately between $12 - 18$ hours. After scanning, cross-sectional slices of the samples are reconstructed, which can then be used for 3D viewing of the reconstructed object; image processing techniques are subsequently exploited on the 3D dataset to determine particle locations and size. Microstructural features are then analyzed as described in section 0.

3.5.2 3D XRCT Reconstruction

In this section, 3D XRCT reconstruction and image processing workflow are described using the manually dispensed and squeezed TIM samples as example datasets. Table 3.5 summarizes the software packages used for (a) reconstructing the cross-sectional slices, (b) 3D viewing, (c) section viewing, and (d) image analysis. First, the raw images or projections collected by the X-ray detector are processed to reconstruct the material cross-sections using the proprietary NRecon software on a PC with 128GB RAM and a dedicated graphics processing unit (GPU). The processing and reconstruction is GPU-accelerated and the entire procedure takes less than 30 minutes. It allows the user to process the raw images before reconstruction as well as enable user control on the reconstruction material domain area.

Table 3.5. Software packages used for processing 3D XRCT image cross-section reconstruction, viewing and analysis

Processing	Software Toolkit
Reconstruction of cross-section slices	NRecon[O]
3D viewing	CTVox[O], ParaView (open-source) [197]
Section viewing	DataViewer[O]
Image analysis	CTAn[O] or FIJI/ImageJ2 (open-source) [198]
Microstructural analysis	Custom MATLAB scripts and open-source package [199]

[O]Bundled software package with the SKYSCAN XRCT equipment
*Third party software, proposed for all future investigation. Currently, results from analysis within FIJI is presented

The processing involves smoothing, correction of beam hardening, removal of ring artifacts, and alignment correction (for compensating minor sample movement during the scan). Parameters are varied independently for each of the aforementioned processing steps and then, visual inspection of its effects is performed on a reconstructed cross-section slice near the largest part of the object. User judgement is critical, especially when optimizing the parameter for ring artifacts correction and smoothing – if appropriate parameters are not chosen, there will be visible "shadow rings" in a reconstructed slice or blurring. Since the scan settings are constant for the different samples (see section 3.5.1), the reconstruction parameters are also held constant for all the datasets. That is, a beam hardening correction of 80%, ring artefacts correction of 20 and a smoothing factor of 6 are applied on the raw projections. The alignment correction parameter was set to the software-determined value as it was qualitatively tedious to determine the optimal value. If the user wishes to modify the parameter values, it can be saved as a separate parameter file that can be loaded at a later time to reprocess the projections. After processing the raw images, the final region of interest (ROI) for reconstruction of object cross-section and the image format type are selected by the user – in this investigation, the largest rectangular ROI was chosen to encompass the object wholly, and images were saved as 8 bit BMP. The reconstructed dispensed and squeezed TIMs are shown in Figure 3.12. 3D object viewing is achieved with the Bruker CTVox software. Notice that the heap-like formation in the line dispense pattern (Figure 3.12 (b)) is evident from the reconstruction. The squeezed TIM bond line thickness is ≈ 2.6 particle diameters (Figure 3.12 (d)) as by constructing a rectangular box around the microstructure.

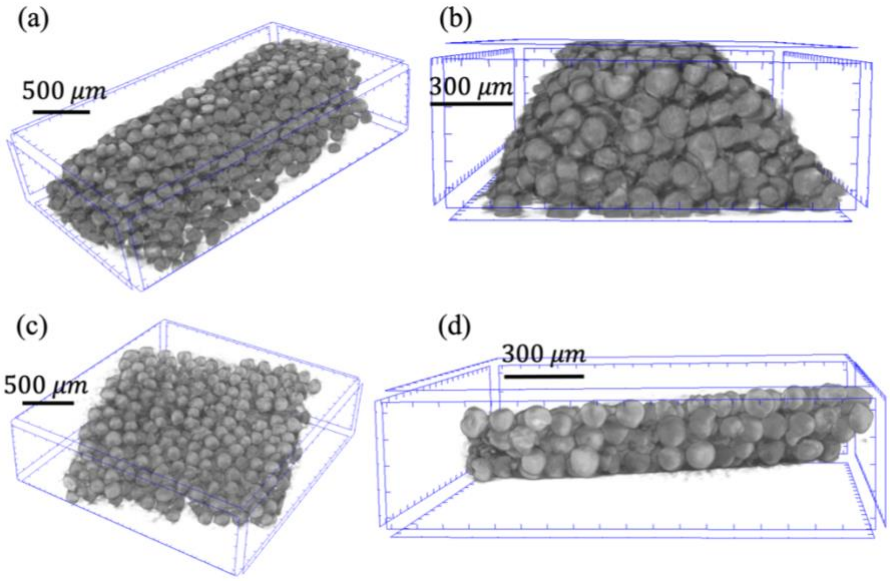

Figure 3.12 3D XRCT reconstruction of the manually **(a, b)** dispensed and **(c, d)** squeezed TIMs performed using CTVox. The voxel resolution is $(1.9\ \mu m)^3$. Samples for imaging are prepared by dispensing a line pattern of the TIM on a glass microscope slide (covered with copper foil) and then, squeezing it manually using another glass slide on top. The two samples are separately cured and small portions were cut out for XRCT imaging (see section 3.3). The median particle diameter is $114\ \mu m$. The squeezed TIM is approximately ~ 2.6 particles thick with a BLT of $\approx 297\ \mu m$.

The next three figures show 3D reconstructions of TIM samples produced using automated application methods. All TIM samples produced from the automated tests were scanned at a voxel resolution of $(3.5\ \mu m)^3$. Figure 3.13 shows the 3D reconstructed images of a line pattern TIM dispensed on bare glass slide. Figure 3.14 shows another line pattern TIM dispensed on glass slide covered with copper foil. Both dispensed TIM samples were cut out from near the center of the line pattern. Figure 3.15 shows a pair of squeezed TIMs scanned simultaneously, as discussed in 3.5.1.

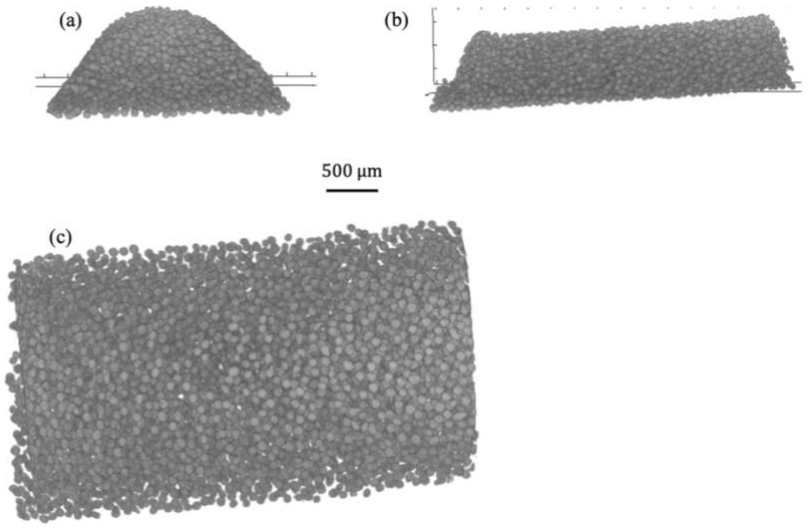

Figure 3.13 **(a)** Front, (**b**) side, and (**c**) top views of the 3D XRCT reconstructed image of a TIM dispensed on bare glass slide using automated procedure. The voxel resolution is $(3.5\ \mu m)^3$.

3.5.3 3D Image Processing Workflow

Individual particle size and location are extracted from the reconstructed cross-sections using 3D image processing algorithms *i.e.*, algorithms are applied on the 3D image dataset. Particle shape is idealized as spherical, and an equivalent sphere volume diameter is computed. This can be achieved either using Bruker's CTAn software or open-source packages such as ImageJ and FIJI

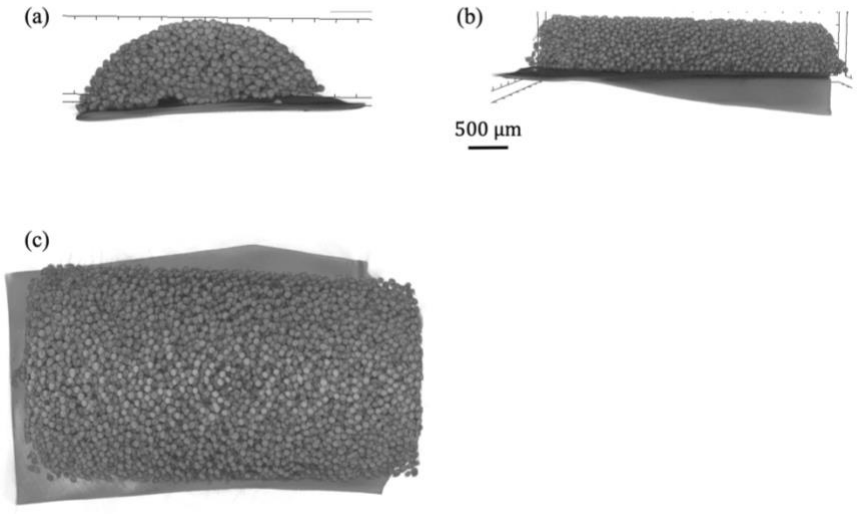

Figure 3.14 **(a)** Front, (**b**) side, and (**c**) top views of the 3D XRCT reconstructed image of the TIM dispensed on a glass slide covered with copper foil using automated procedure. The voxel resolution is $(3.5\ \mu m)^3$.

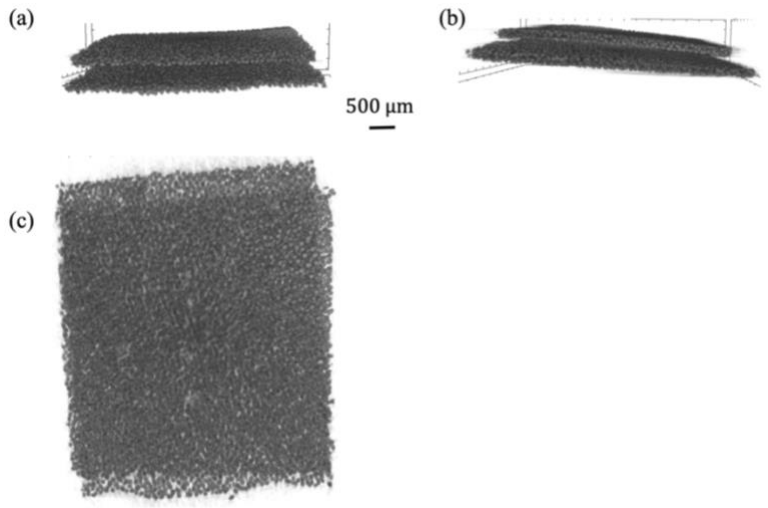

Figure 3.15 **(a)** Front, (**b**) side, and (**c**) top views of the 3D XRCT reconstructed image of the TIM dispensed on a glass slide covered with copper foil and squeezed at $V_S = 1$ µm s^{-1} and $F_S = 50$ N using automated procedures. The voxel resolution is $(3.5\ \mu m)^3$.

[198]. Initially, particle size, location, and porosity were measured using CTAn software. While it provides a wide array of 2D/3D image processing algorithms including noise reduction, binarization and microstructure analysis (such as porosity, microstructural anisotropy), FIJI provides a more versatile functionality via built-in functions and numerous plug-ins, all of which are open-source (see Appendix A). Moreover, it was found that some critical operations like the watershed segmentation in CTAn software did not process as expected and the results were visually confirmed to not be acceptable. Therefore, in this work, image processing is performed with FIJI.

The XRCT image processing flowchart is shown in Figure 3.16 and examples of the image processing steps are shown in Figure 3.17. It is not the intention of this thesis to delve into the mathematical details of the image processing algorithms, rather a simplified explanation is provided, and the reader is referred to relevant works. Irrespective of the software that have been used for image processing, based on prior work focused on analyzing particulate media [54,55,144,146,200], the basic algorithm involved the following: **(a) noise removal/reduction** of the gray scale data by filtering and/or despeckling to remove small voxel to voxel variation; **(b) thresholding** to identify polymer matrix and particle voxels yielding binarized data; **(c) removal**

of artifacts such as holes within particles; **(d) segmenting** or breaking apart touching particles (induced by previous processing steps); and **(e) identification of individual object**s including the

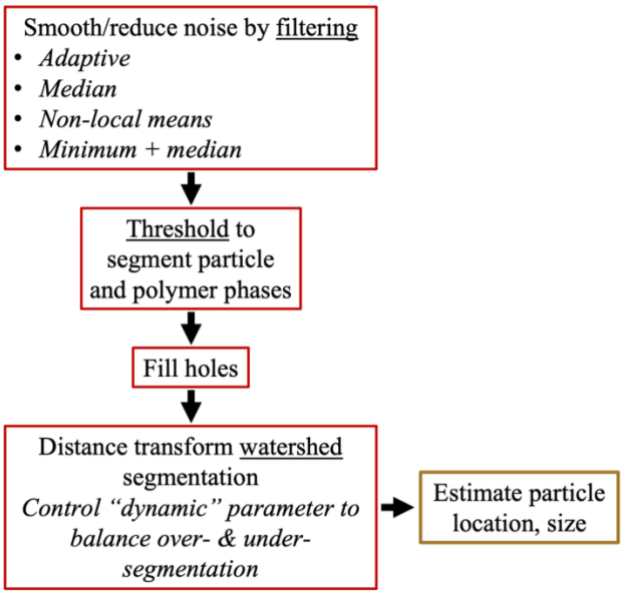

Figure 3.16 Flowchart of the 3D image processing using FIJI toolkit to extract particle locations and sizes. The algorithm involves noise filtering, thresholding, artifact removal (*i.e.*, a fill hole operation), watershed segmentation, and analysis of individual particles. Noise filters such as median, adaptive, non-local means, and minimum + median are available. The watershed segmentation involves a user-controlled "dynamic" parameter that balances over- and under-segmentation.

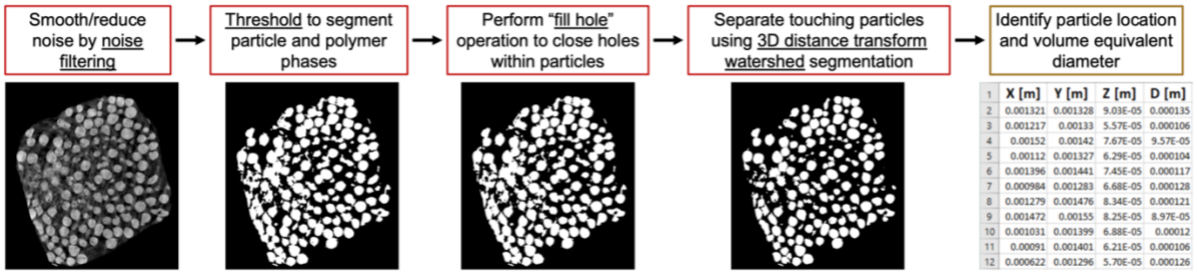

Figure 3.17 3D image processing flowchart showing the effect of various image operations such as filtering, thresholding, filling of holes, and watershed segmentation on a manually squeezed TIM sample. In this figure, a 3D median filter is used on the raw image dataset. As noted in the text, the NLM filter is used for all samples from the automated tests. The image size is approximately 1.88 mm x 2.03 mm.

particle centers and sizes (*e.g.*, equivalent sphere diameter). Based on the volume of objects from step (e), an equivalent sphere diameter is calculated and interpreted in physical units based on the voxel resolution.

Noise Removal

Various noise filters are available such as median, adaptive, non-local means (NLM) and minimum + median. The main objective of filtering is to minimize blurring, smoothen the image and sharpen particle edges. Median [201–203], adaptive [204,205] and NLM [206] are ideal for this. Median filter (and most other morphological operations) requires specification of a kernel shape (*e.g.*, box or sphere) and size (δ_k) [207], whereas the NLM plug-in is fully automated. In this work, $\delta_k \approx 0.05\ D_{p,m}$ where $D_{p,m}$ is the measured median particle diameter, was used for processing images of the manually prepared TIM samples. Owing to the particle size distribution, this may adversely affect detection of smaller particles. Therefore, NLM is desirable in this case.

Thresholding

Next, a thresholding operation is needed to binarize the data with white voxels representing particles, and black voxels representing the matrix and/or air bubbles. For the purpose, an automated Otsu's thresholding [208] method is used.

Artifact Removal

In the 3D reconstructed images, some particles were hollow (see Appendix Figure A1) and this appeared as black voxels enclosed within white voxels after thresholding. Either morphological reconstruction [146] or closing operation [144] can be performed to close the holes. A morphological closing is a combination of dilation and erosion operations [145]. A dilation operation adds more white voxels to a given dataset and an erosion operation deletes white voxels. Erosion is necessary because the former operation will add white voxels globally and that is not desirable – only the holes must be eliminated by dilating the white voxels surrounding the black ones to occupy the entire hole. Initial tests showed that, with a reasonable spherical kernel (*i.e.*, size not exceeding 10% average particle diameter), all the holes could not be filled. Therefore, a 3D "fill hole" operation using the MorphoLibJ plug-in library [209] is chosen as it (a) has been

used in prior work [146] to fill holes and cracks in particles and (b) is fully automated. Thus, the trial-and-error nature of sizing the dilation and erosion operations is eliminated. This algorithm identifies and fills black voxels that are completely enclosed within white voxels. It is possible to observe particles with partial black regions inside them that are not filled. The equivalent sphere volume diameter of such particles with holes in them may result in smaller particle diameters post processing.

Segmentation

The next task is to separate particles that appear to be touching. Neighboring particle boundaries connect as a result of image noise and thresholding artifact. This is an effect of the competition between voxel resolution and particle size. The segmentation is implemented using the distance transform watershed algorithm [56,201,210,211] available in the MorphoLibJ plug-in library. This algorithm involves a flooding operation to "fill basins" and construct "dams" when the basins are filled [212]. Flooding of the basin begins at local minima, which in this case are the particle centers, and the basin is the particle volume. Ideally, if this algorithm works perfectly, dams must be constructed at the real boundaries of particles. However, it was observed that (a) several individual particles were improperly broken apart or segmented by the watershed algorithm and (b) multiple particles merged to make up large particles. These issues plausibly arise due to a combination of the unfilled holes within particles and lower image resolution, respectively. Generally, the watershed segmentation works well if the scale parameter, $s_v = \frac{\bar{D}_p}{p_v} > 30$, where $\bar{D}_p$ is the average or median particle diameter and p_v is voxel size [213,214]. At lower resolution, interparticle regions are difficult to resolve and thresholding usually merges the neighboring particles. So, it is critical that edge-preserving noise filters are used for lower resolution datasets. The "dynamic" parameter, d_w, in the watershed operation can be set to balance the over- and under-segmentation. Higher d_w leads to particle agglomeration (under-segmentation) and lower d_w causes more particle breakage (over-segmentation). For the manually dispensed and squeezed TIM samples, $d_w = 2$ (default value) and that worked well as the voxel resolution was higher ($p_v = 1.9$ μm) with $s_v = \frac{114}{1.9} = 60$. But for all other image datasets the voxel resolution is lower ($p_v = 3.5$ μm) with $s_v = \frac{107.7}{3.5} \approx 30.8$. In this case, the default value of $d_w = 2$ led to significant particle agglomeration and, hence, we use $d_w = 1$.

Particle Analysis

Finally, particle sizes and centers are computed using the 3D Objects Counter plug-in [215]. The object volume and centroid location are stored in a spreadsheet format. Equivalent sphere volume particle diameter is calculated from the volume output in the 3D Objects Counter plug-in. Figure 3.17 shows the application of various image processing algorithms on the manually squeezed TIM dataset. Although only one image slice is shown, the algorithms were applied in 3D for the entire dataset. The XRCT detected particle sizes and locations are plotted as idealized spheres using open-source visualization software toolkit ParaView [197].

Analysis of the Manually Dispensed and Squeezed TIMs

Figure 3.18 shows the microstructure for the manually dispensed line pattern and the manually squeezed TIM samples. These samples are analyzed mainly to help establish an image processing workflow. The squeezed TIM sample (Figure 3.18 (c, d)) is cut out from a central region, and therefore does not provide insights into particle redistribution with respect to the dispensed state.

Figure 3.19 shows the particle size distribution of particles detected from XRCT image processing of the dispensed and squeezed TIMs compared to the laser diffraction measured PSD. The differences are attributed to (a) incomplete filling of holes within particles (size underestimation), (b) breakage of individual particles during watershed separation (size underestimation), and (c)

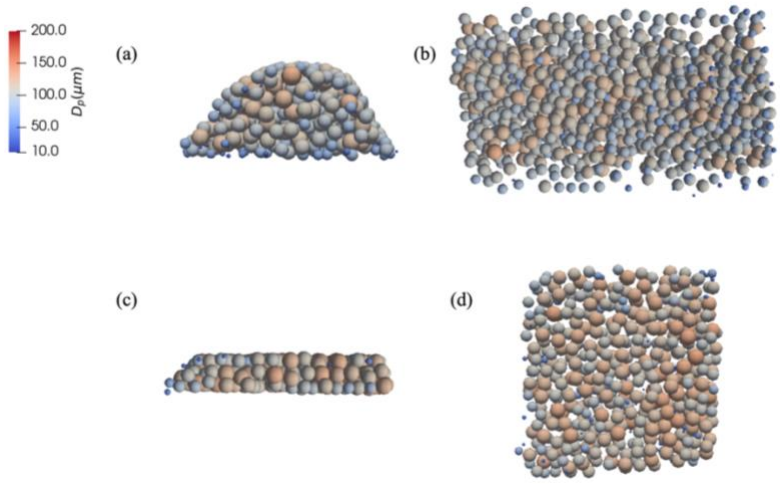

Figure 3.18 Detected particle locations and sizes (*i.e.*, equivalent sphere diameter D_p) plotted using the open-source visualization software ParaView. Front and top views of the manually (**a, b**) dispensed and (**c, d**) squeezed TIM samples.

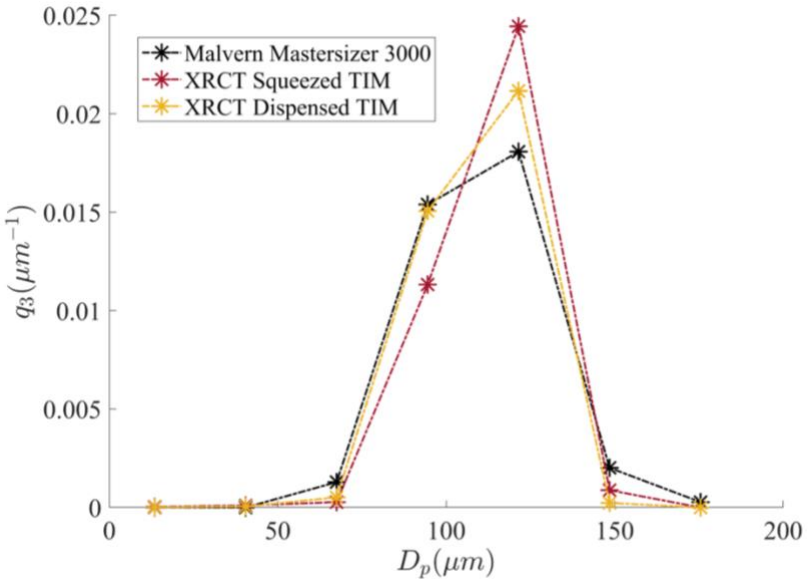

Figure 3.19 Particle size distribution (PSD) comparison between the XRCT-detected particle sizes of squeezed and dispensed TIMs, and that of laser diffraction measurement using Malvern Mastersizer 3000.

merging of particles to form one large particle (size overestimation). Also, statistical differences in detected particle sizes are expected. Note that the particle size measurement using Malvern Mastersizer was performed only once due to limited amount of particles. Ideally at least two measurements are needed to average out the results and check for repeatability of measurement. Table 3.6 compares the characteristic D10, D50, and D90 particle diameters from the 3D analysis of the dispensed and squeezed TIM XRCT images with the Mastersizer measured sizes.

Table 3.6 Comparison of the volume distribution-based D-sizes of the equivalent sphere diameter between laser-diffraction measured and XRCT-detected particle sizes. The TIMs were manually dispensed and squeezed, and the particles (dry state) were measured using Malvern Mastersizer 3000.

D-size	**Malvern Mastersizer 3000 (µm)**	**XRCT Dispensed TIM (µm)**	**XRCT Squeezed TIM (µm)**
D10	91.8	95.5	99.1
D50	114	110.5	115.2
D90	140	125.5	129.5

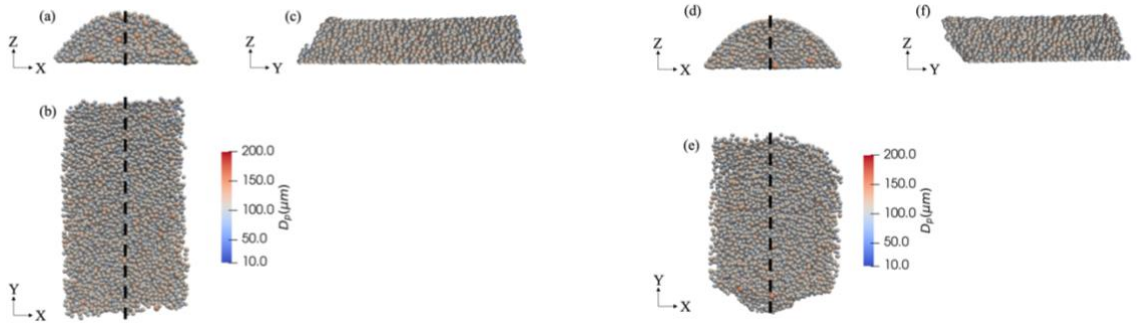

Figure 3.20 Visualization of line pattern dispensed TIM microstructure of the (**a-c**) center (*Sample 1*) and (**d-f**) off-center (*Sample 2*) samples. In both cases, the heap shape of the dispense pattern is distinctly visible (**a, d**). These TIMs are dispensed on bare glass microscope slide using automated procedures.

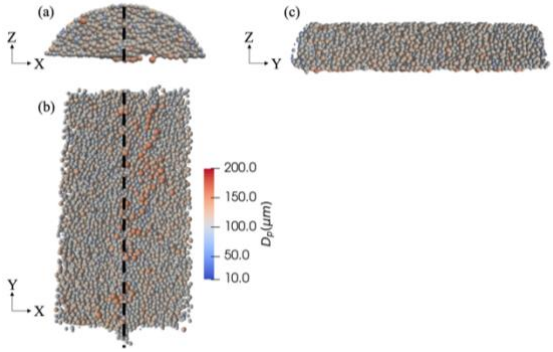

Figure 3.21 Visualization of line pattern dispensed TIM microstructure of a central sample (*Sample 3*). (**a**) Front, (**b**) top and (**c**) side views. This TIM is dispensed on glass microscope slide covered with copper foil using the automated procedures.

Analysis of the Automated Tests: Line Dispense Pattern TIM

Figure 3.20 shows a center (*Sample 1*) and an off-center (*Sample 2*) sample of the automated dispensed TIM that are deposited on bare glass slide. Figure 3.21 shows a center sample (*Sample 3*) of the TIM dispensed on glass slide covered with copper foil. The maximum particle diameter analyzed from the sample in Figure 3.20 is $D_{p,max} \approx 143$ µm. However, unusually large particles ($D_p > 150$ µm) were observed near the base of the heap shape (*i.e.*, the bottom portion) in Figure 3.21. This is an artifact of the presence of copper foil remaining in place during imaging of this sample (see Figure 3.14), which then manifests as unusually large particles in the 3D image processing. Such large particles ($D_p > 150$ µm) that were present near the bottom of the heap shape of the dispensed TIM were manually deleted before analyzing microstructure properties.

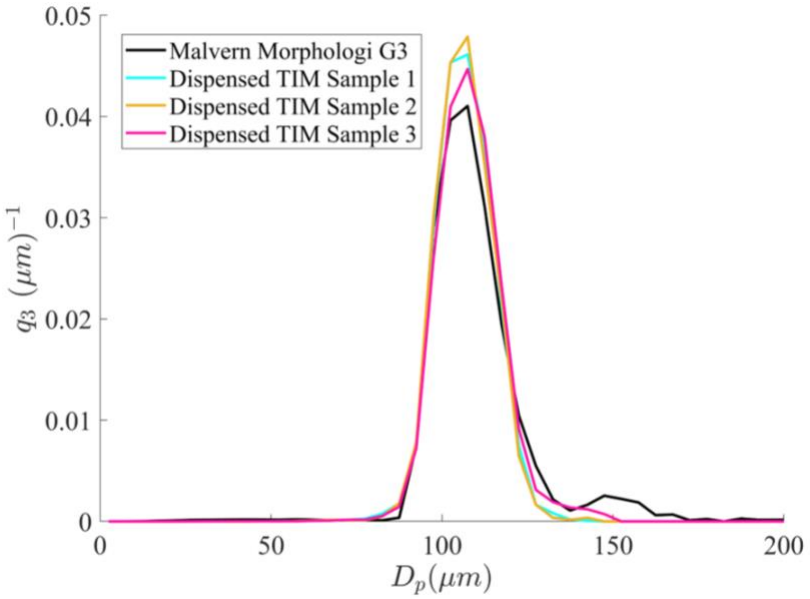

Figure 3.22 Volume distribution of particle size, q_3, analyzed from the processed 3D images of dispensed TIM samples. There is a good agreement between measured size distribution from Malvern Morphologi G3-ID instrument and from the 3D XRCT image analysis. The XRCT scans are obtained at a voxel resolution of $(3.5\ \mu m)^3$. The plot also suggests that the particle sizes do not significantly vary between the different samples. Note that area under each curve is ≈ 1.

Figure 3.22 compares the PSD of the three dispensed TIM samples analyzed from XRCT images with the high resolution optical image-based measurement from Malvern Morphologi G3-ID. The plot shows that these samples are statistically equivalent. Table 3.7 presents values of the D10, D50 and D90 particle sizes of the three samples and the optical-image based measurement.

Table 3.7 Comparison of the volume distribution-based D-sizes of the equivalent sphere diameter between high resolution optical image-based measurements and XRCT-detected particle sizes of dispensed TIM samples produced via automated procedures.

D-size	**Malvern Morphologi G3-ID (µm)**	**Dispensed TIM**		
		Sample 1* (center)	**Sample 2* (off-center)**	**Sample 3⁺ (center)**
D10	97.1	97.2	97.3	97.6
D50	107.7	106.5	106.5	107.6
D90	124.6	117.4	116.9	119.2

*Dispensed on a bare glass microscope slide
⁺Dispensed on a glass slide covered with copper foil

Analysis of Automated Tests: Squeezed TIMs Set 1

Figure 3.23 and Figure 3.24 show top view of TIM microstructure post image analysis for *Set 1* Center-Edge and Central samples, respectively. These samples were prepared via automated procedures. Qualitatively, different local concentration characteristics are discernible and are discussed later.

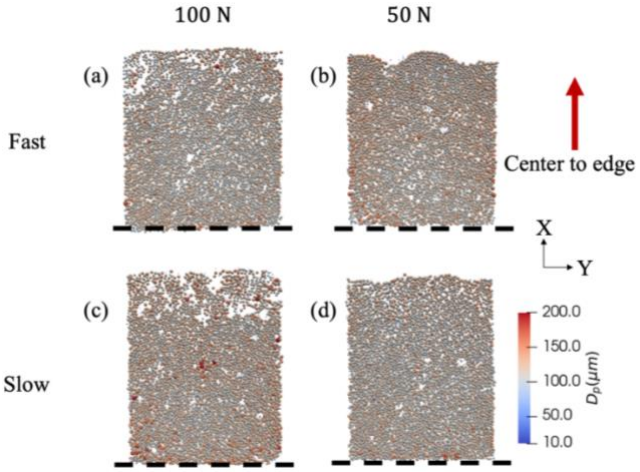

Figure 3.23 Detected particle locations and sizes (*i.e.*, equivalent sphere diameter D_p) plotted using ParaView. Top view of the *Set 1* Center-Edge samples produced via the automated dispense and squeeze procedures. The centerline of the line dispense pattern is denoted by the black dashed line.

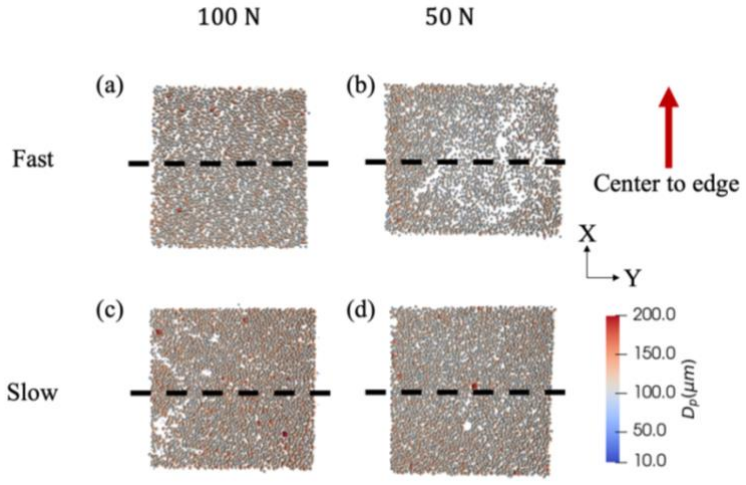

Figure 3.24 Detected particle locations and sizes (*i.e.*, equivalent sphere diameter D_p) plotted using ParaView. Top view of the *Set 1* Central samples produced via the automated dispense and squeeze procedures. The centerline of the line dispense pattern is denoted by the black dashed line.

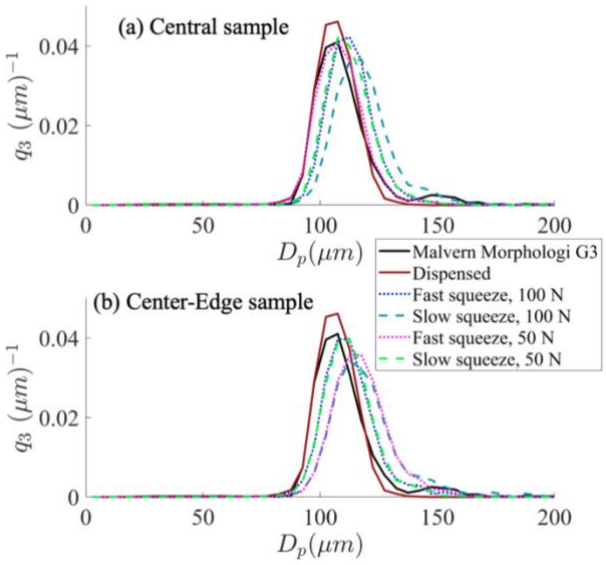

Figure 3.25 Volume distribution of particle size, q_3, analyzed from the processed 3D images of the two types of squeezed TIM samples from *Set 1* test: (a) Central and (b) Center-Edge samples. There is an acceptable level of agreement between the size distributions measured using the Malvern Morphologi G3-ID instrument and detected by processing the 3D XRCT images. The XRCT scans are obtained at a voxel resolution of $(3.5\ \mu m)^3$. Note that area under each is ≈ 1.

Figure 3.25 compares the PSD from image analysis of *Set 1* of TIM samples prepared using automated procedures with that of a single measurement using the Malvern Morphologi G3 equipment. Comparing the volume equivalent sphere diameter to the optical imaging results is not strictly correct because the particles are not perfectly spherical (see Figure 3.10 (b)). Nevertheless, this measurement provides a reference for validating the image processing. The PSD for one dispensed TIM sample (corresponding to Figure 3.20 (a-c)) is shown in the figure. The PSD of the dispensed TIM gives a close agreement against the optical measurement. The agreement between PSDs of the optical measurement and squeezed TIMs is acceptable, however, the shift of the peak towards right (larger diameter) is observed. This clearly indicates agglomeration of particles induced by insufficient resolution at the interparticle regions, despite implementing the distance transform watershed segmentation with dynamic parameter, $d_w = 1$. At higher resolutions, watershed segmentation should work more efficiently and object detection will be more accurate. Table 3.8 compares the measured particle D-sizes with that from the image analysis of CE and C samples from *Set 1* squeeze tests.

Table 3.8 Comparison of the volume distribution-based D-sizes of the equivalent sphere diameter between high resolution optical image-based measurements and XRCT-detected particle sizes of squeezed TIM samples from *Set 1* produced via automated procedures. Note C refers to the Central and CE to the Center-Edge samples.

D-size	**Malvern Morphologi G3-ID (µm)**	**Fast Squeeze**				**Slow Squeeze**			
		$F_S = 100$ N		$F_S = 50$ N		$F_S = 100$ N		$F_S = 50$ N	
		C (µm)	**CE (µm)**	**C (µm)**	**CE (µm)**	**C (µm)**	**CE (µm)**	**C (µm)**	**CE (µm)**
D10	97.1	101.9	100.2	96.9	103.8	104.5	103.9	100.7	100.2
D50	107.7	112.2	111.4	107.9	116.6	116.8	117.2	111.5	111.6
D90	124.6	125.1	125.9	121	133	133.4	138	125.1	125.6

Figure 3.26 shows measured BLT and squeeze pressure. BLT is measured using a micrometer. Three measurements per sample are averaged and the error bars in Figure 3.26(a) show one standard deviation. At fast squeeze rates, the BLT appears to be largely independent of the load, whereas at slower rate, the BLT decreases with increasing load, in the range of $50 - 100$ N squeeze force. The pressure is the ratio of average force recorded by the Instron to the TIM area computed using FIJI by manually constructing a polygonal region around the TIM. The squeeze rig was designed to enable axisymmetric squeezing – this must result in equivalent applied

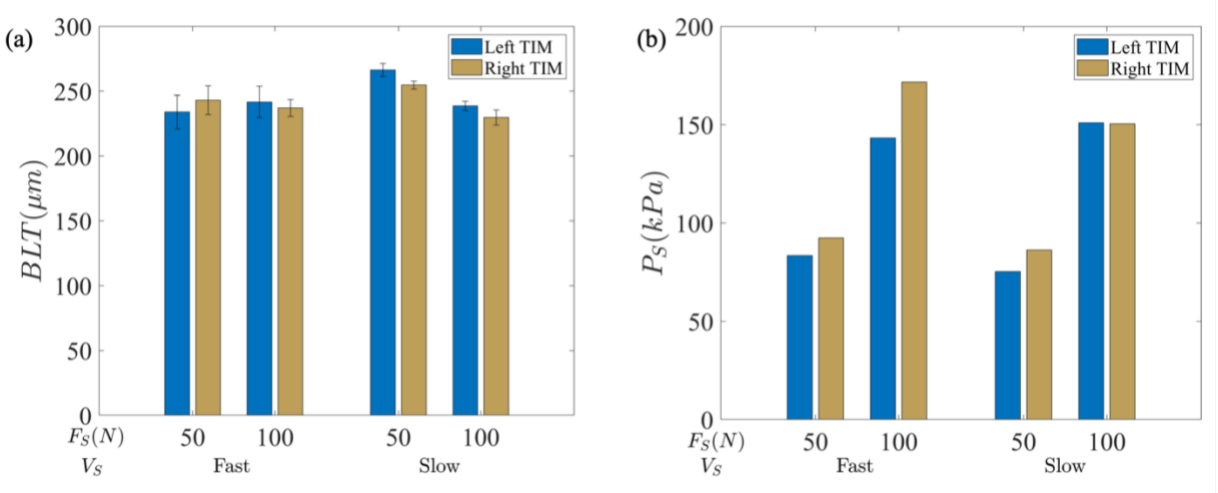

Figure 3.26 Measured (a) BLT and (b) squeeze pressure, P_S, for the TIM samples from Set 1 test. F_S is the set force and V_S the squeeze rate. To compute pressure, the average force during the load-holding phase is estimated. Fast = 10 mm s^{-1} and Slow = 10^{-3} mm s^{-1}

pressures on the left/right TIM samples produced in a single test. However, as seen from Figure 3.26 (b), the samples from fast squeeze case and $F_S = 100$ N were squeezed to different pressures, whereas for other test cases, the pressures are nearly equal.

Analysis of Automated Tests: Squeezed TIMs Set 2

The four squeeze tests are repeated to produce eight additional TIM specimens. The difference between set 1 and set 2 is the positioning of the curing lamp that results in more complete curing of set 2. The 3D reconstructed images of the Center-Edge and Central samples are analyzed for particle sizes and locations. Figure 3.27 and Figure 3.28 show top view of TIM microstructure post image analysis for *Set 2* Center-Edge and Central samples, respectively. These samples were prepared via automated procedures. The curved nature of the TIM samples is evident at the outer edge in Figure 3.27. Qualitatively, different local concentration characteristics are discernible, and it is analyzed and discussed in a subsequent section.

Figure 3.29 compares the PSD from image analysis of *Set 2* of TIM samples prepared using automated procedures with that of a single measurement using the Malvern Morphologi G3 equipment. The data for this measurement and that of the dispensed TIM data are the same from

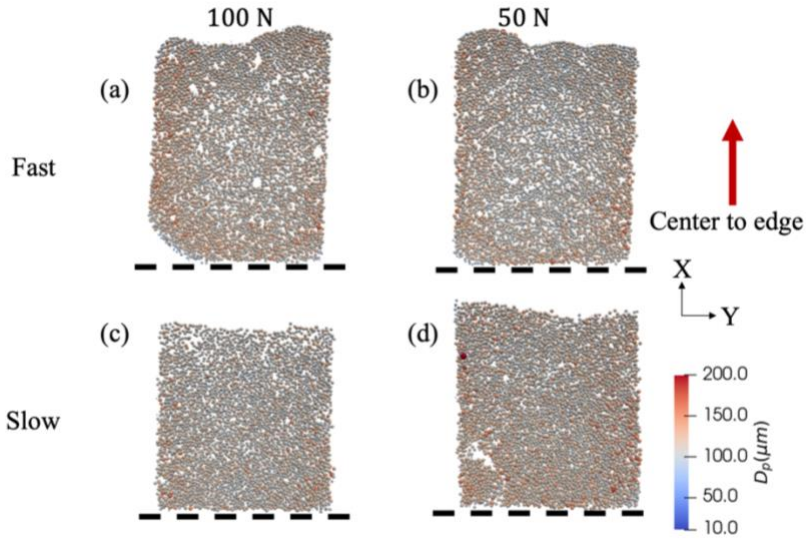

Figure 3.27 Detected particle locations and sizes (*i.e.*, equivalent sphere diameter D_p) plotted using ParaView. Top view of the *Set 2* Center-Edge samples produced via the automated dispensing and squeezing procedures.

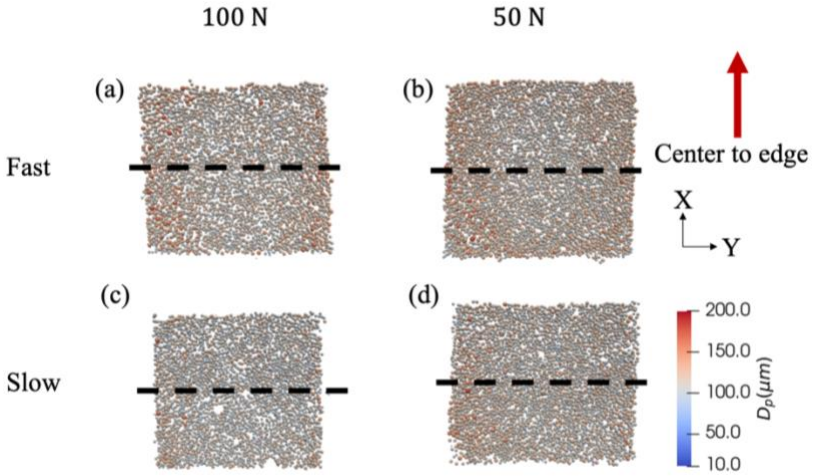

Figure 3.28 Detected particle locations and sizes (*i.e.*, equivalent sphere diameter D_p) plotted using ParaView. Top view of the *Set 2* Central samples produced via the automated dispensing and squeezing procedures.

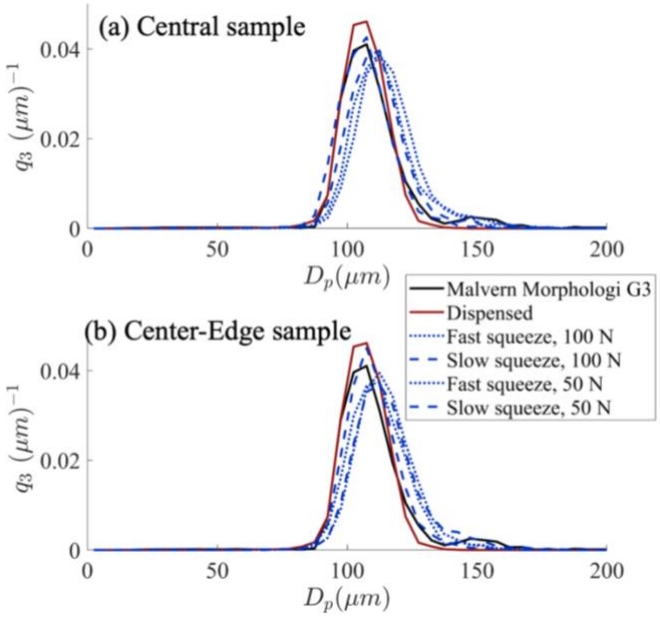

Figure 3.29 Volume distribution of particle size, q_3, analyzed from processing 3D images of the two types of squeezed TIM samples from *Set 2* test: (**a**) Central and (**b**) Center-Edge samples. There is an acceptable level of agreement between the size distributions measured using the Malvern Morphologi G3-ID instrument and detected by processing the 3D XRCT images. The XRCT scans are obtained at a voxel resolution of $(3.5\ \mu m)^3$. Note that area under each is ≈ 1.

Figure 3.25. Table 3.9 compares the D-sizes of the TIM samples with that of the measurement using Malvern Morphologi G3.

Table 3.9 Comparison of the volume distribution-based D-sizes of the equivalent sphere diameter between high resolution optical image-based measurements and XRCT-detected particle sizes of squeezed TIM samples from *Set 2* produced via automated procedures. Note C refers to the Central and CE to the Center-Edge samples.

D-size	**Malvern Morphologi G3-ID (µm)**	**Fast Squeeze**				**Slow Squeeze**			
		$F_S = 100$ N		$F_S = 50$ N		$F_S = 100$ N		$F_S = 50$ N	
		C (µm)	**CE (µm)**	**C (µm)**	**CE (µm)**	**C (µm)**	**CE (µm)**	**C (µm)**	**CE (µm)**
D10	97.1	100.8	102	102.2	99.2	95.3	98.4	98.8	101.4
D50	107.7	112.6	113.6	114.2	111.4	106.5	108.7	110.7	113.5
D90	124.6	130.7	128.3	129.9	126.1	119.9	122.2	124.6	131.8

Figure 3.30 shows measured BLT and squeeze pressure for *Set 2* samples. BLT is measured using a micrometer. Three measurements per sample are averaged and the error bars in Figure 3.30 (a) show one standard deviation. BLT seems to be largely load independent for the two squeeze rates. However, from *Set 1* tests, BLT showed a dependence on the load at slower squeeze rates. Pressure for left/right samples are nearly equal in all cases, except at slower squeeze rate and $F_S = 100$ N. These sample-to-sample variations suggest process-induced uncertainty, which is discussed in a subsequent section.

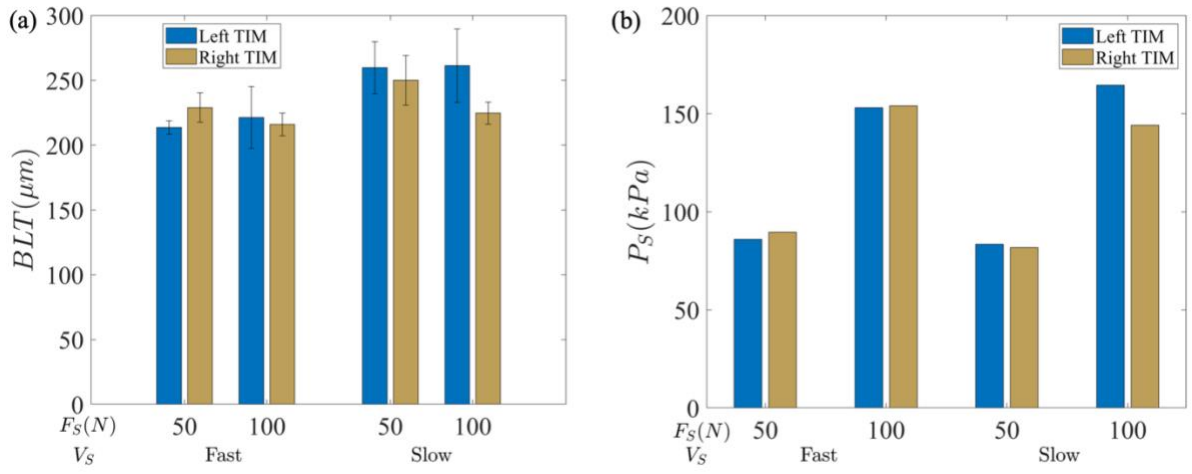

Figure 3.30 Measured (**a**) BLT and (**b**) squeeze pressure, P_S, for the TIM samples from *Set 2* tests. F_S is the set force and V_S the squeeze rate. To compute pressure, the average force during the load-holding phase is estimated. Fast = 10 mm s^{-1} and Slow = 10^{-3} mm s^{-1}.

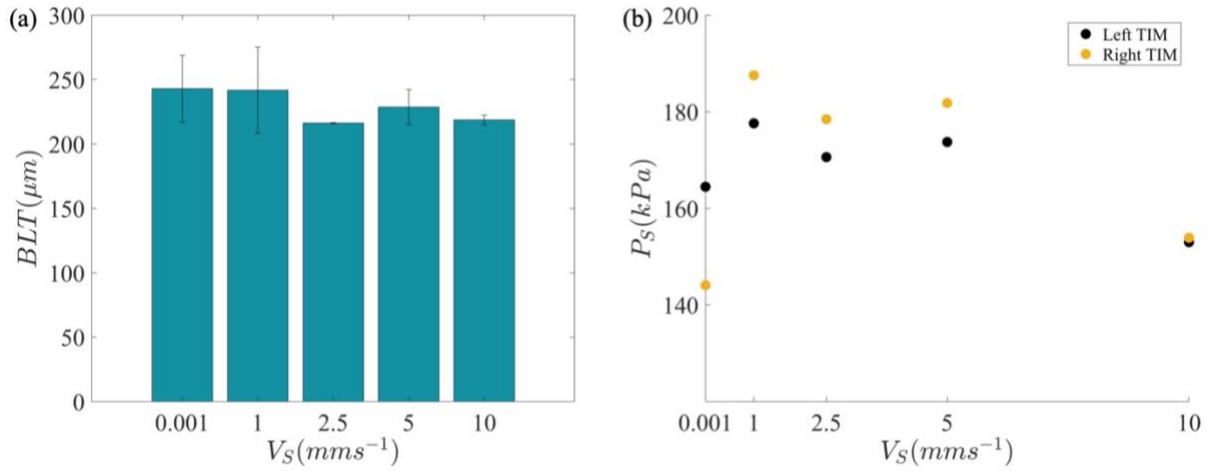

Figure 3.31 Measured (**a**) BLT and (**b**) squeeze pressure as a function of squeeze rate V_S for a fixed load of 100 N. The error bars are one standard deviation based on measurement of two TIM samples per test. The BLT values are almost constant in the range of $V_S = 10^{-3} - 10$ mm s^{-1}.

Variation of BLT with Squeeze Rate

Additional squeeze tests at $V_S = \{1, 2.5, 5\}$ mm s^{-1}, $F_S = 100$ N are conducted to measure the influence of squeeze rate on the BLT. Figure 3.31 (a) shows that the BLT does not vary significantly with squeeze rate at $F_S = 100$ N. The BLT shown is the average of left and right sample thickness (each measured at three locations on the TIM) from the tests. The error bars are one standard deviation based on the two values measured per test. Figure 3.31 (b) shows that the squeeze pressure first increases with squeeze rate, but then decreases between $V_S = 5$ mm s^{-1} and $V_S = 10$ mm s^{-1}.

3.6 Squeeze Process-induced Variation

Sample-to-sample variations, for the same squeeze process parameters, are suspected based on variability in the squeezing induced by manual assembly of the (a) copper foil on bottom glass slide, (b) 3M Scotch packaging tape on top glass slide, and (c) squeeze rig in the Instron machine. Moreover, the void regions in the central sample from Figure 3.24 (b) at $V_S = 10$ mm s^{-1}, $F_S = 50$ N, is unexpected and not seen under other test conditions. Therefore, tests are repeated at $V_S = 10$ mm s^{-1}, $F_S = 50$ N and $V_S = 1$ µm s^{-1}, $F_S = 100$ N (arbitrarily chosen), and Figure 3.32 shows the plot of detected particle sizes and locations of the Center-Edge and Central TIM samples

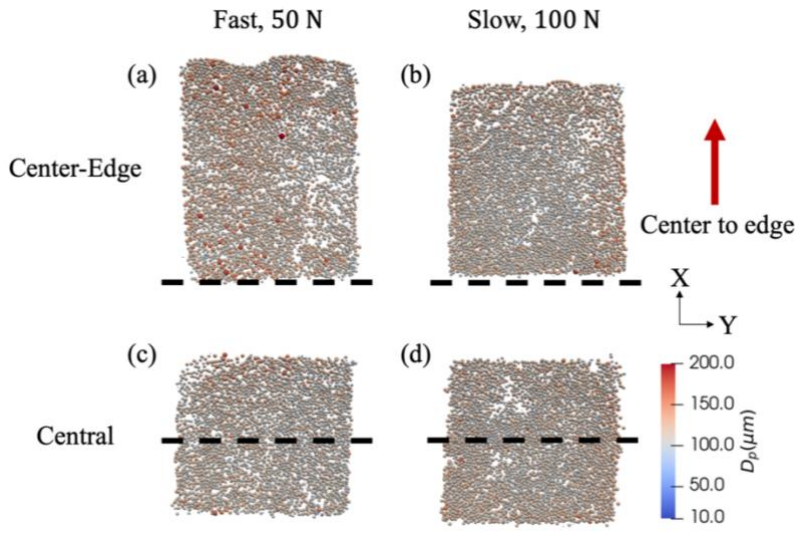

Figure 3.32 Detected particle locations and sizes (*i.e.*, equivalent sphere diameter D_p) plotted using ParaView. These samples are produced by repeating two tests (parameters noted in the figure) based on results from *Set 1*. Top view of the (**a**) Center-Edge and (**b**) Central samples produced via the automated dispense and squeeze procedures. The axis of the line dispense pattern is denoted by the black dashed line.

from these data. The Central sample from Figure 3.32 (c) does not exhibit void regions under the same test conditions. This suggests sample-to-sample variation in the TIM microstructure at the same squeeze rate and load.

Figure 3.33 compares PSD analyzed from XRCT-detected particles with the high resolution optical microscopy-based measurement using the Malvern Morphologi G3. The agreement is good in most cases and acceptable in the case of fast squeeze, 50 N load (panel (b), dotted markers). That potentially arises from noise in the XRCT scan that renders the watershed segmentation inefficient at the voxel resolution of $(3.5\ \mu m)^3$, thus resulting in agglomeration of particles (see Figure 3.32 (a)).

Multiple Squeeze Tests at Fixed Conditions

Four squeeze tests are conducted at $V_S = 10\ \text{mm s}^{-1}$ and $F_S = 100\ \text{N}$ using the set-up described in section 3.4.2 to produce eight samples in total (two per test). TIM images are captured using a digital camera and the sample-to-sample variation is evaluated using metrics such as (a) area of TIM and (b) gray-scale image intensity profile at various locations. Imaging is performed

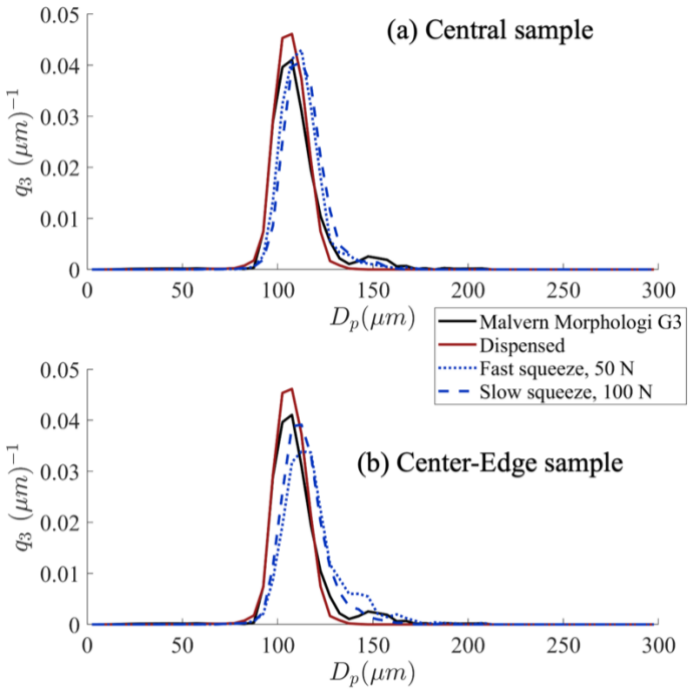

Figure 3.33 Volume distribution of particle size, q_3, analyzed from processing 3D images of the two types of squeezed TIM samples – (**a**) Central and (**b**) Center-Edge. These samples are produced from repeat tests at two different test conditions based on results from *Set 1*. The XRCT scans are obtained at a voxel resolution of $(3.5\ \mu m)^3$. Note that area under each curve is ≈ 1.

immediately after squeezing and curing, and prior to sample removal from the squeeze rig. Image analysis is discussed only for the last three tests as the image length scale for the first test was different. The squeeze pressure for all these cases is 171.1 ± 3.9 kPa and the variation in spreading distance or width of the TIM (measured approximately near the center) is 7.1%. Overall, the BLT is 234.8 ± 30.8 µm (Figure 3.34). The BLT is measured is performed at three different locations per sample and the micrometer head was wiped clean using alcohol after measuring every sample. Differences in BLT between the left and right TIMs are significant only for samples from the first test. In all other cases, the BLT variation between samples from the same test is within one standard deviation.

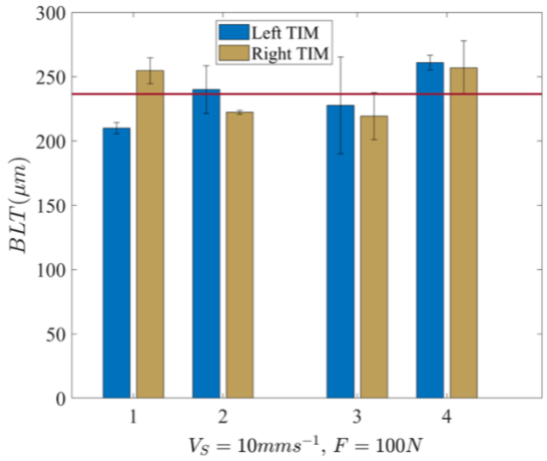

Figure 3.34 Measured TIM bond line thickness, BLT (μm), for samples produced from four tests, labeled "1" through "4", at the same squeeze condition of $V_S = 10$ mm s^{-1} and $F_S = 100$ N. The red horizontal line (236.5 µm ≈ 2.2 $D_{m,ce}$) is the average from all measurements. The error bars are one standard deviation based on three measurements per sample. Left and Right TIMs denote the two samples produced in a single test.

Figure 3.35 shows optical images of the left and right TIMs. Qualitatively, lower particle concentration regions are seen near the edge of the two left TIM samples (Figure 3.35 (d, e)), whereas for panel (f) the particle spatial distribution appears uniform at this length scale. In other

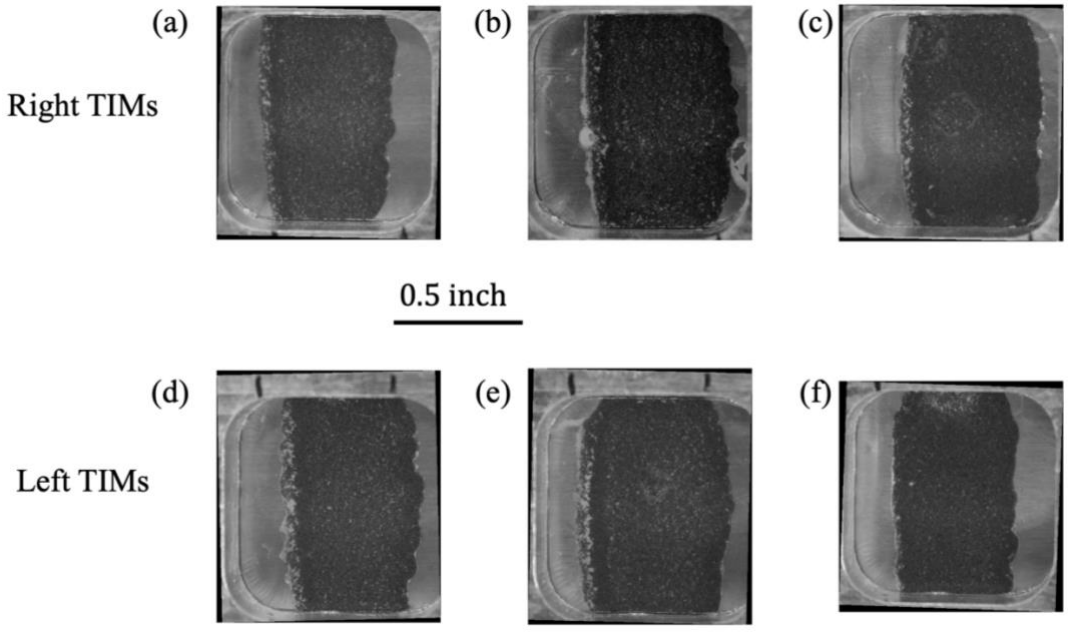

Figure 3.35 Optical images of the (**a**) right and (**b**) left TIM samples from three tests under the same squeezing conditions. Lower particle concentration regions are observed near the edges for some cases. Its occurrence is not uniform, despite test conditions being held constant.

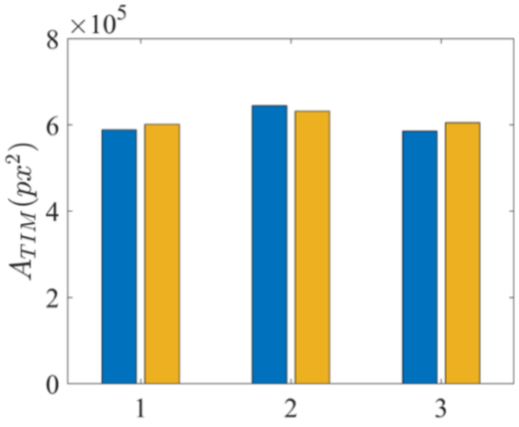

Figure 3.36 Comparison of TIM area, A_{TIM} measured in pixel units, for the samples from the last three tests.

panels, the particle concentration non-uniformity appears to be present only near one edge. For the right TIM samples, there is a ring-type void region visible near the center of panel (c).

The TIM area is compared for the samples from the three tests in Figure 3.36. This is the area of a polygonal region (constructed manually) binding the TIM. The bar plot shows that the areas are comparable. Gray-scale image intensity profile along three horizontal lines (Figure 3.37 (a)) are

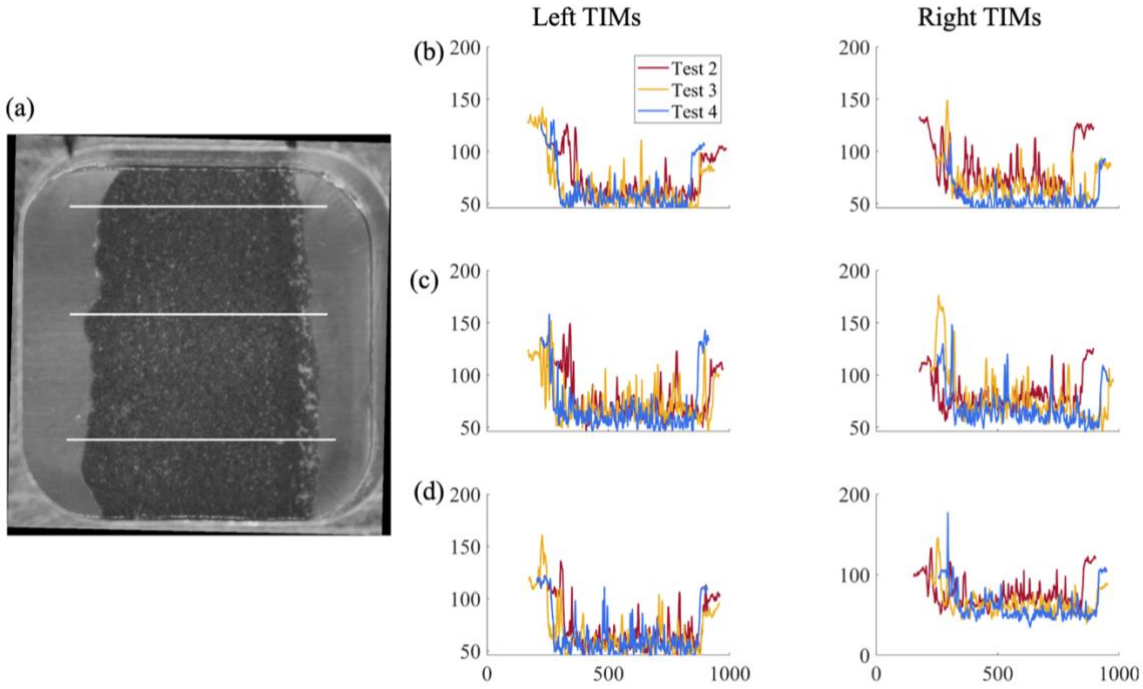

Figure 3.37 (**a**) Gray-scale image of a TIM sample showing three horizontal lines along which the image intensity is compared for samples from the three tests. Line intensity profile at three locations near the (**b**) top, (**c**) center and (**d**) bottom.

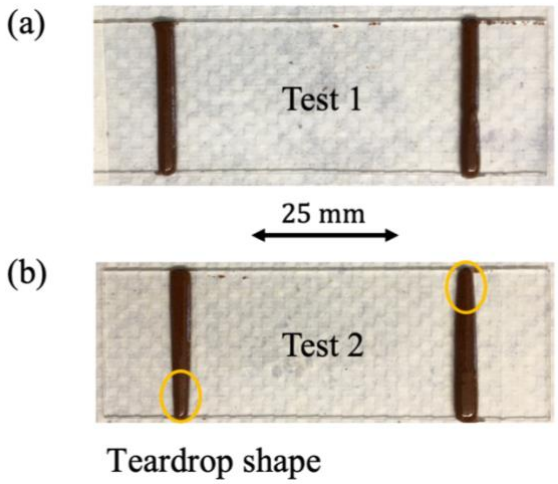

Figure 3.38 Isolated line patterns of TIM dispensed on bare glass microscope slide for investigating the squeeze process induced variation under fixed test conditions. In (**b**), the teardrop shape at the edges of the dispensed TIM is highlighted by yellow ovals. The spreading area of the TIM is lower there.

shown in Figure 3.37 (b-d). The intensity profiles do not exactly overlap for the same squeezing conditions, suggesting process-induced variations.

Analysis of Squeeze Tests with Bare Glass Microscope Slide Substrates

Finally, process-induced variation is discussed with a bare glass microscope slide as the substrate. It is suspected that the manual attachment of copper foil and tape on the bottom and top glass slides, respectively, perturb the squeeze flow of TIMs and lead to sample-to-sample variations noted in the previous sections. Two tests (*Test 1* and *Test 2*) are conducted at $V_S = 10$ mm s^{-1} and $F_S = 100$ N. The dispensed TIM images are shown in Figure 3.38. The intensity profile along three horizontal lines are shown in Figure 3.40. For the different samples, intensity profiles match well. There is, however, a noticeable difference in the intensity profile for the right TIMs near the edges (Figure 3.40 (b)). Note that in Figure 3.38 (b), the edges of the dispensed TIM exhibit a teardrop shape. The teardrop shape in the line dispense pattern lowers the redistribution area of the TIM during squeeze, as seen in Figure 3.39 (b), but only near the edges.

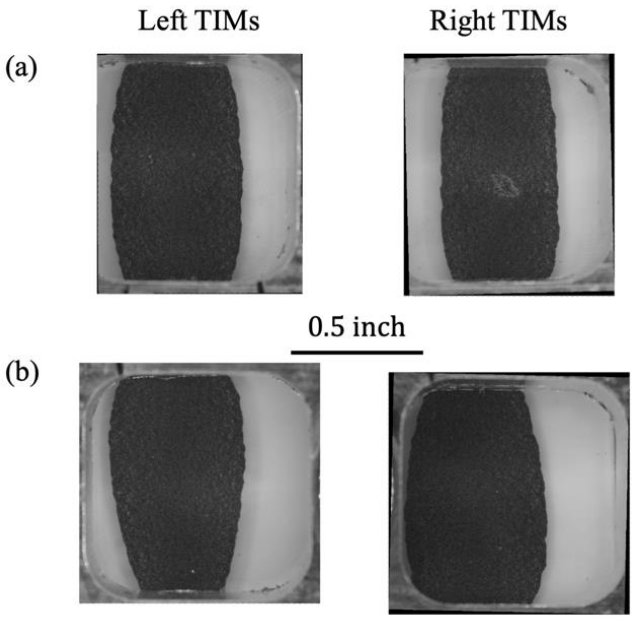

Figure 3.39 Optical images of the TIM squeezed on bare glass slide substrate (**a**) *Test 1* and (**b**) *Test 2*. In (b), the teardrop shape in the dispensed TIM has reduced the width near the edges.

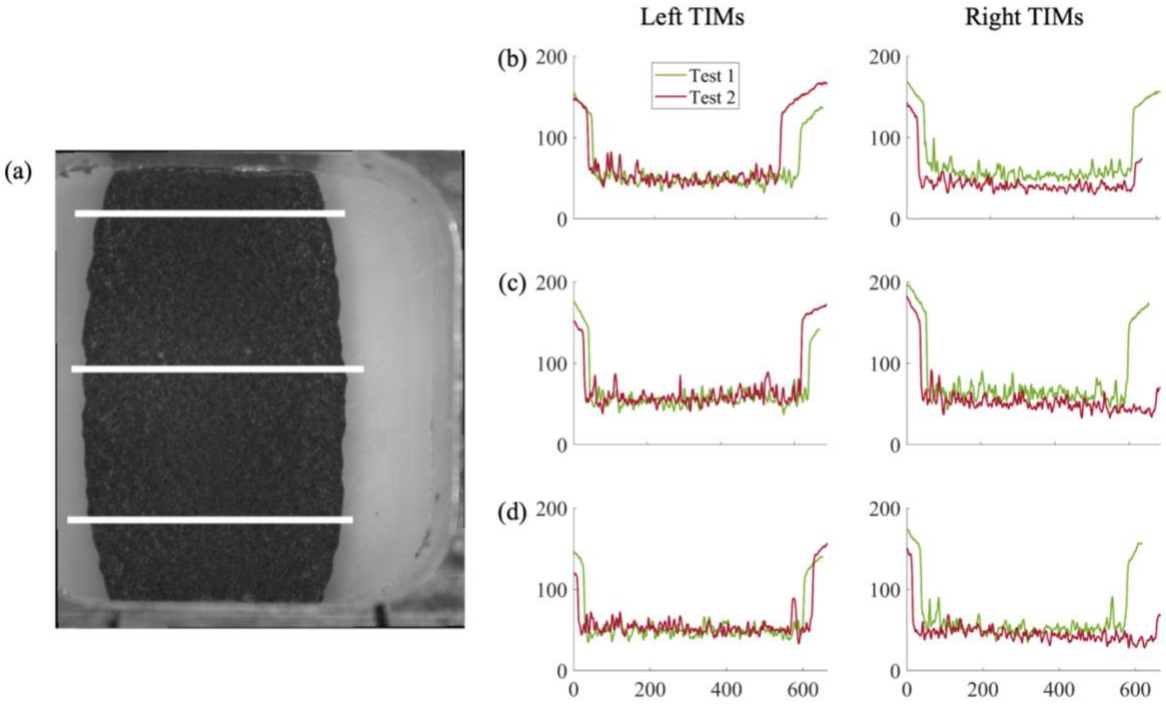

Figure 3.40 (**a**) Gray-scale image of a TIM sample showing three horizontal lines along which the image intensity is compared. (**b**) Intensity profile of the squeezed TIM at the edges and near the center, from the samples shown in Figure 3.39.

3.7 TIM Microstructure Analysis

In this section, microstructural analyses of dispensed and squeezed TIMs produced via the automated procedures are discussed to reveal the dependence of particle spatial distribution on the squeeze rate and load. Bulk particle volume fraction (ϕ_p), coordination number (C_N), radial distribution function (RDF, $g(r)$) and local particle concentration ($\phi_{p,local}$) are discussed.

3.7.1 Bulk Particle Volume Fraction and Coordination Number

The *bulk particle volume fraction*, ϕ_p, is computed as the ratio of total particle volume to that of a convex hull that binds the TIM microstructure:

$$\phi_p = \frac{\sum \mathcal{V}_{particles}}{\mathcal{V}_{convex\ hull}}, \tag{3.2}$$

where ϕ_p is particle volume fraction $\sum \mathcal{V}_{particles}$ is the sum of particle volume, and $\mathcal{V}_{convex\ hull}$ is the convex hull volume.

First, the particle locations and sizes that are analyzed from processing 3D XRCT images are imported into COMSOL Multiphysics by exploiting LiveLink™ for MATLAB® functionality to construct the TIM microstructure geometry. The Standard Triangle Language (STL) format of the geometry is then processed to obtain the facets such as vertices and faces [216]. Then, the convex hull is computed. This is the bounding box for the TIM microstructure.

Figure 3.41 shows the convex hull (light blue region) constructed around the dispensed and squeezed TIM samples. The top and side views show that this convex hull tightly binds the microstructure and is, therefore, ideal for the computation of the bulk particle volume fraction, ϕ_p.

The *coordination number* is computed as the mean number of geometrically intersecting pairs of particles and particle pairs that are in close proximity. The latter condition is necessary because the watershed segmentation potentially disconnects two physically touching particles. Moreover, idealization of spherical shape and equivalent sphere diameter based on object centroid and volume computations from ImageJ can render neighboring particles non-touching (or induce large overlaps if sphericity of participating particles are relatively low). In this work, an interparticle surface

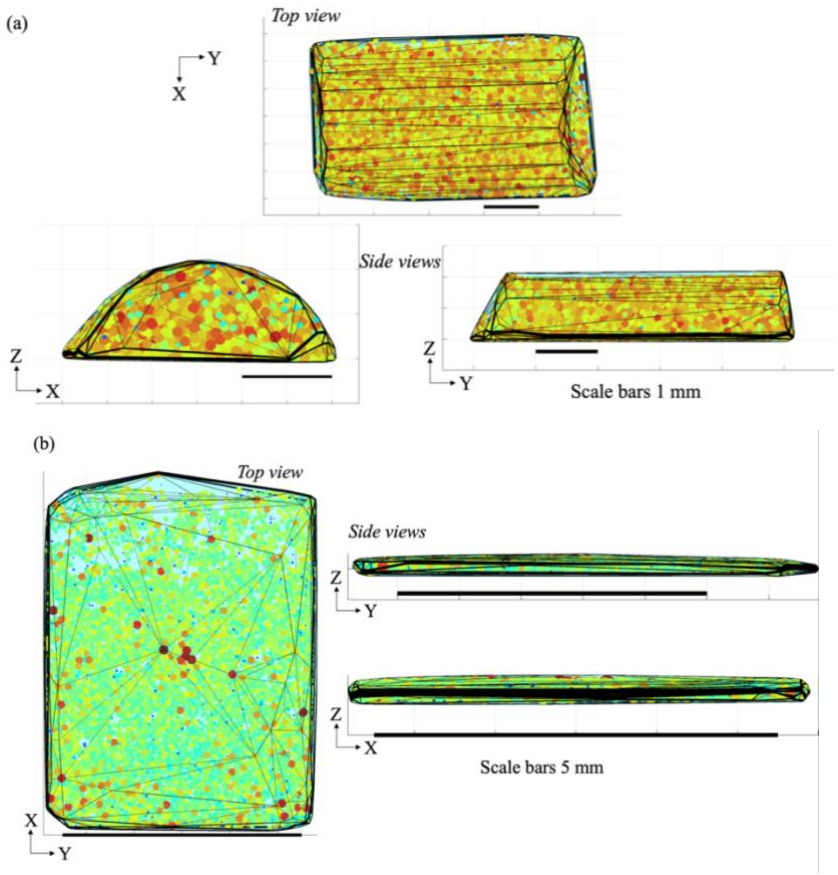

Figure 3.41 Examples of convex hull constructed over the representative microstructures of (**a**) dispensed and (**b**) squeezed TIM. This is the bounding box for computing the bulk particle volume fraction. Particles are colored based on size, but the color bar is omitted in this figure.

separation limit of 10% of the smallest particle radius is considered for computing the number of interacting or contacting pairs. From the perspective of heat conduction, the coordination number is correlated with the magnitude of heat conduction through the composite material. Isolated particles do not contribute to enhancing conduction and, therefore, their number proportion could be a metric for optimizing the TIM application parameters.

The squeezed TIM is made up of approximately three sheets of particle in the thickness direction. Ideally, to compute ϕ_p and C_N, a subset of the microstructure must be analyzed to account for wall/edge effects. Prior simulation works usually incorporate periodic boundary conditions to generate the microstructures, and the properties are computed on a representative volume element. But in this work the squeezed TIM microstructure obtained from 3D XRCT imaging is finite and the entire dataset is analyzed.

Table 3.10 Comparison of the basic microstructural features, ϕ_p and C_N, of the three dispensed TIM samples.

Microstructural Features	**Dispensed TIM**		
	Sample 1* (center)	**Sample 2* (off- center)**	**Sample 3⁺ (center)**
ϕ_p	35.7	36.5	35.8
C_N	~2	~2.1	~2

*Dispensed on bare glass microscope slide
⁺Dispensed on glass slide covered with copper foil

Table 3.10 below shows ϕ_p and C_N for the dispensed TIM samples and Figure 3.46 shows the RDF. During TIM preparation, the target filler loading was $\phi_{p,target} \approx 30\%$ based on mass measurements. However, as seen in Table 3.10 the dispensed TIM bulk volume fraction is $\phi_p > 30\%$. This increase likely resulted in the material preparation stage. Some amount of the epoxy stuck to the sides of the beaker in which the particles and epoxy were mixed. This could have slightly increases the particle volume fraction compared to the target. The three dispensed TIM samples (*Sample 1, 2* and *3*) are statistically equivalent based on particle size distribution (see Figure 3.22), bulk particle volume fraction, coordination number and RDF. Statistical equivalence of suggests that the dispensed the sample from the center of the dispense patter (*Sample 1*) and from off center (*Sample 2*) indicate that TIM microstructure is similar along the dispensed line. For comparative analysis with squeezed TIM microstructures, average properties of dispensed TIM *Sample 1* and *2* (Figure 3.20) are used.

Sample-to-Sample Variation

Statistical variations in the two TIMs produced in a single squeeze test are analyzed based on ϕ_p and C_N. This calibration analysis is essential to understand within-sample and sample-sample variations between TIMs produced in a single squeeze test. Three Center-Edge samples are used in this assessment – two from the first TIM sample (left/right halves), and another from the second TIM sample (left half). The former helps with within-sample analysis and the latter helps with sample-to-sample analysis. These samples are prepared at a squeeze rate of $V_S = 10$ mm s^{-1} and $F_S = 100$ N. XRCT imaging is expensive and time intensive; so, only one squeeze test is conducted here. This accounts for noise in the data that is potentially a consequence of the bottom

Table 3.11 Statistical variation in bulk microstructural properties, $\bar{\phi}_p$ and C_N, of the two Center-Edge squeezed TIM calibration samples. These samples were produced at $V_S = 10$ mm s^{-1} and $F_S = 100$ N. <> denotes mean of the bulk property values of the two samples.

TIM Center-Edge Samples	$\frac{\Delta \phi_p}{< \phi_p >}$ (%)	$\frac{\Delta C_N}{< C_N >}$ (%)
Within-sample	11.1%	12.8%
Sample-to-sample	9.6%	8.3%

and top surfaces not being parallel to each other during squeeze resulting from the (a) manual assembly of squeeze rig in the Instron machine holder and (b) surface micro bumps on the copper foil and the packaging tape used on bottom and top glass slides. The maximum sample-to-sample and within sample variation (with respect to the mean) in the volume fraction of the calibration samples was 9.6% and 11.1%, respectively, for sample pairs. The maximum variation in coordination number for these sample pairs was 8.3% and 12.8%, respectively (see Table 3.11). This suggests that, in the subsequent analyses, only those property variations greater than this can be considered significant. This calibration analysis also revealed that imaging the same sample twice led to a difference of ≈ 0.3% in the computed average particle volume fraction, and negligible difference in the coordination number (when rounded up to 1 decimal point).

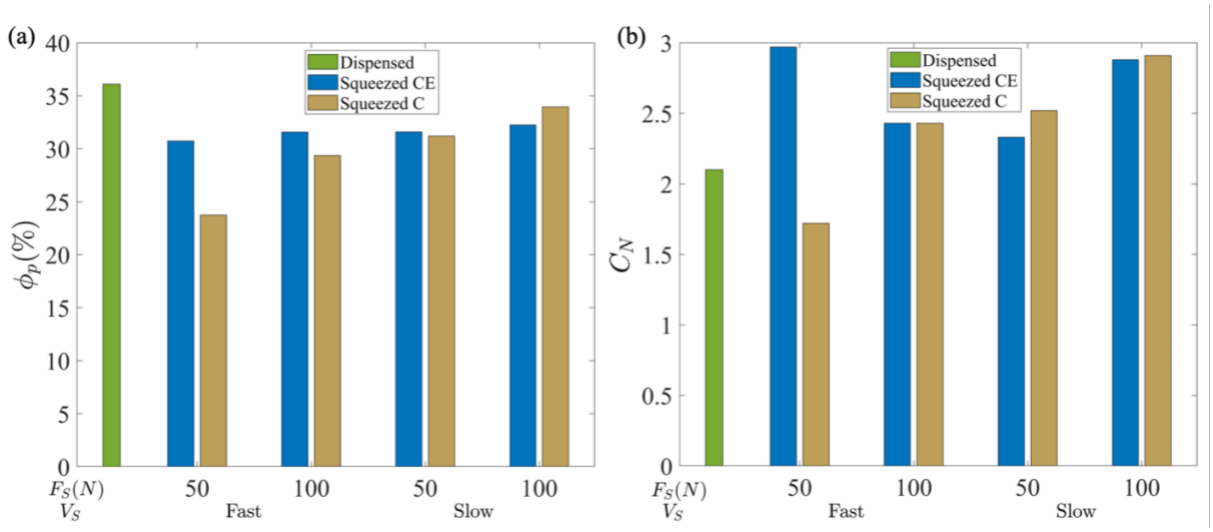

Figure 3.42 (**a**) Bulk volume fraction, ϕ_p, and (**b**) coordination number, C_N, for *Set 1* squeezed TIM samples compared with the average properties of dispensed TIM based on *Sample 1* and *Sample 2* (see Table 3.10). Squeezing lowers ϕ_p and slightly increases C_N. Center-Edge and Central samples are denoted by CE and C, respectively. Fast = 10 mm s^{-1} and Slow = 10^{-3} mm s^{-1}.

Analysis of Automated Tests: Squeezed TIMs Set 1

Figure 3.42 shows the variation of ϕ_p and C_N for the *Set 1* squeezed TIM samples. Center-Edge and Central samples are abbreviated as CE and C, respectively. The dispensed TIM data is averaged based on the two samples dispensed on bare glass slides (see Table 3.10). Squeezing appears to lower the bulk particle volume fraction in the region of observation as the material spreads out. Ideally, the average particle volume fraction is expected to be the equal to that in the dispensed state although the local distribution may change. However, if voids or air bubbles are introduced during squeezing, volume expansion can occur and this can potentially lower the bulk particle volume fraction. The variation in ϕ_p is not significant with respect to squeeze rate and load explored for this mock TIM consisting of moderately low filler loading of large spherical filler particles.

One notable observation is the significantly lower ϕ_p and C_N of the central (C) sample from fast squeeze rate and 50 N load case. This is due to the presence of void regions observed in the microstructure (see Figure 3.24 (b)). The void regions are not observed when the test is repeated (Figure 3.32 (a)). Another test case of slow squeeze rate and 100 N load is repeated (Figure 3.32 (b)).

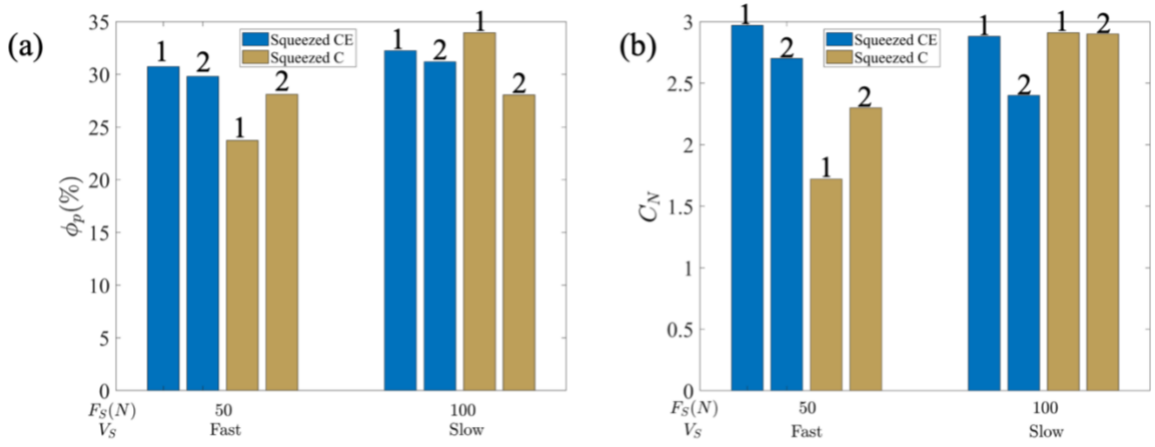

Figure 3.43 Sample-to-sample variation in (**a**) bulk volume fraction, ϕ_p, and (**b**) coordination number, C_N, for repeat tests of a subset of *Set 1* squeezed TIM samples. The numbers 1 (original test) and 2 (repeat test) on top of the bars denote the test type. Center-Edge and Central samples are denoted by CE and C, respectively. Fast = 10 mm s^{-1} and Slow = 10^{-3} mm s^{-1}.

For these squeezed TIMs, ϕ_p and C_N are computed for CE and C samples. Figure 3.43 compares these two cases and highlights the squeeze process-induced variation in TIM microstructure. First, the C sample from fast squeeze rate and 50 N load case has a higher ϕ_p and C_N. In the Center-Edge samples from fast and slow squeeze rate cases, ϕ_p does not appear to vary significantly. However, the variation in C_N is more significant. The Central sample from slow squeeze rate, 100 N case, has a more significant variation in ϕ_p than in C_N. Overall, the variation in the properties does not appear to be significant with respect to squeeze rate and load in *Set 1* tests.

Analysis of Automated Tests: Squeezed TIMs Set 2

The second squeezing test used a flexible/bendable UV lamp fixture to improve the curing of the samples. Figure 3.44 shows the variation of ϕ_p and C_N for the *Set 2* squeezed TIM samples. The variation in squeezed TIM ϕ_p appears to be more significant with respect to squeeze rate and load for *Set 2* samples than for *Set 1*. One notable observation is the higher ϕ_p of the CE samples in almost all cases compared to C samples. This suggests that the particles flow outward *i.e.*, away from the centerline of the dispensed TIM. At fast squeeze rate, ϕ_p of the CE sample increases with load whereas the opposite trend was seen at slow squeeze rate. The trends in C_N match that of ϕ_p.

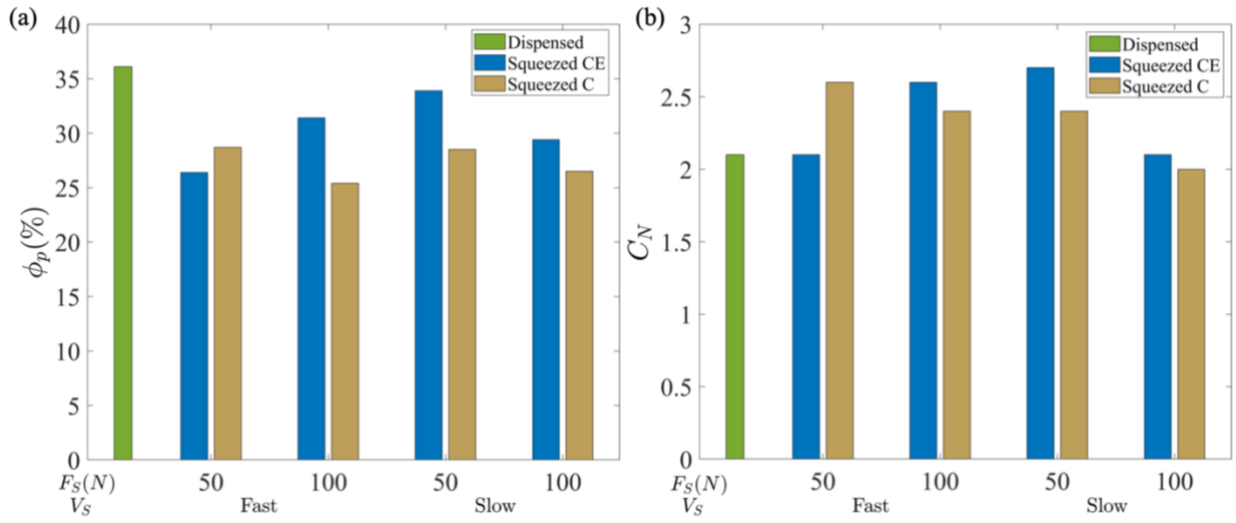

Figure 3.44 (**a**) Bulk volume fraction, ϕ_p, and (**b**) coordination number, C_N, for *Set 2* squeezed TIM samples compared with the average properties of dispensed TIM based on *Sample 1* and *Sample 2* (see Table 3.10). Squeezing lowers ϕ_p and slightly increases C_N. Center-Edge and Central samples are denoted by CE and C, respectively. Fast = 10 mm s^{-1} and Slow = 10^{-3} mm s^{-1}.

Overall, the variation in ϕ_p of the C samples across squeeze rates and loads was less significant when compared with that of the CE samples.

The trends in ϕ_p and C_N do not match between the two test sets *Set 1* and *Set 2*. This is likely due to the reasons mentioned in section 3.6. Note that the main difference in these two test sets is the positioning of the UV lamp that results in better curing of the TIM in the same duration of 1 hour, as confirmed visually by examining the backside of the TIM. Thus, the variation between the test sets is indicative of sample-to-sample process induced variations.

3.7.2 Radial Distribution Function

The computation of the RDF generally exploits periodic boundary conditions, which are commonly employed in particulate systems modeling. Clearly, the experiments do not involve such boundary conditions. The finite nature of such microstructures was considered in a recent work [199], and an analytical solution was presented to calculate the RDF of finite-sized particulate microstructures. The solution involves computing the volume of intersection between a spherical shell and the bounding box for the microstructure, especially for reference particles

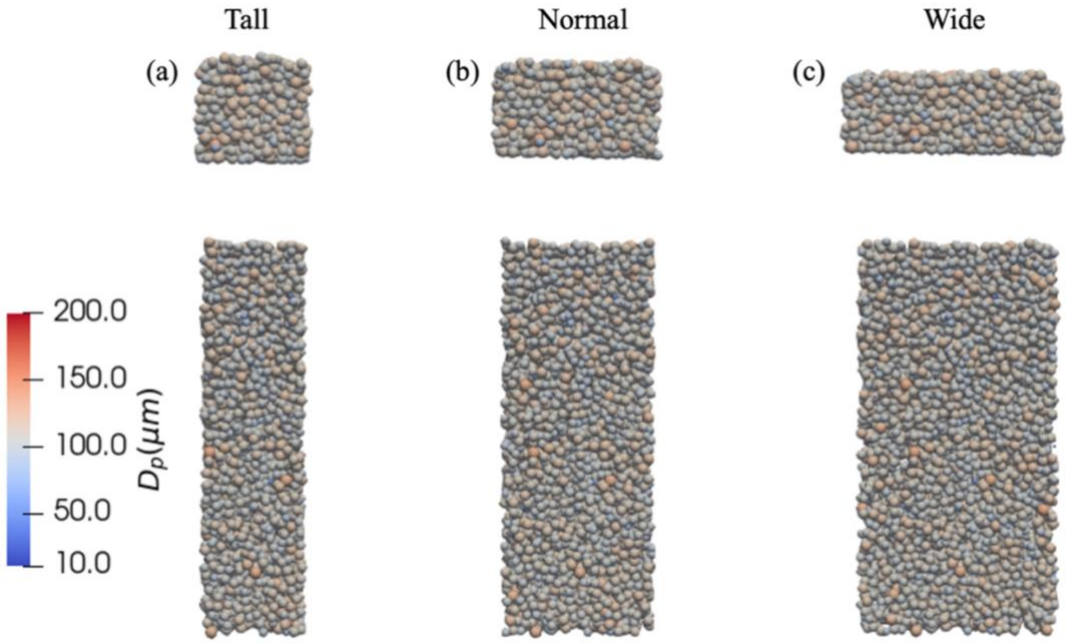

Figure 3.45 Front and top views of three different rectangular subdomain selections from the dispensed TIM microstructure. (**a**) "Tall" box, (**b**) "Normal" box, and (**c**) "Wide" box. These are named according to their appearance and aspect ratio. The number of particles in these regions are, respectively, $2656, 3572,$ and 4021.

near the box edges or larger search radius. Without this modification, the RDF artificially decays to zero. We use the open-source Python code from Kopera and Retsch [199] to compute the RDF of dispensed and squeezed TIM microstructures. A search radius of 5x the maximum particle diameter and 100 bins are used to plot the RDF. A large rectangular subdomain is selected manually from the squeezed TIM microstructures seen in Figure 3.23, Figure 3.24, Figure 3.27 and Figure 3.28 for computing the RDF. This is necessary especially for Center-Edge samples whose edges are curved/jagged. Large rectangular regions are selected so that ϕ_p and C_N are similar between the subdomains and whole microstructures. Similarly, a rectangular subdomain must be selected from the dispensed TIM microstructure. Multiple selections are possible for the heap-shape dispensed TIM and these selections are named according to their appearance and aspect ratio – "tall" and "wide". The average of these two results in a "normal" box shape *i.e.*, almost square cross-section. Figure 3.45 plots the TIM microstructure from these regions. The RDF code constructs a box around the given microstructure and the curved edges of the TIM will add additional void volume that potentially distorts the analysis.

The mean of bulk particle volume fraction for the three rectangular subdomains is $< \phi_p > \approx 35.6\%$ with a standard deviation of $\approx 0.5\%$. The mean coordination number for these subdomains

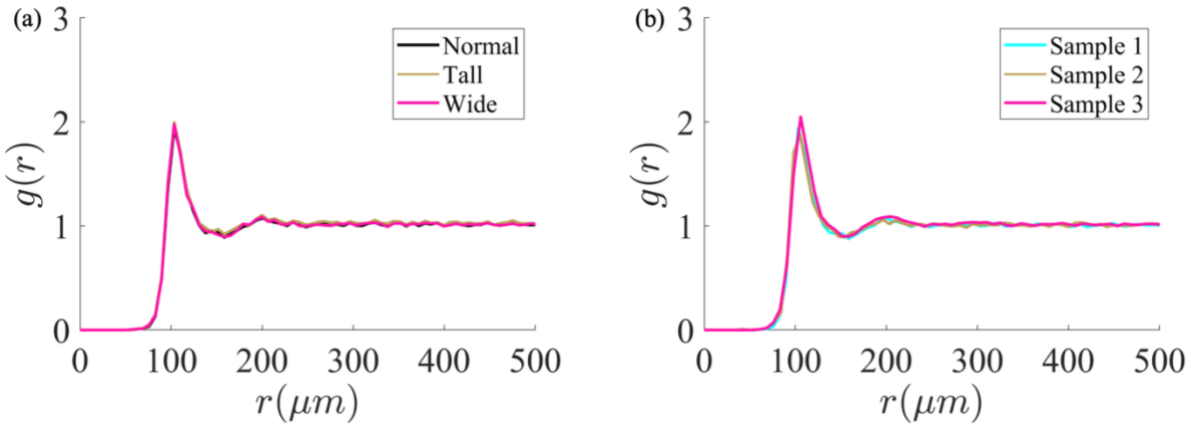

Figure 3.46 (**a**) RDF of dispensed TIM Sample 1 for three different rectangular subdomains, namely, "Normal", "Tall" and "Wide", selected manually from the whole microstructure. The agreement is great, suggesting that the computation is region-independent. The number of particles in these regions are, respectively, 3572, 2656 and 4021. (**b**) Dispensed TIM RDFs for the three samples described earlier (see Table 3.10). The RDFs agree well with each other, suggesting a statistically similar microstructure. The rectangular subdomains analyzed here consist of 3572, 2628 and 4714 number of particles.

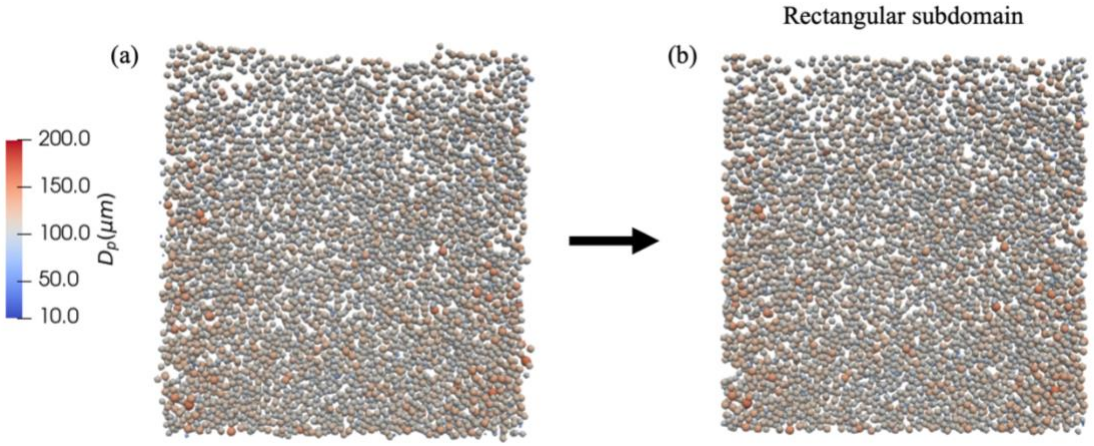

Figure 3.47 Top view of a large rectangular subdomain selected for RDF computation from a squeezed TIM Center-Edge microstructure.

is $< C_N > \approx 2.1$. The $< \phi_p >$ agrees well with the bulk particle volume fraction measured for the whole dispensed TIM microstructure $\phi_p = 35.7\%$ and $C_N = 2$ (see Table 3.10).

Figure 3.46 (a) shows the RDF of *Sample 1* dispensed TIM analyzed for the three rectangular regions from Figure 3.45. The RDFs agree well. Further, Figure 3.46 (b) shows that the RDF of the three dispensed TIM samples agree well, suggesting a statistically equivalent microstructure. In addition, it is inferred that, along the axis of the line pattern, the microstructure is statistically similar.

Figure 3.47 shows the rectangular subdomain for a Center-Edge squeezed TIM microstructure sample produced at $V_S = 1$ µm $s^{-1}, F_S = 100$ N from *Set 2*. Table 3.12 compares ϕ_p and C_N for the *Set 1* and *Set 2* samples computed using the whole microstructure and the rectangular subdomains. The property values agree well, thus justifying the computations using the subdomain microstructure.

Figure 3.48 shows the RDF of squeezed TIM samples from *Set 1* and *Set 2*. Overall, the RDFs of both dispensed and squeezed TIMs resemble disordered microstructures owing to the presence of just two peaks. The first peak occurs at a radial distance of $r \approx D_{m,ce} \approx 110$ µm particle diameter. The first peak of all the squeezed TIM samples is taller than that of the dispensed TIM, suggesting a better connectivity of the particles. This is explained by the higher coordination number of

Table 3.12 Comparison of bulk microstructural properties, ϕ_p and C_N, of the whole microstructures and rectangular subdomains used in the RDF computation and local particle volume fraction analysis. Center-Edge and Central squeezed TIM samples from *Set 1* and *Set 2* are denoted by CE and C, respectively.

	Squeeze Parameters			$\boldsymbol{\phi_p}$(%)		$\boldsymbol{C_N}$	
Test Set	**Velocity (mm s^{-1})**	**Force (N)**	**TIM Sample**	**Whole TIM**	**Subdomain**	**Whole TIM**	**Subdomain**
Set 1	10	50	C	23.7	23.9	1.7	1.7
			CE	30.7	31.8	3	3
	10	100	C	29.4	29.5	2.4	2.5
			CE	31.6	31.6	2.4	2.4
	10^{-3}	50	C	31.2	31.3	2.5	2.5
			CE	31.6	32.2	2.3	2.3
	10^{-3}	100	C	33.4	33.4	2.9	2.9
			CE	32.2	33.1	2.9	2.9
Set 2	10	50	C	28.7	29.1	2.6	2.6
			CE	29.4	30.6	2.1	2.2
	10	100	C	25.4	26.5	2.4	2.4
			CE	31.4	31.7	2.6	2.5
	10^{-3}	50	C	28.5	29.4	2.4	2.5
			CE	33.9	35	2.7	2.7
	10^{-3}	100	C	26.5	27.4	2	2
			CE	29.4	30.5	2.1	2.1

squeezed TIMs than that of the dispensed TIM observed for most of the samples seen in Figure 3.42 (b) and Figure 3.44 (b).

One potential anomaly can be seen in the computation RDF from Figure 3.48 (a). The sample from fast squeeze, 50 N load case had significant void regions, thus resulting in ϕ_p and C_N significantly lower than that of the dispensed TIM. However, the RDF for this sample (black dotted line in Figure 3.48 (a)) has a higher first peak that occurs approximately at the same radial distance as that for the dispensed TIM. The curvature in the TIM geometry adds void space within the rectangular bounding box, thus increasing the overall microstructure volume and likely causing an increase in the value of $g(r)$ – see the mathematical formulation in Kopera and Retsch [199]. Analyzing thicker TIM samples should eliminate this issue.

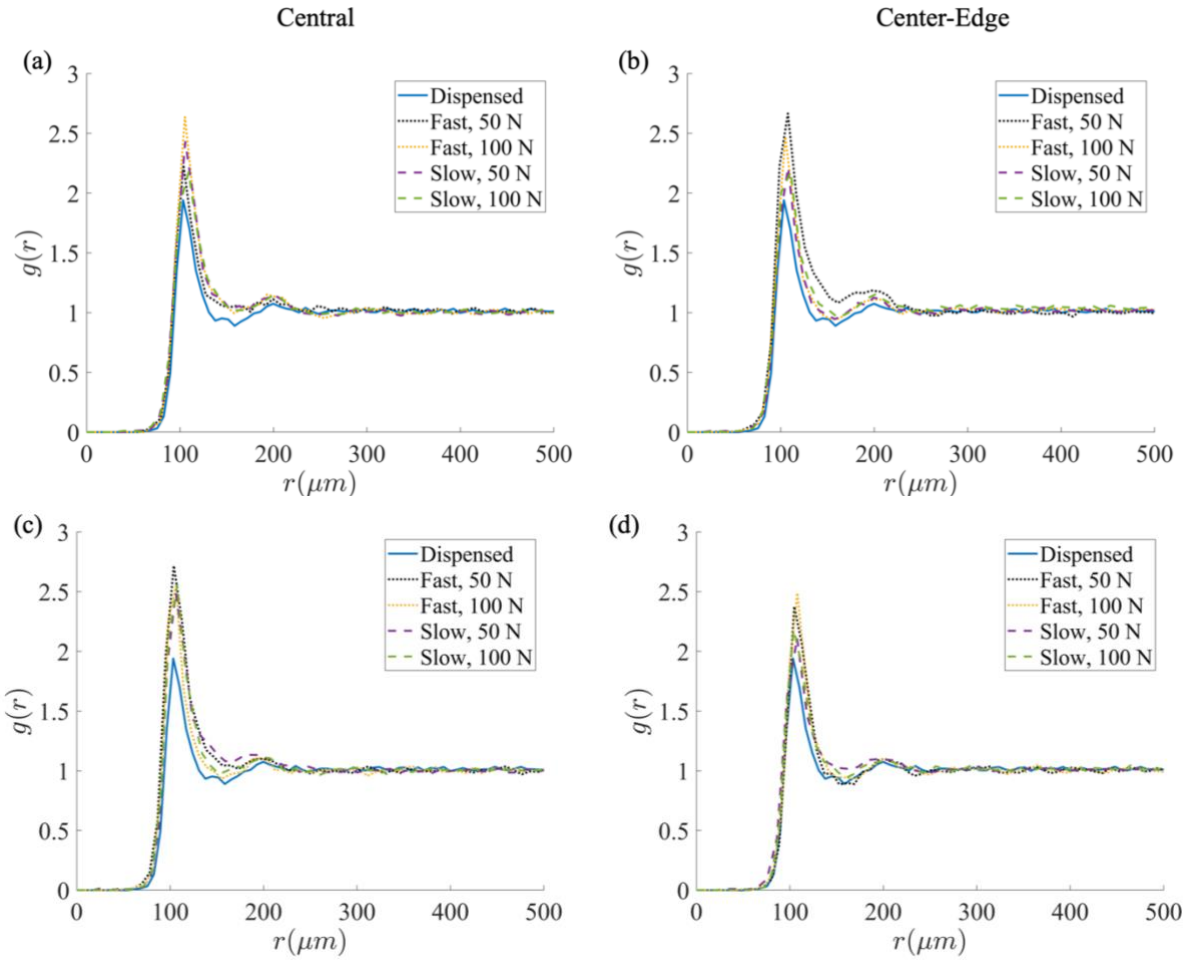

Figure 3.48 RDF, $g(r)$, of *Set 1* (**a, b**) and *Set 2* (**c, d**) squeezed TIM samples compared with the dispensed TIM *Sample 1*. The radial distance is denoted by r. Fast = 10 mm s^{-1} and Slow = 10^{-3} mm s^{-1}.

3.7.3 Local Particle Volume Fraction

The local particle volume fraction, $\phi_{p,local}$, is a critical microstructural metric for squeezed TIMs. This quantifies the impact of squeeze rate and force on the spatial distribution of particles within the TIM. A homogeneous distribution of particles after squeezing likely leads to uniform thermal conduction on the substrate area occupied by the TIM, whereas a heterogeneous distribution will potentially lead to hot spots depending on the size and number of void regions present in the TIM after squeezing. Note that a homogeneous distribution of particles in an insufficient, but necessary, condition to ensure enhanced thermal conduction across the TIM bond line. It is insufficient because homogeneous spreading cannot ensure interconnectivity of particle networks across the bond line. However, theoretically, if the particle size is monodisperse, and if the squeezing process

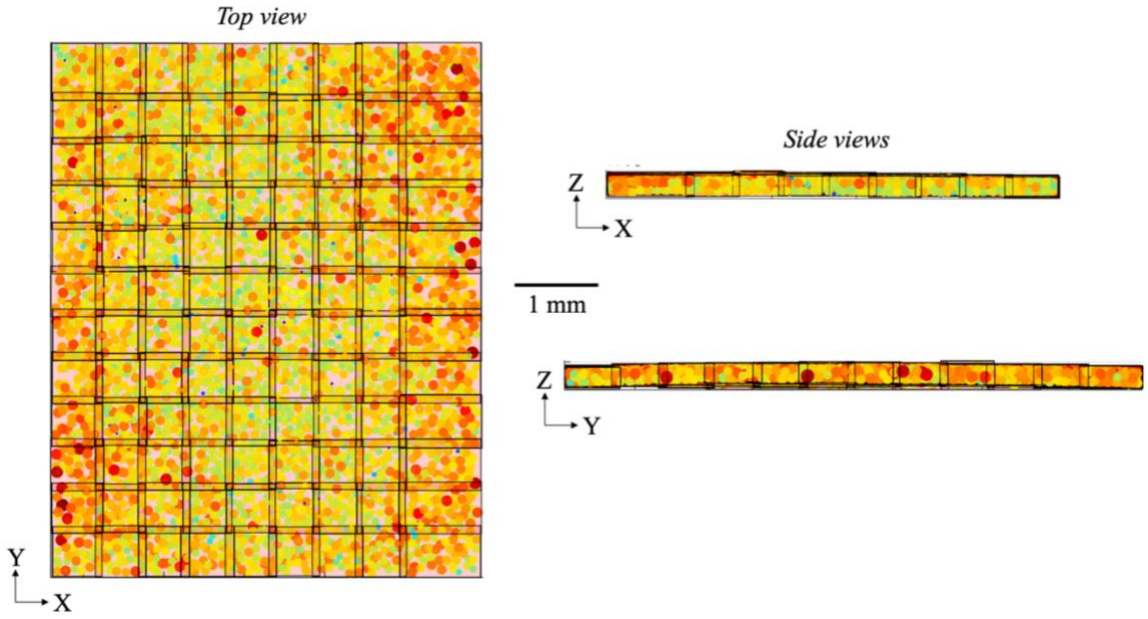

Figure 3.49 Top and side views of the rectangular boxes of size ≈ 5 x 5 particle diameters used in the computation of local volume fraction. This microstructure corresponds to a TIM produced at $V_S = 10$ mm s^{-1} and $F_S = 50$ N. As seen in the side views, the box thickness varies to ensure a tight fitting. An average box thickness is used in the local volume fraction computation.

is optimized to produce a bond line thickness of one particle diameter, then homogeneity in the particle spatial distribution should enhance thermal conduction. But, commercial TIMs always consist of a distribution of particle sizes and shapes, with the largest particle limiting the bond line thickness. In this case, it is critical to optimize squeezing for uniform spreading and high interparticle connectivity across the bond line.

In this section, the local volume fraction of the squeezed TIMs is analyzed by computing Eqn. 3.2 within local rectangular regions of size ≈ 5 x 5 particle diameters. Figure 3.49 shows the boxes constructed around a rectangular subdomain of the squeezed TIM sample produced at $V_S = 10$ mm s^{-1} and $F_S = 50$ N. The side views show that the box thickness varies to ensure a local tight fitting. An average thickness, $\bar{\delta}_{box}$, is used for calculating the box volumes.

Figure 3.50 shows the local volume fraction map for *Set 1* squeezed TIM samples. The Center-Edge (left-hand side) and Central (right-hand side) samples are arranged beside each other in every panel of the figure. The black dashed line represents the centerline or axis of the line pattern dispensed TIM. The particle concentration is lower near the TIM outer edges for both fast and

slow squeeze rates at $F_S = 100$ N (see Center-Edge samples), whereas it is not as significant in the 50 N load case. The void regions in the Central sample are clearly observed in Figure 3.50 (b), whereas the Central samples from other test conditions exhibit relatively more uniform spatial distribution of particles. A notable observation is the intersection of neighboring boxes in Figure 3.49. The search for particles in a given neighborhood is performed based on the location of the particle center within the local rectangular regions. Then, a box is constructed to tightly encompass the set of local particles. This results in a slight expansion of box size. Due to this expansion, neighboring boxes intersect each other. This does not distort the analysis as the bulk particle volume fraction for the TIM microstructures lies approximately near the center of the distribution of $\phi_{p,local}$ (see Figure 3.51 and Figure 3.53) for most samples.

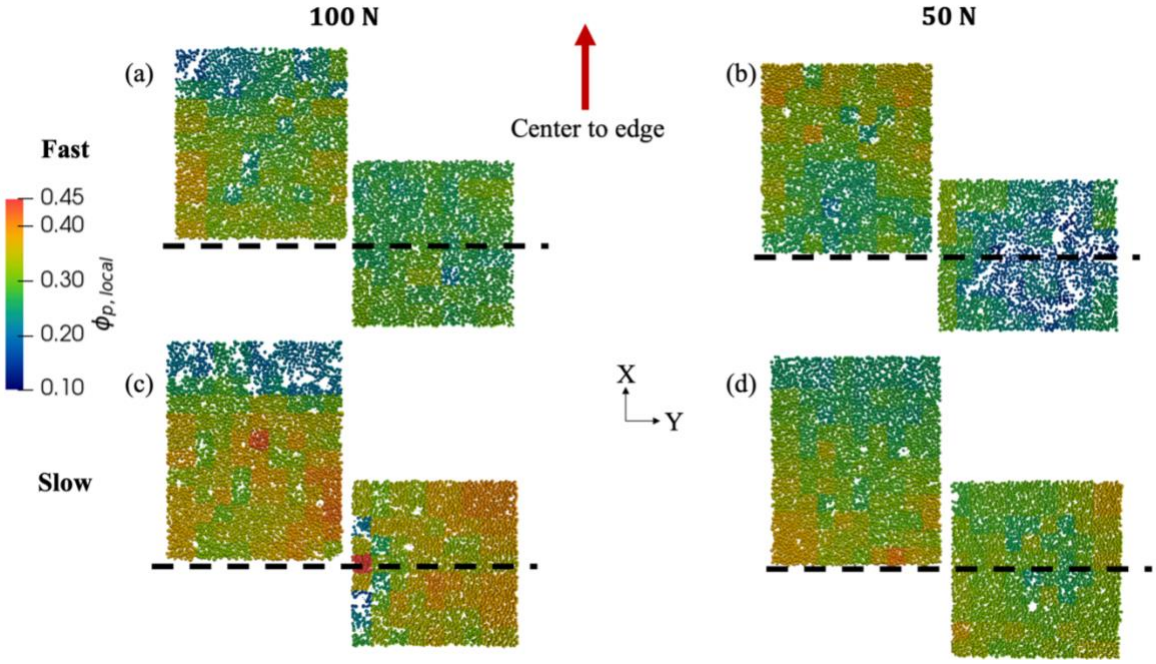

Figure 3.50 Top view of the local volume fraction map for *Set 1* squeezed TIM samples. The computation is performed on a large rectangular subdomain whose bulk properties are approximately equal to that of the whole microstructure. The center to edge direction denotes the primary direction along which particles rearrange after squeezing. In the panels, the Center-Edge and Central samples are arranged left and right figures, respectively. Black dashed line represents centerline of the dispense pattern. Fast = 10 mm s^{-1} and Slow = 10^{-3} mm s^{-1}.

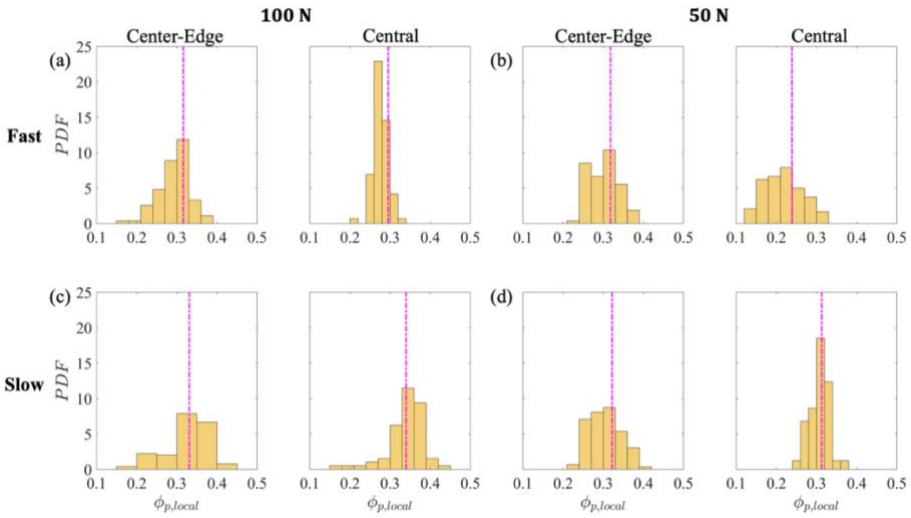

Figure 3.51 Local volume fraction histogram for *Set 1* squeezed TIM samples. The vertical magenta, dash-dot line is the bulk particle volume fraction computed using the convex hull method for the subdomain microstructure.

Figure 3.52 shows the local volume fraction map for *Set 2* squeezed TIM samples. The arrangement of the figures is similar to that of Figure 3.50. Particle concentration is lower near the

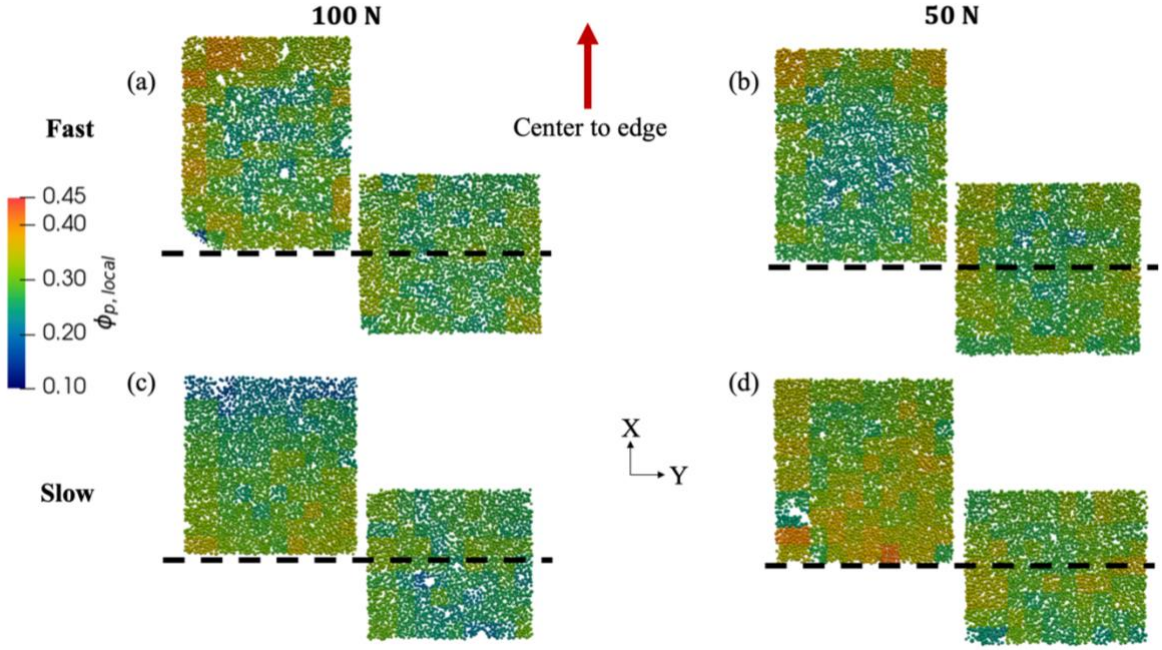

Figure 3.52 Top view of the local volume fraction map for *Set 2* squeeze TIM samples. The computation is performed on a large rectangular subdomain whose bulk properties are approximately equal to that of the whole microstructure. The center to edge direction denotes the primary direction along which particles rearrange after squeezing. In the panels, the Center-Edge and Central samples are arranged left and right figures, respectively. Black dashed line represents centerline of the dispense pattern. Fast = 10 mm s^{-1} and Slow = 10^{-3} mm s^{-1}.

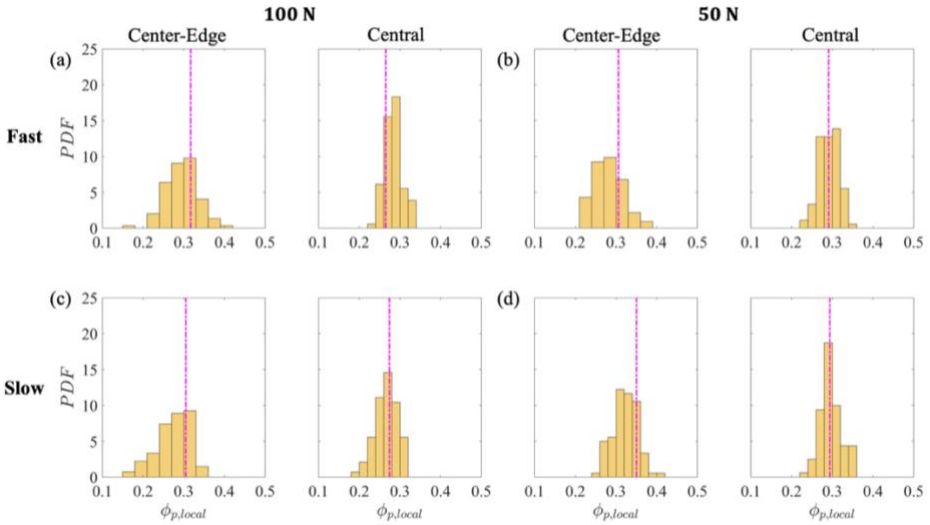

Figure 3.53 Local volume fraction histogram for *Set 2* squeezed TIM samples. The vertical magenta, dash-dot line is the bulk particle volume fraction computed using the convex hull method for the subdomain microstructure.

TIM outer edges only at the slow squeeze rate and 100 N load (see the Center-Edge samples), whereas it is not as significant for the other test conditions. Central samples in all test conditions exhibit relatively uniform spatial distribution of particles. Moreover, the trends are not comparable with *Set 1* data. This is likely a consequence of faster curing time in *Set 2* tests, which results in faster spatial locking of particle positions. In *Set 1* test, the slower curing may have caused a greater relaxation of particles during the load-holding phase. The manual application of copper foil and packaging tape on the glass slide substrate noted earlier could have potentially led to these differences.

The variation of local volume fraction from the center to the edge (*i.e.*, the X direction as obtained by averaging in the regions along Y) is shown in Figure 3.54. Particle concentration near the edges for CE samples is lower only for some of the squeeze conditions, and this effect is not consistent between the test sets. Fast squeezing in *Set 2* leads to a slight increase in the particle concentration near the TIM edges compared to that near the center. This is likely due to the impact-type application of load at fast squeeze rates. Whereas, for *Set 1*, this occurred only for $F_S = 50$ N. Slow squeezing results in lower particle concentration near the outer edges. This trend is seen in both sets of tests, but of varying magnitudes (except for *Set 2* at the slow rate and $F_S = 50$ N). Particle concentration is relatively uniform for all the Central samples except that of $V_S = 10$ mm s^{-1} and $F_S = 50$ N from *Set 1* test.

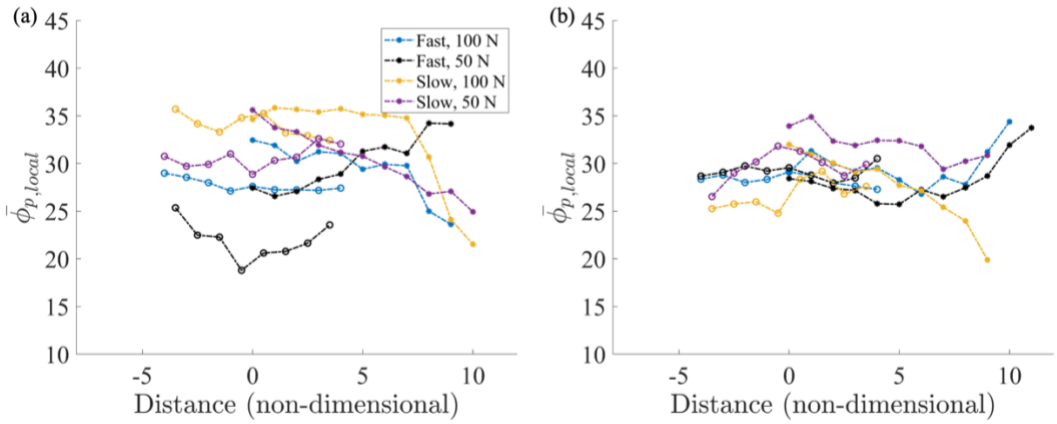

Figure 3.54 Local volume fraction plot along center-to-edge direction for (**a**) *Set 1* and (**b**) *Set 2* squeezed TIM samples. This is obtained by averaging the local volume fraction along Y, and then plotting along X, with reference to Figure 3.50 and Figure 3.52. Open circles are for Central samples and star markers are for Center-Edge samples. Fast = 10 mm s^{-1} and Slow = 10^{-3} mm s^{-1}.

3.8 Discussion on the Péclet Number

Rae *et al.* [35] provided a Péclet number (Pe) framework to understand the impact of squeeze rate on particle spatial distribution heterogeneity in the TIM (see Eqn. 3.3). The Péclet number is defined as the ratio of two time scales: $Pe = \frac{\tau_{matrix}}{\tau_{solid}}$, where τ_{matrix}, is the time scale of the polymer fluid filtration through the particle network in the initial dispensed state and τ_{solid} is the time scale of the movement or deformation of the composite material as a whole, *i.e.*, the TIM, during squeeze. A power law approximation for the fluid flow was used in their work. Marked heterogeneity in the particle spatial distribution is attributed to relatively large τ_{solid} compared with τ_{matrix} *i.e.*, $Pe \ll 1$ [111,122]. This implies that the polymer matrix has sufficient time to filter through the particle network during squeezing, thus leaving behind a local concentration of particles. In the case of a line dispense pattern, this local region is near the centerline of the pattern. In general, as explained in the thesis of Rae [129], local concentration occurs along the stagnation points or zones that are controlled by the dispense pattern.

An energy-based scaling analysis can provide insight into the impact of the squeeze rate on matrix filtration during the squeeze process [116]. The energy dissipation is the sum of contributions from the (a) composite material as a whole and (b) matrix filtration. Competition between these two

components will result in the observed homogeneity/heterogeneity of particle spatial distribution in the squeezed TIM. Similarly, the ratio of these components is the Péclet number [116]:

$$Pe = \frac{\frac{\mu_f}{\mu_D} V_S^2}{\tau \dot{\gamma}} \qquad 3.3$$

where τ is fluid shear stress, $\dot{\gamma}$ is fluid shear strain, μ_f is the polymer viscosity and μ_D is Darcy's permeability, given the initial dispensed TIM microstructure. The competition is determined by the particle size distribution, polymer viscosity, initial arrangement of particles in the dispensed TIM and squeeze rate. Materials processing and application parameter (*i.e.*, squeeze rate) govern the overall TIM flow characteristics, its microstructure and bulk thermal conductivity.

The Herschel-Bulkley (HB) approximation has been more commonly employed to describe the macroscopic flow behavior of TIMs [14,36,39,46,118] through an expression for the fluid shear stress, τ:

$$\tau = \tau_y + K\,\dot{\gamma}^n \qquad 3.4$$

where τ_y is fluid yield stress, K is consistency, $\dot{\gamma}$ is fluid shear strain, n is fluid flow index. The shear stress (τ_y), consistency (K), and fluid flow index (n) of particle-polymer composites can be correlated with the particle volume fraction, matrix viscosity and particle size. For composites consisting of monodisperse particles (spherical and faceted, separately) with mean diameter 100 μm in silicone oil ($\rho_{f,s} \approx 1000$ kg m^{-3}, $\mu_{f,s} \approx 41$ Pa s $\approx 2\,\mu_f$), shear-thinning behavior was observed for spherical particle suspension and for $\phi_p < 0.4$ and $n > 0.95$ and empirical formulations were derived for τ_y, n [217]. Using the formulations, $\tau_y \approx 0.22$ Pa at $\phi_p = 0.35$ (approximate particle volume fraction in the TIM dispensed state) and $n \approx 0.98$ at $\phi_p = 0.35$. The Maron-Pierce equation [218] proved to be a good fit to the data of K vs ϕ_p, where the maximum particle volume fraction ($\phi_{p,max}$) for spherical particle packing was used as the fitting parameter. Using these formulations, *Pe* can now be calculated for varying V_S (Eqn. 3.5), where the Darcy's permeability formulation is adopted from Davidson *et al*. [20]. Note that the ratio of particle-to-fluid density in their work is different from that investigated in this thesis. But their

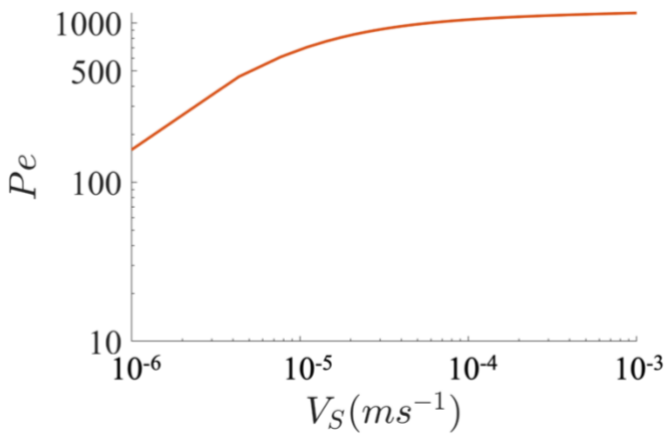

Figure 3.55 Péclet number, Pe, as a function of squeeze rate, V_S, for the mock TIMs investigated in this work.

characterization provides a starting point for Péclet number analysis of the squeezing process studied in this work.

$$Pe = \frac{\frac{\mu_f}{\mu_D} V_S^2}{\tau\,\dot{\gamma}} = \frac{\frac{\mu_f}{\mu_D} V_S^2}{(\tau_y + K\,\dot{\gamma}^n)\,(\frac{V_S}{h})} \tag{3.5}$$

$$\mu_D = \left(1 - \phi_p\right)^3 \frac{D_p^2}{151.2\,\phi_p^2} \tag{3.6}$$

Figure 3.55 shows the variation of Pe with squeeze rate for the TIM. As seen from the plot, $Pe \gg 1$ even at the slowest squeeze rate explored in this work. Thus, there appears to be no tendency for a marked heterogeneity in the particle spatial distribution after squeezing the mock TIMs investigated in this thesis.

3.9 Concluding Remarks

In summary, this chapter experimentally evaluated the microstructure of dispensed and squeezed mock TIMs, prepared at a target 30 vol% of spherical copper particles ($D_{m,ce} \approx 107.7$ µm) hand-mixed in a UV curable epoxy. Automated procedures are developed to dispense line patterns of the TIM and squeeze them at constant velocity up to a desired force. Two sets of tests at squeeze rates of 10 mm s^{-1} (fast) and 10^{-3} mm s^{-1} (slow) and two different squeeze forces (50 N and 100 N) are employed in the experimental investigation. High-resolution 3D XRCT imaging is used

to quantify the dispensed and squeezed TIM microstructures. Metrics such as the bulk and local particle volume fraction, coordination number, and RDF are computed.

The BLT of the squeezed TIM ranges between $200 - 260$ μm ($2 - 2.4$ median particle diameters) at the applied pressure of ≈ 11 psi ($F_S = 50$ N) and ≈ 23 psi ($F_S = 100$ N). Based on the average BLT of left and right TIMs, it is largely independent of the load at the fast squeeze rate, likely due to the impact nature of load application. At the slow squeeze rate, the BLT decreased with increasing load. The dispensed TIM microstructure is similar along the axis of the line pattern with average properties of $\phi_p \approx 36.1\%$ and $C_N \approx 2.1$. Squeezing reduces the bulk particle volume fraction to the range of $\approx 25.4 - 34\%$ likely due to the formation of voids or air bubbles that can cause a volume expansion. Overall, the RDFs of the dispensed and squeezed TIM samples suggest a disordered microstructure due to the presence of just two peaks. The first peak in the RDF of the squeezed TIMs is taller than that of the dispensed TIM. This is supported by the higher coordination number (for most cases).

The local particle volume fraction is approximately uniform near the central region of the squeezed TIM, whereas at the higher load, the local particle concentration is lower near the edges. However, the variation is not consistent between the two test sets. Trends in the bulk microstructural properties as a function of squeeze rate and force are also not consistent between the test sets likely due to the manual assembly of the (a) copper foil on bottom glass slide, (b) 3M Scotch packaging tape on top glass slide, and (c) squeeze rig in the Instron machine. Items (a) and (b) potentially impart a pseudo-surface roughness that can influence the rheology of the TIMs during squeezing, and (c) can cause non-parallelism between the top and bottom substrates. Optical image analysis of the TIM revealed uniform and similar particle spatial distribution when squeezed on the bare glass slide (based on two tests under fixed conditions). Differing characteristics are observed when squeezed on glass slides covered with copper foil and packaging tape (under fixed test conditions). This suggests process induced variation and is a crucial observation because real surfaces are rough and will potentially influence the rheology during squeezing. Thus, the TIM microstructure and performance can differ for the same application protocols and varying surface roughness.

Automation of the dispensing and squeezing protocols, and control of the surface roughness of the metallic lid and heat sink surfaces are critical to ensuring optimal particle spatial distribution and thermal performance. Predictive simulations can potentially aid the engineer in squeeze process optimization and that is the focus of the next chapter. Future experimental work should investigate high filler loading TIMs consisting of realistic particle shapes and size distribution. More complicated dispense patterns such as serpentine, spiral, star- and "X"-shapes must be investigated. Voids in the squeezed TIM may be characterized via 3D XRCT imaging using metrics such as void size, number density and their spatial location in the squeezed TIM. The analysis should focus on large voids which can potentially impede heat conduction. Further, a systematic investigation of squeezing on substrates with controlled surface roughness should be conducted to reveal the impact of substrate roughness on the TIM rheology during squeezing.

4. PREDICTIVE MICROSTRUCTURE MODELING OF TIMS

4.1 Introduction

During application, the TIM is squeezed by the heat sink or metallic lid often with a constant velocity until the desired ultimate squeeze force (or pressure) is reached. Non-uniform particle distribution within the TIM can occur during the squeezing process and is detrimental to performance [35]. Validated microstructure models of TIM squeezing will enable thermal engineers to optimize application parameters such as squeeze pressure and velocity to achieve best thermal performance at desired BLT for a given dispense pattern.

In this chapter, a discrete element method (DEM) simulation framework is used to predict the spatial distribution of particles and other TIM microstructural characteristics. Accurate predictions of TIM squeezing (a) require appropriate knowledge of initial particle distribution in the dispensed state, and (b) necessitate modeling of complex particle-fluid interactions in addition to the interparticle interactions. Coupling the fluid and particle dynamics is the main challenge addressed in this work. The predicted statistics of the microstructure are compared with that of the experimentally characterized microstructure based on 3D XRCT imaging (previously discussed in Chapter 3). An open-source DEM software package Multiphase Flow with Interphase Exchanges (MFIX) [193,219] is employed in this thesis. MFIX was developed by the National Energy Technology Laboratory (NETL) and it is capable of modeling dry particulate media, particle-fluid, and two fluid systems. The methods within MFIX have been subject to extensive verification [193] and validation [219]. In this work, MFIX 18.1.5 (or MFIX-DEM) is used and user-defined functions (UDFs) are developed to simulate constant velocity squeezing of TIM. In the following sections, the simulation workflow (section 4.2), the constant velocity squeeze model framework (section 4.3), microstructural analysis (section 4.4) and comparison with experiments (section 4.5) are discussed.

4.2 Simulation Workflow in MFIX

This section details the modifications to the DEM simulation for modeling TIM squeezing through the development of the user defined functions (UDFs). To model squeezing, after the particles are

initiated in the domain, a fictitious top wall is defined to enable squeezing and its dynamics are implemented through the UDFs. The top wall moves down at a constant velocity and exerts forces on the particles, thus squeezing them out. In addition, particles are coupled with the polymer matrix phase via drag force, and this is incorporated within the UDF. In this squeeze model, particle-fluid interactions are one-way coupled (*i.e.*, fluid exerts a drag force on the particles, but it is assumed that the particles do not perturb the fluid flow field). While this is not physically correct especially at higher filler volume fractions such as those found in commercial TIMs, it provides a starting point for modeling the squeeze process. As described in the previous chapter, mock TIMs in this work were loaded with spherical particles at moderately low volume fraction. Depending on the various stages of DEM simulation such as set-up of modeling domain and initial particle positions, time integration of forces to compute future particle positions and velocities, and end of simulation, different types of UDFs can be executed [220]. Code templates for these UDFs are provided within MFIX. In this work, the UDF *usr0_des* is executed in the simulation set-up phase to read initial particle spatial positions obtained from 3D XRCT image analysis, and *usr1_des* is executed within the DEM time integration loop to compute forces between the top wall and particles, and account for drag forces between the fluid and particles. Variables such as top wall position, relative change in its position and net force/pressure acting on the wall are continuously monitored during the simulation. Figure 4.1 describes the DEM squeeze simulation workflow. This flowchart specifically shows a BLT-controlled simulation. This workflow can also be used in a pressure-controlled framework by examining the history of the simulated data and back-calculating the appropriate BLT that matches the desired squeeze pressure.

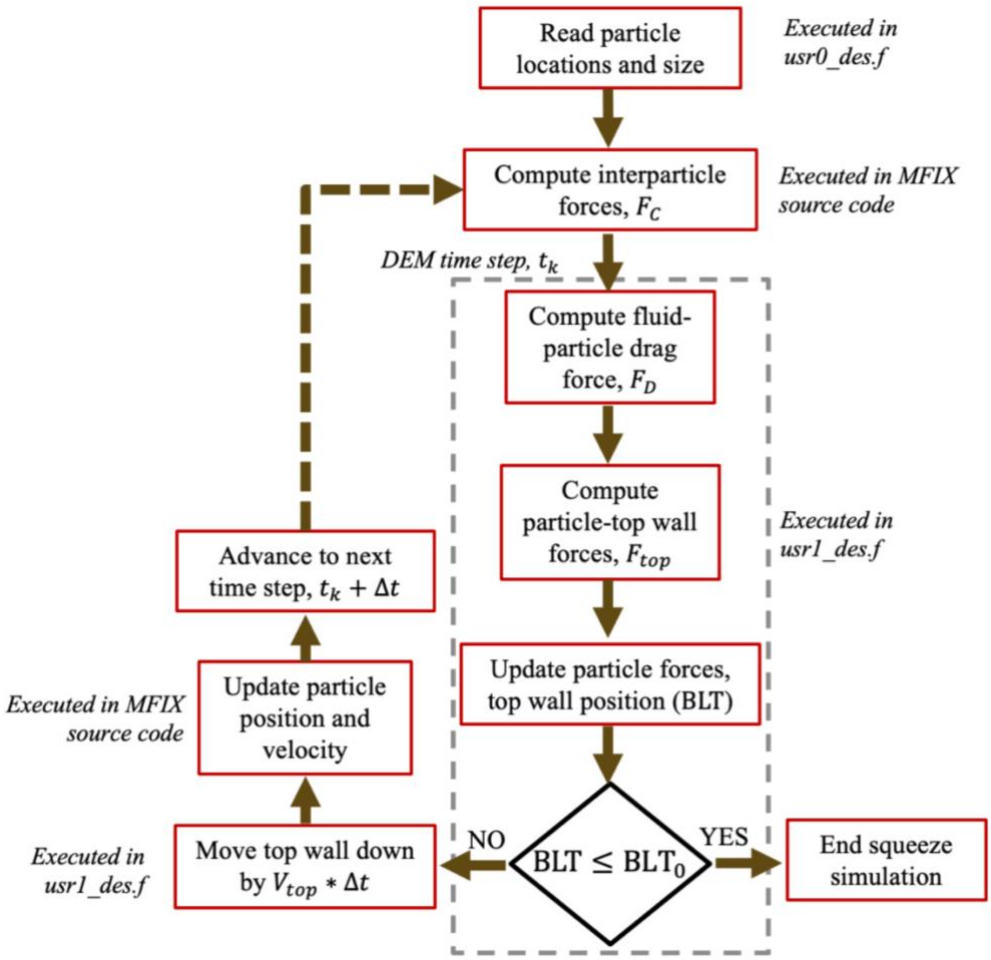

Figure 4.1. DEM squeeze simulation work flow in MFIX showing the use of two user-defined functions (*usr0_des* and *usr1_des*). These two functions are used to read initial particle configuration, and compute particle-top wall interactions and assist in drag force calculations, respectively.

Simulation results such as particle positions and velocities are imported to open-source ParaView software for visualization. Subsequently, using ParaView, particle positions in the squeezed state are extracted to perform microstructure analysis. All simulations are performed using Purdue University's supercomputer cluster maintained as Rosen Center for Advanced Computing (RCAC) consisting of two 10-core Intel Xeon-E5 processors, thus making up 20 cores per node with a total of 128 GB memory. Two broad stages of squeeze simulation development are carried out in this work. First, only the dry particles are simulated, followed by a coupling of the particles with a Newtonian fluid of known velocity profile (analytically calculated assuming Newtonian behavior) via drag forces.

4.3 Constant Velocity Squeeze Model

4.3.1 Simulation Set-up in MFIX

A section of the line pattern dispensed TIM about 5 median particle diameters wide is cut out from the central region of the 3D XRCT image dataset. Figure 4.2 shows the dispensed TIM sample used in XRCT imaging, the reconstructed image, and the front/top views post image analysis. This is imported to MFIX as initial configuration and then squeezed. Although MFIX reads particle locations directly from an input file called *particle_input.dat*, it cannot handle a particle size distribution natively. Dispensed TIM particle locations analyzed from image processing are provided in the *particle_input.dat* with a constant, dummy value of diameter, $\widetilde{D}_p = 100$ μm. Then, *usr0_des* is used to assign the correct particle diameters using another input file *part_diameter.txt*. In addition, the particle volume, mass, and moment of inertia arrays are updated in *usr0_des* based on the correct particle diameters.

Figure 4.3 shows the initialized particle configuration (top and front views) inside the rectangular simulation box. The domain length along X direction is 20 mm. This was arbitrarily chosen to be

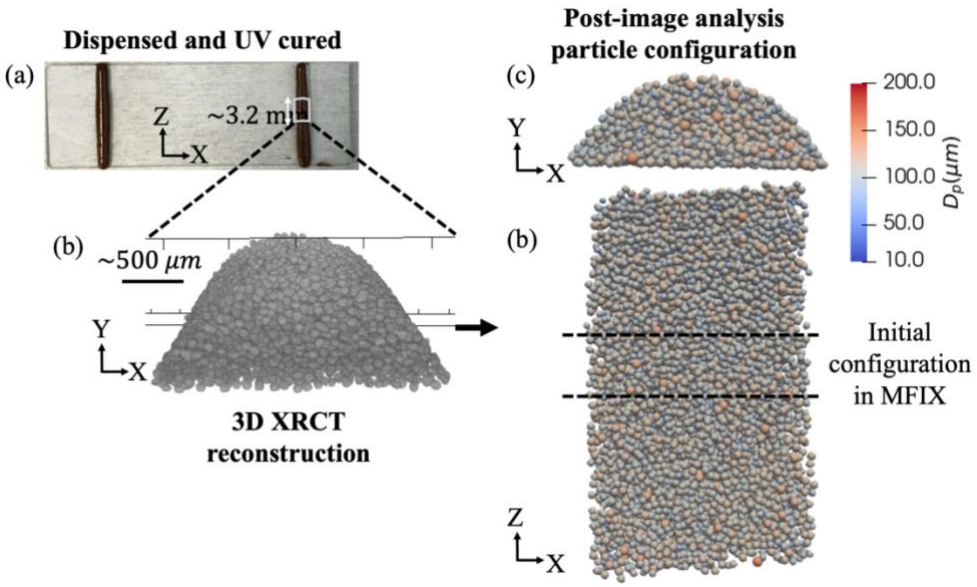

Figure 4.2. Initial configuration for DEM simulation obtained from 3D XRCT image analysis of a line pattern dispensed TIM. (**a**) Dispensed TIM central sample (*Sample 1*) used for 3D XRCT imaging, (**b**) 3D reconstructed image dataset for that sample, (**c, d**) particle sizes and locations of the sample from (b) plotted using ParaView. The horizontal black dashed lines represent a section of the dispensed TIM ≈ 5 median particle diameters in length used in the squeeze simulation.

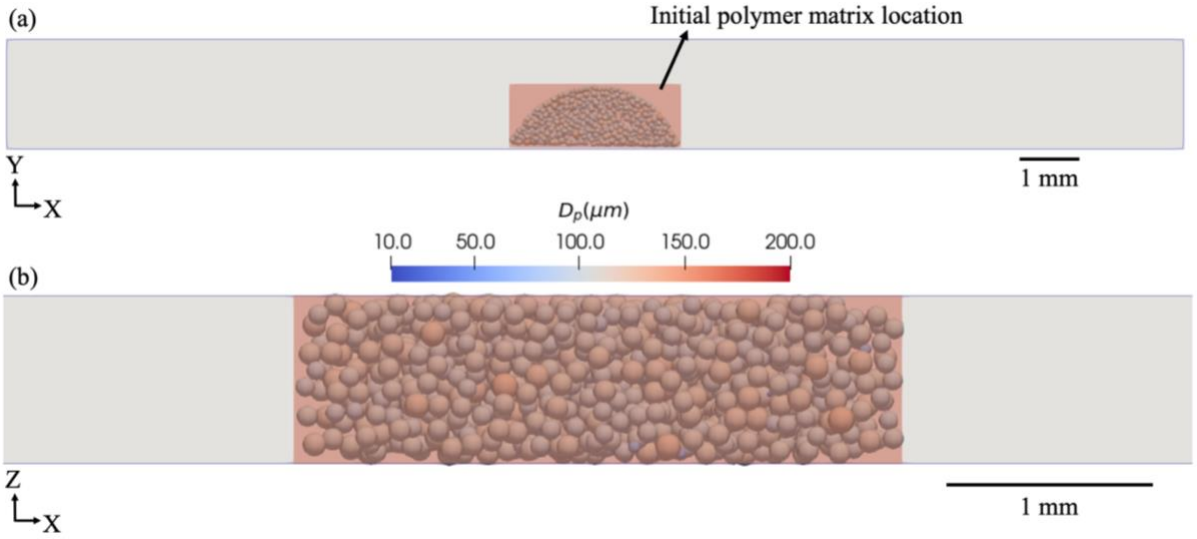

Figure 4.3. Initial configuration (**a**) front and (**b**) top views, consisting of 966 particles, showing the gray simulation domain box. The initial location of the polymer matrix is highlighted by the light red region around the particles. Squeezing occurs along the $-Y$ direction and particles spread along the X direction, whereas the Z direction (along the axis of dispensing) is periodic. Although the domain height along the Y direction is large and there is a significant amount of empty space above the particle bed, the top wall is placed right above the topmost particle along Y. The length scale is different in (b) to clearly show the edge region where particles intersect the walls.

significantly large to allow for flow of particles. Similarly, the initial height along the Y direction is also sufficiently large to encompass the entire system. The Z direction is assumed to be periodic to mimic an infinitely long line of dispensed TIM. The particles rest on the ground at $Y = 0$ and the front/back walls along Z partially intersect the particles. This is computed based on the particle positions and diameters, and a user-controlled intersection depth, $d_{part-wall} = 20\%$ (Figure 4.3 (b)). This parameter represents the fraction of particle radius that will lie outside the domain. If $d_{part-wall}$ is relatively large, it is not realistic and particles may be swept out of the domain during the simulation leading to physical and numerical errors. If $d_{part-wall}$ is relatively small, periodic boundary conditions may not be appropriately applied owing to regions devoid of particles in the vicinity of the walls.

The initial location of the polymer matrix is indicated by the light red region. The top wall is positioned at the surface of the topmost particle in the bed. During the simulation, this wall moves downward (*i.e.*, along the $-Y$ direction) at a user-specified velocity. Gravity is present along the $-Y$ direction. Particle properties similar to those used in experiments are used in the simulations.

Table 4.1 DEM squeeze simulation parameters

Simulation Parameter	Value
Particle density, ρ_p	$9000\ \text{kg m}^{-3}$
Fluid density, ρ_f	$1000\ \text{kg m}^{-3}$
Fluid viscosity, μ_f	$20\ \text{Pa s}$
Acceleration due to gravity, g	$9.81\ \text{m s}^{-2}$
Normal stiffness constant (interparticle, particle-wall), K_{p-p}, K_{p-w}	$100,000\ \text{N m}^{-1}$
Tangential stiffness constant (interparticle, particle-wall), $K_{T,p-p}, K_{T,p-w}$	$\frac{2}{7}\ K_{p-p}, \frac{2}{7}\ K_{p-w}$
Coefficient of friction (interparticle, particle-wall), μ_{p-p}, μ_{p-w}	0.5
Coefficient of restitution (interparticle, particle-wall), ν_r	0.7

Table 4.1 lists important simulation parameters. In the next section, top wall dynamics and fluid-particle coupling via drag force are discussed.

Initial Polymer Matrix Location

The polymer matrix initial location shown in Figure 4.3 is strictly not correct, but provides a starting point for the squeeze simulation. Physically, the fluid profile in the line dispense pattern used in this work should be heap-like. An approximate outline is shown in Figure 4.4. The heap shape will dynamically evolve during the squeeze simulation. Accurate computation of fluid-top wall interaction and fluid-particle coupling requires shape tracking of the fluid domain. This will likely require fluid-structure interaction physics and is computationally more expensive.

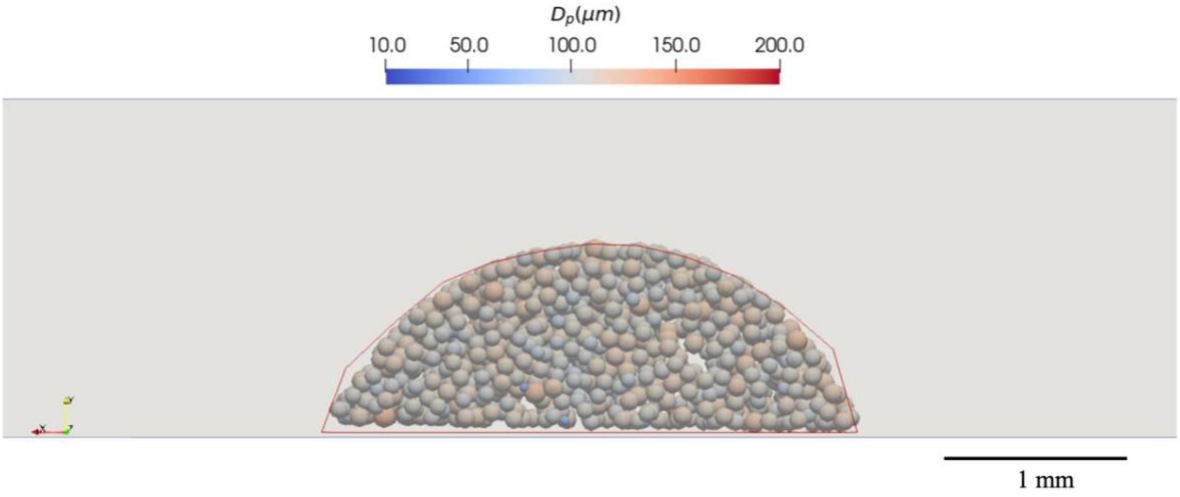

Figure 4.4. Ideal polymer matrix initial location outlined in red. This is an approximate polygonal representation of the heap shape.

4.3.2 Top Wall Dynamics and Fluid-Particle Coupling

In this section, further development of the MFIX source code via the UDF *usr1_des* to incorporate top wall dynamics and enable one-way fluid-particle coupling via drag force are discussed.

Top Wall Dynamics

To squeeze the particles, a top wall exerts forces on the particles as it moves downward at a constant velocity. The particle-wall interaction force is governed by a linear spring model (no damping) as:

$$F_{p-wall} = K_{p-w}\,\delta_{pw} \qquad 4.1$$

where F_{p-wall} is force on particle exerted by the top wall, K_{p-w} is stiffness of particle-wall interaction (see Table 4.1), and δ_{pw} is overlap between particle and top wall. The interaction force is added to the Y component of the net force on a particle. The total force acting on the top wall is the sum of the particle-wall interaction forces and the force exerted by the fluid. In the subsequent sections, fluid velocity profile and force exerted on the top wall are formulated.

Fluid Velocity Profile

For the one-way fluid-particle coupling, the fluid velocity profile must be known. Here, the 2D velocity profile within the fluid is solved for as the squeezing of a semi-infinite expanse of Newtonian fluid following the derivation for squeezing of a line of fluid in the work of Marois and Lacroix [57]. In their work, all three dimensions were considered, but here we simplify to 2D. Further, the flow was assumed to be creeping and time independent and pressure variation was two dimensional. In this work, the flow profile is assumed to be 2D and the pressure variation is one dimensional. A string of fluid of width α is considered (see Figure 4.5 (a)) between two plates separated by a distance b that decreases with time at constant velocity, V_S. The system is axisymmetric about the vertical dashed line in Figure 4.5 (a). Following the same procedure outlined in Marois and Lacroix [57], we arrive at the following equations for the normalized fluid velocity components, $\tilde{v}_{f,x}\ and\ \tilde{v}_{f,y}$ (normalized by $6\dot{b}$), and pressure, $P_f(x)$:

$$\tilde{v}_{f,x} = -\tilde{x} * (\tilde{y}^2 - \tilde{y}) \qquad 4.2$$

$$\tilde{v}_{f,y} = \left(\frac{1}{3}\tilde{y}^3 - \frac{1}{2}\tilde{y}^2\right) \quad 4.3$$

$$P_f(x) = -\frac{6\mu_f V_S}{b^3}\left(x^2 - \frac{\alpha^2}{4}\right) \quad 4.4$$

where V_S is the squeeze velocity (positive value), b is the separation between the bottom and top plates, $\tilde{v}_{f,(x,y)} = \frac{v_{f,(x,y)}}{6V_S}$ is the normalized fluid velocity components, $\tilde{x} = \frac{x}{b}\ and\ \tilde{y} = \frac{y}{b}$ are normalized coordinates, α is the width of the fluid string, $P_f(x)$ is the fluid pressure, and μ_f is the fluid viscosity. Derivation of the pressure assumed boundary conditions of $P_f(x|_{\pm\frac{\alpha}{2}} = 0)$. Figure 4.5 (b) shows the normalized velocity vectors in normalized spatial coordinates. Figure 4.5 (c) shows the evolution of the fluid front for a few time stamps. This is the profile of the outer right-side edge that is initially a straight vertical line as seen in Figure 4.5 (a).

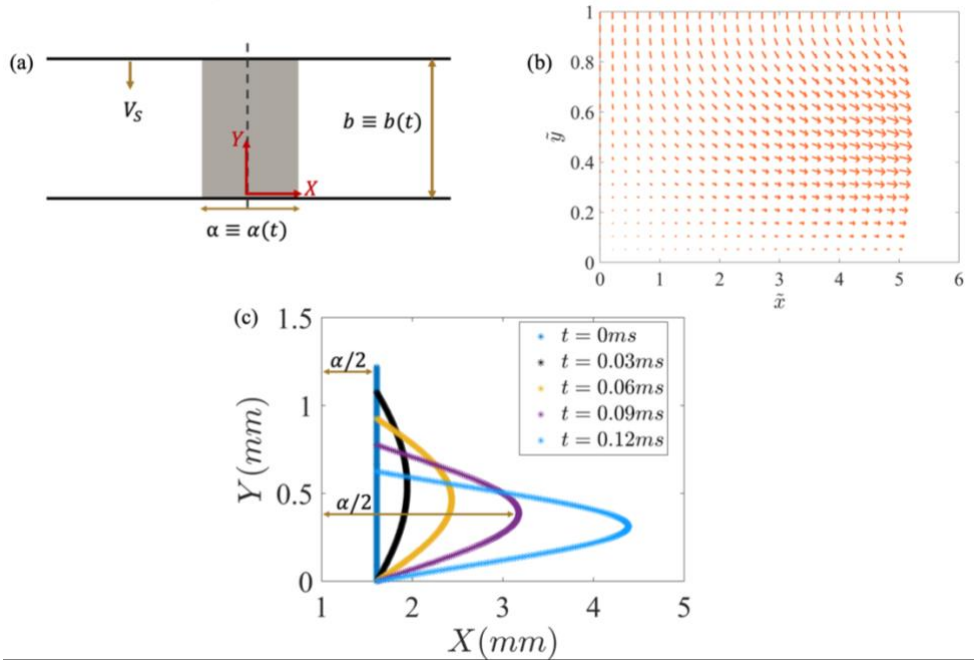

Figure 4.5. Analytically derived 2D Newtonian fluid squeeze velocity profile based on [57]. The flow is creeping and time independent with pressure variation is only along X. (**a**) Domain set-up with a string of fluid of width α squeezed at a constant velocity, V_S, between the plates separated by a distance b; (**b**) 2D velocity profile, as described by Eqns. 4.2 and 4.3, and (**c**) Evolution of the fluid front with time for a constant velocity squeezing simulation, highlighting the increasing width of the fluid string, $\alpha(t)$. Exploiting symmetry in (a), only the evolution of one half (the right-side) of the fluid front is shown with a half-width, $\alpha/2$.

To implement the above fluid flow field in MFIX for calculation of drag forces, the TIM particle configuration is first centered about its mean position to coincide with the vertical black dashed line from Figure 4.5 (a). The initial width of the TIM is calculated based on farthest particle position along X and their diameter. This provides the initial value of α. The squeeze velocity, V_s, is constant, thus variation of the thickness parameter, b, is linear with time: $b = h_D - V_S\, t$, where h_D is the initial position of the top wall.

One-Way Fluid-Particle Coupling

One of the main challenges in modeling of TIM squeezing process is the coupling of particle and fluid dynamics. It is assumed that the presence of particles does not affect the fluid flow field. We recognize that accurate predictions of the squeezed TIM microstructure is feasible only if the fluid and particles are two-way coupled. Physically, these two material phases affect the motion of one another, *i.e.*, the fluid velocity analytically derived in the previous section will be perturbed due to the presence of particles. This effect can be especially strong in the specific case of TIM squeezing owing to the characteristic flow length scale (*i.e.*, separation between plates) being comparable to a few particle diameters. Moreover, at higher filler particle loadings in the TIM, the perturbation is more pronounced. The polymer matrix transport occurs through the pore networks. In this work, a one-way fluid-particle coupling is implemented via drag force.

A Stokes [221] drag model is first implemented in the squeeze simulations based on the relative velocity between particle and the fluid motions, via a UDF, that calculates the drag forces based on:

$$F_{d,x} = 6\pi\mu_f R_i(v_{f,x} - V_{p,x}) \qquad 4.5$$

$$F_{d,y} = 6\pi\mu_f R_i(v_{f,y} - V_{p,y}) \qquad 4.6$$

where $F_{d,(x,y)}$ is fluid drag force on particle in x, y directions, μ_f is the fluid viscosity, R_i is the radius of particle i, and $\vec{V}_f = v_{f,x}\,\hat{\imath} + v_{f,y}\,\hat{\jmath}$ is fluid velocity evaluated at the center of particle i $\overrightarrow{V_p} = V_{p,x}\,\hat{\imath} + V_{p,y}\,\hat{\jmath}$ – velocity of particle i. However, it does not consider the effect of local particle volume fraction on the drag force around a reference particle. Therefore, results from simulations that incorporate a Stokes drag force are not discussed in this thesis.

To account for local particle volume fraction, the Ding and Gidaspow drag model [222] is used. This model is a combination of the Wen and Yu and Ergun drag correlations [223]. MFIX source code implements this and other drag models, but appropriate inputs such as the fluid velocity profile and local volume fraction must be provided. The Ding and Gidaspow model covers a wide range of local particle volume fraction, $\phi_{s,IJK}$, and provides two distinct drag formulations based on $\phi_{s,IJK}$. Physically, at lower particle volume fractions, the fluid drags the particles (Wen and Yu formulation) and at higher particle volume fractions, drag is the equivalent of fluid pressure drop through the packed particle bed (Ergun equations). In the Ding and Gidaspow drag correlations, this transition occurs at $\phi_{s,IJK} = 0.2$. Furthermore, the formulation at lower local particle concentration takes on two different forms depending on Re, which governs the drag coefficient, C_d. The drag force is calculated as the product of drag force coefficient and the relative fluid-particle velocity [222]:

$$\vec{F}_{drag} = D(\vec{V}_f - \vec{V}_p), \tag{4.7}$$

where F_{drag} is fluid drag force on particle, $\vec{V}_f = v_{f,x}\,\hat{\imath} + v_{f,y}\,\hat{\jmath}$ is fluid flow field evaluated at the center of reference particle, $\vec{V_p} = V_{p,x}\,\hat{\imath} + V_{p,y}\,\hat{\jmath}$ is velocity of particle, $D = \beta\frac{\mathcal{V}_p}{\phi_{s,IJK}}$ is drag force coefficient, β – drag coefficient for particle, $\mathcal{V}_p$ is volume of particle, and $\phi_{s,IJK}$ is local particle volume fraction in the cell containing particle. The drag force coefficient is a function of the relative particle-fluid velocity, fluid viscosity and density, particle diameter, local particle volume fraction and local Reynolds number.

Figure 4.6 shows the variation of the Ding and Gidaspow drag force normalized by the Stokes drag force (magnitude from Eqn. 4.5 and 4.6) with local particle volume fraction, $\phi_{p,local}$ ($= \phi_{s,IJK}$ in MFIX). Normalized force expressions are computed for various Reynolds numbers $Re = \frac{\rho_f|\vec{V}_f - \vec{V}_p|D_p}{\mu_f}$:

$$\tilde{F}_{DG} = \frac{150\phi_{s,IJK} + 1.75\phi_{f,IJK}\,Re}{18\,\phi_{f,IJK}}, \text{ if } \phi_{s,IJK} \geq 0.2 \tag{4.8}$$

$$\tilde{F}_{DG} = \frac{C_D}{24}\,Re\,\phi_{f,IJK}^{-3.65}, \text{ if } \phi_{s,IJK} < 0.2 \tag{4.9}$$

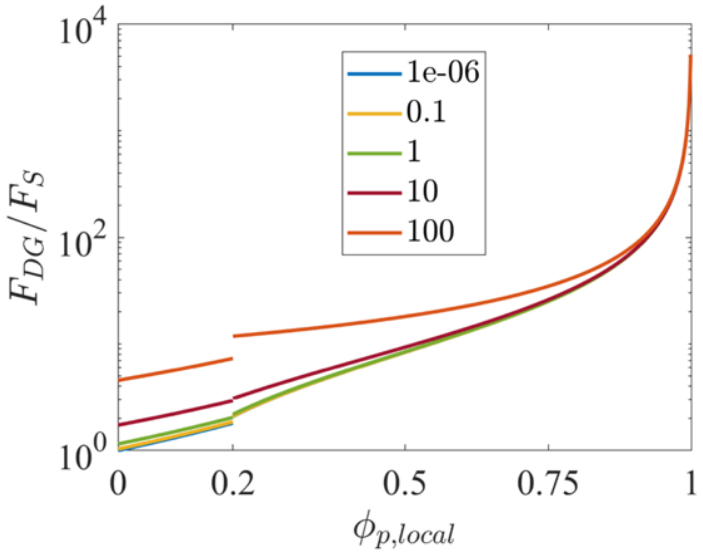

Figure 4.6. Ding and Gidaspow drag force normalized by the Stokes drag force, $\frac{F_{DG}}{F_S}$, plotted as a function of the local particle volume fraction, $\phi_{p,local}$, for various Reynolds number Re.

where $\tilde{F}_{DG}$ is the normalized drag force for a particle, $\phi_{s,IJK}$ is the local solids volume fraction in the cell containing the reference particle, $\phi_{f,IJK}$ is local fluid volume fraction in the cell containing the reference particle, C_D is the drag force coefficient, and Re is Reynolds number of reference particle. One of the drawbacks of this model is the discontinuity at $\phi_{p,IJK} = 0.2$ where the force formulation switches.

MFIX partitions the simulation domain into computational cells and $\phi_{s,IJK}$ is computed in each cell as:

$$\phi_{s,IJK} = \sum_{i \in IJK} \mathcal{V}_{p,i} / \mathcal{V}_{IJK} \qquad 4.10$$

where $\phi_{p,IJK}$ is local particle volume fraction in cell $IJK, \sum_{i \in IJK} \mathcal{V}_{p,i}$ is total volume of all particles whose center lies in cell $IJK, and\ \mathcal{V}_{IJK}$ is volume of cell IJK. The computational cells are cubic and its side length is 5 particle diameters (based on the maximum particle diameter). Particles whose center lies in a computational cell are identified and the entire particle volume is considered in the calculation $\phi_{p,IJK}$, even if the particle partially lies in an adjacent cell. As the top wall moves downward and squeezes the particles, it intersects some of the computational cells (see Figure 4.7) and this must be accounted for when computing $\mathcal{V}_{IJK}$. In those cells, the actual particle fraction

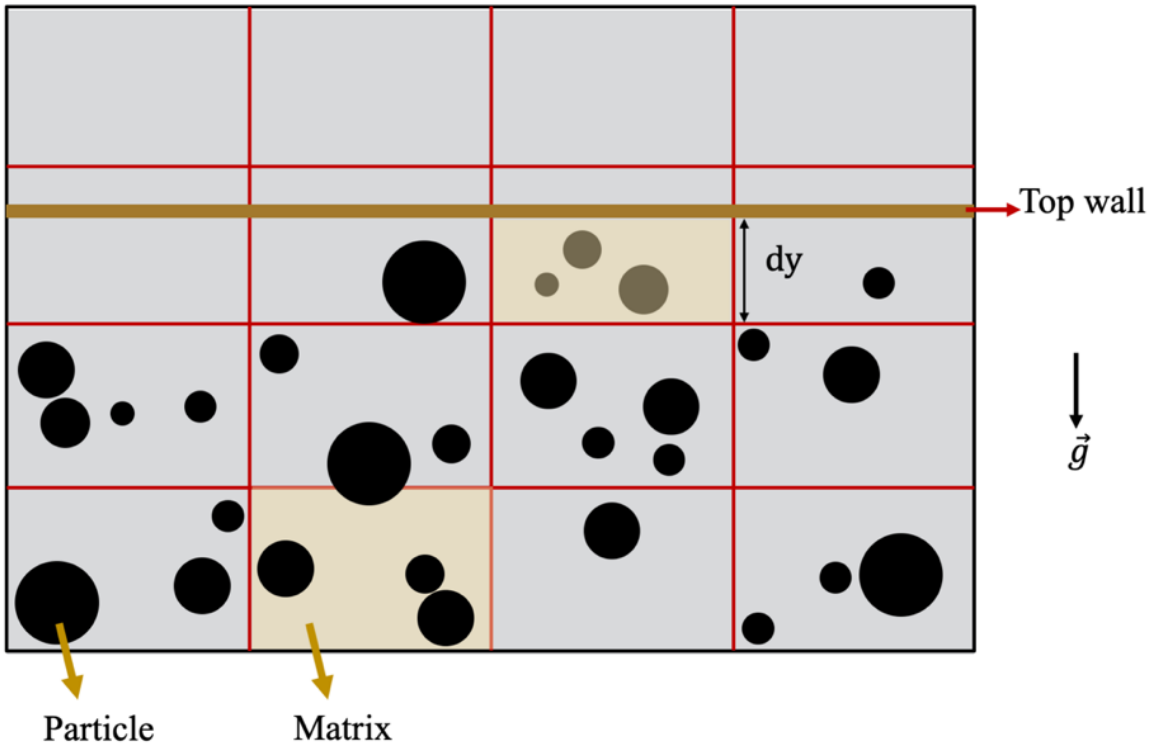

Figure 4.7. Schematic of the simulation domain at an arbitrary time step showing the particles and the computational cells. Some of the cells are far away from the top wall, whereas some are intersected by it. Any partial or whole cell that lies above the top wall does not participate in the squeeze simulation. For cells intersected by the top wall, the local particle volume fraction is corrected by accounting for the actual cell volume.

will be lower due to the reduced volume of the cell. Thus, a correction for local particle (and fluid) volume fraction, $\phi_{p,IJK}$ is needed. That is implemented in the user defined function *usr1_des*. The volume of those cells that are not intersected by the top wall is the cube of side length. In Figure 4.7, two cells are highlighted in light yellow, one of which is intersected by the top wall. The corrected cell volume, $\tilde{\mathcal{V}}_{IJK}$, for this cell is given by $\tilde{\mathcal{V}}_{IJK} = a_{IJK}\, dy\, a_{IJK}$, where a_{IJK} is cell side length (*i.e.*, 5 D_p) and dy is cell height. Then, the local fluid volume fraction is calculated by $\phi_{f,IJK} = 1 - \phi_{s,IJK}$, where $\phi_{f,IJK}$ is local fluid volume fraction.

Finally, the fluid drag force and particle-top wall interaction force are added to the particle force array within *usr1_des*, followed by time integration of forces to compute particle velocity and time integration of velocity to update particle positions. The latter part is dealt within the MFIX source code.

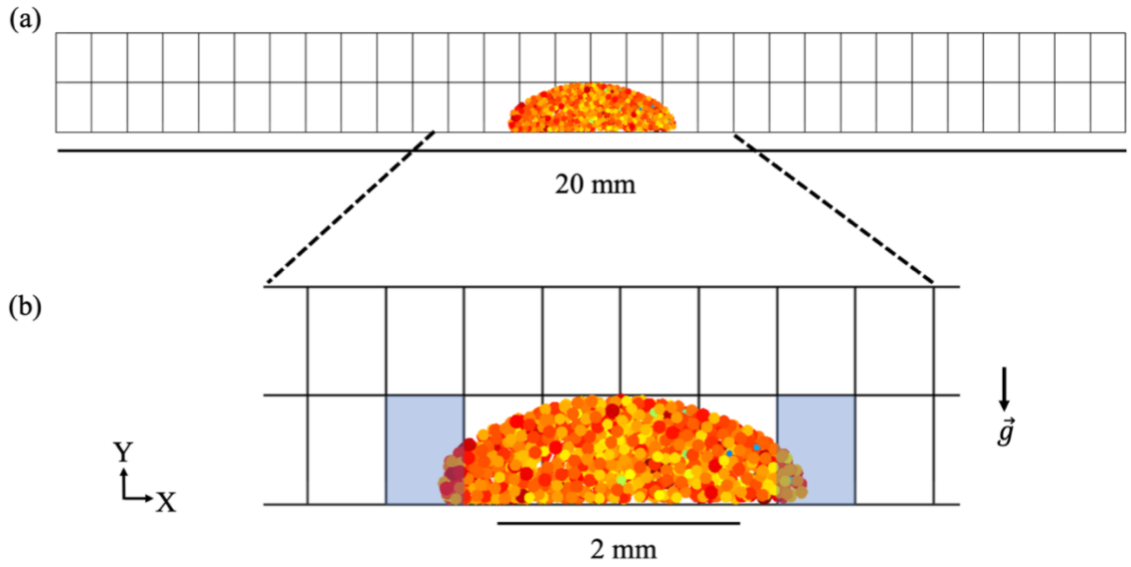

Figure 4.8. Initial particle configuration plotted with rectangular computational cells. MFIX subdivides the simulation domain into these cells based on the domain length and maximum number of cells in X, Y, and Z.

Calculation of the Local Volume Fraction

The computed value of $\phi_{p,IJK}$ will be lower than realistic value especially near the left/right outer edges (*i.e.*, in the highlighted light-blue cells from Figure 4.8 (b)). This can potentially be avoided if the realistic heap shape of the dispense pattern is considered, but that will significantly increase the computational expense. For particles initially positioned within the light-blue cells in Figure 4.8 (b), the drag force will be relatively higher than that for other particles. The drag force will then push these particles outward, and this is a potential cause of lower particle concentration towards the outer edges (see section 4.4).

Calculation of Squeeze Pressure

Squeeze pressure is computed as the ratio of total force acting on the top wall, F_{total}, to the effective cross-section area, A_c. The total force is the sum of particle-top wall interaction force, F_{p-wall} (Eqn. 4.1), and the fluid force, F_{fluid}:

$$F_{total} = F_{p-wall} + F_{fluid} \qquad 4.11$$

where the fluid pressure field, $P_f(x)$ (from Eqn. 4.4) is integrated over the area as

$$F_{fluid} = 2\int_0^{x_{o,f}} P_f(x)\; z_o\; d = 2\int_0^{x_{o,f}} -\frac{6\mu_f V_S}{b^3}\left(x^2 - \frac{\alpha^2}{4}\right) z_o\; dx \qquad 4.12$$
$$= -\frac{12\mu_f V_S}{b^3} z_o\left(\frac{1}{3}x_{o,f}^3 - \frac{\alpha^2}{4} * x_{o,f}\right)\Big|_0^{x_{o,f}=\frac{\alpha}{2}}$$
$$= \frac{8\mu_f V_S}{b^3} z_0 \left(\frac{\alpha}{2}\right)^3 .$$

This integration is performed from the center of the particle-fluid system to the fluid front (*i.e.*, approximated to a distance of $x_{o,f} = \alpha/2$ from the axis of symmetry (see Figure 4.5 (c)). Figure 4.9 shows the evolution of rectangular box bounding the TIM as it is squeezed. The box length is α, whose value is dynamically varying and determined by the fluid front tip-to-tip distance. The fluid front is shown by the black curves. Finally, the effective squeeze pressure, P_s, can be estimated from $P_S = \frac{F_{total}}{A_c}$, where $A_c = z_o\alpha$ is effective cross-section area and z_o is the width into the plane of the page.

4.3.3 Verification of the Squeeze Model

In this section, the squeeze model is verified to show that it is consistent with the laws of physics. The evolution of (a) the maximum overlap between particle and top wall expressed as a fraction of the particle radius, $\delta_{max} = \left(\frac{\delta_{pw}}{R_p}\right)_{max}$, and (b) the polymer fluid front and farthest particle positions are discussed.

For the simulation to be realistic, the vertical height of the particles must be lower than the position of the top wall with a $\delta_{max} < 0.2$ (*i.e.*, the limiting value that MFIX uses to check for significantly

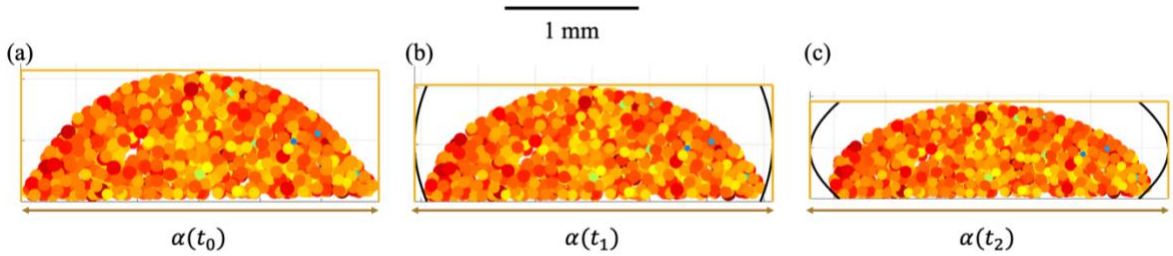

Figure 4.9. Evolution of the fluid width α during a squeeze simulation. The position of the fluid front is shown by the black curves visible in (b, c), whereas in (a) it coincides with the yellow vertical edges of the box. Effective area for squeeze pressure is calculated as $A_c = \alpha\, z_o$, where z_o is width into the plane of the page. The images are taken at x arbitrary time stamps during the squeezing process.

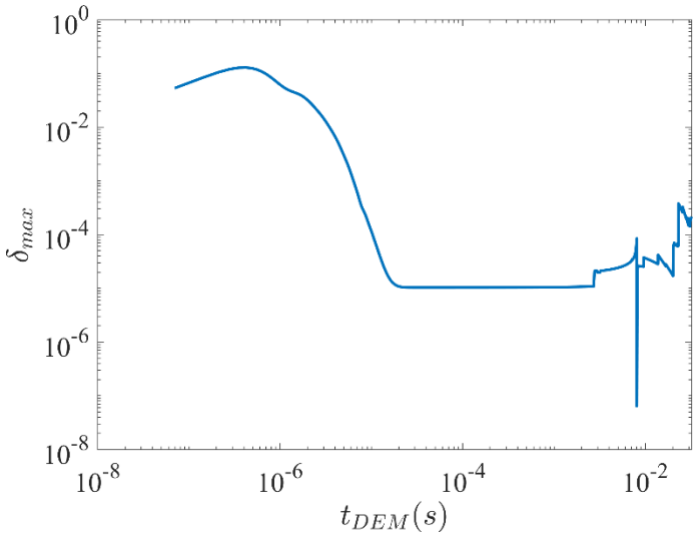

Figure 4.10. Evolution of the maximum overlap-to-particle radius ratio for squeezing at $V_S = 15$ mm s^{-1}. The overlap increases first and then drops. Then, it levels out until the end of simulations, where some variations are observed. Throughout the simulations, $\delta_{max} \ll 0.2$.

large interparticle intersections). In the initial stages of squeezing, occurrence of large overlaps is likely but that will self-correct from the large repulsive forces exerted by the wall on the particles. The likelihood of this occurrence is expected to increase at large squeeze rates. At $V_S = 1$ mm s^{-1}, $\delta_{max} \approx 7.3\%$ and at $V_S = \{5, 10, 15\}$ mm s^{-1}, it is $\approx 12.5\%$. At the end of simulation, $\delta_{max} < 1\%$ for all squeeze rate cases. Figure 4.10 shows the variation of δ_{max} for $V_S = 15$ mm s^{-1}. The low value of δ_{max} is a result of the relatively large value of particle-top wall stiffness, K_{p-w}. This, in turn, ensures that the particles are always below the top wall during squeeze.

The particle positions in the distance from the axis of symmetry (X direction) must be such that the particle is always bound by the fluid. First, based on the initial configuration, the farthest particle along X direction is selected as the reference particle and this particle is tracked during the squeezing process. Figure 4.11 (a) shows the evolution of fluid front profile and the position of the reference particle for five different time stamps from a squeeze simulation at $V_S = 5$ mm s^{-1}. Figure 4.11 (b) plots the time dependent position away from the line of symmetry of the reference particle and that of the fluid corresponding to the height of this particle. It is seen that the fluid front is always ahead of the particle and particles do not abnormally flow out and escape from the fluid. Thus, the analysis in this section verifies the applicability of the Ding and Gidaspow drag model based on the Newtonian assumption for the polymer fluid.

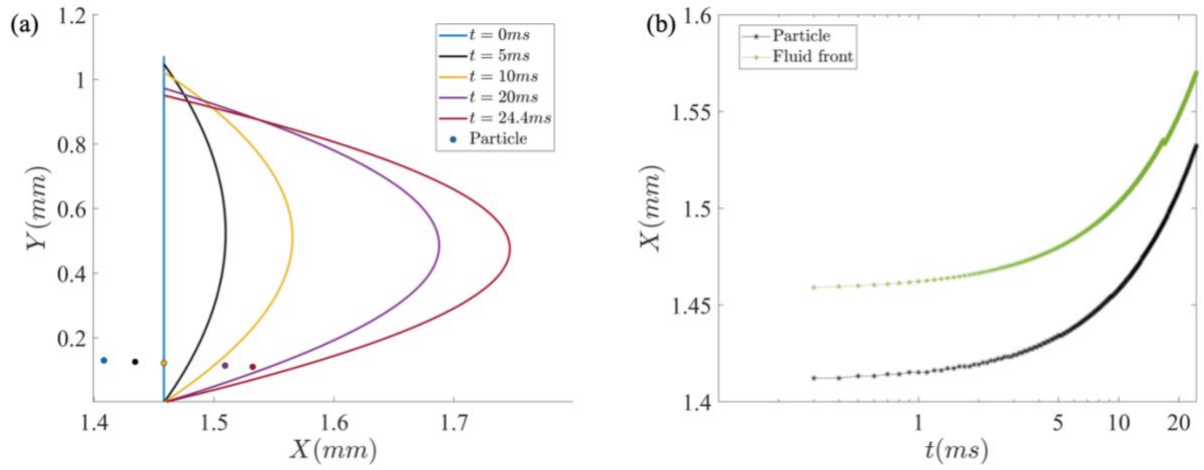

Figure 4.11. Evolution of the (**a**) fluid front profile and (**b**) farthest particle X positions during a squeeze simulation. The filled circles are the positions of the reference particle. Circles are colored the same as that of the fluid front profiles. The plot shows that the particles are always bound by the fluid, as they should be physically. For illustration, only five time stamps are shown in (a).

4.4 Squeezed TIM Microstructural Features

In this section, the predicted microstructure from squeeze simulations are analyzed and compared with experimental data. The simulations are carried out until a critical BLT of two particle diameters is reached. At this BLT, the squeeze pressure is significantly higher than experimental conditions. Then, the desired state of the squeezed TIM microstructure is back-calculated based on the pressure evolution. Experimentally, squeezing in the range of $V_S = 1 - 10$ mm s^{-1}and $F_S = 100$ N resulted in a pressure of $P_S = 171.1 \pm 11.9$ kPa. So, a critical pressure of $P_{critical} = 171.1$ kPa is used. The predicted BLT is the separation distance between the bottom wall of the domain and the top wall at the corresponding state. Squeezing is simulated at various squeeze rates of $V_S = \{1, 2, 2.5, 5, 7.5, 10, 12.5, 15\}$ mm s^{-1}. It is computationally infeasible to simulate squeezing at $V_S < 1$ mm s^{-1} due to the non-parallelized user defined function where a loop is executed to compute local volume fraction for every particle, apply computational cell volume correction based on the top wall position, compute fluid velocity at the particle center, and compute particle-top wall interaction forces. As a result, the code is compiled in serial mode, and only one core from a node ($\approx$ 6.5 GB of memory) in the RCAC supercomputer cluster can be used to execute the simulations. The simulation took a total of $\approx$ 10 hours at the fastest squeeze rate and $\approx$ 13 days at the slowest squeeze rate, and at least two runs to complete the simulations accounting

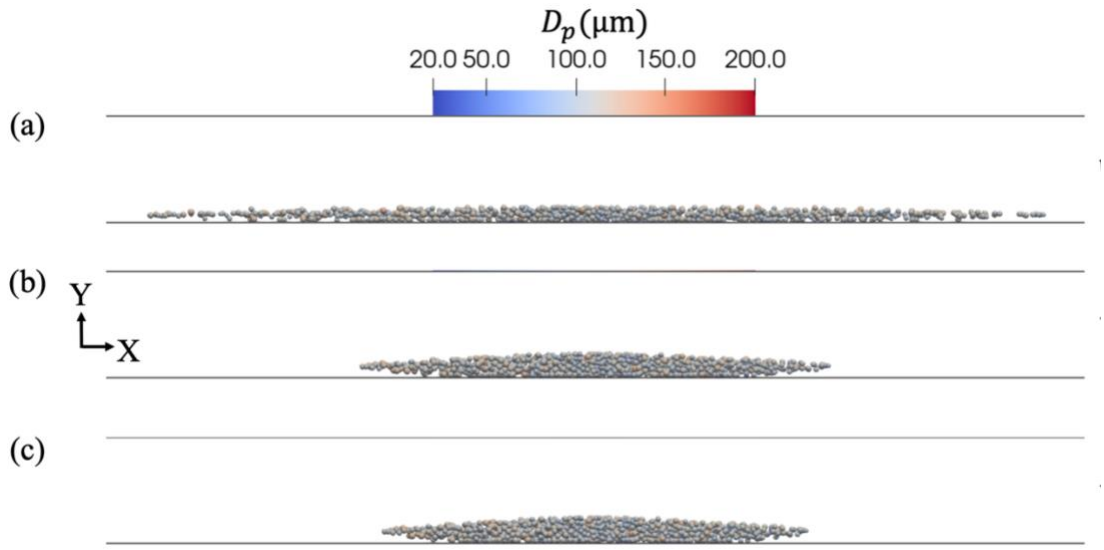

Figure 4.12. Front view of the squeezed state predicted from DEM simulations at three different velocities: (**a**) $V_S = 1$ mm s^{-1}, (**b**) $V_S = 10$ mm s^{-1}, and (**c**) $V_S = 15$ mm s^{-1}. The dispensed TIM configuration obtained from dispensed *Sample 1* is used to simulate squeezing.

for restarts. Restarts are needed when velocity of one particle increases significantly and it exits the domain, causing MFIX to crash.

Figure 4.12 shows front views of the squeezed state for $V_S = \{5, 10, 15\}$ mm s^{-1}. The squeezed state appears bulged near the center for higher V_S, primarily due to the microstructure state being determined by critical pressure, which increases rapidly at higher squeeze rate. Experimentally, the squeezed TIM is macroscopically flat. This observation highlights a potential drawback of the Newtonian assumption for the fluid and the associated pressure calculations.

4.4.1 Predicted BLT, Bulk Particle Volume Fraction and Coordination Number

The predicted BLT monotonically increases with squeeze rate (Figure 4.14) based on simulations using data from *Sample 1* and *Sample 2* dispensed TIMs as the initial configuration. The two microstructures yield similar squeezed state, with a maximum relative difference of ≈ 2.5%. It appears to exhibit a tendency to flatten beyond $V_S = 15$ mm s^{-1}, owing to bulging of the microstructure noted in the preceding section. Simulations are not conducted for $V_S > 15$ mm s^{-1} in this work as there will be significantly more bulging near the center of the microstructure that is unrealistic. The two initial configurations used in the squeezing simulation consist of 966 and 1070 particles, respectively.

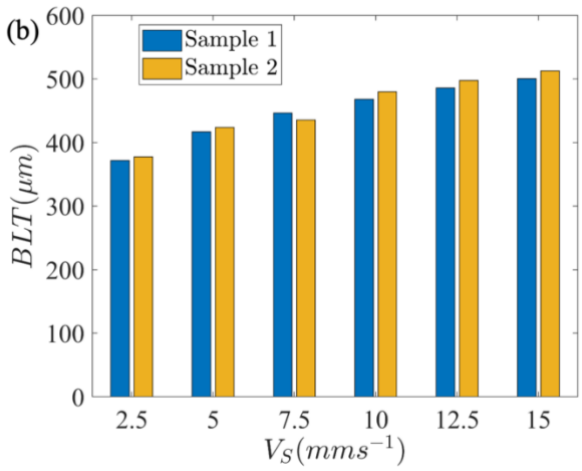

Figure 4.14. Predicted BLT vs squeeze rate, V_S for squeezing of *Sample 1* and *Sample 2* dispensed TIMs across a range of squeeze rates, V_S. BLT increases monotonically with squeeze rate in this modeling framework.

The predicted bulk particle volume fraction, ϕ_p, and coordination number, C_N, are compared for these two sets of simulations in Figure 4.13. The maximum relative difference in ϕ_p is $\approx 2.7\%$ and the maximum relative difference in C_N is 12.5%. This suggests that there are no significant microstructural differences between these two sets of simulations. Note that squeezing simulations with initial configuration from *Sample 2* dispensed TIM are conducted only in the range of $V_S = 2.5 - 15$ mm s^{-1} due to the computational time expense at the lowest squeeze rates. In the subsequent analyses, data from *Sample 1* squeezing simulations are considered.

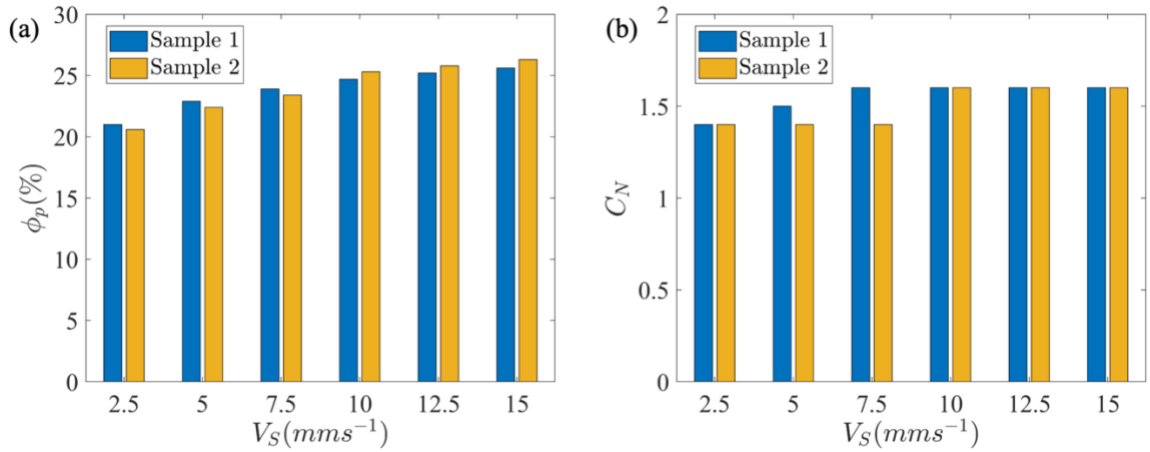

Figure 4.13. Predicted (**a**) bulk particle volume fraction, ϕ_p, and (**b**) coordination number, C_N, across a range of squeeze rates, V_S, for squeezing of *Sample 1* and *Sample 2* dispensed TIMs. ϕ_p is computed via the convex hull method described in Chapter 3.7.1.

Figure 4.15 plots the variation of ϕ_p and C_N for squeezed TIM microstructure obtained by squeezing at various velocities and up to a pressure of $P_S = 171.1$ kPa, starting with the dispensed TIM *Sample 1* configuration. At slower squeeze rates, the squeeze model predicts more spreading and, thus, lower ϕ_p and C_N. More spreading occurs at lower squeeze rates because the fluid pressure increases at a slower rate compared to that during fast squeezing. Since the desired end state is determined by the pressure, this provides more time for the particles to spread out at slower squeeze rates. The observed increase in ϕ_p and C_N with squeeze rate is attributed to bulging near the center where neighboring particles are closer. To emphasize again, this is an effect of the Newtonian assumption of the fluid velocity profile. As V_S increases in the simulations, pressure increases at a faster rate and the predicted microstructure will possess an apparent higher BLT, ϕ_p and C_N.

Bulk properties of Central vs Center-Edge subdomains

In this section, ϕ_p and C_N, are analyzed for Center-Edge and Central subdomains (see Figure 4.16) from squeezing simulations of *Sample 1* dispensed TIM to further understand the variation in ϕ_p and C_N. Center-Edge subdomain is consistently chosen, that is, particles lying in the positive X direction. The Central subdomain consists of particles lying in a section of 10 $D_{p,m}$ in length, where $D_{pm} = D50 = 106.5$ µm for *Sample 1* (see Table 3.7). Note that the width of the microstructure along Z is ≈ 5 $D_{p,max}$ where $D_{p,max}$ is the maximum particle diameter extracted from image processing of the XRCT image dataset.

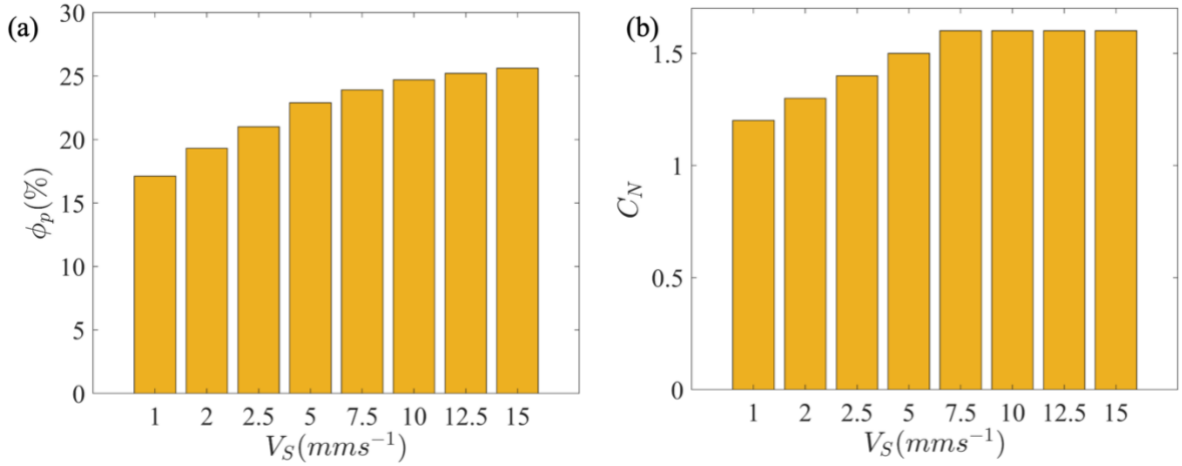

Figure 4.15. Predicted (**a**) bulk particle volume fraction, ϕ_p, and (**b**) coordination number, C_N, across a range of squeeze rates, V_S, for squeezing of the dispensed TIM *Sample 1*.

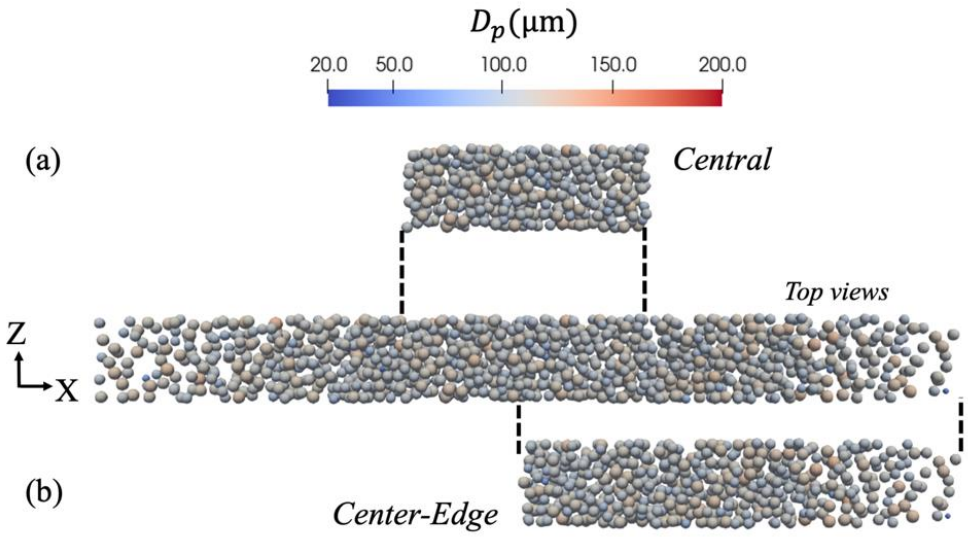

Figure 4.16. Whole TIM predicted microstructure (center image) with (**a**) Central and (**b**) Center-Edge subdomains. The Central region is a section of length 10 particle diameters, whereas the Center-Edge region is the right-half subdomain.

Figure 4.17 shows that the bulk particle volume fraction and coordination number for Central (C) subdomain is significantly higher than that of Center-Edge (CE) subdomain. This means that, with the one-way particle fluid coupling model used in the squeeze simulations, there is a higher concentration of particles near the axis of the line dispense pattern. Drag force was insufficient to carry away these particles during the squeeze process. Instead, particles near the edges of the initial dispense pattern were dragged away by the fluid. The difference in volume fraction between C and CE subdomains decreases at higher squeeze rates due to bulging of the microstructure.

4.4.2 Radial Distribution Function (RDF) and Local Particle Volume Fraction

In this section, the RDF, $g(r)$, and local particle volume fraction, $\phi_{p,local}$, are analyzed for the simulated microstructures based on the initial configuration corresponding to *Sample 1* dispensed TIM. Figure 4.18 shows the RDF for Central and Center-Edge subdomain microstructures compared with the dispensed TIM initial configuration (with 966 particles) for the simulation. The plot is shown only for $V_S = \{1, 5, 10, 15\}$ mm s^{-1}.

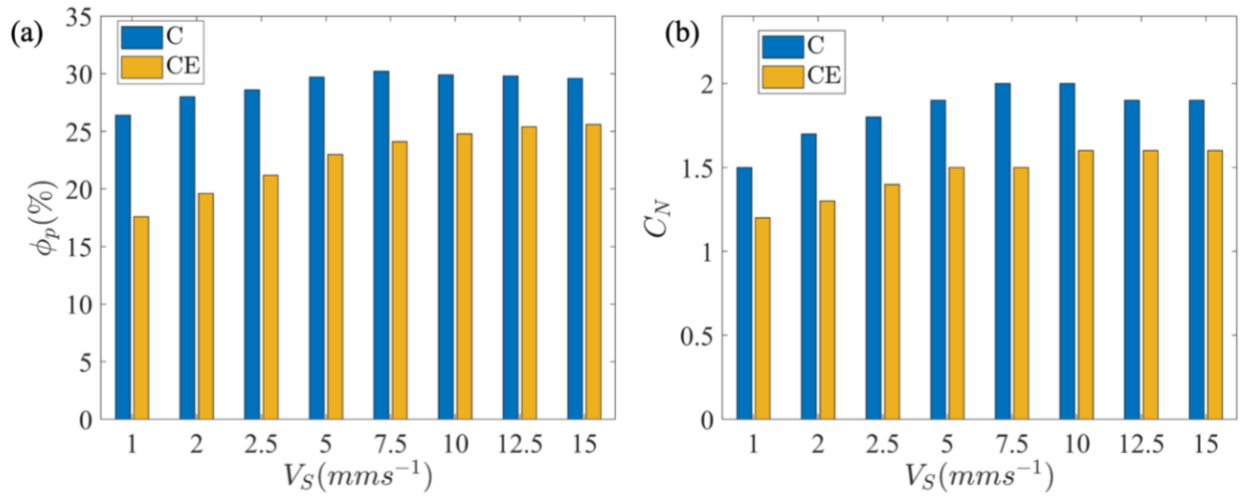

Figure 4.17. Variation of the predicted (**a**) bulk particle volume fraction, ϕ_p, and (**b**) coordination number, C_N, analyzed for the Central (C) and Center-Edge (CE) subdomain microstructures.

The first peak in the RDFs occurs at approximately the same radial distance for all subdomain microstructures. The first peak is lower for the dispensed TIM compared with that of C or CE subdomain microstructures. Note that the dispensed TIM RDF corresponds to that of the *normal box* configuration (see Figure 3.45 (b)). Artifacts are potentially induced by the RDF computation methodology. As noted in chapter 3.7.2, a rectangular box is constructed around the given microstructure in the RDF analysis. This box may have significant void space that is not occupied by the TIM, especially with CE subdomain microstructures. Although, the RDF analysis method corrects for the spherical shell-box intersection volume, the additional void space in the box cannot

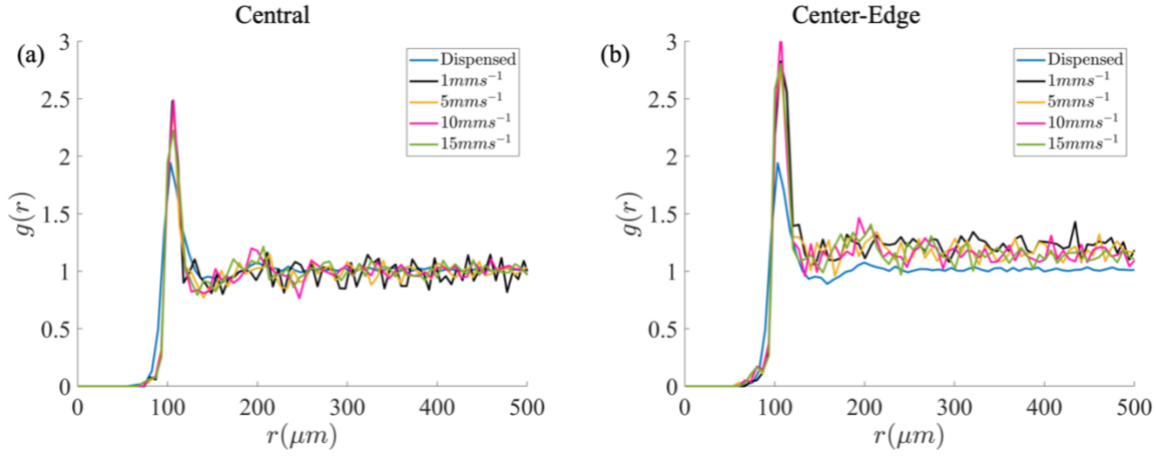

Figure 4.18. RDF, $g(r)$, of the predicted squeezed TIM subdomain microstructures: (**a**) Central (C) and (**b**) Center-Edge (CE), at a few different squeeze rates $V_S = \{1, 5, 10, 15\}$ mm s^{-1} compared with the dispensed TIM initial configuration.

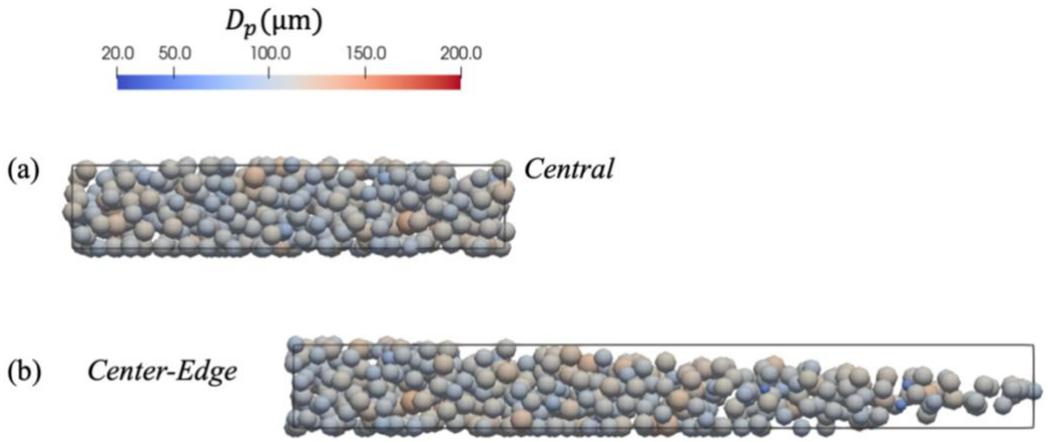

Figure 4.19. Rectangular box constructed around the (**a**) Central and (**b**) Center-Edge subdomain microstructures from a simulation with $V_S = 15$ mm s^{-1}. This box is used in the RDF computation.

be accounted for. Without the void correction, the RDF cannot be interpreted appropriately. This is illustrated in Figure 4.19 for C and CE subdomain microstructures generated at squeeze rate $V_S = 15$ mm s^{-1}. The void space is evident in Figure 4.19 (b) and the impact is relatively more significant at higher squeeze rates.

A second peak in the RDF is not discernible and there appears to be noise as it fluctuates about $g(r) \approx 1$. These fluctuations may be attributed to small sample size. In the C and CE subdomains, respectively, there were 228 and 482 particles at the slowest squeeze rate, and 402 and 484 particles at the fastest squeeze rate. Overall, the TIM microstructures are disordered. A major learning is that unlike numerous existing simulation research works, where RDF and other microstructural properties are computed on rectangular microstructure domains (usually with periodic boundary conditions), working with microstructures that are generated with an experimentally measured initial configuration pose difficulties in analyzing basic properties. Working with larger microstructures, both experimentally measured and simulated, can help in analyzing rectangular subdomains.

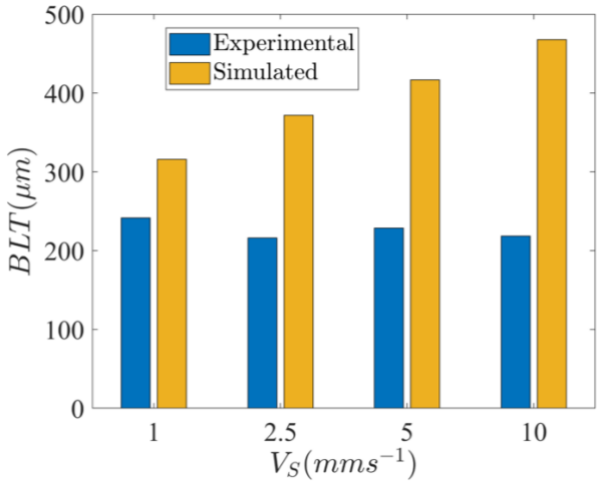

Figure 4.20. Comparison of measured and predicted BLT of the squeezed TIM for a range of squeeze rates. In experiments, the maximum force is set to $F_S = 100$ N. The top wall pressure in the predicted squeezed state corresponds to the experimental pressure.

4.5 Comparison with Experimental Data

In this section, the basic microstructural features of experimental and simulated data are compared for squeeze rates in the range of $V_S = \{1, 10\}$ mm s^{-1} and squeeze force $F_S = 100$ N. Since XRCT imaging is time consuming and expensive, the metrics of interest (ϕ_p, C_N, and RDF) are compared only for the slowest and fastest squeeze rates. Note that it does not make much sense to compare higher squeeze rate predictions with experimental data since a bulging near the central portion of the microstructure was observed in the simulations that was not observed experimentally. The BLT is compared across a range of squeeze rates (see Figure 4.20). The disagreement in BLT

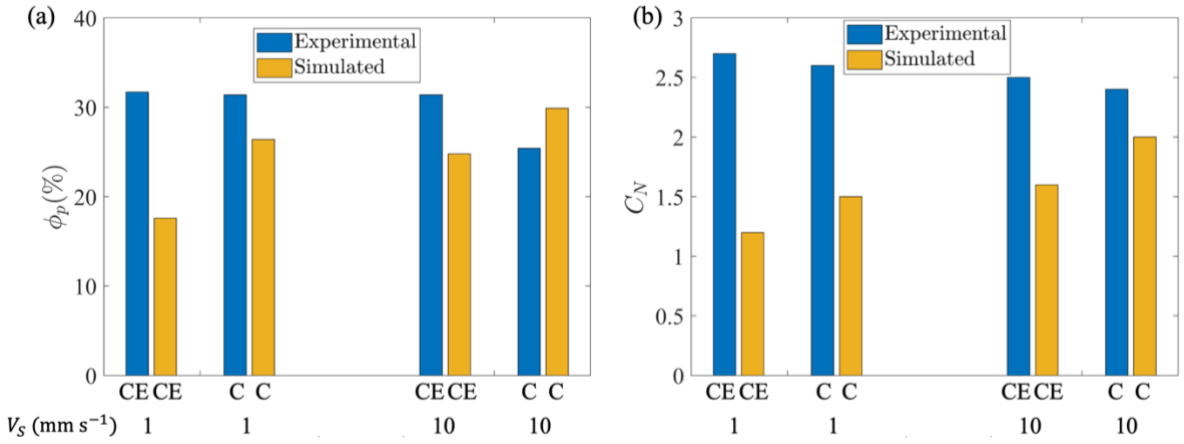

Figure 4.21. Comparison of ϕ_p and C_N for the experimental and simulated squeezed TIM, computed for the Central (C) and Center-Edge (CE) microstructures. In experiments, the maximum force is set to $F_S = 100$ N. Simulations are carried out up to a critical squeeze pressure that corresponds to the pressure in experiments.

at the slowest squeeze rate is $\approx 30.8\%$. This increases at higher squeeze rates. The microstructural properties, ϕ_p and C_N, do not agree well between experimental and simulated data (see Figure 4.21). For each squeeze rate, the values for the C and CE subdomains originate from a single simulation. However, in experiments, the C and CE squeezed TIM microstructures are independently analyzed via XRCT imaging from two separate samples produced in a single squeeze test (*i.e.*, at a given squeeze rate).

Evaluation of Other Drag Models

Squeezing simulations are performed at $V_S = 10\ \text{mm s}^{-1}$ using other well-known drag models: the BVK model developed by Beetstra *et al*. [224] and Koch Hill model by Hill *et al*. [225]. Both these models are derived using lattice-Boltzmann simulations of fluid flow through particle packing, whereas the Ding and Gidaspow model is based on empirical correlations. The BVK and Koch Hill drag models, respectively, are derived from simulations of fluid flow through (a) monodisperse and bi-disperse random sphere packing, and (b) simple cubic, face-centered cubic and random packing of spherical particles. The predicted bulk particle volume fraction and coordination number in these two cases, compared with the Ding and Gidaspow model is $\phi_p = 24.7\%$ and $C_N = 1.6$ with negligible differences.

Figure 4.22 shows the RDF of the squeezed TIMs predicted using these drag models at $V_S = 10\ \text{mm s}^{-1}$. The three different drag models resulted in statistically similar microstructures.

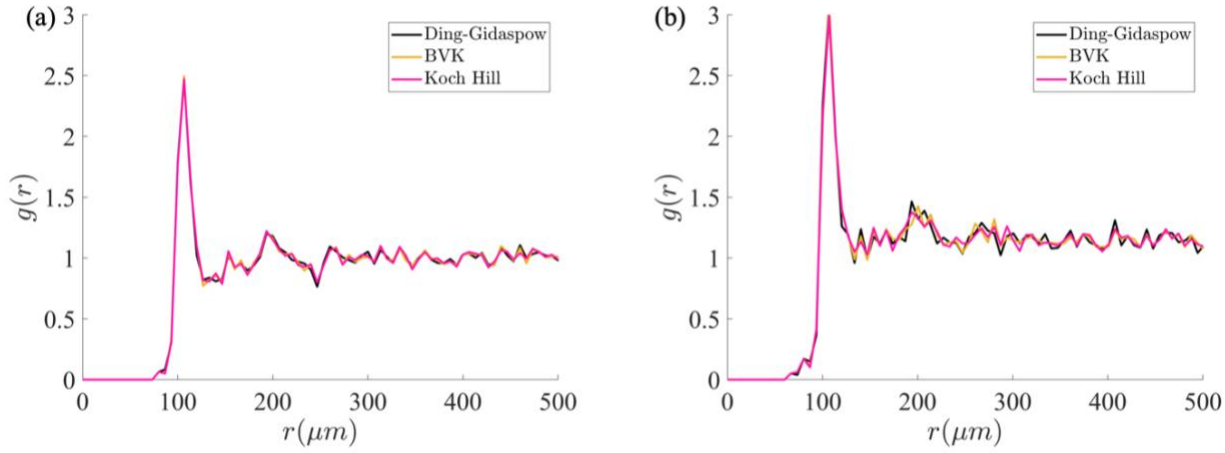

Figure 4.22. Comparison of the RDF ($g(r)$) for (a) the Central (C) and (b) the Center-Edge (CE) subdomain microstructures of the predicted squeezed state for simulations at squeeze rate $V_S = 10\ \text{mm s}^{-1}$.

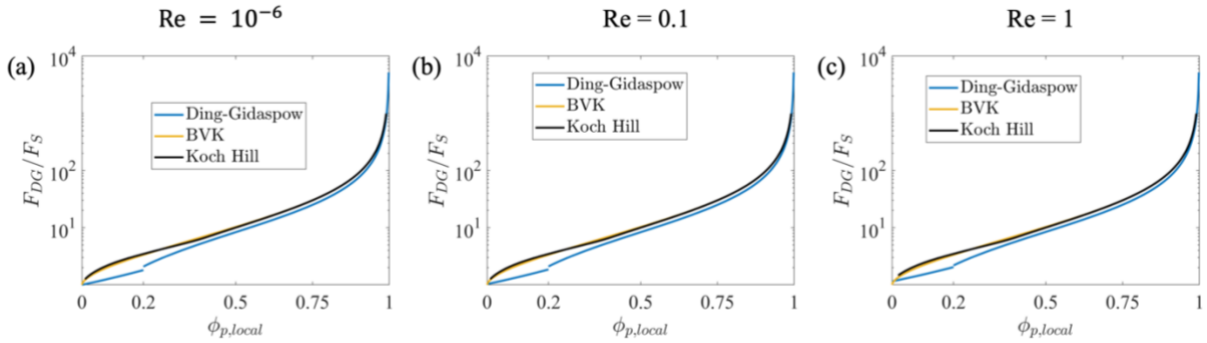

Figure 4.23. Normalized drag force, $\frac{F_{DG}}{F_S}$, versus local particle volume fraction, $\phi_{p,local}$, for three different models at various Reynolds numbers: (**a**) $Re = 10^{-6}$, (**b**) $Re = 0.1$ and (**b**) $Re = 1$.

Statistically similar microstructures suggest equivalent drag forces on the particles. So, the drag force variation with local volume fraction is compared for the Ding and Gidaspow, BVK and Koch Hill models in Figure 4.23 illustrating that there is no significant impact of the differing correlations on the magnitude of drag force on particles at various Reynolds numbers. Therefore, squeezed states with almost exactly same bulk properties are predicted using these drag models.

4.6 Concluding Remarks

Constant velocity squeezing simulations are developed to predict the microstructure of the squeezed TIM using as input the experimentally measured dispensed TIM configuration. The capabilities of open-source DEM software package MFIX are further expanded by building UDFs. The polymer matrix is assumed to exhibit Newtonian behavior and its velocity profile and pressure are analytically computed. Using that, the particles and fluid are one-way coupled via drag forces. Simulations are conducted at various squeeze rates and it ends when the top wall pressure attains a prescribed critical value.

In the range of squeeze rate of $V_S = 2.5 - 15$ mm s^{-1} and critical pressure $P_{critical} = 171.1$ kPa, the predicted BLT monotonically increases with squeeze rate for two different initial configurations with a maximum relative difference of $\approx 2.5\%$. There are also no significant differences in the predicted ϕ_p and C_N from squeezing these two configurations and that is expected as it is shown in chapter 3 that these two dispensed TIM microstructures are statistically equivalent. At the slowest squeeze rate, $\phi_p = 17.1\%$ and at the fastest rate, $\phi_p = 25.6\%$, while

the coordination number gradually increases from 1.2 to 1.6. These variations are likely a limitation arising from the Newtonian assumption and one-way fluid and particle coupling. The analytically derived fluid pressure exerted on the top wall rapidly increases with squeeze rate. That resulted in bulging of the TIM microstructure near the center, whereas the particles near the edge are carried away by the fluid drag force as there is negligible resistance from collision with neighboring particles. Therefore, for a fixed pressure, the predicted BLT increases with squeeze rate and, for a fixed BLT, the predicted pressure is higher than that is experimentally observed. The RDFs exhibit characteristics of disordered microstructures because it fluctuates about $g(r) = 1$ right after the first peak. However, as noted in the previous sections, the RDF computation must be re-evaluated due to the presence of void regions within the rectangular microstructural bounding box. The agreement between experimental and simulated data is poor based on the analysis of the BLT, ϕ_p and C_N of C and CE samples. The best case disagreement in BLT is $\approx 30.8\%$ at $V_S = 1$ mm s^{-1}.

Future work should derive the velocity profile based on the Herschel-Bulkley non-Newtonian model for better predictive capability. This would still involve a homogenization, but can potentially be a better estimate of the fluid flow profile. In reality, local fluctuations in the flow may be induced by the high filler particle loading (*e.g.*, in commercial TIMs) and as the BLT approaches a few particle diameters. The polymer fluid then flows through the interparticle networks or chains. This effect is neglected in the current work and may be captured via a two-way momentum coupling between the particles and fluid. The fluid velocity profile is then not known a priori but solved for during the squeezing simulation. Although complex to implement and computationally expensive, this may potentially provide accurate insights into the particle redistribution after squeezing.

5. THERMAL CONDUCTION MODELING IN TIMS

5.1 Introduction

The desired thermal characteristics of TIMs are high bulk conductivity and low total thermal resistance. Prior work has shown that squeezed TIM microstructure is a function of the application parameters: the BLT is governed by the applied squeeze pressure and particle rearrangement is governed by squeeze velocity. This in turn can impact thermal conduction. Specifically, the microstructure of heterogeneous media correlate with effective macroscopic properties (such as thermal conductivity, electrical conductivity, or elastic modulus). But there is no standard approach for predicting such properties from microstructural metrics with accuracy. In this chapter, heat conduction models are developed for predicting the TIM bulk thermal conductivity starting from the microstructural details quantified experimentally and computationally in the previous chapters. Specifically, the network thermal model and a finite element (FE) thermal conduction model are evaluated.

5.2 Network Thermal Model

The fundamentals of this steady-state numerical modeling framework were discussed in chapter 2.3.1. Particle position, size, and particle and matrix conductivities are the main inputs to the network thermal model. Since copper was used in the experiments, a thermal conductivity of $k_p = 400\ \mathrm{W\ m^{-1}\ K^{-1}}$ is set as the particle conductivity in the model and a conductivity of $k_m = 0.13\ \mathrm{W\ m^{-1}\ K^{-1}}$ for the polymer. In Kanuparthi *et al.* [65], a value of 0.5 was used for both the radius tolerance parameter (ε_T) and radius tolerance parameter (α_T). The parameter ε_T was estimated based on the matrix exclusion probability [74] of simulated microstructures in their study, and the value of the latter parameter was chosen to yield the best match to higher fidelity thermal simulations that the authors had earlier developed [73]. These two parameters, together with the particle positions and sizes are used to compute effective thermal conductance of interparticle thermal contacts, which when combined in a matrix form yields the global conductance. Constant temperature (Dirichlet) boundary conditions are applied on two opposite faces (*i.e.*, along the through-thickness direction) with values of $T_C = 300\ \mathrm{K}$ and $T_H = 400\ \mathrm{K}$. The boundary

temperature choice is arbitrary as the final prediction of conductivity will not be affected by its magnitude.

Verification of Network Thermal Model

A simple cubic arrangement of spheres ($\phi_p \approx 52.4\%$) of diameter $D_p = 100$ μm (arbitrarily chosen) was first investigated to verify that the model predicts physically acceptable values of the bulk thermal conductivity. The thickness of the ordered packing is 3 particle diameters, thus resembling that of the experimentally measured microstructures. A grid of N_S x N_S number of particles are parametrically varied from $N_S = 3 - 15$. The ordered packing with $N_S = 15$ is shown in Figure 5.2. The variation of predicted conductivity for the ordered sphere packing, k_{TIM}, with N_S is shown in Figure 5.2. Here, $\alpha_T = 0.5 \; and \; \varepsilon_T = 0.5$. There is an initial drop from $k_{TIM} \approx 6.7$ W m^{-1} K^{-1} likely associated with smaller system size. Then, k_{TIM} saturates to around ≈ 5.3 W m^{-1} K^{-1} as N_S increases. Overall, the predictions make physical sense, that is $k_m < k_{TIM} < k_p$. In all cases, it is verified that the difference in heat flow in to and out of the system is negligible, verifying steady-state nature. Therefore, the network model constructed based on prior work is verified.

Prediction of the Bulk TIM Thermal Conductivity

To apply boundary conditions, the top and bottom layer of particles must be identified. To do so, the particle positions along the bond line (*i.e.*, Z) direction are examined with the help of histogram, and the boundary particles are selected based on user-input position percentiles, for instance <2.5% and >97.5%. That is, particles with Z-coordinates below the lower (p_l) or above the upper (p_u)

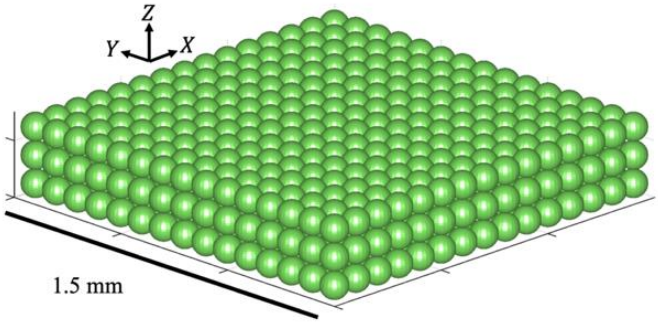

Figure 5.1. Simple cubic packing of spherical particles of diameter $D_p = 100$ μm. The packing fraction is $\phi_p \approx 52.4\%$. Here, the XY plane consists of a 15 x 15 grid of spheres.

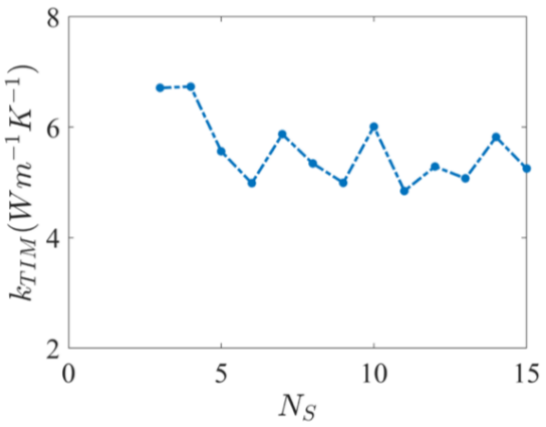

Figure 5.2. Variation of bulk thermal conductivity, k_{TIM}, of simple cubic packing with N_S, the number of spheres along one side of the XY plane. The thickness of the packing is three particle diameters. The predicted conductivity is an order of magnitude higher than matrix conductivity.

percentiles are labeled as boundary particles, and these particles are assigned a temperature of T_C and T_H, respectively. The remaining particles constitute the bulk of the material. All other boundaries are assumed to be insulated. Then, the heat flowing in to and out of the TIM microstructure are computed and, to verify that the steady-state assumption holds good, the net heat flow is calculated and verified to be numerically equal to zero. The main challenge encountered here is boundary particle assignment.

Using the network model, the bulk TIM conductivity is over predicted for high α_T and high ε_T, and underpredicted otherwise. Higher values of ε_T may not make physical sense. That is, a particle near the bottom surface (see Figure 5.4) cannot interact with a particle near the top surface. These two parameters are varied between 0 and 0.5 at fixed position percentiles, and $k_{TIM} \ll k_m$ for all cases. For fixed $\alpha_T = \varepsilon_T = 0.5$, the predicted conductivity for the sample shown in Figure 5.4 is $k_{TIM} \approx 0.04\ \mathrm{W\ m^{-1}\ K^{-1}} \ll k_m$ with $p_l = 2.75\ and\ p_u = 97.5$. By increasing the width of the position percentiles to $p_l = 5\ and\ \ p_u = 95$, $k_{TIM} \approx 0.07\ \mathrm{W\ m^{-1}\ K^{-1}}$. The network model is insufficient to accurately predict the TIM through-plane conductivity, owing to its inability to model heat conduction in the bulk of the matrix phase and due to the difficulty in selecting boundary particles. The boundary particle selection is easier for in-plane thermal computations due to higher "thickness", and the network model predicted sensible values of bulk thermal conductivity in the range of $3 - 5\ \mathrm{W\ m^{-1}K^{-1}}$ (see Figure 5.3). Thus, the through-plane conductivity predictions are expected to improve for samples with higher BLT which makes the

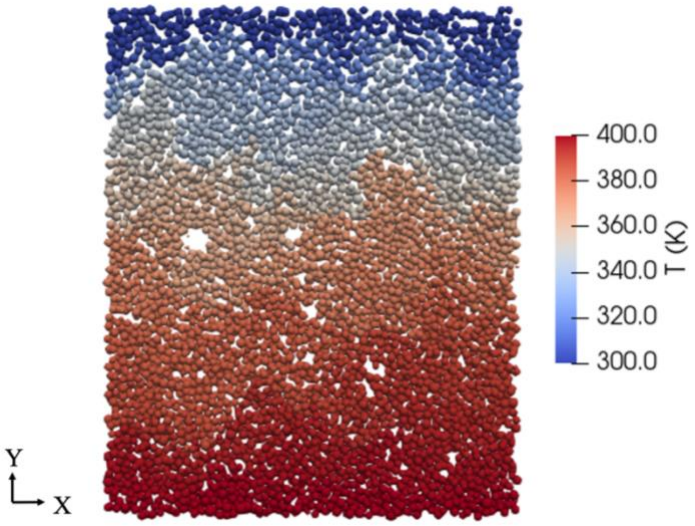

Figure 5.3. Predicted in-plane temperature profile for a squeezed TIM sample using the network thermal model.

boundary particle assignment easier. Note that the predicted in-plane conductivity is not of primary interest and, moreover, may not be accurate due to neglecting heat conduction in the matrix phase. In the next section, a finite element thermal conduction model that is capable of modeling heat conduction in both particle and matrix phases is presented.

5.3 Particle Geometry-based Finite Element Thermal Model

A finite element (FE) thermal conduction model is developed to predict the TIM bulk cross-plane thermal conductivity by accounting for heat conduction within the particles as well as the polymer matrix. In principle, this methodology should predict heat conduction within the TIM more

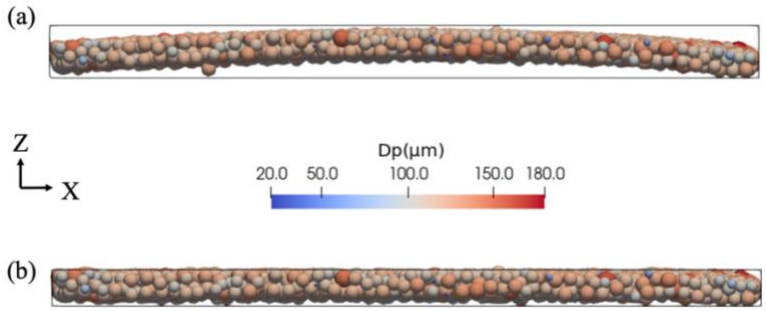

Figure 5.4. (**a**) Curved geometry of the squeezed TIM resulting from sample preparation. (**b**) Flattened TIM sample. Particles in (a) are displaced downward to flatten the microstructure. This is a Central sample produced at $V_S = 10$ mm s^{-1} and $F_S = 100$ N.

accurately than the network thermal model. Solving for thermal conduction involves building the TIM geometry, that is the particles and matrix phases, and then solving for steady-state heat conduction in the material. Particle locations and sizes, which were extracted by processing the 3D XRCT images in section 0, are imported to COMSOL Multiphysics using the LiveLink™ for MATLAB® feature. Then, a tight-bounding rectangular box is constructed around the particles to represent the matrix phase. The box side lengths are calculated based on extrema particle positions and their diameters. The TIM microstructure is flattened prior to thermal modeling by displacing particles along the *Z* direction to approximately equalize their position with that of the edge particles. This algorithm is implemented in small particle regions of size ~0.5 mm x ~0.5 mm. During the flattening process, it is assumed that the in-plane displacement is small and negligible. For some of the TIM samples, a few particles from near the central region are deleted to ensure appropriate flattening. The *Z* position of the deleted particles is approximately equal to that of the edge particles, thus they would not enable flattening of particles in their vicinity. In all cases, $< 0.5\%$ of particles (by number) are deleted. This is not expected to significantly impact the predicted thermal conductivity.

Meshing the particle or matrix domains is challenging due to three primary reasons (see Figure 5.5):

(a) small intersection region between neighboring particles, relative to their diameter,
(b) narrow region created when multiple particles are in close proximity, but not touching or intersecting each other, and
(c) narrow region between particle and rectangular bounding box.

The narrow region between particles (Figure 5.5 (b)) was also observed by Lee *et al.* [140], whereas the intersecting regions and narrow edge regions are observed specifically in this work. The overlapping particles are generally a result of spherical shape idealization from 3D image processing of XRCT data. That is, the equivalent sphere volume diameter approximation for the detected objects from 3D XRCT image datasets may cause two neighboring objects, that are not physically intersecting, to overlap. The narrow edge regions are a result of tight bounding box construction around the TIM. In these cases, the mesh quality must be enhanced in the narrow regions, resulting in significantly smaller mesh element size and a larger number of mesh elements.

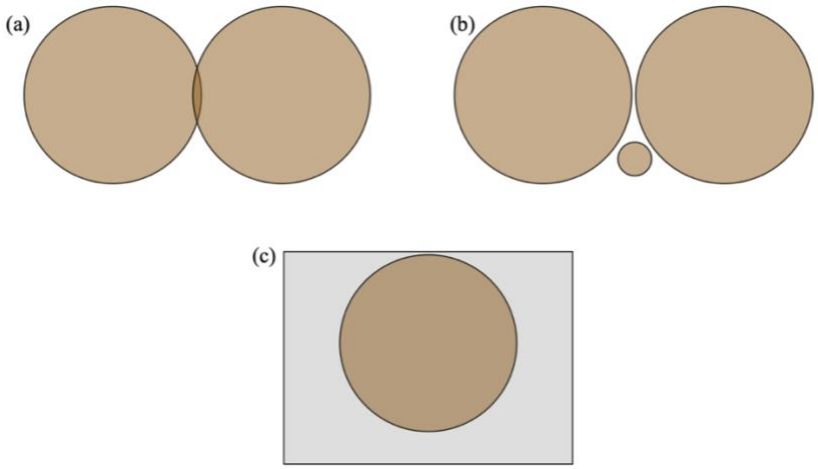

Figure 5.5. Schematics of the TIM particles showing regions where meshing can potentially become a heavy computational expense. (**a**) Intersecting neighboring particles, (**b**) multiple particles in close proximity and (**c**) edge particle surface near the bounding box.

Meshing will then be computationally expensive and, in turn, it increases the overall computational expense.

To overcome the meshing issue, especially for particles that overlap or are in close proximity, a particle size reduction method, similar to that of Lee *et al*. [140], enables estimation of the composite thermal conductivity. In this approach, thermal conduction is solved for TIMs with artificially reduced particle diameters (Figure 5.6). This is executed based on a particle diameter reduction factor, χ, and fourteen models are solved for parametrically varying values of χ, where $\chi \in [0.3,\ 0.99]$. In Figure 5.6, L_1 and L_2 are the bounding box side lengths determined by the particle locations and their true diameter. Particle size reduction does not impact the box size because the main purpose of this methodology is to circumvent meshing issues. Physically, this

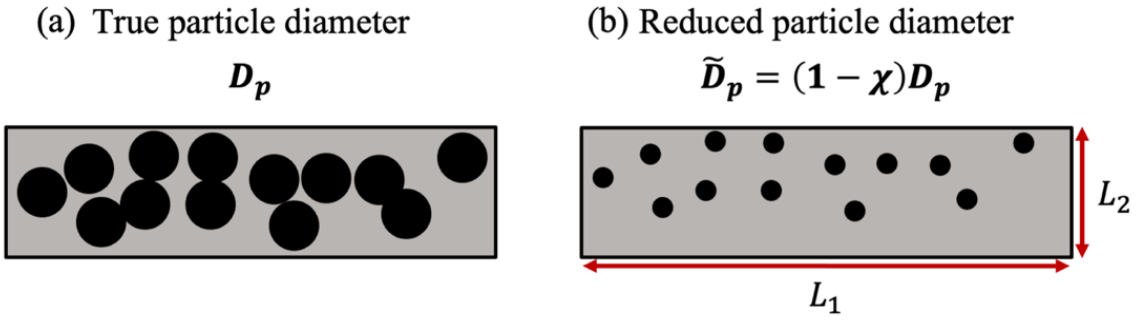

Figure 5.6. 2D schematic of the particle size reduction method showing the TIM with (**a**) true and (**b**) reduced particle diameters. L_1 and L_2 are the bounding box side lengths that are fixed based on the true particle locations and size.

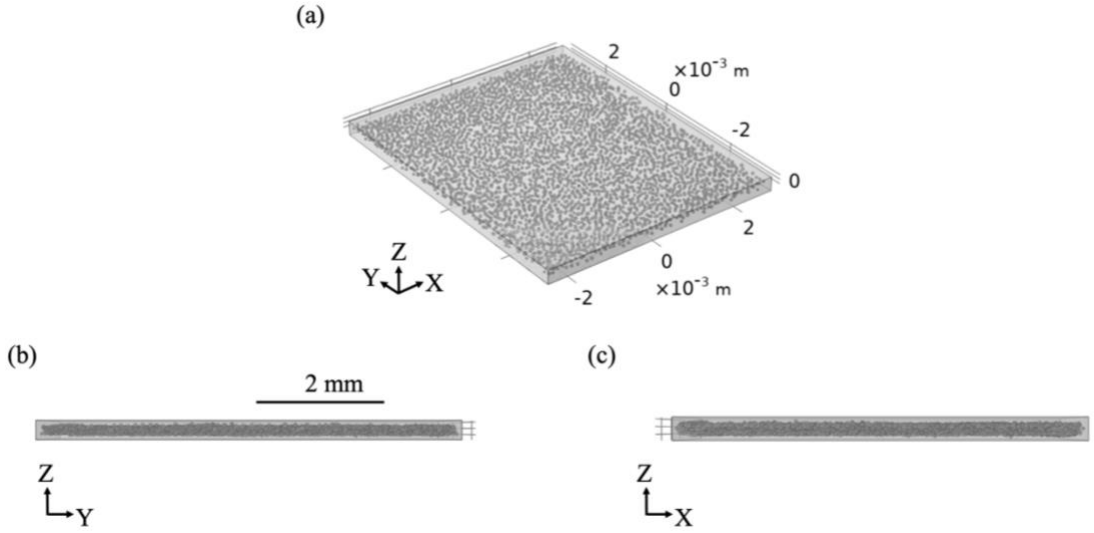

Figure 5.7. TIM microstructure constructed in COMSOL.

methodology does not affect the overall system size. Otherwise, k_{bulk} would exhibit a dependence on the TIM thickness which will then impact the prediction.

5.4 Model Construction and Analysis

The largest rectangular subdomain of particles that was used in the local volume fraction analysis in section 3.7.3 is used here in the thermal models. Figure 5.7 shows the geometry of a Central sample (produced at $V_S = 10$ mm s^{-1}, $F_S = 50$ N) constructed in COMSOL. Thermal conductivities of $k_p = 400$ W m^{-1} K^{-1} for the particles and $k_m = 0.13$ W m^{-1} K^{-1} for the matrix are assigned. Constant temperature boundary conditions of $T_H = 400$ K at the bottom and $T_C = 300$ K at the top surfaces of the polymer material (along Z direction) are set. Particle-polymer interface thermal resistance is neglected. Tetrahedral meshes are generated for all microstructures using the "Extra fine" built-in feature in COMSOL and default solver configurations are used. The number of mesh elements, for instance, in one of the microstructures (produced at $V_S = 10$ mm s^{-1} and $F_S = 100$ N) is 30.5 million at $\chi = 0.3$ and 28.9 million at $\chi = 0.99$. Solving each model takes approximately an hour, and completing the parametric variation for a given microstructure takes about 15 hours using the RCAC resources (128 GB memory). As $\chi \to 0$, the particle sizes approach their true value ($k_{bulk} \to k_{TIM}$), and as $\chi \to 1$, the particles vanish, thus leaving behind the matrix phase ($k_{bulk} \to k_m$). Bulk thermal conductivity, k_{bulk}, is predicted for each size reduction factor from:

$$k_{bulk}(\chi) = q"_{avg} / \frac{dT}{dz}, \quad 5.1$$

where $k_{bulk}(\chi)$ is bulk thermal conductivity at a particular size reduction factor, $q''_{avg} = (q''_{in} + q''_{out})/2$ is the average heat flux in the TIM cross-plane direction, $\frac{dT}{dz} = \frac{\Delta T}{\Delta z} = \frac{(T_H - T_C)}{\Delta z}$ is the imposed temperature gradient and $q"_{in}$ and $q"_{out}$ are the heat flux into and out of the material. The true predicted bulk thermal conductivity, k_{TIM}, for the given TIM microstructure is extracted by fitting a two-term exponential expression to k_{bulk} as a function of χ.

Figure 5.8 shows the steady-state temperature profile for one TIM microstructure. Figure 5.9 shows the cross-section averaged temperature profile along the bond line direction for various values of χ. That is, the bulk average surface temperature is computed for a hundred cross-sections, combining the particle and polymer phases. The particles are essentially isothermal due to orders of magnitude higher thermal conductivity *i.e.*, $\frac{k_p}{k_m} \sim O(10^3)$. Note that there is temperature continuity at the particle-polymer interface owing to zero thermal interface resistance.

The temperature profile exhibits waviness or deviation from linear profile due to the presence of particles. This is significant only at lower values of $\chi < 0.5$ (*i.e.*, at larger particle sizes) (see Figure 5.9). At the smallest particle sizes modeled in this work, the temperature profile is linear.

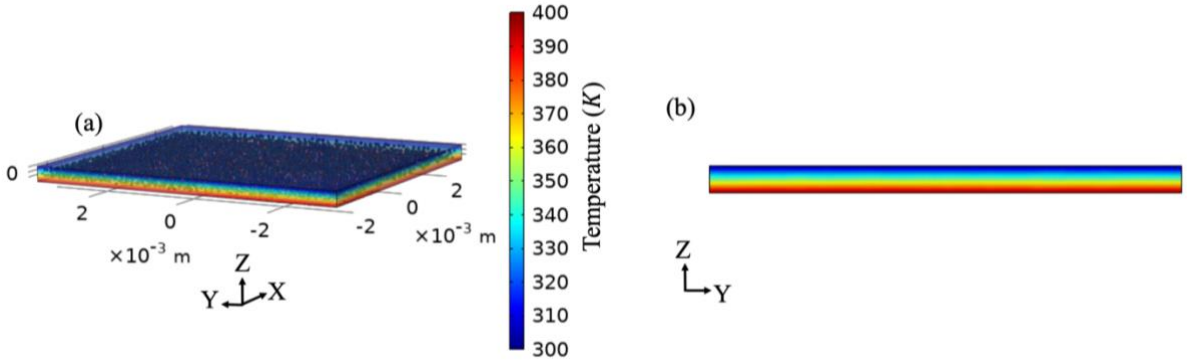

Figure 5.8. (**a, b**) Steady-state temperature profile in the TIM. (**b**) Side view shows nearly parallel isotherms, suggesting an approximately 1D conduction in the Z direction.

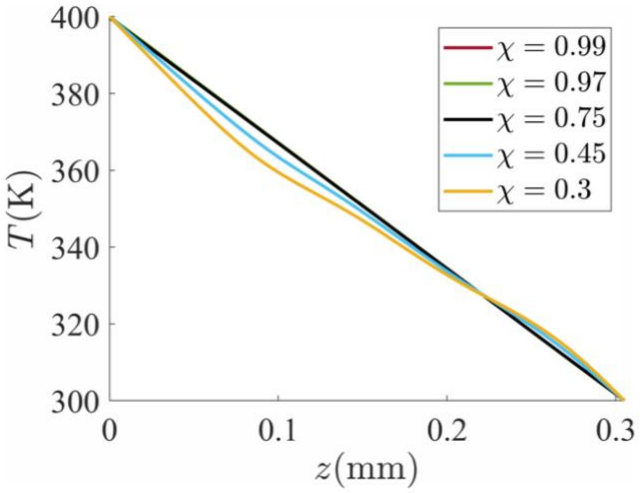

Figure 5.9. Cross-section averaged temperature, T, versus distance along the Z direction for various values of χ.

Figure 5.10 (a) shows the two-term exponential fit of bulk conductivity as a function of the size reduction parameter. The fit is performed using eleven data points (*training set*) and then verified using three data points (*testing set*). The red-filled pentagram at $\chi = 0$ is the extrapolated thermal conductivity value. The fit is performed on a Central sample produced experimentally at $V_S = 10\ \text{mm s}^{-1}, F_S = 50\ \text{N}$. The error in the fit (Figure 5.10 (b)), expressed as the deviation of the calculated conductivity using the fit expression with respect to the testing dataset values, is $< 1\%$ for all cases.

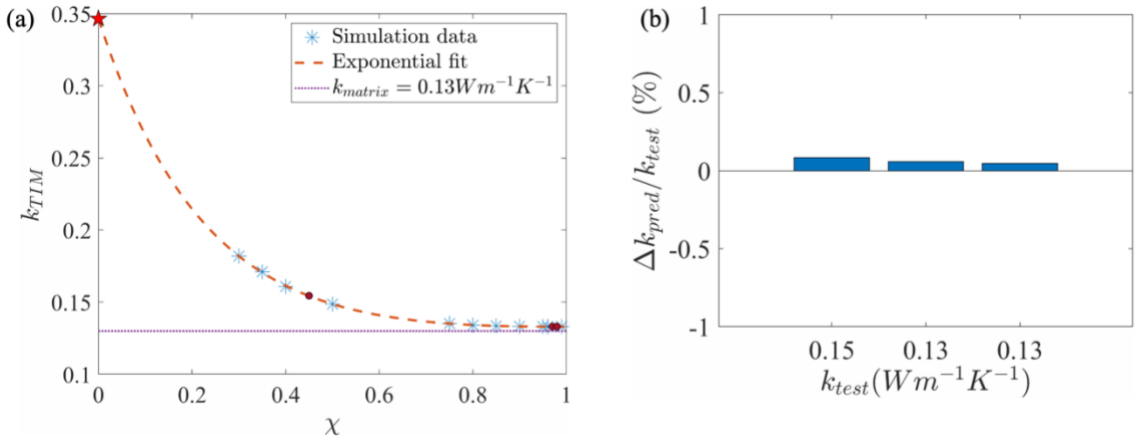

Figure 5.10. (**a**) Two-term exponential fit for a Central TIM sample produced at $V_S = 10\ \text{mm s}^{-1}$ and $F_S = 50\ \text{N}$ described by $k_{bulk} \approx 0.23\, e^{-4.39x} + 0.12\, e^{0.11x}$ and (**b**) error in the predicted bulk conductivity using the fit relative to the testing dataset. The pentagram marker and filled circles in (a) are, respectively, the extrapolated true bulk TIM thermal conductivity for this sample and the validation data points.

A mesh independence study was conducted for one of the microstructures ($V_S = 1$ µm s^{-1}, $F_S = 100$ N). The mesh is enhanced for the matrix phase since its conductivity is orders of magnitude lower than that of the particles. The built-in mesh size features named as "Normal", "Fine", "Finer", "Extra fine", and "Extremely fine" are used in this study. With a "Normal" mesh size, the mesh could not be successfully generated for all values of χ and the predicted conductivity from the two-term fit for this case is $k_{TIM} \approx 0.61$ W m^{-1}K^{-1}, whereas for all other cases the predicted conductivity $k_{TIM} \approx 0.28$ W m^{-1} K^{-1}. There is no variation up to the third decimal place. However, despite this conclusion, "Extra fine" mesh type was chosen because for some of the microstructures, mesh could not be generated using either "Fine" or "Finer" types. This reduces the amount of simulated datasets available for the exponential fit.

Figure 5.11 shows the variation of predicted conductivity with squeeze rate and load for the microstructures produced from *Set 1* and *Set 2* squeeze tests. Overall, for *Set 1* data, the predicted conductivity is $k_{TIM} \approx 0.27$ W m^{-1}K^{-1} with a standard deviation of ≈ 15.4% for CE samples, and $k_{TIM} \approx 0.3$ W m^{-1}K^{-1} with a standard deviation of ≈ 13% for C samples. For *Set 2* data, the predicted conductivity is $k_{TIM} \approx 0.3$ W m^{-1}K^{-1} with a standard deviation of ≈ 13.7% for CE samples, and $k_{TIM} \approx 0.3$ W m^{-1}K^{-1} with a standard deviation of ≈ 14.2% for C samples. The predicted conductivity of the CE samples is higher than that of the C samples in many cases, and that is unexpected since the particle spatial distribution is relatively more uniform in the C samples. Moreover, the extrapolation method may not be able to capture the impact of percolating particle

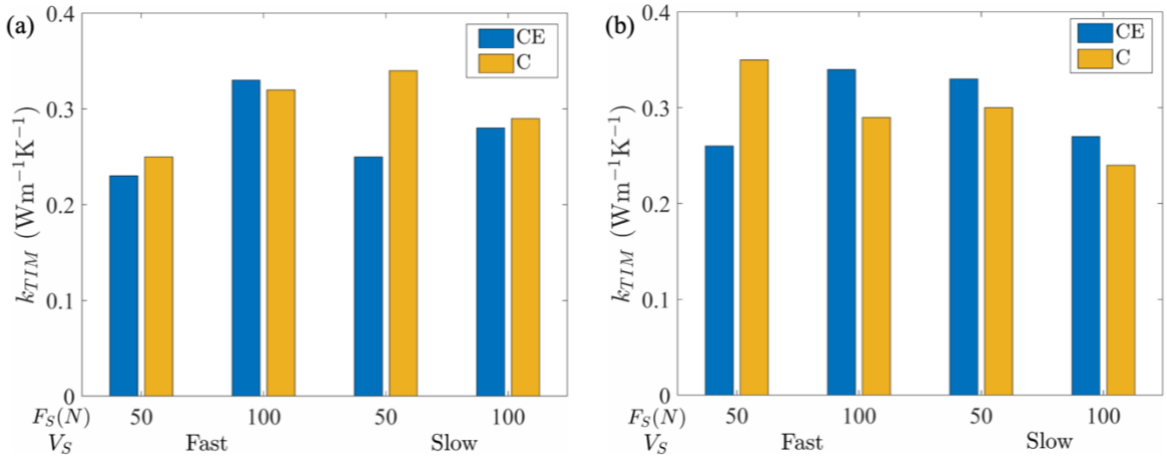

Figure 5.11. Predicted bulk TIM thermal conductivity for (**a**) *Set 1* and (**b**) *Set 2* squeezed TIM microstructures of Central (C) and Center-Edge (CE) samples. These values are obtained by extrapolating the two-term exponential fit to $\chi = 0$. Fast = 10 mm s^{-1} and Slow = 10^{-3} mm s^{-1}.

pathways on the heat conduction enhancement. The significantly low predicted conductivity may be due to a combination of this model drawback and the moderately low filler volume fraction. The trends do not match between the two test sets likely due to the reasons noted in section 3.6. A non-zero interface resistance can be supplied as model input. However, that will decrease the predicted value of conductivity. Validation of the predictive accuracy with thermal measurements is crucial to further understand the limitations of the parametric variation exploited in this steady-state conduction model. Further, note that the fabric anisotropy of the microstructures $\rho_{fabric} \approx 1$, suggesting no preferential alignment of particles.

Figure 5.12 shows the predicted thermal conductivity for the simulated squeezed TIM microstructures using the two-term exponential method described earlier. The predicted conductivity for the simulated microstructures decreases from $k_{TIM} = 0.3\ \mathrm{W\ m^{-1}K^{-1}}$ at $V_S = 1\ \mathrm{mm\ s^{-1}}$ to $k_{TIM} = 0.25\ \mathrm{W\ m^{-1}K^{-1}}$ at $V_S = 10\ \mathrm{mm\ s^{-1}}$. There is just about 4% increase in conductivity from the intermediate to fastest velocity. The conductivity is highest at the slower squeeze rate likely due to more spreading of particles and formation of layers or sheets of particles over a larger substrate area, thus leading to a lower BLT. So, there are potentially more heat conduction pathways and a shorter distance across which heat is conducted. At higher squeeze rates, the microstructure bulges near the center, whereas particles that are initially near the edges of the dispensed TIM spread out farther due to the drag force. The BLT is larger in this case, and particles are non-uniformly spread over the substrate area. Heat conduction is enhanced only in a relatively small area near the bulged region, thus resulting in smaller bulk thermal conductivity.

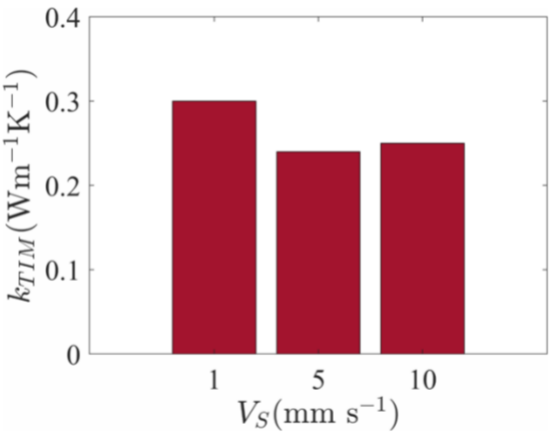

Figure 5.12. Predicted TIM bulk thermal conductivity, k_{TIM}, for the simulated squeezed TIM microstructures at different squeeze rates, V_S.

The decrease in conductivity with squeeze rate may be explained using a simple 2D reduced order model that approximates bulging of the microstructure as a triangular region (see Appendix B).

Selection of the Range of Size Reduction Factors

Here, the size reduction factor, χ, is varied between 0.3 and 0.99. The choice of χ is such that the asymptotic nature of $f(\chi \to 1)$ is captured after the rapid decay in the range $0 < \chi < 0.5$. So, a sufficient number of data points are needed for $\chi \geq 0.8$. Meshing errors consistently arose for some of the microstructures for $\chi < 0.3$ and hence the lower bound for χ is set at 0.3. For each model, the heat flux in, $q"_{in}$, and out, $q"_{out}$, of the system (normal to the bottom and top boundaries) are computed to verify that steady-state is reached. All experimental microstructures considered, the maximum relative difference is $< 2\%$.

5.5 Concluding Remarks

In this chapter, network thermal model and FE thermal conduction model are developed based on existing methodologies described in prior work. Due to thin TIM bond lines of ≈ 2.5 particle diameters, assignment of boundary particles in the network model is difficult. This led to severe underprediction of the bulk thermal conductivity. However, the network model predicts sensible values of the bulk in-plane thermal conductivity. This and the verification using simple cubic particle packing suggest that the implementation of the network model is acceptable. In the FE model, the bulk conductivity is predicted via an extrapolation method. By fitting a two-term exponential function to the predicted conductivity versus χ, the true TIM conductivity is calculated by extrapolating the fit to $\chi \to 0$ (*i.e.*, true particle size). The fit is verified by ensuring a good agreement with the testing dataset as well as observing that the predicted conductivity approaches that of the polymer matrix as $\chi \to 1$ (*i.e.*, vanishing particle size). For *Set 1* experimental data, the conductivity is in the range of $0.23 - 0.34$ W m^{-1} K^{-1}, and significantly increases with load at the fast squeeze rate. For *Set 2* experimental data, the conductivity is in the range of $0.24 - 0.35$ W m^{-1} K^{-1}, and decreases for most cases by $\approx 15 - 19\%$ with load at both fast and slow squeeze rates. The trends do not match between the two test sets likely due to the reasons noted in section 3.6. The conductivity of the CE samples is higher than that of the C samples in many cases, and that is unexpected since the particle spatial distribution is relatively more uniform in the C

samples. Moreover, the extrapolation method may not be able to capture the impact of percolating particle pathways on the heat conduction enhancement, thus resulting in a significantly low value of the predicted conductivity. The predicted thermal conductivity of the simulated microstructures decreases by $\approx 16.7\%$ with squeeze rate, from $k_{TIM} = 0.3\ \mathrm{W\ m^{-1}K^{-1}}$ (at $V_S = 1\ \mathrm{mm\ s^{-1}}$) to $k_{TIM} = 0.25\ \mathrm{W\ m^{-1}K^{-1}}$ (at $V_S = 10\ \mathrm{mm\ s^{-1}}$), likely due to the higher concentration of particles near the center observed at higher squeeze rate. The variation in conductivity is relatively insignificant from the intermediate to fastest velocity. The conductivity is higher at slower squeeze rate likely because the particles squeeze out farthest to occupy a larger area, forming sheets of particles with a lower BLT. This could yield a greater density of high conductivity pathways across a smaller bond line. This variation is explained by a simple reduced order model (see Appendix B). Commercial TIMs are highly loaded with filler particles up to $60 - 70$ vol%. The network model may be used at that particle loading, provided that thicker samples are analyzed for ease of boundary particle assignment. Future work should further explore both the network and FE models, and validate those with thermal measurements for a wide range of filler loadings.

6. CONCLUSIONS AND FUTURE WORK

6.1 Summary

This thesis investigates the impact of application processes on the microstructure of TIMs via a combined experimental and modeling framework. Mock TIM consisting of 30 vol% spherical copper particles (sieved size range $90 - 106$ μm) in a UV-curable epoxy is prepared in-house by manual mixing. Automated application procedures are developed to investigate dispensing and constant velocity squeezing of TIMs. The microstructures of the UV-cured line dispense pattern and squeezed TIMs are experimentally measured via high resolution 3D XRCT imaging. Bulk particle volume fraction, coordination number, local particle volume and RDF are computed to analyze the microstructure. Constant velocity squeezing model is developed using a DEM framework by building user-defined functionality into the open-source software MFIX. The novelty of the modeling is that it uses as input the experimentally measured dispensed TIM particle configuration. This is a major development compared to numerous other existing works which generally use a randomized particle configuration as the initial state. Thermal conduction models are developed to predict bulk TIM thermal conductivity of the measured and simulated microstructures.

Experimentally, the BLT ranges between $200 - 260$ μm ($2 - 2.4$ median particle diameters) at the applied pressure of ≈ 11 psi ($F_S = 50$ N) and ≈ 23 psi ($F_S = 100$ N) based on two test sets conducted at squeeze rates of 10^{-3} mm s^{-1} (slow) and 10 mm s^{-1} (fast). The BLT is largely independent of the load at the fast squeeze rate. This is likely a consequence of the impact type load application at this squeeze rate. At the slow squeeze rate, the BLT decreased with increasing load. The dispensed TIM microstructure is similar along the axis of the line pattern with $\phi_p \approx 36.1\%$ and $C_N \approx 2.1$. Squeezing lowers the bulk particle volume fraction to the range of $\phi_p \approx 25.4 - 34\%$ likely due to the formation of voids or air bubbles that can cause a volume expansion. The coordination number is in the range of $\approx 2.1 - 2.7$. Trends in the volume fraction and coordination number did not match between the two test sets with similar conditions, likely due to differing substrate surface characteristics resulting from the manual application of the copper foil and packaging tape. The first peak in the RDF of the squeezed TIMs was taller than that of the

dispensed TIM and that is supported by the higher coordination number (for most cases). Overall, the RDFs of the dispensed and squeezed TIM samples suggest a disordered microstructure due to the presence of just two peaks. The local particle volume fraction is approximately uniform near the central region of the squeezed TIM, whereas at the higher load, the local particle concentration is lower near the edges. However, the variation is not consistent between tests. Optical image analysis of the TIMs revealed uniform and similar particle spatial distribution when squeezed on the bare glass slide, and differing characteristics when squeezed on glass slides covered with copper foil and packaging tape. This is a crucial observation because real surfaces are rough and will potentially influence the rheology during squeezing and thus govern the TIM microstructure and performance.

Computationally, the predicted BLT from the DEM simulations monotonically increased with squeeze rate in the range of $V_S = 1 - 15\ \mathrm{mm\ s^{-1}}$ at $P_S \approx 171.1\ \mathrm{kPa}$ (corresponding to the experimentally measured pressure at $F_S = 100\ \mathrm{N}$). This is a limitation arising from the Newtonian fluid assumption. For a fixed pressure, the predicted BLT will increase with squeeze rate and, for a fixed BLT, the predicted pressure will be higher than that is experimentally observed. The current model is not capable of accurately predicting the experimentally observed microstructures based on the analysis of BLT, ϕ_p and C_N. While the network thermal model was verified using a simple cubic particle packing and by obtaining physically sensible predictions of bulk in-plane conductivity, it was infeasible to predict the cross-plane thermal conductivity. This is due to difficulties in the assignment of boundary particles for thin microstructures. An extrapolation-based calculation combined with the FE thermal conduction model is also developed based on prior work. For the experimental data sets, the predicted conductivity is in the range of $0.23 - 0.35\ \mathrm{W\ m^{-1}\ K^{-1}}$, and trends with squeeze rate and load differ between tests. The predicted conductivity of the simulated microstructures decreases with squeeze rate, from $k_{TIM} = 0.28\ \mathrm{W\ m^{-1}K^{-1}}$ to $k_{TIM} = 0.25\ \mathrm{W\ m^{-1}K^{-1}}$, with relatively insignificant variation from the intermediate to fastest velocity. The conductivity is highest at the slowest squeeze rate because the particles squeeze out the farthest to occupy a larger footprint area and likely form sheets of particles across a smaller bond line. The extrapolation method may not be able to capture the impact of percolating particle pathways on the heat conduction enhancement, thus resulting in a significantly low value of the predicted conductivity.

6.2 Future Research Directions

Automating the dispensing and squeezing protocols and controlling the roughness of the metallic lid and heat sink surfaces are critical to ensuring consistent squeezed states. Optimizing the dispense pattern and squeeze rate and load are critical for enhanced thermal performance. The novelty of this thesis lies in the (a) experimental microstructure measurement of dispensed and squeezed TIMs produced using automated application protocols and (b) development of squeezing simulations to predict TIM microstructure using an initial configuration that is supplied by experimental data and by incorporating one-way fluid-particle coupling via drag forces. The present work tackled a challenging engineering problem of investigating the impact of TIM application protocols on the material microstructure and thermal performance. Future research directions are presented in Table 6.1 and discussed below.

Materials

The present work focused on microstructure and thermal conduction in TIMs consisting of large spherical filler particles at moderate filler volume fraction. Future work should investigate TIMs consisting of (a) bidisperse size distribution (spherical particles), (b) realistic particle sizes that are found in commercial TIMs. High filler loadings of > 50 vol%, and both spherical and faceted

Table 6.1 Directions for future work

	Experimental Research	**Predictive Modeling**

Microstructure of Squeezed TIMs	• Higher filler volume fraction (>50%)
	  ○ Spherical vs faceted particles
	  ○ Mono- vs bi-disperse PSD
	• Impact of substrate roughness and dispense patterns
	• Macroscopic-scale analysis of voids using lower resolution XRCT imaging
		• Compute polymer fluid velocity profile using (a) realistic shape of the dispense pattern, and (b) non-Newtonian behavior
		• Two-way coupling of particles and fluid during squeezing
		• Interaction between different parts of the dispense pattern

TIM Thermal Conduction	• Develop infrared thermal metrology to characterize bulk TIM thermal conductivity • Investigate in-plane heat spreading in the TIM • Correlate voids with cross-plane thermal conductivity	• Revisit network thermal model for high filler loading TIMs • Assess validity of FE model developed in this work for high filler loading TIMs • Factor of enhancement to account for percolation

particles should be considered. At these filler loadings, strong non-Newtonian behavior is expected and the microstructure will likely be more significantly impacted by the squeeze rate.

Microstructure and Thermal Characterization

More complicated dispense patterns such as serpentine, spiral, star- and "X"-shapes must be investigated. A wider range of squeeze loads may be explored. Thermal curing as a cost-effective method could be considered as an alternative to UV curing. For this purpose, an environmental chamber for the Instron mechanical tester may be viable. Larger samples or, if possible, whole squeezed TIMs could be analyzed via XRCT imaging. Separation of substrates and the squeezed and cured TIM must be avoided. This can be achieved with the use of low-density substrates such as acrylic (that could also be used in thermal characterization tests). The substrates along with the squeezed and cured TIM can be machined to prepare samples for imaging. Multiple tests must be conducted at various squeeze rates and loads, accompanied by an extensive error analysis to understand and isolate process-induced variation from the actual variations induced by process parameters such as squeeze rate and load. Large voids and local clustering of particles could be investigated by examining whole squeezed TIMs, followed by thermal characterization to understand the impact of the heterogeneities on the conductivity. Image resolution may be sacrificed to ignore individual particle-level details, thereby focusing on large voids which potentially impede heat conduction. Void statistics such as the average size and number density (per unit volume or area) can potentially be correlated with bulk TIM thermal conductivity. Although individual particles may not be revealed at the lower resolution, it is worthwhile to examine whole TIM samples. Further, a systematic investigation of squeezing with controlled surface roughness could potentially reveal the impact of roughness on TIM rheology during squeezing.

A standardized infrared (IR) microscope-based thermal characterization method must be developed for the TIMs to measure the cross-plane thermal conductivity. The proposed acrylic substrate for the squeeze tests must be first characterized using a reference material with previously measured or well-known thermal conductivity. Then, using the acrylic-TIM-acrylic set up, steady-state tests may be employed to measure thermal conductivity. In-plane heat spreading could be investigated (using lower magnification) to examine the macroscopic-level characteristics with

respect to a constant power load. This will provide insights into the potential hot spot locations in real applications.

Predictive Microstructure and Thermal Models

Polymer fluid velocity profile may be improved by considering non-Newtonian behavior *e.g.*, Herschel-Bulkley model, and solving for the velocity profile using finite element or finite volume methods using commercial simulation toolkits. Realistic shape of the dispense pattern *e.g.*, heap shape, should be considered for more accurate velocity profile solution. At higher filler particle loading, the fluid velocity will likely be perturbed. For instance, during squeeze flow the polymer matrix may flow through the particle networks. This behavior may deviate from that observed during squeezing of the bare polymer. Therefore, it is essential to model a two-way fluid particle coupling in future investigations. The network thermal model may be used for TIMs with higher filler loading. The FE thermal model developed in this work must be validated using experimental data. This modeling framework cannot account for thermal conductivity enhancement via percolating chains. A factor of enhancement based on the fabric tensor may be incorporated as a fitting parameter based on model predictions and experimental measurements. Alternatively, in-plane FE thermal conductivity predictions may be validated using transient IR thermal measurements. The validated FE thermal model may then be used to predict cross-plane thermal conductivity with a higher confidence than that in the present work.

APPENDIX A. 3D XRCT IMAGE ANALYSIS

Figure A1 shows some reconstructed cross-sections from the 3D XRCT scan of a squeezed TIM sample. Some of the particles are clearly observed to be hollow. This impacts the accuracy of particle size analysis. Although some of the holes can be filled using morphological image operations, other holes extended to the outer surface and the algorithm fails to fill such holes. Open-source ImageJ plug-ins used in this work are listed in Table A1.

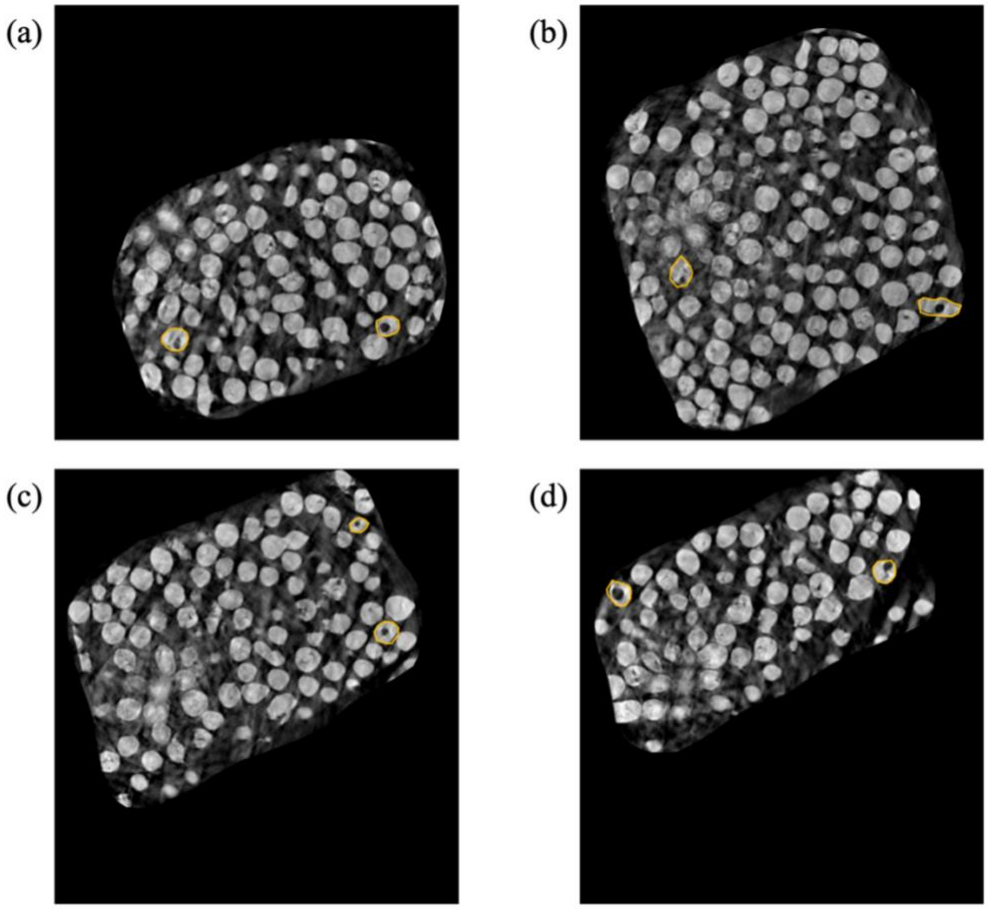

Figure A1. Gray scale XRCT-reconstructed cross-sections of a squeezed TIM sample showing some hollow particles. Image resolution is $(1.9\ \mu m)^3$.

Table A1. Open-source ImageJ plug-ins

Plug-in Name	Brief Description
Non Local Means Denoise	Non-local means filtering
3D Plugins Suite	Various noise reduction filters and other numerous operations
3D Objects Counter	Particle size, location and many other features
MorphoLibJ: Morphological Operations Library	Fill holes in particles, various watershed separation algorithms

APPENDIX B. REDUCED ORDER THERMAL MODEL

A simple 2D reduced order model (Figure B1) is discussed to explain the trend of decreasing conductivity with increasing squeeze rate with respect to simulated squeezed TIM microstructures (section 5.4). The TIM is approximated as the triangular region, whereas the region outside the triangle and within the rectangular box is assumed to be the matrix phase. For simplicity, the TIM is assumed to be made of particles. One of the angles of the triangle is θ. As squeeze rate increases, θ increases due to bulging of the microstructure. The goal of this model is to express effective resistance, R_{eff}, as a function of θ. This relationship should support the observed change in k_{TIM} with squeeze rate.

The effective resistance of the TIM is computed as the effective resistance of vertical strips in parallel (Figure B1 (b)). So, the strip resistance is first calculated by computing the strip conductivity

$$k_{strip} = \left(\frac{y}{L_o}\right) k_p + \frac{L_o - y}{L_o} k_m$$

$$k_{strip} = \left(\frac{y}{L_o}\right)\left(k_p - k_m\right) + k_m$$

$$R_{strip} = \frac{L_o}{k_{strip}\, A_{c,strip}}$$

Many such strips are in parallel. An integration is then performed to compute R_{eff}.

$$\frac{1}{R_{eff}} = \frac{1}{R_1} + \frac{1}{R_2} + \frac{1}{R_3} + \cdots + \frac{1}{R_n}$$

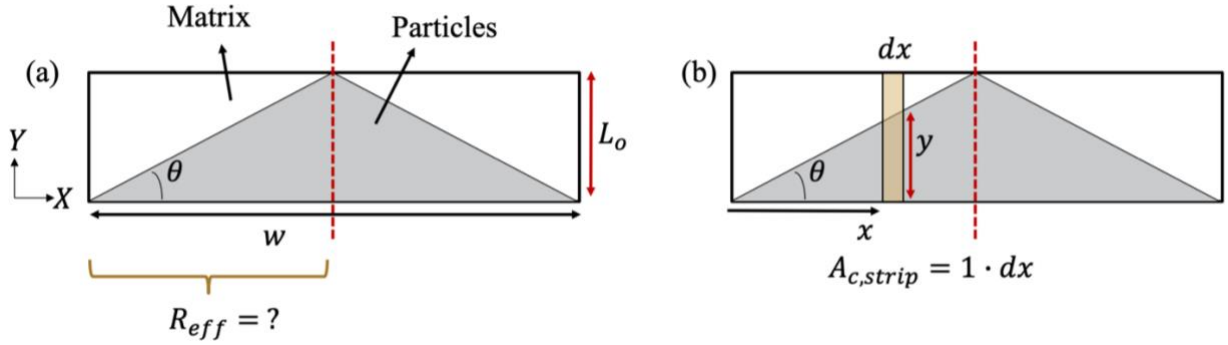

Figure B1. Predicted TIM thermal conductivity, k_{TIM}, for the simulated squeezed TIM microstructures at different squeeze rates, V_S.

$$\frac{1}{R_{eff}} = \sum \frac{k_{strip}\, A_{c,\, strip}}{L_o} = \int_0^{w/2} \left(\left(\frac{y}{L_o}\right)\left(k_p - k_m\right) + k_m \right) \frac{1 \cdot dx}{L_o}$$

$$\frac{1}{R_{eff}} = \frac{\frac{m}{L_o}\left(k_p - k_m\right)\left(\frac{1}{2}\left(\frac{w}{2}\right)^2\right) + k_m\left(\frac{w}{2}\right)}{\mathrm{L_o}} = \frac{\frac{1}{2}\left(\mathrm{k_p} - \mathrm{k_m}\right)\left(\frac{\mathrm{w}}{2}\right) + \mathrm{k_m}\left(\frac{\mathrm{w}}{2}\right)}{\mathrm{L_o}} = \frac{\mathrm{w}}{2}\,½\,\frac{\left(\mathrm{k_p} + \mathrm{k_m}\right)}{\mathrm{L_o}}$$

The geometry parameters are expressed as a function of the slope of a line, tan (θ). We see that $R_{eff} \propto$ tan (θ) suggests that as θ increases, R_{eff} increases. So, k_{TIM} decreases.

$$\boldsymbol{R_{eff} = \frac{2\left(\frac{L_o}{\frac{W}{2}}\right)}{(k_p + k_m)} = \frac{2\tan(\theta)}{(k_p + k_m)}}$$

REFERENCES

[1] V.P. Atluri, R. V Mahajan, P.R. Patel, D. Mallik, J. Tang, V.S. Wakharkar, G.M. Chrysler, C. Chiu, G.N. Choksi, and R.S. Viswanath, "Critical Aspects of High-Performance Microprocessor Packaging," *MRS Bulletin*, vol. 28, Jan. 2003, pp. 21–34, DOI:10.1557/mrs2003.14.

[2] K. Rupp, "42 Years of Microprocessor Trend Data," *https://www.karlrupp.net/2018/02/42-years-of-microprocessor-trend-data/*.

[3] T.M. Braun, D. Josell, J. John, and T.P. Moffat, "Editors' Choice—Simulation of Copper Electrodeposition in Through-Hole Vias," *Journal of The Electrochemical Society*, vol. 167, Oct. 2020, p. 013510, DOI:10.1149/2.0102001JES.

[4] J.L. Smoyer and P.M. Norris, "Brief Historical Perspective in Thermal Management and the Shift Toward Management at the Nanoscale," *Heat Transfer Engineering*, vol. 40, 2019, pp. 269–282, DOI:10.1080/01457632.2018.1426265.

[5] M.H. Nasr, C.E. Green, P.A. Kottke, X. Zhang, T.E. Sarvey, Y.K. Joshi, M.S. Bakir, and A.G. Fedorov, "Hotspot Thermal Management With Flow Boiling of Refrigerant in Ultrasmall Microgaps," *Journal of Electronic Packaging*, vol. 139, Mar. 2017, pp. 1–8, DOI:10.1115/1.4035387.

[6] R. Mahajan, Chia-pin Chiu, and G. Chrysler, "Cooling a Microprocessor Chip," *Proceedings of the IEEE*, vol. 94, Aug. 2006, pp. 1476–1486, DOI:10.1109/JPROC.2006.879800.

[7] S.A. Jajja, W. Ali, H.M. Ali, and A.M. Ali, "Water cooled minichannel heat sinks for microprocessor cooling: Effect of fin spacing," *Applied Thermal Engineering*, vol. 64, Mar. 2014, pp. 76–82, DOI:10.1016/j.applthermaleng.2013.12.007.

[8] R.D. Dickinson, S. Novotny, M. Vogel, and J. Dunn, "A system design approach to liquid-cooled microprocessors," *InterSociety Conference on Thermal and Thermomechanical Phenomena in Electronic Systems, ITHERM*, vol. 2002-Janua, 2002, pp. 413–420, DOI:10.1109/ITHERM.2002.1012486.

[9] J. Fontaine, C. Gonzalez, P. Kumar, F. Pigache, P. Lavieille, F. Topin, and M. Miscevic, "Liquid cooling of a microprocessor: experimentation and simulation of a sub-millimeter channel heat exchanger," *Heat Transfer Engineering*, vol. 0, Jul. 2019, pp. 1–17, DOI:10.1080/01457632.2019.1628485.

[10] Y. Yadavalli, J.A. Weibel, and S. V. Garimella, "Performance-governing transport mechanisms for heat pipes at ultrathin form factors," *IEEE Transactions on Components, Packaging and Manufacturing Technology*, vol. 5, 2015, pp. 1618–1627, DOI:10.1109/TCPMT.2015.2477275.

[11] R.S. Prasher, "A Simplified Conduction Based Modeling Scheme for Design Sensitivity Study of Thermal Solution Utilizing Heat Pipe and Vapor Chamber Technology," *Journal of Electronic Packaging*, vol. 125, 2003, p. 378, DOI:10.1115/1.1602479.

[12] K. Mizuta, R. Fukunaga, K. Fukuda, S. Nii, and T. Asano, "Development and characterization of a flat laminate vapor chamber," *Applied Thermal Engineering*, vol. 104, Jul. 2016, pp. 461–471, DOI:10.1016/j.applthermaleng.2016.05.080.

[13] J.A. Weibel and S. V. Garimella, "Recent Advances in Vapor Chamber Transport Characterization for High-Heat-Flux Applications," *Advances in Heat Transfer*, Copyright © 2013 Elsevier Inc. All rights reserved., 2013, pp. 209–301, DOI:10.1016/B978-0-12-407819-2.00004-9.

[14] R. Prasher, "Thermal Interface Materials: Historical Perspective, Status, and Future Directions," *Proceedings of the IEEE*, vol. 94, Aug. 2006, pp. 1571–1586, DOI:10.1109/JPROC.2006.879796.

[15] K.M. Razeeb, E. Dalton, G.L.W. Cross, and A.J. Robinson, "Present and future thermal interface materials for electronic devices," *International Materials Reviews*, vol. 6608, 2017, pp. 1–21, DOI:10.1080/09506608.2017.1296605.

[16] R.S. Prasher, J. Shipley, S. Prstic, P. Koning, and J. Wang, "Thermal Resistance of Particle Laden Polymeric Thermal Interface Materials," *Journal of Heat Transfer*, vol. 125, 2003, p. 1170, DOI:10.1115/1.1621893.

[17] B. Wunderle, J. Kleff, R. Mrossko, M.A. Ras, D. May, R. Schacht, H. Oppermann, J. Keller, and B. Michel, “In-situ measurement of various thin bond-line-thickness thermal interface materials with correlation to structural features,” *14th International Workshop on THERMal INvestigation of ICs and Systems, THERMINIC 2008*, 2008, pp. 112–117, DOI:10.1109/THERMINIC.2008.4669890.

[18] Jue Li, P. Myllykoski, and M. Paulasto-Krockel, “Study on thermomechanical reliability of power modules and thermal grease pump-out mechanism,” *2015 16th International Conference on Thermal, Mechanical and Multi-Physics Simulation and Experiments in Microelectronics and Microsystems*, IEEE, 2015, pp. 1–6, DOI:10.1109/EuroSimE.2015.7103076.

[19] F. Sarvar, D.C. Whalley, P.P. Conway, and E.: Cu, “Thermal Interface Materials-A Review of the State of the Art,” 2006, pp. 1292–1302.

[20] D.A. Davidson, G.L. Lehmann, and B.T. Murray, “Study of a gel thermal interface material with micron-size particles,” *Thermal and Thermomechanical Proceedings 10th Intersociety Conference on Phenomena in Electronics Systems, 2006. ITHERM 2006.*, IEEE, 2006, pp. 497–504, DOI:10.1109/ITHERM.2006.1645385.

[21] Y. Zhang, Y.J. Heo, Y.R. Son, I. In, K.H. An, B.J. Kim, and S.J. Park, “Recent advanced thermal interfacial materials: A review of conducting mechanisms and parameters of carbon materials,” *Carbon*, vol. 142, 2019, pp. 445–460, DOI:10.1016/j.carbon.2018.10.077.

[22] A. Yu, P. Ramesh, M.E. Itkis, E. Bekyarova, and R.C. Haddon, “Graphite nanoplatelet-epoxy composite thermal interface materials,” *Journal of Physical Chemistry C*, vol. 111, 2007, pp. 7565–7569, DOI:10.1021/jp071761s.

[23] S. Desai and J. Njuguna, “Enhancement of thermal conductivity of materials using different forms of natural graphite,” *IOP Conference Series: Materials Science and Engineering*, vol. 40, Sep. 2012, p. 012017, DOI:10.1088/1757-899X/40/1/012017.

[24] S. Zhou, J. Xu, Q.H. Yang, S. Chiang, B. Li, H. Du, C. Xu, and F. Kang, “Experiments and modeling of thermal conductivity of flake graphite/polymer composites affected by adding carbon-based nano-fillers,” *Carbon*, vol. 57, 2013, pp. 452–459, DOI:10.1016/j.carbon.2013.02.018.

[25] K.M.F. Shahil and A.A. Balandin, “Thermal properties of graphene and multilayer graphene: Applications in thermal interface materials,” *Solid State Communications*, vol. 152, 2012, pp. 1331–1340, DOI:10.1016/j.ssc.2012.04.034.

[26] D. Cui and C. Wong, “Vertically Aligned and Interconnected Graphene Networks for High Thermal Conductivity of Epoxy Composites with Ultralow Loading,” 2016, DOI:10.1021/acs.chemmater.6b01595.

[27] Y. Sun, B. Tang, W. Huang, S. Wang, Z. Wang, X. Wang, Y. Zhu, and C. Tao, “Preparation of graphene modified epoxy resin with high thermal conductivity by optimizing the morphology of filler,” *Applied Thermal Engineering*, vol. 103, 2016, pp. 892–900, DOI:10.1016/j.applthermaleng.2016.05.005.

[28] K.M.F. Shahil and A.A. Balandin, “Graphene-multilayer graphene nanocomposites as highly efficient thermal interface materials,” *Nano Letters*, vol. 12, 2012, pp. 861–867, DOI:10.1021/nl203906r.

[29] X. Tian, M.E. Itkis, and R.C. Haddon, “Application of Hybrid Fillers for Improving the Through-Plane Heat Transport in Graphite Nanoplatelet-Based Thermal Interface Layers,” *Nature Publishing Group*, 2015, pp. 1–7, DOI:10.1038/srep13108.

[30] A.M. Marconnet, N. Yamamoto, M.A. Panzer, B.L. Wardle, and K.E. Goodson, “Thermal Conduction in Aligned Carbon Nanotube–Polymer Nanocomposites with High Packing Density,” *ACS Nano*, vol. 5, Jun. 2011, pp. 4818–4825, DOI:10.1021/nn200847u.

[31] V. Singhal, T. Siegmund, and S.V. Garimella, “Optimization of Thermal Interface Materials for Electronics Cooling Applications,” *IEEE Transactions on Components and Packaging Technologies*, vol. 27, Jun. 2004, pp. 244–252, DOI:10.1109/TCAPT.2004.828587.

[32] P. Chowdhury, K. Sikka, A. De Silva, and I. Seshadri, “On Thermal Interface Materials With Polydisperse Fillers: Packing Algorithm and Effective Properties,” *ASME 2018 International Technical Conference and Exhibition on Packaging and Integration of Electronic and Photonic Microsystems*, American Society of Mechanical Engineers, 2018, p. V001T01A007, DOI:10.1115/IPACK2018-8337.

[33] M. Müller, K. Hilarius, M. Liebscher, D. Lellinger, I. Alig, and P. Pötschke, “Effect of Graphite Nanoplate Morphology on the Dispersion and Physical Properties of Polycarbonate Based Composites,” *Materials*, vol. 10, 2017, p. 545, DOI:10.3390/ma10050545.

[34] Q.A. Poutrel, Z. Wang, D. Wang, C. Soutis, and M. Gresil, “Effect of pre and Post-Dispersion on Electro-Thermo-Mechanical Properties of a Graphene Enhanced Epoxy,” *Applied Composite Materials*, vol. 24, 2017, pp. 313–336, DOI:10.1007/s10443-016-9541-0.

[35] D.F. Rae, P. Borgesen, and E.J. Cotts, “The effect of filler-network heterogeneity on thermal resistance of polymeric thermal bondlines,” *JOM*, vol. 63, Oct. 2011, pp. 78–84, DOI:10.1007/s11837-011-0180-5.

[36] M.R.S. Shirazy, S. Allard, M. Beaumier, and L.G. Frechette, “Effect of squeezing conditions on the particle distribution and bond line thickness of particle filled polymeric thermal interface materials,” *Thermomechanical Phenomena in Electronic Systems - Proceedings of the Intersociety Conference*, 2014, pp. 251–259, DOI:10.1109/ITHERM.2014.6892289.

[37] R. Linderman, T. Brunschwiler, B. Smith, and B. Michel, “High-performance thermal interface technology overview,” *2007 13th International Workshop on Thermal Investigation of ICs and Systems (THERMINIC)*, IEEE, 2007, pp. 129–134, DOI:10.1109/THERMINIC.2007.4451762.

[38] R.J. Linderman, T. Brunschwiler, U. Kloter, H. Toy, and B. Michel, “Hierarchical Nested Surface Channels for Reduced Particle Stacking and Low-Resistance Thermal Interfaces,” *Twenty-Third Annual IEEE Semiconductor Thermal Measurement and Management Symposium*, IEEE, 2007, pp. 87–94, DOI:10.1109/STHERM.2007.352392.

[39] T. Brunschwiler, U. Kloter, R.J. Linderman, H. Rothuizen, and B. Michel, “Hierarchically Nested Channels for Fast Squeezing Interfaces With Reduced Thermal Resistance,” *IEEE Transactions on Components and Packaging Technologies*, vol. 30, Jun. 2007, pp. 226–234, DOI:10.1109/TCAPT.2007.897991.

[40] B. Smith, H. Rothuizen, R. Linderman, T. Brunschwiler, and B. Michel, “Design of thermal interfaces with embedded microchannels to control bond line formation,” *2008 11th Intersociety Conference on Thermal and Thermomechanical Phenomena in Electronic Systems*, IEEE, 2008, pp. 410–418, DOI:10.1109/ITHERM.2008.4544299.

[41] N. Bajaj, G. Subbarayan, and S. V. Garimella, “Topological design of channels for squeeze flow optimization of thermal interface materials,” *International Journal of Heat and Mass Transfer*, vol. 55, Jun. 2012, pp. 3560–3575, DOI:10.1016/j.ijheatmasstransfer.2012.03.020.

[42] T.Z. Fullem, D.F. Rae, A. Sharma, J.A. Wolcott, and E.J. Cotts, “Thermal characterization of thermal interface material bondlines,” *2008 11th Intersociety Conference on Thermal and Thermomechanical Phenomena in Electronic Systems*, IEEE, 2008, pp. 174–179, DOI:10.1109/ITHERM.2008.4544268.

[43] X. Hu, S. Govindasamy, and K.E. Goodson, “Two-Medium Model for the Bond Line Thickness of Particle Filled Thermal Interface Materials,” *Heat Transfer, Volume 3*, ASME, 2004, pp. 337–342, DOI:10.1115/IMECE2004-62027.

[44] R.S. Prasher, J. Shipley, S. Prstic, P. Koning, and J.-L. Wang, “Rheological Study of Micro Particle Laden Polymeric Thermal Interface Materials: Part 1 — Experimental,” *Heat Transfer, Volume 7*, ASMEDC, 2002, pp. 47–51, DOI:10.1115/IMECE2002-32117.

[45] C. Lin and D.D.L. Chung, “Rheological Behavior of Thermal Interface Pastes,” *Journal of Electronic Materials*, vol. 38, Oct. 2009, pp. 2069–2084, DOI:10.1007/s11664-009-0883-3.

[46] R.S. Prasher, J. Shipley, S. Prstic, P. Koning, and J.-L. Wang, “Rheological Study of Micro Particle Laden Polymeric Thermal Interface Materials: Part 2 — Modeling,” *Heat Transfer, Volume 7*, ASMEDC, 2002, pp. 53–59, DOI:10.1115/IMECE2002-32118.

[47] R.S. Prasher, P. Koning, J. Shipley, and A. Devpura, “Dependence of Thermal Conductivity and Mechanical Rigidity of Particle-Laden Polymeric Thermal Interface Material on Particle Volume Fraction,” *Journal of Electronic Packaging*, vol. 125, 2003, p. 386, DOI:10.1115/1.1602703.

[48] E.T. Swartz and R.O. Pohl, “Thermal boundary resistance,” *Reviews of Modern Physics*, vol. 61, Jul. 1989, pp. 605–668, DOI:10.1103/RevModPhys.61.605.

[49] I. Srivastava, S. Sadasivam, K.C. Smith, and T.S. Fisher, “Combined Microstructure and Heat Conduction Modeling of Heterogeneous Interfaces and Materials,” *Journal of Heat Transfer*, vol. 135, 2013, p. 061603, DOI:10.1115/1.4023583.

[50] C. Sangrós, C. Schilde, and A. Kwade, “Effect of Microstructure on Thermal Conduction within Lithium-Ion Battery Electrodes using Discrete Element Method Simulations,” *Energy Technology*, vol. 4, Dec. 2016, pp. 1611–1619, DOI:10.1002/ente.201600144.

[51] R. Shertzer, “Fabric tensors and effective properties of granular materials with applications to snow,” Thesis, 2011, http://search.proquest.com/docview/888508961?accountid=28148%5Cnhttp://scholarworks.montana.edu/xmlui/handle/1/2264.

[52] A. Vadakkepatt, B.L. Trembacki, S.R. Mathur, and J.Y. Murthy, “Effective Thermal Conductivity of Lithium Ion Battery Electrodes Employing Fully Resolved Simulations for Use in Volume Averaged Models,” *Volume 3: Gas Turbine Heat Transfer; Transport Phenomena in Materials Processing and Manufacturing; Heat Transfer in Electronic Equipment; Symposium in Honor of Professor Richard Goldstein; Symposium in Honor of Prof. Spalding; Symposium in Honor of Prof.*, American Society of Mechanical Engineers, 2013, pp. 1–13, DOI:10.1115/HT2013-17577.

[53] D.-W. Chung, P.R. Shearing, N.P. Brandon, S.J. Harris, and R.E. García, “Particle Size Polydispersity in Li-Ion Batteries,” *Journal of The Electrochemical Society*, vol. 161, Jan. 2014, pp. A422–A430, DOI:10.1149/2.097403jes.

[54] C. Tan, M.D.R. Kok, S.R. Daemi, D.J.L. Brett, and P.R. Shearing, “Three-dimensional image based modelling of transport parameters in lithium–sulfur batteries,” *Physical Chemistry Chemical Physics*, vol. 21, 2019, pp. 4145–4154, DOI:10.1039/C8CP04763D.

[55] O.O. Taiwo, “3D and 4D Characterisation of Lithium Ion Battery Electrode Microstructures using X-ray Tomography,” Thesis, 2016.

[56] A. Gillman, K. Matouš, and S. Atkinson, “Microstructure-statistics-property relations of anisotropic polydisperse particulate composites using tomography,” *Physical Review E*, vol. 87, Feb. 2013, p. 022208, DOI:10.1103/PhysRevE.87.022208.

[57] M.A. Marois and M. Lacroix, “Fundamentals of the squeeze-flow between a heat sink and a FLIP-chip,” *Transactions of the Canadian Society for Mechanical Engineering*, vol. 32, 2008, pp. 467–485.

[58] M. Mathew, T. Schilling, and M. Oettel, “Connectivity percolation in suspensions of hard platelets,” *Physical Review E - Statistical, Nonlinear, and Soft Matter Physics*, vol. 85, 2012, pp. 1–7, DOI:10.1103/PhysRevE.85.061407.

[59] M. Shtein, R. Nadiv, M. Buzaglo, K. Kahil, and O. Regev, “Thermally Conductive Graphene-Polymer Composites: Size, Percolation, and Synergy Effects,” *Chemistry of Materials*, vol. 27, Mar. 2015, pp. 2100–2106, DOI:10.1021/cm504550e.

[60] C.-W. Nan, R. Birringer, D.R. Clarke, and H. Gleiter, "Effective thermal conductivity of particulate composites with interfacial thermal resistance," *Journal of Applied Physics*, vol. 81, May. 1997, pp. 6692–6699, DOI:10.1063/1.365209.

[61] J. Kim, Y. Goo, I. Choi, S. Kim, and D. Lee, "Toward high-accuracy and high-applicability of a practical model to predict effective thermal conductivity of particle-reinforced composites," *International Journal of Heat and Mass Transfer*, vol. 131, Mar. 2019, pp. 863–872, DOI:10.1016/j.ijheatmasstransfer.2018.11.107.

[62] J. Ordonez-Miranda, M. Hermens, I. Nikitin, V.G. Kouznetsova, O. van der Sluis, M.A. Ras, J.S. Reparaz, M.R. Wagner, M. Sledzinska, J. Gomis-Bresco, C.M. Sotomayor Torres, B. Wunderle, and S. Volz, "Measurement and modeling of the effective thermal conductivity of sintered silver pastes," *International Journal of Thermal Sciences*, vol. 108, Oct. 2016, pp. 185–194, DOI:10.1016/j.ijthermalsci.2016.05.014.

[63] P. Furman˜ski, "Heat Conduction in Composites: Homogenization and Macroscopic Behavior," *Applied Mechanics Reviews*, vol. 50, Jun. 1997, pp. 327–356, DOI:10.1115/1.3101714.

[64] T.S. Yun and T.M. Evans, "Three-dimensional random network model for thermal conductivity in particulate materials," *Computers and Geotechnics*, vol. 37, Nov. 2010, pp. 991–998, DOI:10.1016/j.compgeo.2010.08.007.

[65] S. Kanuparthi, G. Subbarayan, T. Siegmund, and B. Sammakia, "An Efficient Network Model for Determining the Effective Thermal Conductivity of Particulate Thermal Interface Materials," *IEEE Transactions on Components and Packaging Technologies*, vol. 31, 2008, pp. 611–621, DOI:10.1109/TCAPT.2008.2001839.

[66] B. Dan, S. Kanuparthi, G. Subbarayan, and B.G. Sammakia, "An Improved Network Model for Determining the Effective Thermal Conductivity of Particulate Thermal Interface Materials," 2011, pp. 69–81, DOI:10.1115/interpack2009-89116.

[67] S. Kanuparthi, X. Zhang, G. Subbarayan, B.G. Sammakia, T. Siegmund, A. Gowda, and S. Tonapi, "Random network percolation models for particulate thermal interface materials," *Thermomechanical Phenomena in Electronic Systems -Proceedings of the Intersociety Conference*, IEEE, 2006, pp. 1192–1198, DOI:10.1109/ITHERM.2006.1645480.

[68] J. Lee, T. Yun, and S.-U. Choi, "The effect of particle size on thermal conduction in granular mixtures," *Materials*, vol. 8, 2015, pp. 3975–3991, DOI:10.3390/ma8073975.

[69] H.W. Zhang, Q. Zhou, H.L. Xing, and H. Muhlhaus, "A DEM study on the effective thermal conductivity of granular assemblies," *Powder Technology*, vol. 205, Jan. 2011, pp. 172–183, DOI:10.1016/j.powtec.2010.09.008.

[70] I. Terreros, I. Iordanoff, and J.L. Charles, "Simulation of continuum heat conduction using DEM domains," *Computational Materials Science*, vol. 69, Mar. 2013, pp. 46–52, DOI:10.1016/j.commatsci.2012.11.021.

[71] X.D. Liu, J.S. Zhang, X.M. Cao, and H. Zhang, "Finite element simulation of the thermal properties of particulate and continuous network-reinforced metal-matrix composites," *Proceedings of the Institution of Mechanical Engineers, Part B: Journal of Engineering Manufacture*, vol. 219, Jan. 2005, pp. 111–121, DOI:10.1243/095440505X8055.

[72] D. Kumlutas and I.H. Tavman, "A Numerical and Experimental Study on Thermal Conductivity of Particle Filled Polymer Composites," *Journal of Thermoplastic Composite Materials*, vol. 19, Jul. 2006, pp. 441–455, DOI:10.1177/0892705706062203.

[73] X. Zhang and G. Subbarayan, "jNURBS: An object-oriented, symbolic framework for integrated, meshless analysis and optimal design," *Advances in Engineering Software*, vol. 37, May. 2006, pp. 287–311, DOI:10.1016/j.advengsoft.2005.08.001.

[74] S. Torquato, "Random Heterogeneous Media: Microstructure and Improved Bounds on Effective Properties," *Applied Mechanics Reviews*, vol. 44, 1991, p. 37, DOI:10.1115/1.3119494.

[75] S. Torquato, "Statistical Description of Microstructures," *Annual Review of Materials Research*, vol. 32, Aug. 2002, pp. 77–111, DOI:10.1146/annurev.matsci.32.110101.155324.

[76] Y. Singh, N. Bajaj, and G. Subbarayan, "Simultaneous thermal/flow characterization of thermal interface materials," *2016 15th IEEE Intersociety Conference on Thermal and Thermomechanical Phenomena in Electronic Systems (ITherm)*, IEEE, 2016, pp. 1360–1365, DOI:10.1109/ITHERM.2016.7517707.

[77] C. Feger, J.D. Gelorme, M. McGlashan-Powell, and D.M. Kalyon, "Mixing, rheology, and stability of highly filled thermal pastes," *IBM Journal of Research and Development*, vol. 49, Jul. 2005, pp. 699–707, DOI:10.1147/rd.494.0699.

[78] S. Luding, "Granular matter: So much for the jamming point," *Nature Physics*, vol. 12, 2016, pp. 1–2, DOI:10.1038/nphys3680.

[79] J.D. BERNAL and J. MASON, “Packing of Spheres: Co-ordination of Randomly Packed Spheres,” *Nature*, vol. 188, Dec. 1960, pp. 910–911, DOI:10.1038/188910a0.

[80] L. Oger, M. Lichtenberg, A. Gervois, and E. Guyon, “Determination of the coordination number in disordered packings of equal spheres,” *Journal of Microscopy*, vol. 156, 1989, pp. 65–78, DOI:10.1111/j.1365-2818.1989.tb02906.x.

[81] M. Suzuki, H. Kada, and M. Hirota, “Effect of size distribution on the relation between coordination number and void fraction of spheres in a randomly packed bed,” *Advanced Powder Technology*, vol. 10, 1999, pp. 353–365, DOI:10.1163/156855299X00208.

[82] H. Iwata and T. Homma, “Distribution of coordination numbers in random packing of homogeneous spheres,” *Powder Technology*, vol. 10, Jul. 1974, pp. 79–83, DOI:10.1016/0032-5910(74)85035-7.

[83] T. Aste, M. Saadatfar, and T.J. Senden, “Local and global relations between the number of contacts and density in monodisperse sphere packs,” *Journal of Statistical Mechanics: Theory and Experiment*, vol. 2006, Jul. 2006, pp. P07010–P07010, DOI:10.1088/1742-5468/2006/07/P07010.

[84] M. Roozbahani, R. Borela, and J. Frost, “Pore Size Distribution in Granular Material Microstructure,” *Materials*, vol. 10, Oct. 2017, p. 1237, DOI:10.3390/ma10111237.

[85] M.P. Allen and D.J. Tildesley, *Computer Simulation of Liquids*, Oxford University Press, 1990, DOI:10.1093/oso/9780198803195.001.0001.

[86] J.G. Kirkwood and E.M. Boggs, “The Radial Distribution Function in Liquids,” *The Journal of Chemical Physics*, vol. 10, Jun. 1942, pp. 394–402, DOI:10.1063/1.1723737.

[87] T. Aste, M. Saadatfar, and T. Senden, “Geometrical structure of disordered sphere packings,” *Physical Review E*, vol. 71, Jun. 2005, p. 061302, DOI:10.1103/PhysRevE.71.061302.

[88] S. Franchetti, “Radial distribution functions in solid and liquid argon,” *Il Nuovo Cimento B Series 11*, vol. 26, Apr. 1975, pp. 507–521, DOI:10.1007/BF02738574.

[89] B.J. Yoon, M.S. Jhon, and H. Eyring, “Radial distribution function of liquid argon according to significant structure theory,” *Proceedings of the National Academy of Sciences*, vol. 78, Nov. 1981, pp. 6588–6591, DOI:10.1073/pnas.78.11.6588.

[90] J.J. Becerríl-González, F. Peñuñuri, M.A. Zambrano, C. Acosta, and O. Carvente, “Radial distribution function at the particle-bottom interface in granular self-assembly,” *Journal of Physics: Conference Series*, vol. 792, Jan. 2017, p. 012052, DOI:10.1088/1742-6596/792/1/012052.

[91] M. ODA, “INITIAL FABRICS AND THEIR RELATIONS TO MECHANICAL PROPERTIES OF GRANULAR MATERIAL,” *SOILS AND FOUNDATIONS*, vol. 12, 1972, pp. 17–36, DOI:10.3208/sandf1960.12.17.

[92] S.C. Cowin, “The relationship between the elasticity tensor and the fabric tensor,” *Mechanics of Materials*, vol. 4, Jul. 1985, pp. 137–147, DOI:10.1016/0167-6636(85)90012-2.

[93] K. Ken-Ichi, “Distribution of directional data and fabric tensors,” *International Journal of Engineering Science*, vol. 22, Jan. 1984, pp. 149–164, DOI:10.1016/0020-7225(84)90090-9.

[94] A.J. Stershic, S. Simunovic, and J. Nanda, “Modeling the evolution of lithium-ion particle contact distributions using a fabric tensor approach,” *Journal of Power Sources*, vol. 297, Nov. 2015, pp. 540–550, DOI:10.1016/j.jpowsour.2015.07.088.

[95] T. Olsen and K. Kamrin, “Modeling tensorial conductivity of particle suspension networks,” *Soft Matter*, vol. 11, 2015, pp. 3875–3883, DOI:10.1039/C5SM00093A.

[96] M. Kachanov and I. Sevostianov, “On quantitative characterization of microstructures and effective properties,” *International Journal of Solids and Structures*, vol. 42, Jan. 2005, pp. 309–336, DOI:10.1016/j.ijsolstr.2004.06.016.

[97] J. Choo, Y.J. Kim, J.H. Lee, T.S. Yun, J. Lee, and Y.S. Kim, “Stress-induced evolution of anisotropic thermal conductivity of dry granular materials,” *Acta Geotechnica*, vol. 8, Feb. 2013, pp. 91–106, DOI:10.1007/s11440-012-0174-7.

[98] W. L. Vargas and J.J. McCarthy, “Stress effects on the conductivity of particulate beds,” *Chemical Engineering Science*, vol. 57, Aug. 2002, pp. 3119–3131, DOI:10.1016/S0009-2509(02)00176-8.

[99] E.W. Tiedje and P. Guo, “Modeling the influence of particulate geometry on the thermal conductivity of composites,” *Journal of Materials Science*, vol. 49, 2014, pp. 5586–5597, DOI:10.1007/s10853-014-8268-2.

[100] U. El Shamy, O. De Leon, and R. Wells, “Discrete Element Method Study on Effect of Shear-Induced Anisotropy on Thermal Conductivity of Granular Soils,” *International Journal of Geomechanics*, vol. 13, Feb. 2013, pp. 57–64, DOI:10.1061/(ASCE)GM.1943-5622.0000165.

[101] T.P. Harrigan and R.W. Mann, “Characterization of microstructural anisotropy in orthotropic materials using a second rank tensor,” *Journal of Materials Science*, vol. 19, Mar. 1984, pp. 761–767, DOI:10.1007/BF00540446.

[102] M.A. Klatt, G.E. Schröder-Turk, and K. Mecke, “Mean-intercept anisotropy analysis of porous media. I. Analytic formulae for anisotropic Boolean models:,” *Medical Physics*, vol. 44, 2017, pp. 3650–3662, DOI:10.1002/mp.12281.

[103] M.A. Klatt, G.E. Schröder-Turk, and K. Mecke, “Mean-intercept anisotropy analysis of porous media. II. Conceptual shortcomings of the MIL tensor definition and Minkowski tensors as an alternative,” *Medical Physics*, vol. 44, Jul. 2017, pp. 3663–3675, DOI:10.1002/mp.12280.

[104] L.M. Cruz-Orive, L.M. Karlsson, S.E. Larsen, and F. Wainschtein, “Characterizing anisotropy: A new concept,” *Micron and Microscopica Acta*, vol. 23, Jan. 1992, pp. 75–76, DOI:10.1016/0739-6260(92)90076-P.

[105] Smit, Schneider, and Odgaard, “Star length distribution: a volume-based concept for the characterization of structural anisotropy,” *Journal of Microscopy*, vol. 191, Sep. 1998, pp. 249–257, DOI:10.1046/j.1365-2818.1998.00394.x.

[106] D. Inglis and S. Pietruszczak, “Characterization of anisotropy in porous media by means of linear intercept measurements,” *International Journal of Solids and Structures*, vol. 40, Mar. 2003, pp. 1243–1264, DOI:10.1016/S0020-7683(02)00595-4.

[107] X. Li and H.-S. Yu, “Fabric, force and strength anisotropies in granular materials: a micromechanical insight,” *Acta Mechanica*, vol. 225, Aug. 2014, pp. 2345–2362, DOI:10.1007/s00707-014-1120-6.

[108] E. Azéma, F. Radjai, and G. Saussine, “Quasistatic rheology, force transmission and fabric properties of a packing of irregular polyhedral particles,” *Mechanics of Materials*, vol. 41, Jun. 2009, pp. 729–741, DOI:10.1016/j.mechmat.2009.01.021.

[109] A.G. Gibson, G. Kotsikos, J.H. Bland, and S. Toll, “Squeeze flow,” *Rheological Measurement*, Dordrecht: Springer Netherlands, 1998, pp. 550–592, DOI:10.1007/978-94-011-4934-1_18.

[110] E.C. McIntyre, “Compression of Smart Materials: Squeeze Flow of Electrorheological and Magnetorheological Fluids,” Thesis, University of Michigan, 2008, https://deepblue.lib.umich.edu/bitstream/handle/2027.42/60702/ecarlm_1.pdf?sequence=1&isAllowed=y.

[111] J. Engmann, C. Servais, and A.S. Burbidge, “Squeeze flow theory and applications to rheometry: A review,” *Journal of Non-Newtonian Fluid Mechanics*, vol. 132, 2005, pp. 1–27, DOI:10.1016/j.jnnfm.2005.08.007.

[112] J.D. Jackson, “A study of squeezing flow,” *Applied Scientific Research*, vol. 11, Jan. 1963, pp. 148–152, DOI:10.1007/BF03184719.

[113] M.M. Rashidi, H. Shahmohamadi, and S. Dinarvand, “Analytic Approximate Solutions for Unsteady Two-Dimensional and Axisymmetric Squeezing Flows between Parallel Plates,” *Mathematical Problems in Engineering*, vol. 2008, 2008, pp. 1–13, DOI:10.1155/2008/935095.

[114] J. Lang, S. Santhanam, and Q. Wu, “Exact and approximate solutions for transient squeezing flow,” *Physics of Fluids*, vol. 29, Oct. 2017, p. 103606, DOI:10.1063/1.4999071.

[115] S. Chatraei, C.W. Macosko, and H.H. Winter, “Lubricated Squeezing Flow: A New Biaxial Extensional Rheometer,” *Journal of Rheology*, vol. 25, Aug. 1981, pp. 433–443, DOI:10.1122/1.549648.

[116] N. Delhaye, A. Poitou, and M. Chaouche, “Squeeze flow of highly concentrated suspensions of spheres,” *Journal of Non-Newtonian Fluid Mechanics*, vol. 94, Nov. 2000, pp. 67–74, DOI:10.1016/S0377-0257(00)00130-0.

[117] S. Mascia and D.I. Wilson, “Rheology of concentrated granular suspensions undergoing squeeze flow,” *Journal of Rheology*, vol. 51, May. 2007, pp. 493–515, DOI:10.1122/1.2716448.

[118] N. Bajaj, G. Subbarayan, and S. V. Garimella, “Squeeze flow characterization of particle-filled polymeric materials through image correlation,” *2010 12th IEEE Intersociety Conference on Thermal and Thermomechanical Phenomena in Electronic Systems, ITherm 2010*, 2010, pp. 1–6, DOI:10.1109/ITHERM.2010.5501302.

[119] A. Poitou and G. Racineux, “A squeezing experiment showing binder migration in concentrated suspensions,” *Journal of Rheology*, vol. 45, 2002, pp. 609–625, DOI:10.1122/1.1366717.

[120] A. Ramachandran and D.T. Leighton, “Particle migration in concentrated suspensions undergoing squeeze flow,” *Journal of Rheology*, vol. 54, May. 2010, pp. 563–589, DOI:10.1122/1.3372837.

[121] R.J. Phillips, R.C. Armstrong, R.A. Brown, A.L. Graham, and J.R. Abbott, “A constitutive equation for concentrated suspensions that accounts for shear-induced particle migration,” *Physics of Fluids A: Fluid Dynamics*, vol. 4, Jan. 1992, pp. 30–40, DOI:10.1063/1.858498.

[122] J. Collomb, F. Chaari, and M. Chaouche, “Squeeze flow of concentrated suspensions of spheres in Newtonian and shear-thinning fluids,” *Journal of Rheology*, vol. 48, Mar. 2004, pp. 405–416, DOI:10.1122/1.1645514.

[123] M. Nikkhoo, A. Hofman, and F. Gadala-Maria, “Radial filtration in highly concentrated suspensions undergoing constant-force squeeze flow and its effect on the normal stress distribution,” *Rheologica Acta*, vol. 53, Apr. 2014, pp. 303–314, DOI:10.1007/s00397-014-0763-5.

[124] M. Nikkhoo, “Squeeze flow of highly concentrated suspensions,” Thesis, University of South Carolina, 2013, https://scholarcommons.sc.edu/etd/2512.

[125] F. Kolenda, P. Retana, G. Racineux, and A. Poitou, “Identification of rheological parameters by the squeezing test,” *Powder Technology*, vol. 130, Feb. 2003, pp. 56–62, DOI:10.1016/S0032-5910(02)00227-9.

[126] F. Chaari, G. Racineux, A. Poitou, and M. Chaouche, “Rheological behavior of sewage sludge and strain-induced dewatering,” *Rheologica Acta*, vol. 42, May. 2003, pp. 273–279, DOI:10.1007/s00397-002-0276-5.

[127] M. Nikkhoo, K. Khodabandehlou, L. Brozovsky, and F. Gadala-Maria, “Normal stress distribution in highly concentrated suspensions undergoing squeeze flow,” *Rheologica Acta*, vol. 52, Feb. 2013, pp. 155–163, DOI:10.1007/s00397-013-0681-y.

[128] J.D. Sherwood, “Liquid–solid relative motion during squeeze flow of pastes,” *Journal of Non-Newtonian Fluid Mechanics*, vol. 104, Apr. 2002, pp. 1–32, DOI:10.1016/S0377-0257(02)00011-3.

[129] D.F. Rae, “THERMAL INTERFACE MATERIAL BONDLINES: PARTICULATE FLOWS IN CONFINED GEOMETRIES; PROCESS DEPENDENT MICROSTRUCTURE AND THERMAL PERFORMANCE,” Thesis, Binghamton University, 2016.

[130] R.H. Khiabani, Y. Joshi, and C.K. Aidun, “Thermal properties of particulate TIMs in squeeze flow,” *International Journal of Heat and Mass Transfer*, vol. 53, 2010, pp. 4039–4046, DOI:10.1016/j.ijheatmasstransfer.2010.05.023.

[131] K. Pietrak and T.S. Winiewski, “A review of models for effective thermal conductivity of composite materials,” *Open Access Journal Journal of Power Technologies*, vol. 95, 2015, pp. 14–24, DOI:10.1109/TPAMI.1986.4767851.

[132] R. Dayal and T. Gambaryan-Roisman, “Heat transfer in granular medium for application to selective laser melting: A numerical study,” *International Journal of Thermal Sciences*, vol. 113, Mar. 2017, pp. 38–50, DOI:10.1016/j.ijthermalsci.2016.11.014.

[133] W.L. Vargas and J.J. McCarthy, “Heat conduction in granular materials,” *AIChE Journal*, vol. 47, May. 2001, pp. 1052–1059, DOI:10.1002/aic.690470511.

[134] Y. Liang and X. Li, “A new model for heat transfer through the contact network of randomly packed granular material,” *Applied Thermal Engineering*, vol. 73, Dec. 2014, pp. 984–992, DOI:10.1016/j.applthermaleng.2014.08.063.

[135] W. Dai, D. Hanaor, and Y. Gan, “The effects of packing structure on the effective thermal conductivity of granular media: A grain scale investigation,” *International Journal of Thermal Sciences*, vol. 142, Aug. 2019, pp. 266–279, DOI:10.1016/j.ijthermalsci.2019.04.028.

[136] G.K. Batchelor, F.R. S., and R.W. O’Brien, “Thermal or electrical conduction through a granular material,” *Profeedings of the Royal Society A*, 1976, DOI:10.1098/rspa.1983.0054.

[137] A. Khoubani, T.M. Evans, and T.S. Yun, “Thermal percolation in mixtures of monodisperse spheres,” *Granular Matter*, vol. 22, Aug. 2020, p. 60, DOI:10.1007/s10035-020-01028-8.

[138] W.L. Vargas and J.. McCarthy, “Conductivity of granular media with stagnant interstitial fluids via thermal particle dynamics simulation,” *International Journal of Heat and Mass Transfer*, vol. 45, Nov. 2002, pp. 4847–4856, DOI:10.1016/S0017-9310(02)00175-8.

[139] B. Dan, B.G. Sammakia, G. Subbarayan, S. Kanuparthi, and S. Mallampati, "The Study of the Polydispersivity Effect on the Thermal Conductivity of Particulate Thermal Interface Materials by Finite Element Method," *IEEE Transactions on Components, Packaging and Manufacturing Technology*, vol. 3, Dec. 2013, pp. 2068–2074, DOI:10.1109/TCPMT.2013.2286996.

[140] D. Lee, K. Pham, M. Kang, S. Park, and H. Choi, "Stepwise DE/FE combined approach for estimating effective thermal conductivity of frozen spherical particulate media," *Computers and Geotechnics*, vol. 128, Dec. 2020, p. 103837, DOI:10.1016/j.compgeo.2020.103837.

[141] S.R. Stock, "X-ray microtomography of materials," *International Materials Reviews*, vol. 44, Apr. 1999, pp. 141–164, DOI:10.1179/095066099101528261.

[142] M. Kampschulte, A. Langheinirch, J. Sender, H. Litzlbauer, U. Althöhn, J. Schwab, E. Alejandre-Lafont, G. Martels, and G. Krombach, "Nano-Computed Tomography: Technique and Applications," *RöFo - Fortschritte auf dem Gebiet der Röntgenstrahlen und der bildgebenden Verfahren*, vol. 188, Jan. 2016, pp. 146–154, DOI:10.1055/s-0041-106541.

[143] P. Chaurand, W. Liu, D. Borschneck, C. Levard, M. Auffan, E. Paul, B. Collin, I. Kieffer, S. Lanone, J. Rose, and J. Perrin, "Multi-scale X-ray computed tomography to detect and localize metal-based nanomaterials in lung tissues of in vivo exposed mice," *Scientific Reports*, vol. 8, Dec. 2018, p. 4408, DOI:10.1038/s41598-018-21862-4.

[144] A. Yermukhambetova, C. Tan, S.R. Daemi, Z. Bakenov, J.A. Darr, D.J.L. Brett, and P.R. Shearing, "Exploring 3D microstructural evolution in Li-Sulfur battery electrodes using in-situ X-ray tomography," *Scientific Reports*, vol. 6, 2016, pp. 1–9, DOI:10.1038/srep35291.

[145] A. Etiemble, J. Adrien, E. Maire, H. Idrissi, D. Reyter, and L. Roué, "3D morphological analysis of copper foams as current collectors for Li-ion batteries by means of X-ray tomography," *Materials Science and Engineering: B*, vol. 187, Sep. 2014, pp. 1–8, DOI:10.1016/j.mseb.2014.04.006.

[146] M. Ebner, F. Geldmacher, F. Marone, M. Stampanoni, and V. Wood, "X-Ray Tomography of Porous, Transition Metal Oxide Based Lithium Ion Battery Electrodes," *Advanced Energy Materials*, vol. 3, Jul. 2013, pp. 845–850, DOI:10.1002/aenm.201200932.

[147] E. Maire and P.J. Withers, "Quantitative X-ray tomography," *International Materials Reviews*, vol. 59, 2014, pp. 1–43, DOI:10.1179/1743280413Y.0000000023.

[148] N.R. Backeberg, F. Iacoviello, M. Rittner, T.M. Mitchell, A.P. Jones, R. Day, J. Wheeler, P.R. Shearing, P. Vermeesch, and A. Striolo, "Quantifying the anisotropy and tortuosity of permeable pathways in clay-rich mudstones using models based on X-ray tomography," *Scientific Reports*, vol. 7, Dec. 2017, p. 14838, DOI:10.1038/s41598-017-14810-1.

[149] E. Herremans, P. Verboven, B.E. Verlinden, D. Cantre, M. Abera, M. Wevers, and B.M. Nicolaï, "Automatic analysis of the 3-D microstructure of fruit parenchyma tissue using X-ray micro-CT explains differences in aeration," *BMC Plant Biology*, vol. 15, Dec. 2015, p. 264, DOI:10.1186/s12870-015-0650-y.

[150] I.C. Sinka, S.F. Burch, J.H. Tweed, and J.C. Cunningham, "Measurement of density variations in tablets using X-ray computed tomography," *International Journal of Pharmaceutics*, vol. 271, Mar. 2004, pp. 215–224, DOI:10.1016/j.ijpharm.2003.11.022.

[151] J. ZEITLER and L. GLADDEN, "In-vitro tomography and non-destructive imaging at depth of pharmaceutical solid dosage forms," *European Journal of Pharmaceutics and Biopharmaceutics*, vol. 71, Jan. 2009, pp. 2–22, DOI:10.1016/j.ejpb.2008.08.012.

[152] C. Chappard, A. Basillais, L. Benhamou, A. Bonassie, B. Brunet-Imbault, N. Bonnet, and F. Peyrin, "Comparison of synchrotron radiation and conventional x-ray microcomputed tomography for assessing trabecular bone microarchitecture of human femoral heads," *Medical Physics*, vol. 33, Sep. 2006, pp. 3568–3577, DOI:10.1118/1.2256069.

[153] J. Van Dessel, Y. Huang, M. Depypere, I. Rubira-Bullen, F. Maes, and R. Jacobs, "A comparative evaluation of cone beam CT and micro-CT on trabecular bone structures in the human mandible," *Dentomaxillofacial Radiology*, vol. 42, Aug. 2013, p. 20130145, DOI:10.1259/dmfr.20130145.

[154] J. Gelb, D.P. Finegan, D.J.L. Brett, and P.R. Shearing, "Multi-scale 3D investigations of a commercial 18650 Li-ion battery with correlative electron- and X-ray microscopy," *Journal of Power Sources*, vol. 357, Jul. 2017, pp. 77–86, DOI:10.1016/j.jpowsour.2017.04.102.

[155] C.H. Arns, F. Bauget, A. Limaye, A. Sakellariou, T. Senden, A. Sheppard, R.M. Sok, V. Pinczewski, S. Bakke, L.I. Berge, P.E. Oren, and M.A. Knackstedt, "Pore Scale Characterization of Carbonates Using X-Ray Microtomography," *SPE Journal*, vol. 10, Dec. 2005, pp. 475–484, DOI:10.2118/90368-PA.

[156] S.J. Cooper, A. Bertei, P.R. Shearing, J.A. Kilner, and N.P. Brandon, “TauFactor: An open-source application for calculating tortuosity factors from tomographic data,” *SoftwareX*, vol. 5, 2016, pp. 203–210, DOI:10.1016/j.softx.2016.09.002.

[157] J.C. Ferguson, F. Panerai, A. Borner, and N.N. Mansour, “PuMA: the Porous Microstructure Analysis software,” *SoftwareX*, vol. 7, 2018, pp. 81–87, DOI:10.1016/j.softx.2018.03.001.

[158] V. BUSIGNIES, B. LECLERC, P. PORION, P. EVESQUE, G. COUARRAZE, and P. TCHORELOFF, “Quantitative measurements of localized density variations in cylindrical tablets using X-ray microtomography,” *European Journal of Pharmaceutics and Biopharmaceutics*, vol. 64, Aug. 2006, pp. 38–50, DOI:10.1016/j.ejpb.2006.02.007.

[159] D. Wildenschild and A.P. Sheppard, “X-ray imaging and analysis techniques for quantifying pore-scale structure and processes in subsurface porous medium systems,” *Advances in Water Resources*, vol. 51, Jan. 2013, pp. 217–246, DOI:10.1016/j.advwatres.2012.07.018.

[160] G.T. Herman, “Correction for beam hardening in computed tomography,” *Physics in Medicine and Biology*, vol. 24, Jan. 1979, p. 008, DOI:10.1088/0031-9155/24/1/008.

[161] L. a Feldkamp, L.C. Davis, and J.W. Kress, “Practical cone-beam algorithm,” *Journal of the Optical Society of America A*, vol. 1, Jun. 1984, p. 612, DOI:10.1364/JOSAA.1.000612.

[162] R.A. Ketcham and W.D. Carlson, “Acquisition, optimization and interpretation of X-ray computed tomographic imagery: applications to the geosciences,” *Computers & Geosciences*, vol. 27, May. 2001, pp. 381–400, DOI:10.1016/S0098-3004(00)00116-3.

[163] R.A. Ketcham and R.D. Hanna, “Beam hardening correction for X-ray computed tomography of heterogeneous natural materials,” *Computers & Geosciences*, vol. 67, Jun. 2014, pp. 49–61, DOI:10.1016/j.cageo.2014.03.003.

[164] J.F. Barrett and N. Keat, “Artifacts in CT: Recognition and Avoidance,” *RadioGraphics*, vol. 24, Nov. 2004, pp. 1679–1691, DOI:10.1148/rg.246045065.

[165] J. Hsieh, “Adaptive streak artifact reduction in computed tomography resulting from excessive x-ray photon noise,” *Medical Physics*, vol. 25, Nov. 1998, pp. 2139–2147, DOI:10.1118/1.598410.

[166] S. Luding, “Introduction to discrete element methods. Basics of contact force models and how to perform the micro-macro transition to continuum theory,” *Revue européenne de génie civil*, vol. 12, Oct. 2008, pp. 785–826, DOI:10.3166/ejece.12.785-826.

[167] D. Zhao, E.G. Nezami, Y.M. a. Hashash, and J. Ghaboussi, “Three-dimensional discrete element simulation for granular materials,” *Engineering Computations*, vol. 23, Oct. 2006, pp. 749–770, DOI:10.1108/02644400610689884.

[168] A. Munjiza, J.P. Latham, and N.W.M. John, “3D dynamics of discrete element systems comprising irregular discrete elements - integration solution for finite rotations in 3D,” *International Journal for Numerical Methods in Engineering*, vol. 56, Jan. 2003, pp. 35–55, DOI:10.1002/nme.552.

[169] P.A. Cundall and O.D.L. Strack, “A discrete numerical model for granular assemblies,” *Géotechnique*, vol. 29, Mar. 1979, pp. 47–65, DOI:10.1680/geot.1979.29.1.47.

[170] H. Jaeger, S. Nagel, and R. Behringer, “Granular solids, liquids, and gases,” *Reviews of Modern Physics*, vol. 68, 1996, pp. 1259–1273, DOI:10.1103/RevModPhys.68.1259.

[171] L. Staron, P.Y. Lagrée, C. Josserand, and D. Lhuillier, “Flow and jamming of a two-dimensional granular bed: Toward a nonlocal rheology?,” *Physics of Fluids*, vol. 22, 2010, DOI:10.1063/1.3499353.

[172] J. Tang and R.P. Behringer, “How granular materials jam in a hopper,” *Chaos: An Interdisciplinary Journal of Nonlinear Science*, vol. 21, Dec. 2011, p. 041107, DOI:10.1063/1.3669495.

[173] S. Bin Yeom, E. Ha, M. Kim, S.H. Jeong, S.J. Hwang, and D.H. Choi, “Application of the discrete element method for manufacturing process simulation in the pharmaceutical industry,” *Pharmaceutics*, vol. 11, 2019, DOI:10.3390/pharmaceutics11080414.

[174] M.M. Sazzad and K. Suzuki, “Micromechanical behavior of granular materials with inherent anisotropy under cyclic loading using 2D DEM,” *Granular Matter*, vol. 12, Dec. 2010, pp. 597–605, DOI:10.1007/s10035-010-0200-0.

[175] W. Wang, W. Gu, and K. Liu, “Force Chain Evolution and Force Characteristics of Shearing Granular Media in Taylor-Couette Geometry by DEM,” *Tribology Transactions*, vol. 58, Mar. 2015, pp. 197–206, DOI:10.1080/10402004.2014.943829.

[176] C. O'Sullivan and L. Cui, "Micromechanics of granular material response during load reversals: Combined DEM and experimental study," *Powder Technology*, vol. 193, Aug. 2009, pp. 289–302, DOI:10.1016/j.powtec.2009.03.003.

[177] W. Liu, S. Li, A. Baule, and H.A. Makse, "Adhesive loose packings of small dry particles," *Soft Matter*, vol. 11, 2015, pp. 6492–6498, DOI:10.1039/C5SM01169H.

[178] E.J.R. Parteli, J. Schmidt, C. Blümel, K. Wirth, W. Peukert, and T. Pöschel, "Attractive particle interaction forces and packing density of fine glass powders," *Scientific Reports*, vol. 4, May. 2015, p. 6227, DOI:10.1038/srep06227.

[179] E.J.R. Parteli, "DEM simulation of particles of complex shapes using the multisphere method: Application for additive manufacturing," *AIP Conference Proceedings*, 2013, pp. 185–188, DOI:10.1063/1.4811898.

[180] E.J.R. Parteli and T. Pöschel, "Particle-based simulation of powder application in additive manufacturing," *Powder Technology*, vol. 288, Jan. 2016, pp. 96–102, DOI:10.1016/j.powtec.2015.10.035.

[181] J.C. Steuben, A.P. Iliopoulos, and J.G. Michopoulos, "Discrete element modeling of particle-based additive manufacturing processes," *Computer Methods in Applied Mechanics and Engineering*, vol. 305, Jun. 2016, pp. 537–561, DOI:10.1016/j.cma.2016.02.023.

[182] S. Haeri, "Optimisation of blade type spreaders for powder bed preparation in Additive Manufacturing using DEM simulations," *Powder Technology*, vol. 321, Nov. 2017, pp. 94–104, DOI:10.1016/j.powtec.2017.08.011.

[183] S. Li, J.S. Marshall, G. Liu, and Q. Yao, "Adhesive particulate flow: The discrete-element method and its application in energy and environmental engineering," *Progress in Energy and Combustion Science*, vol. 37, Dec. 2011, pp. 633–668, DOI:10.1016/j.pecs.2011.02.001.

[184] H. Tao, B. Jin, W. Zhong, X. Wang, B. Ren, Y. Zhang, and R. Xiao, "Discrete element method modeling of non-spherical granular flow in rectangular hopper," *Chemical Engineering and Processing: Process Intensification*, vol. 49, Feb. 2010, pp. 151–158, DOI:10.1016/j.cep.2010.01.006.

[185] W.R. Ketterhagen, J.S. Curtis, C.R. Wassgren, A. Kong, P.J. Narayan, and B.C. Hancock, "Granular segregation in discharging cylindrical hoppers: A discrete element and experimental study," *Chemical Engineering Science*, vol. 62, Nov. 2007, pp. 6423–6439, DOI:10.1016/j.ces.2007.07.052.

[186] A. Anand, J.S. Curtis, C.R. Wassgren, B.C. Hancock, and W.R. Ketterhagen, "Predicting discharge dynamics from a rectangular hopper using the discrete element method (DEM)," *Chemical Engineering Science*, vol. 63, Dec. 2008, pp. 5821–5830, DOI:10.1016/j.ces.2008.08.015.

[187] H. Kruggel-Emden, E. Simsek, S. Rickelt, S. Wirtz, and V. Scherer, "Review and extension of normal force models for the Discrete Element Method," *Powder Technology*, vol. 171, Feb. 2007, pp. 157–173, DOI:10.1016/j.powtec.2006.10.004.

[188] M. Grob, C. Heussinger, and A. Zippelius, "Jamming of Frictional Particles: a First Order Phase Transition," *arXiv*, vol. 2, 2013, p. 1311.5416, DOI:10.1103/PhysRevE.89.050201.

[189] M.P. Ciamarra, R. Pastore, M. Nicodemi, and A. Coniglio, "Jamming phase diagram for frictional particles," *Physical Review E - Statistical, Nonlinear, and Soft Matter Physics*, vol. 84, 2011, DOI:10.1103/PhysRevE.84.041308.

[190] S. Luding, "Cohesive, frictional powders: Contact models for tension," *Granular Matter*, vol. 10, 2008, pp. 235–246, DOI:10.1007/s10035-008-0099-x.

[191] P.G. Rognon, J.-N. Roux, M. Naaïm, and F. Chevoir, "Dense flows of cohesive granular materials," *Journal of Fluid Mechanics*, vol. 596, 2008, pp. 21–47, DOI:10.1017/S0022112007009329.

[192] A. Jordam Caserta, H.A. Navarro, and L. Cabezas-Gómez, "Damping coefficient and contact duration relations for continuous nonlinear spring-dashpot contact model in DEM," *Powder Technology*, vol. 302, 2016, pp. 462–479, DOI:10.1016/j.powtec.2016.07.032.

[193] R. Garg, J. Galvin, T. Li, and S. Pannala, "Open-source MFIX-DEM software for gas–solids flows: Part I—Verification studies," *Powder Technology*, vol. 220, Apr. 2012, pp. 122–137, DOI:10.1016/j.powtec.2011.09.019.

[194] J. Liu, B. Michel, M. Rencz, C. Tantolin, C. Sarno, R. Miessner, K.V. Schuett, X. Tang, S. Demoustier, and A. Ziaei, "Recent progress of thermal interface material research - an overview," *14th International Workshop on THERMal INvestigation of ICs and Systems, THERMINIC 2008*, 2008, pp. 156–162, DOI:10.1109/THERMINIC.2008.4669900.

[195] P. Kohli, M. Sobczak, J. Bowin, and M. Matthews, “Advanced thermal interface materials for enhanced flip chip BGA,” *2001 Proceedings. 51st Electronic Components and Technology Conference (Cat. No.01CH37220)*, IEEE, 2001, pp. 564–570, DOI:10.1109/ECTC.2001.927784.

[196] R. Kantharaj, I. Srivastava, K.R. Thaker, A.U. Gaitonde, A. Bruce, J. Howarter, T.S. Fisher, and A.M. Marconnet, “Thermal conduction in graphite flake-epoxy composites using infrared microscopy,” *2017 16th IEEE Intersociety Conference on Thermal and Thermomechanical Phenomena in Electronic Systems (ITherm)*, IEEE, 2017, pp. 1–7, DOI:10.1109/ITHERM.2017.8023960.

[197] J. Ahrens, B. Geveci, and C. Law, “ParaView: An End-User Tool for Large Data Visualization,” *Visualization Handbook, Elsevier*, 2005, DOI:ISBN-13: 978-0123875822.

[198] J. Schindelin, I. Arganda-Carreras, E. Frise, V. Kaynig, M. Longair, T. Pietzsch, S. Preibisch, C. Rueden, S. Saalfeld, B. Schmid, J.Y. Tinevez, D.J. White, V. Hartenstein, K. Eliceiri, P. Tomancak, and A. Cardona, “Fiji: An open-source platform for biological-image analysis,” *Nature Methods*, vol. 9, 2012, pp. 676–682, DOI:10.1038/nmeth.2019.

[199] B.A.F. Kopera and M. Retsch, “Computing the 3D Radial Distribution Function from Particle Positions: An Advanced Analytic Approach,” *Analytical Chemistry*, vol. 90, 2018, pp. 13909–13914, DOI:10.1021/acs.analchem.8b03157.

[200] A. Abi-Mansour, S. McClure, and M. Gentzler, “XRCT characterization of mesoscopic structure in poured and tapped cohesive powders and prediction by DEM,” *Powder Technology*, vol. 330, 2018, pp. 386–396, DOI:10.1016/j.powtec.2018.01.081.

[201] I. Vlahinić, E. Andò, G. Viggiani, and J.E. Andrade, “Towards a more accurate characterization of granular media: Extracting quantitative descriptors from tomographic images,” *Granular Matter*, vol. 16, 2014, pp. 9–21, DOI:10.1007/s10035-013-0460-6.

[202] M. Curie, S. Bernard, and P. Cedex, *3D Processing and Analysis with ImageJ*, 2008, http://imagejconf.tudor.lu/_export/pdf/program/workshops/boudier/start.

[203] J. Ollion, J. Cochennec, F. Loll, C. Escudé, and T. Boudier, “TANGO: a generic tool for high-throughput 3D image analysis for studying nuclear organization,” *Bioinformatics*, vol. 29, Jul. 2013, pp. 1840–1841, DOI:10.1093/bioinformatics/btt276.

[204] L. Su, X. Fu, X. Zhang, X. Cheng, Y. Ma, Y. Gan, and Q. Hu, "Delineation of Carpal Bones From Hand X-Ray Images Through Prior Model, and Integration of Region-Based and Boundary-Based Segmentations," *IEEE Access*, vol. 6, 2018, pp. 19993–20008, DOI:10.1109/ACCESS.2018.2815031.

[205] P. Iassonov, T. Gebrenegus, and M. Tuller, "Segmentation of X-ray computed tomography images of porous materials: A crucial step for characterization and quantitative analysis of pore structures," *Water Resources Research*, vol. 45, 2009, pp. 1–12, DOI:10.1029/2009WR008087.

[206] A. Buades, B. Coll, and J.-M. Morel, "Non-Local Means Denoising," *Image Processing On Line*, vol. 1, Sep. 2011, pp. 208–212, DOI:10.5201/ipol.2011.bcm_nlm.

[207] O.I. Camps, T. Kanungo, and R.M. Haralick, "Gray-scale structuring element decomposition," *IEEE Transactions on Image Processing*, vol. 5, 1996, pp. 111–120, DOI:10.1109/83.481675.

[208] N. Otsu, "A Threshold Selection Method from Gray-Level Histograms," *IEEE Transactions on Systems, Man, and Cybernetics*, vol. 9, Jan. 1979, pp. 62–66, DOI:10.1109/TSMC.1979.4310076.

[209] D. Legland, I. Arganda-Carreras, and P. Andrey, "MorphoLibJ: Integrated library and plugins for mathematical morphology with ImageJ," *Bioinformatics*, vol. 32, 2016, pp. 3532–3534, DOI:10.1093/bioinformatics/btw413.

[210] X. Fu, J.A. Elliott, A.C. Bentham, B.C. Hancock, and R.E. Cameron, "Application of X-ray microtomography and image processing to the investigation of a compacted granular system," *Particle and Particle Systems Characterization*, vol. 23, 2006, pp. 229–236, DOI:10.1002/ppsc.200601054.

[211] I. Gueven, S. Frijters, J. Harting, S. Luding, and H. Steeb, "Hydraulic properties of porous sintered glass bead systems," *Granular Matter*, vol. 19, 2017, pp. 1–21, DOI:10.1007/s10035-017-0705-x.

[212] P. Soille and L.M. Vincent, "Determining watersheds in digital pictures via flooding simulations," *Visual Communications and Image Processing '90: Fifth in a Series*, vol. 1360, 1990, pp. 240–250, DOI:10.1117/12.24211.

[213] Y. Wang, C.L. Lin, and J.D. Miller, “Improved 3D image segmentation for X-ray tomographic analysis of packed particle beds,” *Minerals Engineering*, vol. 83, Nov. 2015, pp. 185–191, DOI:10.1016/j.mineng.2015.09.007.

[214] Y. Wang, C.L. Lin, and J.D. Miller, “3D image segmentation for analysis of multisize particles in a packed particle bed,” *Powder Technology*, vol. 301, 2016, pp. 160–168, DOI:10.1016/j.powtec.2016.05.012.

[215] S. BOLTE and F.P. CORDELIÈRES, “A guided tour into subcellular colocalization analysis in light microscopy,” *Journal of Microscopy*, vol. 224, Dec. 2006, pp. 213–232, DOI:10.1111/j.1365-2818.2006.01706.x.

[216] F. Esmonde-White, “Binary STL File Reader” https://www.mathworks.com/matlabcentral/fileexchange/29906-binary-stl-file-reader.

[217] S. Mueller, E.W. Llewellin, and H.M. Mader, “The rheology of suspensions of solid particles,” *Proceedings of the Royal Society A: Mathematical, Physical and Engineering Sciences*, vol. 466, Apr. 2010, pp. 1201–1228, DOI:10.1098/rspa.2009.0445.

[218] S.H. Maron and P.E. Pierce, “Application of Ree-Eyring generalized flow theory to suspensions of spherical particles,” *Journal of Colloid Science*, vol. 11, Feb. 1956, pp. 80–95, DOI:10.1016/0095-8522(56)90023-X.

[219] T. Li, R. Garg, J. Galvin, and S. Pannala, “Open-source MFIX-DEM software for gas-solids flows: Part II — Validation studies,” *Powder Technology*, vol. 220, Apr. 2012, pp. 138–150, DOI:10.1016/j.powtec.2011.09.020.

[220] MFS Development Group, *MFIX User Guide, Release 21.1*, 2021, https://mfix.netl.doe.gov/mfix/mfix-documentation/.

[221] S. Dey, S. Zeeshan Ali, and E. Padhi, “Terminal fall velocity: the legacy of Stokes from the perspective of fluvial hydraulics,” *Proceedings of the Royal Society A: Mathematical, Physical and Engineering Sciences*, vol. 475, Aug. 2019, p. 20190277, DOI:10.1098/rspa.2019.0277.

[222] J. Ding and D. Gidaspow, “A bubbling fluidization model using kinetic theory of granular flow,” *AIChE Journal*, vol. 36, Apr. 1990, pp. 523–538, DOI:10.1002/aic.690360404.

[223] O. Simonin, S. Chevrier, F. Audard, P. Fede, O. Simonin, S. Chevrier, F. Audard, and P. Fede, “Drag force modelling in dilute to dense particle-laden flows with mono-disperse or binary mixture of solid particles,” 2018, http://oatao.univ-toulouse.fr/.

[224] R. Beetstra, M.A. van der Hoef, and J.A.M. Kuipers, “Drag force of intermediate Reynolds number flow past mono- and bidisperse arrays of spheres,” *AIChE Journal*, vol. 53, Feb. 2007, pp. 489–501, DOI:10.1002/aic.11065.

[225] R.J. HILL, D.L. KOCH, and A.J.C. LADD, “The first effects of fluid inertia on flows in ordered and random arrays of spheres,” *Journal of Fluid Mechanics*, vol. 448, Dec. 2001, pp. 213–241, DOI:10.1017/S0022112001005948.